SYNTHESIS AND CHARACTERIZATION OF MIXED OXIDES CONTAINING COBALT, COPPER AND IRON AND STUDY OF THEIR CATALYTIC ACTIVITY

A thesis submitted to the

UNIVERSITY OF PUNE

for the degree of

DOCTOR OF PHILOSOPHY

(in Chemistry)

BY

THOMAS MATHEW

CATALYSIS DIVISION

NATIONAL CHEMICAL LABORATORY

PUNE- 411008

INDIA

OCTOBER 2002

Dedicated to
My
Elder Brother

CERTIFICATE

Certified that the work incorporated in the thesis, **"Synthesis and characterization of mixed oxides containing Cobalt, Copper and Iron and study of their catalytic activity"** submitted by **Mr. Thomas Mathew,** for the Degree of **Doctor of Philosophy,** was carried out by the candidate under my supervision in the Catalysis Division, National Chemical Laboratory, Pune - 411008, India. Such material as has been obtained from other sources has been duly acknowledged in the thesis.

Dr. B. S. Rao

(Research Supervisor)

ACKNOWLEDGEMENTS

CONTENTS

4 CHARACTERIZATION OF SPENT CATALYSTS AND Co-Cu SYNERGISM

SECTION I

SECTION II

ABBREVIATIONS

Chloranil	2,3,5,6-tetrachloro-1-4-benzoquinone
DMC	Dimethyl carbonate
DRIR	Drift infrared
DTA	Differential thermal analysis
FWHM	Full width at half maximum
2,4-DTBP	2,4-Di tertiary butyl phenol
IS	Isomer shift
MHF	Magnetic hyperfine field
PDNB	p-Dinitro benzene
QS	Quadrupole splitting
RI	Relative spectral area
SEM	Scanning electron microscopy
2-TBP	2-Tertiary butyl phenol
4-TBP	4-Tertiary butyl phenol
TCNQ	7,7,8,8- Tetracyanoquino dimethane
TG	Thermogravimetry
TMP	2,4,6- Trimethyl phenol
TOS	Time on stream
TPD	Temperature programmed desorption
TPR	Temperature programmed reduction
VB	Valence band
WHSV	Weight hourly space velocity
XPS	X-ray photoelectron spectroscopy
XRD	X-ray diffraction

List of publications:

1. Cu-Co Synergism in $Cu_{1-x}Co_xFe_2O_4$ – Catalysis and XPS Aspects.

   T. Mathew, N. R. Shiju, K. Sreekumar, B. S. Rao and C. S. Gopinath, *J. Catal.*, **210** (2002) 405.

2. $Cu_{1-x}Co_xFe_2O_4$ ferrospinels in alkylation: structural changes upon reaction.

   K. Lázár, **T. Mathew**, Z. Koppány, J. Megyeri, V. Samuel, S. P. Mirajkar, B. S. Rao, and L. Guczi, *Phys. Chem. Chem. Phys.*, **4** (2002) 3530.

3. Acid-base properties of $Cu1_{-x}Co_xFe_2O_4$ ferrospinels: FT-IR investigations.

   T. Mathew, N. R. Shiju, B. B. Tope, S. G. Hegde, B. S. Rao and C. S. Gopinath, *Phys. Chem. Chem. Phys.*, **4** (2002) 4260.

4. Thermodynamic study of reaction of phenol with methanol over $Cu_{1-x}Co_xFe_2O_4$ (x = 0, 0.25, 0.50, 0.75 & 1) spinel system.

   T. Mathew, N.R. Shiju, R.Y. Nimje, P.M. Adkine, B.S. Rao and V.V. Bokade, *Chem. Eng. Res. Design* (Accepted for publication)

5. Selective synthesis of 3-picoline via the vapour phase methylation of pyridine with methanol over Ni-Co-Fe ternary spinel systems.

   K.Sreekumar, **Thomas Mathew**, R. Rajagopal, R. Vetrivel and B.S. Rao; *Catal. Lett.*, **65** (2000) 99.

6. Oxidative dehydrogenation of ethylbenzene over $Ni_{1-x}Co_xFe_2O_4$ (x = 0,0.2,0.5,0.8 and 1.0) -type ferrites: Influence of spinel composition on acid-base properties and styrene selectivity.

   K.Sreekumar, **Thomas Mathew**, T.M. Jyothi, Biju M. Devassy, S. Sugunan and B.S. Rao; *Polish Journal of Chemistry*, **74** (2000) 509-517.

7. Formation of 3-picoline and 3,5-lutidine using $Zn_{1-x}Co_xFe_2O_4$ (x = 0,0.2,0.5,0.8 and 1.0) -type ferrites.

   K. Sreekumar, **T. Mathew**, B. M. Devassy, R. Rajgopal, R. Vetrivel and B. S. Rao, *Appl. Catal, A:General*, **205** (2001)11.

8. A comparative study on aniline alkylation activity using methanol and dimethyl carbonate as alkylating agent over $Zn_{1-x}Co_xFe_2O_4$ (x = 0,0.2,0.5,0.8 and 1.0) -type ferrites.

K. Sreekumar, **T. Mathew**, S. P. Mirajkar, S. Sugunan and B. S. Rao, *Appl. Catal, A:General*, **201** (2000) L1.

9. Selective N-methylation of aniline with dimethyl carbonate over Zn1-xCoxFe2O4 (x = 0, 0.2, 0.5, 0.8 and 1.0) type systems.

   K. Sreekumar, T.M. Jyothi, **T. Mathew**, M. B. Talwar, S. Sugunan and B. S. Rao, *J. Mol. Catal*. A, **159** (2000) 327.

CHAPTER 1
INTRODUCTION

1.1. INTRODUCTION

Catalyst synthesis and development have become a wide spread research field because of the increasing global demand for better systems in chemical industry. The successful exploitation of a material as a catalyst will give value-added products with better yields. Research in this field is driven by the effort of the fine chemical and pharmaceutical industries to replace wasteful non-catalytic processes by economical and eco-friendly (green) catalytic routes. Three major areas involving catalysts can be broadly classified as (i) petroleum refining (ii) chemicals and (iii) emission control.

Many new catalysts have been discovered which can be broadly classified either into homogeneous catalysis or heterogeneous catalysis systems. Though homogeneous systems possess several advantages such as better selectivity, activity and reproducibility, they are associated with several drawbacks like low thermal stability and short catalyst life-time, which amplify the cost of production. Hence the synthesis of new heterogeneous systems to replace the existing homogeneous systems has become a challenging task in the catalysis field.

1.2. HETEROGENEOUS CATALYSIS

Heterogeneous catalysis is gaining increasing importance in the production of fine chemicals and pharmaceuticals due to its definite technical advantages, which greatly enhance production processes, competitiveness and economics. For example, heterogeneous catalysts employed as main cracking catalysts in petroleum refinery, which is the largest process among the industrial chemical processes. The main advantage of the heterogeneous catalytic process is that it can be operated continuously in a reactor without interruption. Since the catalyst is present in a phase different from the reactants and the products, the separation of the catalyst from the final reaction mass is also quite easy.

Among various heterogeneous catalysts, oxide systems are versatile and widely used for many organic transformations reactions like oxidation, hydrogenation and dehydrogenation, condensation, cracking, isomerization, alkylation etc. Oxides have an ability to bring about electron transfer as well as proton transfer and they can, therefore, be used in both redox and acid base reactions [1]. Hence oxide catalysts are important from

commercial point of view and have been used for manufacturing many value-added products.

1.3. OXIDES

Classifying metal oxides as catalysts are quite tedious since it involves a variety of crystal systems of different compositions with a wide range of physico-chemical properties. Oxide catalysts fall into two general categories. They are either poor electrical conductors or good conductors. Insulator oxides are those in which the cationic material has a single oxidation state, so they have stoichiometric M:O ratios. The simple oxides, MgO, Al_2O_3 and SiO_2 and the more complex zeolites, which are aluminosilicates, fall into this category. These materials are not effective as oxidation catalysts and find most use as solid acids or bases [2,3].

Semiconductor and conducting oxides are most commonly used in oxidations. They are materials in which the metal ion species is relatively easily cycled between two different valence states. There can be two different oxidation states under reaction conditions as in Fe_2O_3, V_2O_5, TiO_2, CuO or NiO, or the interconversion between the positive ion and neutral metal as with the more easily reduced oxides such as ZnO and CdO. Semiconductor oxides can be either n-type (e.g., Fe_2O_3, V_2O_5, TiO_2, CuO etc) or p-type (e.g., NiO, CoO, Cu_2O etc).

In general, oxides are prepared in single component or in multiple components; they may be crystalline or amorphous and they may be supported or unsupported. While simple oxides show activity for some oxidations they are more commonly used as solid acids or bases. Since single component oxides do not come under the purview of the present study, to list a discussion of them in detail is beyond the scope of this chapter. Complex oxides (mixed metal oxides) can act as acids or bases as well as oxidation catalysts. Complex oxides can range in composition from binary oxides to the more complex ternary and quaternary systems.

1.4. MIXED METAL OXIDES

Oxides of two or more different kinds of cations are known as mixed metal oxides. They can be further classified based on whether they are crystalline or amorphous. If the oxides are crystalline the crystal structure can determine the oxide composition. For instance, perovskites have the general formula ABO_3, scheelites are ABO_4, spinels are AB_2O_4 and palmeirites are $A_3B_2O_8$ [4].

The common feature of mixed oxide catalysts, irrespective of the mode of mutual arrangement of their components, is the presence of M_I^{n+}- O_x and M_{II}^{n+}- O_x polyhedra, where M_I and M_{II} are different cations in their structure. These polyhedra can be connected in various ways, e.g., corner, or edge sharing, forming chains M_I-O-M_{II}-O, M_I-O-M_I-O or M_{II}-O-M_{II}. Various arrangements of atoms of a given element, differing by the coordination, nature and the next neighboring cation and type of bonding may be then exposed on the catalyst surface. It could be then anticipated that different environment of atoms that constitute an active center would give rise to different reactivity towards an approaching molecule.

For mixed oxide catalysts it is not always evident which of the constituent elements plays a role of active centers. Although the industrial catalysts are usually multiphase systems, the presence of one phase, for example spinels, appears usually to be indispensable to render the systems active in a given reaction. One of the most important results of the studies on monophasic systems is the demonstration of different catalytic properties of different crystallographic faces in an oxide, which provided an experimental proof for structure sensitivity phenomenon in the oxide systems.

1.5. PREPARATION OF CATALYSTS

A new catalyst can amplify process efficiency, reduce production cost and replace existing processes with better ones. Recently, a number of fundamental studies concerning the influence of preparation procedures on the catalyst performance have been published [5,6]. In all cases, it was stated that the activity and selectivity of the catalysts were dependent on preparation parameters, in particular thermal activation, thereby suggesting that catalyst preparation is a critical factor. The most common methods used to prepare

complex oxides are co-precipitation [7,8], sol-gel method [9,10], complexation method [8], combustion method [11,12] and ceramic method [13].

1.6. TRANSITION METAL OXIDES AS CATALYSTS

The high catalytic activity of transition metals appears to be one of the most significant facts of heterogeneous catalysis. It is believed that a mixture of oxides brings out a combined effect or a sort of synergistic behavior, which is well known among transition metal oxides, enhancing the catalytic activity [14,15]. Moreover, transition metal ions exhibit various oxidation states, due to intrinsic oxidation-reduction processes [16] or by catalytic reaction [14,15] and that can occur at the same or different sites as a consequence of fine balance of the respective preference of the ions concerned. Selective oxidation, ammoxidation and selective dehydrogenation constitute the most important catalytic uses of transition metal oxides [17]. Many workers have explained the high catalytic activity on the basis of the fact that the cations exert an abnormally strong deforming action and that there is a gradual decrease in the potential of the chemical forces in bonds that are formed by d-electrons, in comparisons with bonds formed by s- and p-electrons.

Due to their ability to have various oxidation state, transition metals form non-stoichiometric oxides, and they have excellent potentials for oxidation and reduction (redox) reactions, because they can both give and accept electrons.

$$M^{n+} \quad\Rightarrow\quad M^{(n+1)+} + e^-$$
$$M^{(n+1)+} + e^- \Rightarrow M^{n+}$$
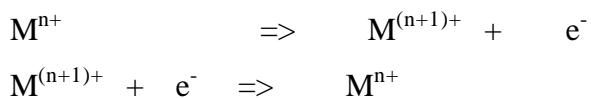
1.7. TYPES OF INTERACTION BETWEEN ORGANIC MOLECULES AND OXIDE SURFACES

The main chemical interactions between the surface of an oxide catalyst and a molecule are:

1. Acid-base interactions (ionic): These can be either of Bronsted or Lewis type involving proton exchange or electron pair donation, respectively. In acid catalyzed reactions,

reactants act as bases toward catalysts which act as acids. On the other hand in a base catalyzed reaction reactants act as acids toward catalysts that act as bases.

2. Redox interactions (electronic): Redox reactions involving the exchange of electrons between the solid and the adsorbed molecules. Such interactions are particularly important in oxidation catalysis.

3. Coordination chemistry interactions: These interactions usually occur when transition metal ions are present in the catalyst or are anchored at the surface of a support and can go from the simple coordination of a ligand in the coordination sphere of the transition metal ion to more complex processes involving activation of the ligand molecule by interaction with 'd' orbitals of the metal ion itself, such as charge transfer between them.

1.8. SURFACE ANALYSIS OF CATALYSTS

Heterogeneous catalysts are sometimes called surface catalysts because they position the reactant molecules on their very surface. Chemisorption of the substances on the surface of the catalyst is the first step in heterogeneous catalysis, which is followed by the reaction of the chemisorbed molecules and the desorption of the products from the catalyst.

The developments in surface science techniques have provided very detailed idea about the surface structures, chemical composition and electronic properties of the surfaces. In particular, the advances in instrumentation and experimental techniques have made it possible to study the chemistry of the interface between the transition metal oxide and the fluid phase in greater detail than ever before. Among various surface techniques, X-ray Photoelectron Spectroscopy (XPS) is the most promising technique due to direct identification of electronic structure details; based on this one can identify three key concepts applicable to the surface chemistry of metal oxides: (1) oxidation state of the surface (2) redox properties of the oxide and (3) coordination environment of surface atoms.

1.9. SPINELS

Among the mixed oxides, spinel-type oxides remain prominent. The spinel oxides have the general formula AB_2O_4, where A and B are cations with oxidation states of $+2$ and $+3$, respectively. Although the most numerous and most interesting compounds with the spinel structure are oxides, some halides and sulphide also crystallize in this structure. The spinel structure, named for the mineral spinel $MgAl_2O_4$, is face centered cubic with a large unit cell containing eight formula units [18-20]. It can be described as a cubic close-packed array of anions (O^{2-} ions) with the metal ions located in interstitial positions in this array. Two types of interstices are available, one formed by four anions at the vertices of a tetrahedron and the other by six anions at the vertices of an octahedron; these interstices are commonly called the tetrahedral (T_d) or A sites and the octahedral (O_h) or B sites, respectively. The preference of the individual ions for the two types of lattice sites are determined by [21-24] ionic radii of the specific ions, size of the interstices, temperature and the orbital preference for specific coordination.

The cation distribution also depends on the method of preparation of the compounds [25] as well as the processing parameters therein, such as the thermal history of the sample which includes, processing temperature, method of annealing etc [20, 26-28] and also on the composition [26,29]. The distribution of cations in different coordinations in several phases of spinel structure as a function of equilibrium temperature has been qualitatively demonstrated by Datta and Roy [27]. When the various factors as mentioned above are counter balancing one another, there can be a completely random arrangement of metal ions among the eight T_d and sixteen O_h sites.

In the unit cell of 32 oxygen ions there are 64 T_d sites and 32 O_h sites. Of these, 8 T_d holes and 16 O_h holes are occupied by cations. In other words, 1/8 of the T_d interstices and 1/2 of the O_h interstices are occupied by cations. The unit cell of an ideal spinel structure is shown in Figure 1.1. From the figure, it is evident that there are two types of cubic building units inside a big fcc O-ion lattice, filling all 8 octants.

The positions of the ions in the spinel lattice are not perfectly regular and some distortion does occur. The T_d sites are often too small for the metal ions so that the oxygen ions move slightly to accommodate them. The oxygen ions connected with the O_h sites

move in such a way as to shrink the size of the O_h cell by the same amount as T_d site expands. Thus the position of the metal ions are fixed by the symmetry of the structure but the anion positions are variable and are specified by the parameter 'u', called the oxygen parameter, which is the distance between the oxygen ion and the face of the cube edge along the cube diagonal of the spinel sub cell. In all ideal spinels the parameter 'u' has a value in the neighborhood of 0.375. But in actual spinel lattices this ideal pattern is slightly deformed, usually, corresponding to u > 0.375 [18-20], in such a way that the oxygen tetrahedron in the A-cubes is somewhat expanded and the oxygen octahedron in the B-cubes is slightly contracted. Accordingly, in that case the octahedrons formed by the 6 oxide ions directly surrounding the positive ions in these B-cubes deviate somewhat from regular octahedrons.
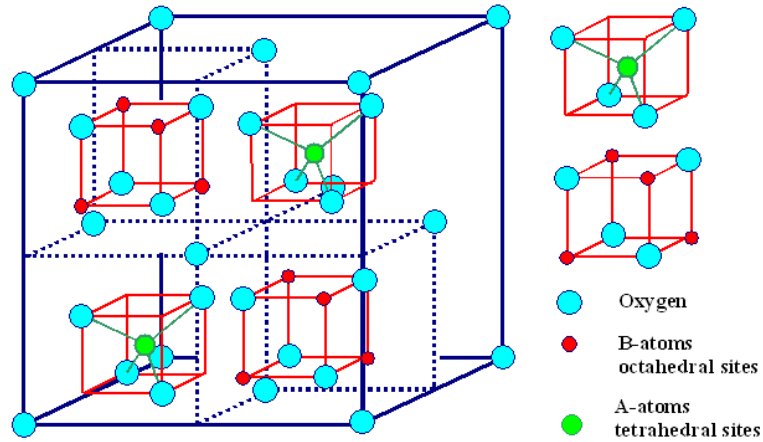
Figure 1.1: The unit cell of an ideal spinel structure.

Each anion (O^{2-} ion) in the spinel structure is surrounded by one A and three B cations. If 'a' denotes the cell edge of the spinel unit cell, the AX distance is a(u-1/4) and BX distance is a(5/8-u) for small deviations from the ideal lattice. Where AX is the distance between anion (O^{2-}) and A cation and BX is the distance between B cation and anion. The angle AXB is about 125^0, the angle BXB about 90^0.

AX = a(u-1/4)

BX = a(5/8-u)

For an ideal spinel, 'u' = 0.375

Hence, AX = a (0.375-1/4) = 0.125a

BX = a(5/8 – 0.375) = 0.25a

This difference in the bond length of two types of cations with the anions is an important factor in determining their electrical and catalytic properties [20].

Further, the spinel structure is very flexible with respect to the cations it can incorporate. There are two end-member cation distributions in the spinels, called normal and inverse spinels. Originally, in accordance with classical principles of crystallography, in the spinels of the type AB_2O_4, if the less abundant A cation is restricted to T_d sites (also called A-sites) and the more abundant B cation is restricted to the O_h sites (also called B-sites) the spinels are called normal spinels. But Barth and Posenjak [30] pointed out a second possibility, in which half of the B cations occupy the T_d sites and all A cations together with the other half of the B cations in the O_h sites. This type of spinel configuration is called 'inverse' spinels. Barth and Posenjak, who based their conclusions up on a detailed discussion of the intensities of x-ray diffraction pictures, have already given a number of examples of both groups. In addition to these two arrangements, there are possibilities for some intermediate arrangements with an averaged distribution of all ions about all spinel cation positions. Recent work such as that of Datta and Roy [27] and Hafner and Laves [31] have shown that there are many 'intermediate' or 'random' spinels which are in between the normal and inverse arrangements. These intermediate spinels are normally labeled in terms of the percent inverse character that they exhibit. Table 1.1 illustrates some of the examples of normal, inverse and intermediate spinels.

Table 1.1: Examples of some normal and inverse spinels

Type	Structure	Examples
Normal	$(A^{+2})[B_2^{+3}]O_4$	$ZnFe_2O_4$, $ZnCrFeO_4$, $ZnCr_2O_4$, $MgCr_2O_4$
Inverse	$(B^{+3})[A^{+2}B^{+3}]O4$	$MgFe_2O_4$, $NiFe_2O_4$, $CoFe_2O_4$
Random	$(A_x^{+2}B_y^{+3})[A^{+2}_{1-x}B^{+3}_{2-y}]O_4$	$MgCrFeO_4$

Deviations from the ideal structure with orthorhombic and tetragonal symmetry are known, although they are scarce and poorly characterized [20]. The distorted structure may exist at relatively low calcinations temperature, but it transforms to the cubic structure at high temperature. There are two origins for these distortions, viz. the Jahn-Teller effect and superstructure formation. $CuFe_2O_4$ is a classical example of spinel, which exists both in cubic and tetragonal form [28].

1.10. FERROSPINELS

Spinel oxides containing iron (III) are called ferrospinels. The interesting electrical, magnetic and catalytic properties of these compounds are governed critically by their chemical composition. Simple ferrospinels ($A^{II}Fe_2O_4$), as well as mixed ferrite spinels of the general formula $A^{II}_{i-x}B^{III}_{x}Fe_2O_4$ are known.

1.11. COPPER AND COBALT FERRITES

Neutron diffraction reveals that cobalt ferrite, $CoFe_2O_4$, is completely inverse and has cubic structure [32]. Smit and Wijn reported a lattice constant of 8.38 Å for $CoFe_2O_4$ [33]. The measured magnetic moment is 4 μ_B, even though the theoretical value is 3 μ_B [34]. In $CoFe_2O_4$, the ferric ions preferentially fill the tetrahedral sites, but there is room for only half of them (eight). The remaining eight go on the octahedral sites, as do the eight Co^{2+} ions. The arrangement of Co^{2+} and Fe^{3+} spins in T_d sites are antiparallel and leads to antiferromagnetic interaction. The Fe^{3+} ion moments will just cancel, but the moments on the Co ions give rise to an uncompensated moment or magnetization.

Copper ferrite spinels show an interesting magnetic, electric, and crystallographic [35-38] properties, which are induced by the mixed valencies of copper and iron atoms in the two crystallographic sub lattices. Single crystals of $CuFe_2O_4$ are prepared by heating stoichiometric amounts of Fe_2O_3 and CuO at 950^0C in air for several hours [39]. $CuFe_2O_4$ has a transformation from cubic to a tetragonal structure [28,40]. In the cubic phase, the Cu ions are situated both in the T_d and O_h sites so that cubic copper ferrite has neither normal nor completely inverse structure [41].

1.12. ACID-BASE AND REDOX PROPERTIES

Two important properties of ferrites directly related to catalytic performance and are (i) acid-base property and (ii) redox property. Since the surface of ferrites may be primarily related to their catalytic properties, the nature and concentration of the surface sites can be evaluated by analysis of the interactions of suitable probe molecules and the surfaces of these oxides. Acid sites in ferrites have been investigated by adsorption of a basic molecule such as pyridine where as basic sites have been evaluated by adsorption of acidic molecules such as carbon oxides. On the other hand, the donor-acceptor properties of ferrite surfaces can be evaluated by adsorption studies of electron acceptors such as 7,7,8,8-Tetracyanoquinodimethane (TCNQ), 2,3,5,6-tetrachloro-1-4-benzoquinone (chloranil) and p-dinitrobenzene (PDNB).

Redox property exhibited by transition metal ions is another important factor that determine the high catalytic performance of ferrites towards many of the organic reactions / transformations. Robust structural features of the ferrospinels enable them to withstand even reducing atmosphere and the lattice configuration remains unchanged even under the reduction of Fe^{3+} to Fe^{2+} [42]. Original state can be regained by simple oxidation. This demonstrates that Fe^{3+} can be easily replaced between T_d and O_h sites by varying the concentration of other cations.

1.13. CATALYTIC ACTIVITY OF SPINELS

The ample diversity of properties that the spinel compounds exhibit is derived from the fact that the possibility of synthesis of multicomponent spinels by partial substitution of cations in position A and B giving rise to compounds of formula $(A_xA'_{1-x})(B_yB'_{2-y})O_4$. This accounts for the variety of reactions in which they have been used as catalyst. Moreover, partial substitution of A and B ions giving rise to complex oxides is possible while keeping the spinel structure.

Spinels used in catalytic applications are generally synthesized by low temperature co-precipitation methods [43-48] are sufficient to overcome the drawbacks such as low surface area, varying morphology, inhomogeniety at atomistic level and large particle with grain boundary, which are generally associated with high temperature preparation [49].

These methods have resulted in tailor-making of materials having desired morphology, microscopic homogeneity, texture, chemical purity etc. Further, co-precipitation methods generate Bronsted acid sites in different cationic environments in addition to Lewis sites, which makes the catalyst active and effective for many of the organic transformations like aromatic alkylation, acylation etc [43-48].

The interesting catalytic properties shown by spinels are controlled by various properties such as, nature of ions, their charge and site distribution among T_d and O_h sites. Differential Neutron Diffraction (DND) studies on spinels revealed that the surface of normal spinel consists of a mixture of (110) and (111) planes [50]. Beaufils and Barbaux have compared the experimental results from DND with some models involving argon-oxygen anions and concluded that these planes contain only O_h cations and oxygen anion, respectively [50]. Later Ziolkowski and Barboux theoretically predicted the same [51]. Additionally, Jacobs et al [52] in a study, using LEIS (Low energy ion scattering, a technique sensitive to the outer most atomic layer), revealed that spinel surface sites are mainly O_h and, hence, the O_h cations are mainly exposed on the surface.

Spinels are reported to be thermally stable and they maintain enhanced and sustained activity for a variety of industrially important reactions such as decomposition of N_2O and H_2O_2 [53-56], hydrodesulphurisation of petroleum crude [57], oxidation of CO, H_2, methane and methanol [58-62], oxidative dehydrogenation of hydrocarbons [63-68], hydrogenation of organic compounds [69,70], treatment of automobile exhaust gases [71,72], and dehydrogenation of ethyl benzene and alcohols etc [42,73-77]. In addition to the above mentioned reactions, a variety of organic transformation reactions are carried out over spinel oxides. For example, Roesky etal [78] reported an improved synthesis method for indenes (from indanones) and styrenes (from acetophenones) by use of a ZnO/Al_2O_3 spinel catalyst.

Cobalt modified $MgAl_2O_4$ used for the production of ethene and other industrial gases by diesel fuel pyrolysis [79]. Spinel catalysts are also employed for reducing NO by using NH_3 and propane as reductants [80,81]. Another synthetically important reaction is the synthesis of methyl formate. Recently Sato et al [82] reported the vapour phase dehydrocoupling reaction of methanol to methyl formate using $CuAl_2O_4$ catalyst.

Reactions such as hydrogenation of maleic anhydride to γ-butyrolactone and tetrahydrofuran [83], oxidation of benzoic acid to phenol [84], reduction of fatty esters into higher alcohols [85], methanation of CO and CO_2 [86,87], synthesis of higher alcohols [88] etc were successfully applied over various types of spinels.

Among the spinel compounds, ferrites have been used as effective catalysts for a number of industrially important reactions as those mentioned above. The catalytic effectiveness of ferrites for many such reactions arises because of the ease with which iron can exchange its oxidation state between 2 and 3. Another important attribute of these materials, from commercial stand point is their stability under extremely reducing conditions, which is due to the spinel structure. Thus the reduction of Fe^{3+} to Fe^{2+} takes place without altering the lattice configurations so that up on reoxidation, the original state is retained [42]. In contrast to the spinel ferrites, the catalyst Fe_2O_3 loses its activity as it is reduced to FeO and metallic iron.

Among various reactions, the most widely studied reaction using spinel type catalyst is perhaps the catalytic selective oxidation of carbon monoxide. Selective removal of CO from CO/H_2 mixed gas is a key step for fuel cell or sensor technology [89]. Tamaura and Tabata [90] have found that at a reaction temperature of 300^0C, oxygen deficient ferrites can be used as an efficient material for decomposing CO_2 gas (since there is need to reduce CO_2 emissions to the atmosphere by decomposition to C and oxygen in order to reduce the greenhouse effect).

Among various ferrites, Co- and Cu- ferrites are found to be very active and have been used widely for many industrially important reactions such as hydrogenation/dehydrogenation, CO oxidation etc. For example, it is reported that both $CoFe_2O_4$ and $CuFe_2O_4$ are highly active for the conversion of butene to butadiene [68]. Surface and lattice oxygen atoms participate in the reactions. Selectivity for the dehydrogenation reaction was strongly dependent on the presence of gaseous oxygen in the case of $CoFe_2O_4$, although the selectivity over the Cu catalyst was not a strong function of gaseous oxygen. The copper catalyst was more active, but selectivity of the oxidation reaction to butadiene was much poorer on the copper ferrite. A probable reason, as

suggested by the authors, for the difference in activity of two catalysts is the greater reducibility of the copper ion relative to the cobalt.

$CuFe_2O_4$ shows an excellent performance towards the catalytic removal of NOx and diesel soot particulates than any other ternary AB_2O_4 spinel-type oxides [72]. Among the metal oxides, spinel type cobalt oxide (Co_3O_4) is the most active catalyst for oxidation of CO [89]. $CoFe_2O_4$ shows excellent activity towards the chemical decomposition of H_2O_2 [55]. Several workers reported the catalytic properties of $CoFe_{3-x}O_4$, $NiFe_{3-x}O_4$ and $CuFe_{3-x}O_4$ ($0 \leq x \leq 3$) for H_2O_2 decomposition [53,54]. According to them the catalytic activity follows the order $Co > Cu > Ni$ and that $Co_{1.5}Fe_{1.5}O_4$ is the most active one.

Recent reports reveal that ferrospinel systems prepared by low temperature coprecipitation methods are highly efficient for aromatic alkylation and acylation reactions. For example, CuCr-ferrites are found to be active for Friedel-Crafts alkylation to form diphenylmethane [48]. Ni-, Co- and Cu-ferrites have been recently applied for benzoylation of toluene [91]. Apart from acylation, modified ferrospinels are stable catalysts for aromatic alkylation as well. One of the simplest ferrospinels, magnetite, (Fe_3O_4), exhibits catalytic activity in production of important intermediates, e.g. in alkylation of phenol with methanol to 2,6-xylenol, to the monomer of the thermoresistant poly-(2,6-dimethyl)-phenylene oxide resin [92]. To improve the catalytic performance of ferrites, modifying cations can be introduced into the structure.

Recently Sreekumar and Rao etal invoked the idea of using single phase ferrites based on Ni, Co and Zn for various aromatic alkylation reactions such as aniline methylation [46,93-95], pyridine methylation [44,45] and phenol methylation [96,97]. Spinel systems with different stoichiometry among divalent ions are extensively studied for this reaction. In alkylation processes the activity is primarily attributed to the presence of Lewis acid sites, as on Bronsted sites deactivation occur [98]. The structure of catalyst may change simultaneously while catalyzing a reaction. For example, in a single-component iron oxide catalyst the active magnetite phase developed from hematite in the course of the alkylation of phenol [92]. In other words hematite, Fe_2O_3, with iron exclusively in ferric state, was converted to Fe_3O_4 with partial reduction, containing $Fe^{2+/3+}$

mixed valent ions in the [B] sublattice of octahedral sites. Hence, a part of Lewis acid centers were modified during reaction.

1.14. ALKYLATION OF PHENOL

Alkyl phenols are compounds having the alkyl group substituted or replaced either in the phenyl ring or in the OH of the side chain. These compounds are industrially important, either used as directly or as chemical intermediates in the manufacture of pharmaceuticals, pesticides, herbicides, plastics, special grade paints and a variety of chemicals [99]. The important applications of some of the alkyl phenols are represented in Table 1.2. The stringent specifications and the demand of these chemicals necessitate the development of catalytic systems and the processes for the selective production.

Conventionally, alkyl phenols can be prepared by Friedel Crafts alkylation reaction [99]. Friedel Craft's alkylation reaction has got several disadvantages such as poor selectivity, high capital cost, reactor corrosion, formation of byproducts and difficulty in catalyst regeneration [100]. Recently, much attention has been paid to the development of environmentally friendly catalysts for the production of industrially important alkylated phenols. Solid acid catalysts are very important alternatives to protonic acids or Friedel Craft's type catalysts. The acidic and basic nature of solids provides a fascinating opportunity to study these reactions by varying their catalytic characteristics. Numerous reports on the production of these alkyl substituted phenols are available in literature, some of which are patents. In the prior art, the catalysts used for the alkylation of the reactions are ranging from ceramics, through zeolites to semiconducting metal oxides and mixed metal oxides. Alkylating agents such as C_1-C_4 alcohols, various olefins, dimethyl carbonate etc are widely employed for alkylation. The reaction is sensitive to acidic and basic properties of the catalysts, reaction parameters such as temperature, mole ratio of reactants and type of alkylating agent.

Metal oxides are good alternative to both zeolites and aluminium phenolate for selective ortho alkylation using olefins/alcohols since with former undesired para alkylated products can be brought down considerably [99]. On zeolites alkylation results a mixture of O- and C- alkylated products [101-105]. Among various metal oxides, transition metal

oxides alone or in combination with other metal oxides are found to be the most active and selective for ortho alkylation [106-108].

Table 1.2: Industrial applications of various alkyl phenols

Alkyl phenol	Applications
o-Cresol	In the production of novolak resins, 4,6-dinitro – 2 – methyl phenol (a herbicide) and antioxidants. o-Cresol is a component of crysilic acids, which are used as solvents in a number of coating applications.
2,6-xylenol	Poly(phenylene oxide) resin, epoxy resin.
Anisole	Additives in gasoline to boost octane, used for the production of dyes, agricultural chemicals and antioxidants.
2-Ethyl phenol	Starting material for photochemicals. Intermediate for the synthesis of benzofuran.
2-Isopropyl phenol	An efficient antiskinning aid in air-drying coatings.
2-tert-butyl phenol	Starting material for the synthesis of antioxidants and agrochemicals.
2,4-di-tert-butyl phenol	In the manufacture of its triphosphite that is employed as a co-stabilizer for poly (vinyl chloride), and of its benzotriazole derivatives that are used as UV absorbers in polyolefins.
2,6-di-tert-butyl phenol	An indispensable building block in the synthesis of higher molecular mass antioxidants and light-protection resins for plastics, especially polyolefins.

1.15. PHENOL METHYLATION

Phenol methylation has got great industrial importance, as methyl phenols are largely used as chemical intermediates for the production of valuable industrial products. 2,6-xylenol obtained by alkylation of phenol with methanol, is an interesting intermediate in the synthesis of poly (2,6-dimethyl) phenylene oxide, a polymer used in the production

housings for electrical equipment and of pipes resistant to high pressure and temperature [109,110].

Several papers and patents have been published on the alkylation of phenol with methanol in the presence of different catalyst systems varying from MgO [111-118], Al_2O_3 [98,119-122], metal oxides [123,124], mixed metal oxides [125-127] and zeolites [101-105]. The commercial process for the synthesis of o-cresol and 2,6-xylenol is based mainly on MgO [117,118] and supported vanadium-iron mixed oxide [128]. Vapour phase methylation of phenol has been investigated over various mixed metal oxides such as MgO-based [115,116], Al_2O_3-based [129-131], Fe_2O_3-based [92,107,132-137], V_2O_5-based [108,125,126], TiO_2-based oxides [111,138] and Al containing hydrotalcites [139,140] and various other oxide systems [141-148].

A literature survey suggests that phenol methylation over both modified and unmodified zeolites mostly results in a mixture of methylated products (both O- and C-methylation), of which anisole is the predominant product. These are less selective for 2,6-xylenol, the most demanded methylated product. The poor selectivity of ortho alkylates, especially for 2,6-xylenol, due to pore constraint and fast deactivation due to coking made industrial chemist to do move work on phenol methylation over promising metal oxide catalysts. Oxides either alone or in combination with other oxides are so far the best for selective formation of 2,6-xylenol. A variety of oxides have been used for studying phenol methylation and among which either one of MgO, Al_2O_3 and Fe_2O_3 are mostly used as one of the component. Oxides of transition metals based on Mn^{2+}, Cu^{2+}, Co^+, Ni^{2+}, V^{5+}, Cr^{3+} and Ti^{4+}, SiO_2, various phosphates, CeO_2 etc were used as second component.

Oxides based on MgO and Al_2O_3 are two classic examples and have been widely employed for phenol methylation. These two oxides are different in their acid-base properties; MgO is basic and Al_2O_3 is acidic in nature. Their acid-base properties considerably affect the product distribution. Considerable amount of anisole is observed along with ortho alkylated products on alumina against predominant orthoalkylation over MgO. This is due to the difference in nature of mode of interaction of phenol molecules over these surfaces due to the difference in their acid-base properties. Hence it is proposed

that addition of any oxide component to MgO or Al_2O_3 modify their acid-base properties and accordingly product selectivity.

It has been reported that the vapour phase reaction of phenol with methanol over MgO gives 2,6-xylenol in an excellent yield. In the US patent 4, 933, 509, GE, USA claims 92.7% conversion with 76.9% selectivity to 2,6-xylenol over MgO catalyst and by the US patent 4,661,638 the claim is that the conversion could be improved to 97.0% by promoting MgO with Mn oxide. Vapour phase synthetic method using TiO_2-MgO [111,115], MgO-CeO_2 [116], MgO-CuO [149], MgO-MnO [150] and MgO-Mn_2O_3 [150] has also been reported. This demonstrates that MgO is most favourable in the synthesis of 2,6-xylenol as compared with other catalysts that are used in the methylation of phenol.

1.15.1. Efficient methylation through synergism

It has been observed that both MgO and Al_2O_3 in combination with a transition metal oxide component show better orthoselectivity than either MgO or Al_2O_3 alone. Transition metal oxide itself or in combination with other transition metal oxides are found to be effective for ortho methylation. Inoe and Enomoto [151] described liquid phase alkylation using transition metal oxides including ZnO, Fe_2O_3, Cr_2O_3 and TiO_2 and observed predominant formation of orthoalkylates. Alkylation of phenol on V_2O_5 [108,125,126] and TiO_2 systems [111,138] are found to be more active than MgO and SiO_2. Addition of V_2O_5 to titania [108] helped to increase 2,6-xylenol selectivity and reduced the formation of undesired products. The alkylation activity and stabilities of vanadia was improved by the addition of chromia, which by itself is a poor alkylation catalyst [125,126]. Similarly TiO_2-ZnO [152] and Al_2O_3-ZnO [129] produce predominantly ring alkylated products in which the high orthoselectivity is attributed to a combination of weakly acidic sites and stongly basic sites. TiO_2-MgO mixed oxides was found to be more active and selective than pure MgO for 2,6-xylenol that has been attributed to a combined effect of weak acidity and strong basicity of the catalyst [111,115]. Recently Sato etal reported MgO-CeO_2 mixed oxide systems are effective for ortho methylation [116]. Catalysts containing MgO-MnO or MnO-Mn_2O_3 are found to be more effective for 2,6-xylenol formation [150]. Grabowska et al reported $ZnAl_2O_4$ spinels

are active for phenol methylation and depending on the method of preparation selectivity of ortho products vary [153].

In all the above cases, there are two disadvantages: (1) the catalyst composition, particularly the active phase is not well defined and hence reproducibility is poor, and (2) there is always para alkylation happening to an extent of at least 4%, thus making the separation of impurities as an essential unit process. In the 1970's a new type of catalysts were developed, the main component being iron oxides (Fe_xO_y) system. Many formulations based on this fundamental system were investigated [136]. Iron oxide possesses acid-base property in between MgO and Al_2O_3 and hence the addition of iron oxide to either MgO or Al_2O_3 results an increase of both phenol conversion and 2,6-xylenol selectivity. Phenol methylation on a Fe-V-O/SiO_2 catalyst is one of the new catalytic processes, which have been developed in Japan during the last few years [135]. Grabowska et al studied the alkylation of phenol to o-cresol and 2,6-xylenol with MeOH in the presence of Fe and Fe-Mg oxides [134]. The catalyst displayed high activity and selectivity towards C-alkylation in ortho position. The active phase in the studied catalysts is highly dispersed magnetite or mixed spinel of Fe(MgFe)O_4 type [134]. Magnetite containing salts of Cr, Si, K and V are found to be highly selective for ortho methylation [154]. Similarly Fe_2O_3 in combination with other oxides such as CdO, SnO_2, CeO_2, NiO, CoO, Cr_2O_3, ZrO_2 etc show excellent selectivity in 2,6-xylenol formation [107,132-136]. Kotanigawa et al carried out phenol methylation over an MO-Fe_2O_3 catalyst containing Cu, Mg, Ca, Ba, Zn, Mn, Co or Ni each as M [107]. All these systems show excellent selectivity for ortho methylation. Thus a specific relation between iron and selective formation of orthoalkylates seemed to exist.

From the literature survey it is clear that multicomponent oxide systems shows better activity and selectivity (for ortho methylation) towards phenol methylation. It is believed that a mixture of oxides brings out a combined effect, in other words synergistic behavior, enhancing the catalytic activity. It is generally observed that multicomponent oxide systems require relatively low temperature for better catalytic performance than the individual components. For example, mixed oxides show their catalytic activity at the temperature range between 300 and 450^{0}C, and they are more selective for 2,6-xylenol

formation. Whereas simple oxides such as MgO, CeO_2, Mn_3O_4 and ThO_2 show their catalytic activities at temperatures higher than 450^0C. Kotanigawa et al reported binary oxides of the system $MO-Fe_2O_3$ (where M = Mg, Ca, Ba, Co, Ni, Zn and Cu) are active and selective for 2,6-xylenol at 350^0C, whereas the individual oxide components such as MgO, Fe_2O_3 etc require more than 400^0C for achieving good conversion and high 2,6-xylenol selectivity [107]. Thus the synergetic or combined effect of metallic components has considerable influence on catalytic performance. Due to synergism, the individual metallic ions show more homogeneity in their property towards a particular reaction. This is possible only if the valence band energy of the metallic ions of mixed oxide system have comparable energy. If VB energy is widely separated, proper overlapping between the metallic orbitals is energetically unfavorable and hence reduces the catalytic effectiveness. For example, addition of vanadia to titania or chromia helped to increase the activity and 2,6-xylenol selectivity. Whereas the effect of V_2O_5 addition to MgO or SiO_2 is insignificant with respect to phenol conversion and selectivity patterns. In the former case, all the ions have valence 3d orbitals, energetically comparable and favourable for overlap. Whereas for both Mg^{2+} and Si^{4+} involve 3s and 3p orbitals are empty and placed on the unoccupied orbitals, which has got considerable energy difference with V 3d for any overlap. In another case, calcined magnesium aluminium hydrotalcites is more active than either MgO or Al_2O_3 [139, 140]. Here both Mg^{2+} and Al^{3+} ions fall same valence level, which makes the situation more favourable for proper overlap and hence the catalyst system behaves more or less like a single component rather than showing individual property. This leads to the catalyst system function as an effective catalyst for the reaction.

1.16. OBJECTIVE OF THE PRESENT WORK

From the above literature survey, MgO catalysts promoted by the transition metal oxides are the ones providing by far the good conversion of phenol to 2,6-xylenol. Later several attempts have been made to develop a better catalysts to achieve much better selectivity, more conversion and to lessen the harsh reaction conditions such as high reaction temperature, the disadvantages existing for conventional MgO catalysts. Most of the attempts were focused more of iron based oxide systems. Japanese patent 101 13561

awarded to Asahi based on again a multimetallic oxide catalyst, with iron oxide as a chief component, claims 93% conversion and 97% selectivity.

Grabowska et al carried out phenol methylation over Fe_2O_3 and Fe_3O_4 prepared by different methods [92]. The x- ray and magnetic investigation of these catalysts indicated highly dispersed magnetite is the active phase. In order to bring down the reduction level on heamatite and to reduce the crystallite size during the reaction, they modified iron catalysts with various ions such as Si, K, Cr or Cs ions [92,154]. Considerably better results were obtained on introducing Cr and Si by cooprecipitation. In this instance the increase in crystallite size is minimized after the use. This is connected with the advantageous influence of Si on the texture of iron catalysts and its action in protecting the catalyst on sintering. A similar effect is observed with Cr. On the other hand, K and Cs ions act as an activator of magnetite. Thus the following important criteria should be taken into account while considering a multicomponent oxide systems based on iron oxide for phenol methylation reaction.

(i) High phenol conversion

(ii) Good selectivity of 2,6-xylenol

(iii) The problem of deactivation should be tackled while introducing other metallic componet to the iron oxide system. This can be achieved only by reducing the reduction level on Fe_2O_3 and by controlling the crystallite size during the course of reaction.

(iv) Explore the possibility of synergism. This is possible only when the energy of valence orbitals of involved ions have comparable energy.

Being Fe_2O_3 as chief component, by introducing other first row transition metal ions such as V^{5+}, Ni^{2+}, Co^{2+}, Zn^{2+}, Mn^{2+} and/or Cu^{2+}, the possibility of synergism can be exploited. Iron oxides in combination with either one or more of these oxides are found to be active and selective for 2,6-xylenol [107]. It has been observed that Cu^{2+} ion has got promoting influence on selective formation of 2,6-xylenol [107,155]. For example, Krishnasamy et al studied the influence of $CuSO_4$ loading on alumina for phenol methylation in the vapour phase and found that addition of $CuSO_4$ to alumina enhance the formation of 2,6-xylenol [155]. Copper-magnesium catalysts promote ortho alkylation of the hydroxy aromatic compound in high yield, minimizing decomposition of the alkanol,

and have long life [149]. In yet another variation, US patent 4048239 describes a process in which alkylation of phenol is carried out selectively at ortho position using aldehydes and H_2 in the presence of a Cu-Cr catalyst [156].

Sreekumar et al invoked the idea of using single phase ferrites based on Ni, Co and Zn for phenol methylation reaction [96,97]. Spinel systems with different stoichiometry among divalent ions are extensively studied for this reaction. All these catalysts are highly selective towards ortho methylation. Among these catalysts, $CoFe_2O_4$ is found to be the more active and selective towards phenol methylation and 2,6-xylenol formation. Rao et al in a patent claim to make 2,6-xylenol with high selectivity and least amount of side products, over a single phase ternary oxide system containing Co and Fe as metals [43]. $CoFe_2O_4$ shows excellent stability over a long period of time. Recently it has been reported that $CuFe_2O_4$ show even better activity and selectivity towards 2,6-xylenol formation than $CoFe_2O_4$ [47]. However $CuFe_2O_4$ deactivates in a reasonable period of time due to sintering and considerable increase of crystallite size during the course of the reaction. Kotanigawa et al [107] reported that over CuO-Fe_2O_3, the degree of reduction obtained experimentally exceeds the calculated value, which infers that the reduction takes place not only in heamatite, but also in cupric oxide. Additionally, Cu^{2+} ion promotes the reduction of Fe^{3+} ion. Whereas in $CoFe_2O_4$, reaction hardly reduces the compound. Moreover both Cu^{2+} and Co^{2+} ions have got diverse character with respect to its activity towards reaction involving H_2; the former is dehydrogenating agent whereas the latter is a hydrogenating agent. The hydrogenation/dehydrogenation ability of these ions is very important in reactions involving methanol. Reaction of phenol with methanol is always associated with unavoidable methanol decomposition. In other words, the alkylating agent methanol reacts through two simultaneous pathways, the methylation of phenol and the decomposition of methanol itself. The gasification of methanol can be demonstrated by

$$CH_3OH \rightarrow CO + 2H_2 \qquad (1)$$

$$CO + 3H_2 \rightarrow CH_4 + H_2O \quad (2)$$

$$CO + H_2O \rightarrow CO_2 + H_2 \quad (3)$$
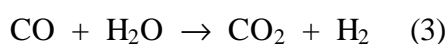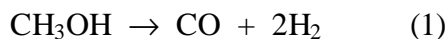
Thus it is recommended to keep methanol/phenol mole ratio more than the required stoichiometric ratio of 2 for 2,6-xylenol production. Hence efficiency of alkylation

catalyst should be discussed from the relation between the main reaction and the ability of these catalysts to govern the undesired side reaction in favour of main reaction.

Elucidation of the nature of Cu and Co interaction in the spinel system is very useful to understand the selective ortho methylation of phenol and in general to explore the role of Cu-Co synergism on the catalytic performance in various industrially important chemical processes. It is also to be emphasized here that the Cu-Co mixed system can act as a dual reaction catalyst depending on the material preparation and reaction conditions. For example, Cu-Co-multicomponent mixed oxide catalysts with different supports, like ZnO and/or Al_2O_3, are being used in important industrial chemical processes such as methanol reforming to H_2 as well as low pressure methanol synthesis from syngas and it is clear from the following equations (Eqs. 4-6) [157]:

$$CH_3OH \ (l) \qquad \Leftrightarrow \qquad 2H_2 \ (g) \ + \ CO \ (g); \qquad\qquad (4)$$
$$\Delta H^0{}_{298} \ (\Delta G^0{}_{298}) \ = \ + \ 128.1 \ (29) \ KJ \ mol\text{-}1$$
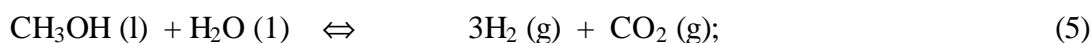
$$CH_3OH \ (l) \ + H_2O \ (1) \quad \Leftrightarrow \qquad 3H_2 \ (g) \ + \ CO_2 \ (g); \qquad\qquad (5)$$
$$\Delta H^0{}_{298} \ (\Delta G^0{}_{298}) \ = \ + \ 130.9 \ (8.9) \ KJ \ mol\text{-}1$$
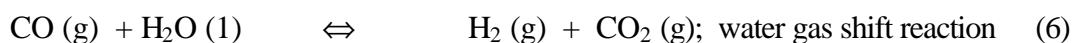
$$CO \ (g) \ + H_2O \ (1) \qquad \Leftrightarrow \qquad H_2 \ (g) \ + \ CO_2 \ (g); \ \text{water gas shift reaction} \quad (6)$$
$$\Delta H^0{}_{298} \ (\Delta G^0{}_{298}) \ = \ + \ 2.8(20.1) \ KJ \ mol\text{-}1$$

Above reactions clearly indicates that irrespective of the support, Cu-Co synergism alone can induce the above reactions, which will affect the course of the reaction.

In the present study effects of simultaneous addition of Cu and Co are studied in a series of $Cu_{1-x}Co_xFe_2O_4$ (x= 0, 0.25, 0.5, 0.75, 1.0) samples. Elucidation of the nature of Cu and Co interaction in the spinel system is very useful to understand the selective orthomethylation of phenol and in general to explore the role of Cu-Co synergism on the catalytic performance in various industrially important chemical processes. Hence, the following important objectives were taken into consideration:

- Preparation of a series of ferrospinels containing Cu and Co having a general formula $Cu_{1-x}Co_xFe_2O_4$ (where x = 0, 0.25, 0.50, 0.75 and 1) by co-precipitation method.

- Characterization of $Cu_{1-x}Co_xFe_2O_4$ by physicochemical and spectroscopic methods such as XRD, XRF, SEM, Surface area (by N_2 sorption), TG-DTA, TPR, Mossbauer and photoemission.

- Most important was the evaluation of the catalytic activity of the systems for phenol methylation using methanol as the alkylating agent and to optimize the process parameters to achieve the synthetically valuable C-alkylated products o-cresol and 2,6-xylenol selectively and in better yield.

- Detailed analysis of the fresh and spent catalysts to understand the changes in electronic, and structural features that occur during phenol methylation. Photoemission and other characterization techniques such as Mössbauer, TPR, TPD, TG-DTA etc have been employed for the above purpose.

- Acid-base properties of the catalysts by *in situ* FTIR technique using pyridine and CO_2 as probe adsorbate. Evaluation of donor-acceptor properties of these materials using electron acceptors having different electron affinity values to understand the strength and distribution of electron donor sites.

- Phenol alkylation by using various alkylating agents such as dimethyl carbonate, ethanol, isopropanol and isobutene and to compare the catalytic performance between various alcohols or alkene as alkylating agent.

- Adsorption behavior of both reactants and products of phenol methylation such as phenol, methanol, o-cresol, 2,6-xylenol, anisole and HCHO over the surfaces of selected compostions of the system $Cu_{1-x}Co_xFe_2O_4$ by *in situ* FTIR technique to get an insight on the mechanism of phenol methylation over these catalyst surfaces.

1.17. REFERENCES

1   J. Halber, in J. A. Thomas and K. I. Zamaraev (Eds), *Perspecitves in Catalysis*, Blackwell Scientific Publications, p-371 (1992).

2   J. M. Thomas, *Sci. Am.*, **266** (1992) 112.

3   H. Hattori, *Stud. Surf. Sci. Catal.*, **78** (1993) 35.

4   Catalytic chemistry of solid-state inorganics, W. R. Moser and J. Happel, Eds., *Ann. N. Y. Acad. Sci.*, **272** (1976) 1-73.

5   A. J. Marchi, J. I. Di Cosimo and C. R. Apesteguia, in "*Proceedings, 4th International Symposium on Scientific Bases for the preparation of Heterogeneous catalysts*",Louvain-la Neuve, Paper H-7, 1986.

6   A. J. Marchi, J. I. Di Cosimo and C. R. Apesteguia, in "*Proceedings, 9th International Congress on Catalysis*" (J. M. Philips and M. Ternan, Eds.), Vol. 2, p. 529-536, Chem. Institute of Canada, Ottawa, 1988.

7   P. Courty, C. Marcilly, in Preparation of Catalysts I, B. Delmon, P. A. Jacobs and G. Poncelet (Eds), *Stud. Surf. Sci. Catal.*, **1** (1976) 119.

8   J. A. Scwarz, C. Contescu and A. Contescu, *Chem. Rev*., **95** (1995) 484.

9   L. Hench and J. K. West, *Chem. Rev*., **90** (1990) 33.

10   M. Schneider and A. Baiker, *Catal. Rev. Sci. & Eng*., **37** (1995) 515.

11   R. Gopichandran and K. C. Patil, *Mater. Lett*., **12** (1992) 437.

12   S. S. Manoharan and K. C. Patil, *J. Amer. Ceram. Soc*., **75** (1992) 1012.

13   A. K. Cheetand and P. Day, *Solid State Chemistry Techniques*, Oxford University Press, 1987.

14   G. M. Schwab, E. Roth, C. H. Grinzoz and N. Mavrakis, in "*Structure and properties of solid surfaces*"(R. Gomer and C. S. Smith, Eds.), Univ. Chicago Press, Chicago, 1953.

15   J. P. Suchet, "*Chemical Physics of Semiconductors*", Chap.5, p.82, 83, Van Nostrand, London, 1965.

16   A. Miller, *J. Appl. Phys*., **30** (1959) 245.

17   K. Tanabe, M. Misono and H. Hattori, *Stud. Surf. Sci. Catal.*, **Vol. 51**, New Solid Acids and Bases and Their Catalytic Properties, 1989.

18   F. C. Romeijn, *Philips Research Reports*, **18** (1953) 304.

19   E. J. W. Verwey and E. L. Heilmann, *J. Chem. Phys*., **15** (1947) 174.

20   G. Blasse, *Philips Research Rep. Supplement*, **3** (1964) 40.

21   J. Smit and H. P. J. Wijn, *Ferrite*, Philips Technical Library, Eindhoven, The Netherlands, p. 137, 1959.

22   E. W. Gorter, *Philips Res. Rept.*, **9** (1954) 302.

23   E. J. W. Verwey, F. De Boer and J. H. Van Santen, *J. Chem. Phys.*, **16** (1948) 1091.

24   B. Viswanathan and V. R. K. Murthy (eds.), *Ferrite Materials (Science and Technology)*, Narosa Publishing House, 1990.

25   A. Meenakshi Sundaram, V. Sreenivasan, *Phys. Status Solidi A*, **69** (1982) K15.

26   R. K. Datta, R. Roy, *J. Am. Ceram. Soc.*, **50** (1967) 578.

27   R. K. Datta and K. Roy, *Nature*, **191** (1961) 169.

28   E. Prince and R. G. Trueting, *Acta Cryst.*, **9** (1956) 1025.

29   R. K. Datta, R. Roy, *Am. Mineral*, **53** (1968) 1456.

30   T. F. W. Barth and E. Posenjak, *Zs. Kristallographie*, **84** (1952) 325.

31   S. Hafner and F. Laves, *Z. Krist.*, **115** (1961) 321.

32   E. Prince, *Phys. Rev.*, **102** (1956) 674.

33   J. Smit and H. P. J. Wijn, *Advan. Electron. Electron Phys.*, **6** (1954) 83.

34   R. Pauthenet, *Compt. Rend.*, **230** (1950) 1842.

35   N. Namba and S. Kobayashi, *Jap. J. appl. phys.*, **17** (1978) 1819.

36   V. A. M. Brabers and J. Klerk, *Thermochimica Acta*, **18** (1977) 287.

37   V. A. M. Brabers, *Mat. Res. Bull.*, **18** (1983) 861.

38   E. Kester and B. Gillot, *J. Phys. Chem. Solids*, **59** (1998) 1259.

39   T. Miyadai, Y. Matsuo and S. Miyahara, *J. Phys. Soc. Japan*, **19** (1964) 1747.

40   T. Inoue and S. Iida, *J. Phys. Soc. Japan*, **13** (1958) 656.

41   L. Weil, F. Bertaut and L. Bochirol, *J. Phys. Radium*, **11** (1950) 208.

42   C. S. Narasimhan and C. S. Swamy, *Appl. Catal.*, **2** (1982) 315.

43   B. S. Rao, K. Sreekumar and T. M. Jyothi, *Indian Patent*, 2707/98, 1998.

44   K. Sreekumar, T. Mathew, R. Rajgopal, R. Vetrivel and B. S. Rao, *Catal. Lett.*, **65** (2000) 99.

45   K. Sreekumar, T. Mathew, B. M. Devassy, R. Rajgopal, R. Vetrivel and B. S. Rao, *Appl. Catal, A:General*, **205** (2001)11.

46   K. Sreekumar, T. Mathew, S. P. Mirajkar, S. Sugunan and B. S. Rao, *Appl. Catal, A:General*, **201** (2000) L1.

47   B. S. Rao, T. Mathew, N. R. Shiju and R. Vetrivel, *Indian Patent filed*.

48   S. Ghorpade, V. S. Darshane and S. G. Dixit, *Appl. Catal. A:General*, **166** (1998) 135.

49   P. S. Anilkumar, J. J. Shrotri, S. D. Kulkarni, C. E. Deshpande and S. K. Date, *Mater. Lett.*, **27** (1996) 293.

50   J. P. Beaufils and Y. Barbaux, *J. Appl. Cryst.*, **15** (1982) 301.

51   J. Ziolkowski and Y. Barbaux, *J. Mol. Catal.*, **67** (1991) 199.

52   J. P. Jacobs, A. Maltha, J. R. H. Reintjes, T. Drimal, V. Ponec, H. H. Brogersma, *J. Catal.*, **147** (1994) 294.

53   J. R. Goldstein and A. C. C. Tseung, *J. Catal.*, **32** (1974) 452.

54   A. I. Onuchukwu, *J. Chem. Soc. Faraday Trans. I.*, **80** (1984) 1447.

55   H. M. Cota, J. Katan, M. Chim and F. J. Schoenweis, *Nature*, **203** (1964) 1281.

56   A. C. C. Tseung and J. R. Goldstein, *J. Phys. Chem.*, **76** (1972) 3646.

57   G. K. Boreskov, V. V. Proporski and V. A. Sezonov, "*Proc. 4th Inter. Congr. Catalysis*", Moscow, 1963.

58   K. Omata, T. Takada, S. Kasahara and M. Yamada, *Appl. Catal.*, **146** (1996) 255.

59   J. Ghose and K. S. R. C. Murthy, *J. Catal.*, **162** (1996) 359.

60   A. A. Awe, G. Miliades and J. C. Vickerman, *J. Catal.*, **62** (1980) 202.

61   K. S. R. C. Murthy and J. Ghose, *J. Catal.*, **147** (1994) 171.

62   F. Severino, J. Brito, O. Carias and J. Lainc, *J. Catal.*, **102** (1986) 172.

63   W. L. Kehl and R. J. Rennard, *U. S. Patent*, 3,450,787 (1969).

64   H. H. Kung and M. C. Kung, *J. Phys. Chem.*, **84** (1980) 383.

65   J. Sloczynski, J. Ziolkowski, B. Grzybowska, R. Grabowski, D. Jachewicz, K. Wcislo and L. Gengembre, *J. Catal.*, **187** (1999) 410.

66   E. Finocchio, G. Busca, V. Lorenzelli and R. J. Willey, *J. Catal.*, **151** (1995) 204.

67   W. R. Cares and J. W. Hightower, *J. Catal.*, **23** (1971) 193.

68   R. J. Rennard and W. L. Kehl, *J. Catal.*, **21** (1971) 282.

69   J. Jenck and J. E. Germain, *J. Catal.*, **65** (1980) 133, 141.

70   J. W. Evans, P. S. Casey, M. S. Wainwright, D. L. Trimm and N. W. Cant, *Appl. Catal.*, **7** (1983) 31.

71   W. F. Shangguan, Y. Teraoka and S. Kagawa, *Appl. Catal. B: Environmental*, **16** (1998) 149.

72   W. F. Shangguan, Y. Teraoka and S. Kagawa, *Appl. Catal. B: Environmental*, **8** (1996) 217.

73   N. John Jebarathinam, M. Eswaramoorthy and V. Krishnasamy, *Appl. Catal.*, **145** (1996) 57.

74   W. S. Chen, M. D. Lee and J. F. Lee, *Appl. Catal.*, **83** (1992) 201.

75   K. Sreekumar, Ph. D Theses, Submitted to Cochin University of Science and Technology,

Kochi, February 1999.

76   G. R. Dube and V. S. Darshane, *J. Mol. Catal.*, **79** (1993) 285.

77   Sreekumar, K.; Thomas, M.; Jyothi, T. M.; Biju, M. D.; Sugunan, S.; Rao, B. S., *Pol. J. Chem.*, **74** (2000) 509.

78   R. Roesky, J. Weiguny, H. Bestgen and U. Dingerdissen, *Appl. Catal. A.*, **176** (1999) 213.

79   G. Xanthopoulou, *Appl. Catal. A: General*, **182** (1999) 285.

80   J. Sloczynski, J. Jans, T. Machej, J. Rynkowski and J. Stoch, *Appl. Catal. B: Environmental*, **24** (2000) 45.

81   G. Fierro, S. Morpurgo, M. Lo Jacono, M. Inversi and I. Pettiti, *Appl. Catal. A: General*, **166** (1998) 407.

82   S. Sato, M. Iijima, T. Nakayama, T. Sodesawa and F. Nozaki, *J. Catal.*, **169** (1997) 447.

83   G. L. Castiglioni, A. Vaccari, G. Fierro, M. Inversi, M. Lo Jacono, G. Minclli, I. Pettiti, P. Porta and M. Gazzano, *Appl. Catal. A: General*, **123** (1995) 123.

84   J. Miki, M. Asanuma, Y. Tachibana and T. Shikada, *J. Catal.*, **151** (1995) 323.

85   B. Miya, F. Hoshino and I. Iwasa, *J. Catal.*, **5** (1966) 401.

86   P. Schoubye, *J. Catal.*, **14** (1969) 238.

87   H. Kato, T. Sano, Y. Wada, Y. Tamaura, M. Tsuji, T. Tsuji and S. Miyazaki, *J. Mater. Sci.*, **30** (1995) 6350.

88   W. S. Epling, G. B. Hoflund, W. M. Hartand and D. M. Minahan, *J. Catal.*, **169** (1997) 438.

89   S. H. Oh and R. M. Sinkevitch, *J. Catal.*, **142** (1993) 254.

90   Y. Tamaura and M. Tabata, *Nature*, **346** (1990) 255.

91   C.G. Ramankutty and S. Sugunan, *Appl. Catal. A: General,* **218** (2001) 39.

92   H. Grabowska, W. Kaczmarczyk and J. Wrzyszcz, *Appl. Catal.*, **47** (1989) 351.

93   K. Sreekumar, T. M. Jyothi, T. Mathew, M. B. Talawar, S. Sugunan and B. S. Rao, *J. Mol. Catal. A: Chem.*, **159** (2000) 327.

94   K. Sreekumar, T. Raja, B. P. Kiran, S. Sugunan and B. S. Rao, *Appl. Catal. A*, **182** (1999) 327.

95   K. Sreekumar, T. M. Jyothi, M. B. Talawar, B. P. Kiran, B. S. Rao and S. Sugunan, *J. Mol. Catal. A: Chem.*, **152** (2000) 225.

96   K. Sreekumar and S. Sugunan, *Appl. Catal. A*, **230** (2002) 245.

97   K. Sreekumar and S. Sugunan, *J. Mol. Catal. A: Chemical*, **185** (2002) 259.

98   E. Santacesaria, D. Grasso, D. Gelosa and S. Carra, *Appl. Catal.*, **64** (1990) 83.

99   Fiege, H.; Bayer, A. G.; Leverkusen. Federal Republic of Germany, in "*Ullmann's Encyclopedia of Industrial Chemistry*", *A19*, 324.

100   S. Patinuin, B. S. Friedman, in "*Alkylation of Aromatics with Alkenes and Alkanes in Friedel Crafts and Related Reactions*", **Vol. 3**, G. A. Olah (ed.), Interscience, New York, p. 75, 1964.

101   X-W. Li, M. Han, X-Y. Liu, Z-F. Pei and L-Q. She, *Stud. Surf. Sci. Catal.*, **105 B** (1997) 1157.

102   K. Zhang, C. Huang, H. Zhang, S. Xiang, S. Liu, D. Xu and H. Li, *Appl. Catal. A*, **166** (1998) 89.

103   K. Zhang, H. Zhang, G. Xu, S. Xiang, D. Xu, S. Liu and H. Li, *Appl. Catal. A*, **207** (2001) 183.

104   L. Garcia, G. Giannetto, M. R. Goldwasser, M. Guisnet and P. Magnoux, *Catal. Lett.*, **37** (1996) 121.

105   M. Marczewski, G. Perot and M. Guisnet, *Stud. Surf. Sci. Catal.*, **41** (1988) 273.

106   M. Inoue and S. Enomoto, *Chem. Pharm. Bull.*, **20** (1972) 232.

107   T. Kotanigawa, M. Yamamoto, K. Shimakowa and Y. Yoshida, *Bull. Chem. Soc. Jpn.*, **44** (1971) 1961.

108   V. Venkatrao, K. V. R. Chary, V. Durgakumari and S. Narayanan, *Appl. Catal.*, **61** (1990) 89.

109   A. S. Hay, G. F. Endres and J. W. Eustance, *J. Amer. Chem. Soc.*, **81** (1959) 6335.

110   A. S. Hay, *J. Polymer Sci.*, **58** (1962) 581.

111   K. Tanabe, H. Hattori, T. Sumiyoshi, K. Tamaru and T. Kondo, *J. Catal.*, **53** (1978) 1.

112   S. Sato, K. Koizumi and F. Nozaki, *Appl. Catal. A*, **133** (1995) L7.

113   T-F. Tsai and F-L. Wang, *Catal. Lett.*, **73** (2001) 167.

114   W. C. Choi, J. S. Kim, T. H. Lee and S. I. Woo, *Catalysis Today*, **63** (2000) 229.

115   K. Tanabe and T. Nishizaki, in "*Proc. 6th Internat. Congr. Catal*"., London, G. C. Bond, P. B. Wells and F. C. Thompkins (eds.), p. 863 (1977).

116   S. Sato, K. Koizumi and F. Nozaki, *J. Catal.*, **178** (1998) 264.

117   G. L. Warner (General Electric Co., USA) US Patent 4933509 (1990).

118   R. A. Battista, J. G. Bennett, J. J. Kokoszka, F. L. Tungate (General Electric Co., USA) *US Patent*, 4661638 (1987).

119   M. Marczewski, G. Perot and M. Guisnet, *React. Kinet. Catal. Lett.*, **57** (1996) 21.

120   R. Pierantozzi and A. F. Nordquist, *Appl. Catal.*, **21** (1986) 263.

121   P. Belitrame, P. L. Belitrame, P. Carniti, A. Castelli and L. Forni, *Appl. Catal.*, **29** (1987) 327.

122   M. C. Samolada, E. Grigoriadou, Z. Kiparissides and I. A. Vasalos, *J. Catal.*, **152** (1995) 52.

123   C. Bezouhanova and M. Al-Zihari, *Appl. Catal.*, **83** (1992) 45.

124   S. Sato, K. Koizumi and F. Nozaki, *Appl. Catal. A*, **133** (1995) L7.

125   S. Narayanan, V. Venkatrao and V. Durgakumari, *J. Mol. Catal.*, **52** (1989) L29.

126   V. Venkatrao, V. Durgakumari and S. Narayanan, *Appl. Catal.*, **49** (1989) 165.

127   H. Grabowska, W. Mista, J. Trawczynski, J. Wrzyszc and M. Zawadzki, *Res. Chem. Intermed.*, **27** (2001) 305.

128   Japanese Patent, 10113561 (1998), Asahi, Japan.

129   K. Tanabe, K. Shimazu and H. Hattori, *J. Catal.*, **57** (1979) 35.

130   F. M. Bautista, J. M. Campelo, A. Garcia, D. Luna, J. M. Marinas and A. A. Romero, *React. Kinet. Catal. Lett.*, **63** (1998) 261.

131   F. M. Bautista, J. M. Campelo, A. Garcia, D. Luna, J. M. Marinas and A. Romero, J. M. Navio and M. Macias, *Appl. Catal. A*, **99** (1993) 161.

132   T. Kotanigawa, *Bull. Chem. Soc. Jpn.*, **47** (1974) 950.

133   T. Kotanigawa and K. Shimakowa, *Bull. Chem. Soc. Jpn.*, **47** (1974) 1535.

134   H. Grabowska, J. Jablonski, W. Mista and J. Wrzyszc, *Res. Chem. Intermed.*, **22** (1996) 53.

135   M. Misono and N. Nojiri, *Appl. Catal.*, **64** (1990) 1.

136   B. E. Leach, *US Patent*, 4227024 (1980).

137   K. A. Adey, F. S. Yates and J. H. Young, *US Patent* 4471149 (1984).

138   J. M. Campelo, A. Garcia, D. Luna, J. M. Marinas and M. S. Moreno, *Stud. Surf. Sci. Catal.*, **41** (1988) 249.

139   S. Velu and C. S. Swamy, *Appl. Catal. A*, **119** (1994) 241.

140   S. Velu and C. S. Swamy, *Appl. Catal. A*, **145** (1996) 141, 225.

141   R. Pierantozzi and A. F. Nordquist, *Appl. Catal.*, **21** (1986) 263.

142   T. Yamanaka, *Bull. Chem. Soc. Jpn.*, **49** (1976) 2669.

143   F. Nozaki and I. Kimura, *Bull. Chem. Soc. Jpn.*, **50** (1977) 614.

144   J. Xu, A-Z. Yan and Q-H. Xu, *React. Kinet. Catal. Lett.*, **62** (1997) 71.

145   E. Santa, M. Diserio, P. Ciambelli, D. Gelosa and S. Carra, *Appl. Catal.*, **64** (1990) 101.

146   S. Balsama, P. Beltrame, P. L. Beltrame, P. Carniti, L. Forni and G. Zuretti, *Appl. Catal.*,

13 (1984) 161.

147   P. D. Chantal, S. Kaliaguine and J. L. Grandmaison, *Appl. Catal.*, **18** (1985) 133.

148   Z. Fu and Y. Ono, *Catal. Lett*., **21** (1993) 43.

149   J. G. Bennett and G. R. Chambers, *European Patent*, 127833 (1984).

150   T. G. Lin, L. W. Ho, A. N. Ko and Y. J. Perng, *US Patent*, 4876398 (1989).

151   M. Inoue and S. Enomoto, *Chem. Pharm. Bull*., **24** (1976) 2199.

152   K. Tanabe, C. Ishiya, I. Matsuzaki, I. Ichikawa and H. Hattori, *Bull. Chem. Soc. Jpn*., **45** (1972) 47.

153   H. Grabowska, W. Mista, J. Trawczynski, J. Wrzyszcz and M. Zawadzki, *Res. Chem. Intermed*., **27** (2001) 305.

154   J. Wrzyszcz, J. Cmielewska, Z. Jaworska-galas, W. Kaczmarczyk, K. Mazur and W. Mista, *Polish Patent*, 159870 (1993).

155   V. Krishnasamy, T. V. Subramaniam and S. Soundararajan, *J. Indian Chemical Society*, **59** (1982) 1067.

156   W. E. Smith, *US Patent*, 4048239 (1977).

157   S. Velu, K. Suzuki, M. Okazaki, M. P. Kapoor, T. Osaki and F. Ohashi, J. Catal., **194** (2000) 373.

CHAPTER 2
EXPERIMENTAL AND
PHYSICO-CHEMICAL
CHARACTERIZATION

2.1. CATALYST PREPARATION

The ferrospinel system having the general formula $Cu_{1-x}Co_xFe_2O_4$ was prepared by co-precipitation technique as described in the literature [1]. AR grade chemicals supplied by Qualigens chemicals were used as supplied, without any further purification. Stoichiometric amounts of premixed metal nitrate solutions were rapidly added to the NaOH solution at room temperature under continuous stirring. Final pH of the resulting solution was adjusted between 9.5 and 10. Aging of the precipitate was carried out for 8 hours and then washed well with demineralized water till both Na^+ and NO_3^- ions disappear. The precipitate was filtered and dried at 80^oC in an air oven for about 36 h. The dried materials were powdered and calcined at 500^oC.

2.2. CATALYTIC ACTIVITY MEASUREMENTS

Vapor phase experiments were performed at atmospheric pressure in a fixed bed, vertical, down-flow, integral silica reactor placed inside a double-zone furnace (Geomechanique, France). Schematic diagram of a reactor setup is shown in Figure 2.1. Three grams of fresh catalyst with a particle size up to 20 mesh was charged each time at the center of the reactor in such a way that the catalyst was sandwiched between the layers of inert porcelain beads. The upper portion of the reactor served as a vaporizer cum pre-heater. All heating and temperature measurements were carried out using 'Aplab' temperature controller and indicator instruments. A thermocouple was positioned at the center of the catalyst bed to monitor the exact temperature of the catalyst. Activation of the catalyst consists of heating in a sufficient flow of dry air at 500^0C for at least 6 hours before each run. The catalyst was then cooled to the desired reaction temperature in presence of nitrogen. The reactant mixture was fed by a syringe pump (ISCO, Model 500D). The products of the reaction were passed through a condenser, circulated with chilled water, and collected in a receiver.

<u>Analytical Method</u>

A gas chromatograph equipped with flame ionization detector (detector temperature = 250^0C) and a 30m X 0.32mm X 0.25μm HP – 1 column (model HP 6890) filled with 5% crosslinked methylstyrene was used to analyse the reaction products.

Response factors of the products with respect to phenol were determined from GC analysis using mixtures of known concentration of each product and phenol. The conversion of phenol and the selectivities of each product were calculated with those response factors. Reaction products were further confirmed by GC-MS and GC-IR. Analytical grade phenol, methanol, dimethyl carbonate, ethanol and isopropanol from Merck were used in the study.

The reproducibility for different samples was checked experimentally, and the measurements were repeated two or three times with a relative error of approximately ±2%. The thermal process without catalyst was negligible in all cases. It is evident from the following discussion that several factors contribute to the total catalytic activity at different extents. Besides, the difficulty in determining the specific surface area of any specific element and the complex nature of active centers in these materials make it unsuitable to express the results in turn over frequency. Hence the results are given in mol%.
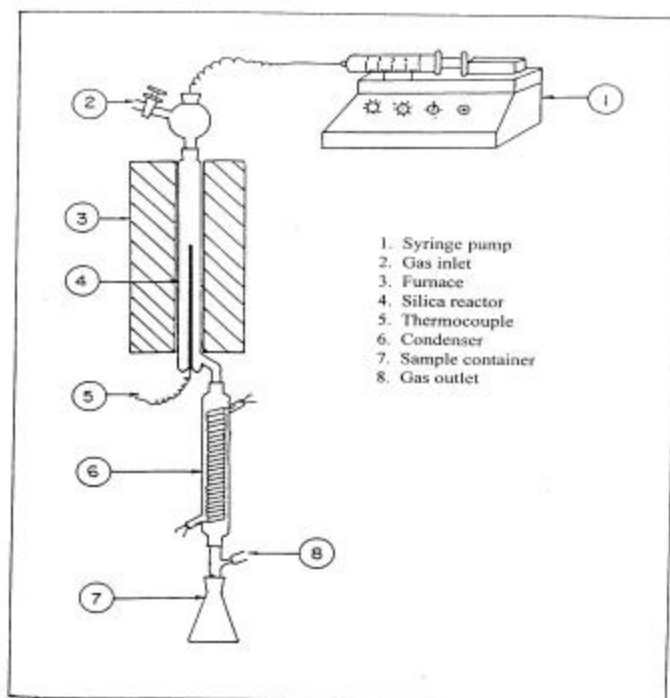
Figure 2.1: Reactor set-up for reactions carried out in vapour-phase.

2.3. PHYSICOCHEMICAL CHARACTERIZATIONS

2.3.1. Introduction

The ultimate goal of research in heterogeneous catalysis is to correlate the structure and composition of a catalyst with its performance. Catalyst performance is judged in terms of its activity, product selectivity and life. Catalyst characterization is one of the crucial aspects of catalyst design since it gives information about crystallinity, surface structure, nature of active sites, particle size and morphology, acidity, and other characteristic features.

The calcined samples were characterized by adopting various physico-chemical methods such as X-ray diffraction analysis, infrared spectroscopy, surface area and pore volume measurements, SEM, TG-DTA, TPR, XPS, adsorption studies of electron acceptors and FTIR adsorption of pyridine and CO_2.

The present chapter gives a brief account of the theory and principle of various characterization techniques used for the current study. The procedure for each experimental technique is described in this chapter. Though the results of some of the characterization techniques are presented in this chapter, characterization techniques such as XPS, Mössbauer, TPR etc, which are extensively used for comparing both fresh and spent catalysts are included in chapter 4. The acid-base properties of the catalyst system are discussed in detail in this chapter.

2.3.2. Theory and experimental procedure

2.3.2.1. X-Ray diffraction analysis

The diffraction patterns can be used to identify various phases in a catalyst. Diffraction can occur whenever Bragg's law $n\lambda = 2d \sin\theta$ is satisfied. The XRD method involves the interaction between the incident monochromatized X-rays (like Cu Kα or MoKα source) with the periodic structures of polycrystalline material. Bragg peaks are measured by observing the intensity of the scattered radiation as a function of scattering angle 2θ. The interplanar distances or d-spacings are calculated from the values of the peaks observed from the above Bragg equation, where, 'n' is order of reflection and the values are 1,2,3 etc. The width of diffraction peaks carries information on the dimensions

of the reflecting planes. Diffraction lines from the perfect crystals are very narrow. For crystals with size below 100 nm, line broadening occurs due to incomplete destructive interference in scattering directions where the X-rays are out of phase. The Debye-Scherrer formula [2],

$$D_{hkl} = 0.9\lambda/B \cos\theta \qquad (1)$$

is used to estimate the crystallite size, where D_{hkl}, λ, B and θ are the volume averaged particle diameter, x-ray wavelength, full width at half maximum (FWHM) and diffraction angle, respectively. It is possible to find out the symmetry and cell constant of a given powder by x-ray diffraction technique.

Powder X-ray diffraction (XRD) patterns of the all catalysts reported in this thesis were recorded using a Rigaku Geigerflex instrument equipped with Cu K_α radiation ($\lambda =$ 1.5405 Å) with Ni-filter.

2.3.2.2. Diffuse reflectance infrared spectroscopy

Infrared techniques have got remarkable importance in the field of heterogeneous catalysis and in the field of surface chemistry and catalysis over metal oxides. A variety of IR techniques have been used in order to get information on the surface chemistry of different solids. With respect to the characterization of metal oxide catalysts two techniques largely predominate, namely, the transmission/absorption and the diffuse reflection techniques.

In recent years, the use of IR spectroscopy in the diffuse reflectance mode is grown strongly since this technique does not need particular efforts in the sample preparation (the powder is simply deposited on a sample holder), especially useful in the case of highly scattering samples employed in heterogeneous catalysis. The theory of diffuse reflectance spectra was developed by Kubelka and Munk [3] and extended by Kortun et al [4]. According to this theory,

$$f(R\alpha) = (1-R\alpha)^2/2R\alpha = K/S \qquad (2)$$

where $R\alpha$ is the diffuse reflectance from an 'infinitely' thick sample, K is the extinction coefficient and S is a scattering coefficient.

It is known that structure plays an important role in the catalytic activity of many heterogeneous systems. In many cases, the positions of the infrared bands are sensitive to the changes in the ratio of metal cations in the catalyst composition. Since, in spinels metal ions are distributed in two different environments, the spinel phase formation can be very well assigned by the appearance of two broad IR bands.

The IR spectrum of the ferrite samples reported here were recorded through a DR mode (Shimadzu) in the range 400 cm^{-1} to 1000 cm^{-1}.

2.3.2.3. Surface area determination by BET method

The Brunauer-Emmett-Teller (BET) method is the most widely used procedure for the determination of surface area of solid materials and involves the use of the BET equation (3).

$$P/V_{ads}(P_0-P) \quad = \quad 1/V_m C \quad + \quad [(C-1)/V_m C]*(P/P_0) \qquad (3)$$

where P = adsorption equilibrium pressure, P_0 = standard vapour pressure of the adsorbent, V_{ads} = volume at STP occupied by molecules adsorbed at pressure P, V_m = volume of adsorbate required for a monolayer coverage, C = constant related to heat of adsorption. A plot of $P/V_{ads}(P_0-P)$ Vs (P/P_0) will yield a straight line usually in the range $0.05 \leq P/P_0 \leq 0.35$. The slope (s) and intercept (i) of the BET plot are $s = (C-1)/V_m C$ and $i = 1/V_m C$. Solving these equations permits the calculation of V_m. Then the specific surface area of the catalyst can be calculated as,

Specific surface area, $m^2 g^{-1}$ cat. $\quad = \quad [(V_m N_a)/22414*Wt]*A_m \qquad (4)$

A_m = mean cross sectional area occupied by adsorbate molecule (16.2 A^2 for N_2), Wt = weight of the catalyst sample, N_a = Avogadro number, V_m = monolayer volume in ml at STP.

To differentiate between the adsorption mechanism in micropore and that occurring in meso and macropores, the t-plot analysis developed by Lippens and de Boer was applied [5]. The method consists of plotting the adsorption isotherm in terms of the volume of the gas adsorbed versus the statistical film thickness, t. The pore size distribution is obtained from the analysis of the desorption isotherms by applying the BJH model [6] which involves the area of the pore walls and uses the Kelvin equation to correlate the partial

pressure of nitrogen in equilibrium with the porous solid to the size of the pores where the capillary condensation takes place.

The BET surface area and pore volume of the catalysts were determined by N_2 adsorption-desorption method at liquid N_2 temperature (77K) using Quantachrome Nova-1200 adsorption unit. About 200 mg of sample was degassed at 300^0C for about 4 hours till the residual pressure was $<10^{-3}$ Torr. The isotherms were analysed in a conventional manner, that includes the BET surface area in the region of the relative pressure $P/P_0 = 0.05$ to 0.3 with the assumption for the nitrogen molecular area in an adsorbed monolayer of $w=0.162$ nm^2. The pore size distribution were calculated via the BJH method. The total pore volumes were taken at $P/P_0 = 0.95$.

2.3.2.4. Scanning electron microscopy (SEM)

Scanning electron microscopy is considered to be a powerful tool to get informations about morphology and particle size. SEM is carried out by passing a narrow electron beam over the surface and detecting the yield of either secondary or back scattered electrons as a function of the position of the primary beam. The size and morphology of the crystals of all the compositions were examined using a JEOL JSM-840A scanning electron microscope.

2.3.2.5. Thermal analysis (TG and DTA)

Thermal analysis includes a group of methods by which the physical and chemical properties of a substance, a mixture and/or reaction mixtures are determined as a function of temperature (or time), while the sample is subjected to a controlled temperature program. In thermogravimetry, the mass of the sample is monitored as a function of temperature (or time), while the sample is subjected to a controlled temperature program. Differential Thermal Analysis (DTA) measures the difference in temperature between a sample and a thermally inert reference as the temperature is raised. A plot of this differential provides information on exothermic and endothermic reactions taking place in the sample, which include phase transitions, dehydration, decomposition, redox, or solid-state reactions.

Thermogravimetry and differential thermal analysis measurements were performed with a Mettler TA-1 apparatus equipped with a control and data acquisiton system developed by the Anatech Bv. About 100 mg samples of spent catalysts were measured in air at a heating ramp of 2 K min^{-1} up to 1070 K.

2.3.2.6. Temperature programmed techniques: TPR and TPD

Temperature programmed reduction (TPR), oxidation (TPO), desorption (TPD) and reaction spectroscopy (TPRS) form a class of techniques in which a chemical reaction is monitored while the temperature increases linearly. The basis set up for TPR, TPO and TPD consists of a reactor and a thermal conductivity detector to measure the hydrogen content in TPR/TPD or the oxygen content in TPO, of the gas mixture before and after reaction. The TPR/TPO methods are used for qualitative and quantitative analysis.

In the TPR technique the catalyst material is subjected to a programmed temperature rise, while a reducing gas mixture is flowing over it (usually, hydrogen diluted in some inert gas like argon). The reduction rate is continuously measured by monitoring the change in composition of the gas mixture after passing through the reactor. The decrease in H_2 concentration in the effluent gas with respect to the initial percentage monitors the reaction progress.

TPD is a technique for studying the kinetics of adsorbates on solid surfaces. The data are collected under well-controlled ultra-high vacuum conditions and after analysis yield values of kinetic parameters as a function of adsorbate surface coverage. The sample temperature is heated (by a variety of means) in a controlled fashion. The mass spectrometer is tuned to monitor one or more mass fragments simultaneously that can be correlated to the sample temperature. The desorption temperature, the shape of the desorption peak, and how all these change with initial surface coverage and heating rate are all analyzed to provide information about the binding character of the adsorbate/substrate system.

TPR and TPD measurements were performed by a SORBSTAR apparatus equipped with thermal conductivity detector (TCD) and mass spectrometer (MS) to

identify the desorbed molecules. TPR measurements were carried out in a flow of 1 % H_2/Ar mixture, TPD studies were performed in pure He stream.

2.3.2.7. Mössbauer spectroscopy

The phenomenon of recoil free resonance absorption of nuclear gamma rays (Mössbauer effect) has been known to be a powerful tool for investigating the properties of internal fields acting on nuclei in solids [7,8]. Due to the presence of surrounding electronic charges, the nuclear energy levels are perturbed and the scanning of these levels gives valuable information about the nature of bonding in solids. Mössbauer isomer shift (IS) is a parameter by which the nature of different cationic oxidation states and the character of chemical entities in a catalyst may be monitored. The isomer shift (IS) is the consequence of the Coulomb interaction between the positively charged nucleus and the negatively charged s-electrons. The electric quadrupole splitting is caused by the interaction of the electric quadrupole moment with an electric field gradient. Quadrupole splitting data may be used to access the structural properties of catalysts and the distribution of electronic charge around the probe atoms. Magnetic hyperfine splitting or the so-called Zeeman effect arises from the interaction between the nuclear magnetic dipole moment and the magnetic field at the nucleus. This interaction splits both nuclear levels and removes all degeneracy. From the eight possible transitions only six are allowed and the spectrum contains six equidistant peaks, called sextet or sextuplet. The separation between the peaks in the spectrum is proportional to the magnetic field at the nucleus.

Mössbauer spectroscopy finds extensive applications and has been largely applied for compounds containing iron. If the iron atoms occupy equivalent lattice positions, the local fields at the iron nuclei are characterized by a single set of parameters. If they occupy two non-equivalent sets of positions, as in the case of ferrites, one would expect to obtain a superimposition of two parameters. If, in addition, both Fe^{2+} and Fe^{3+} ions are present in the lattice, the spectra will be more complex. Mössbauer studies on ferrites provide valuable information on the ratio of the Fe^{3+} in T_d and O_h sites, the type of ordering

(Neel – type or Yafet – Kittal type) and any deviation from stoichiometry leading to mixed valence states such as Fe^{2+} and Fe^{3+}.

Mössbauer spectra were obtained in constant acceleration mode. Spectra were fitted assuming a Lorentzian line shape; none of the positional parameters were constrained. Isomer shift values are related to the center of metallic α-iron spectrum at room temperature. The estimated accuracy of the positional parameters is $\pm$ 0.03 mm/s [9].

2.3.2.8. X-ray photoelectron spectroscopy (XPS)

The X-ray photoelectron spectroscopy [10-12] is based on the photoelectric effect, which involves the bombardment of a sample surface with X rays and the measurement of the concomitant photoemitted electrons. The photoemitted electrons have discrete kinetic energies that are characteristic of the emitting atoms and their bonding states. The kinetic energy, E_k, of these photoelectrons is determined by the energy of the X-ray radiation, $h\nu$, and the electron binding energy, E_b, as given by:

$$E_k = h\nu - E_b \qquad\qquad (5)$$

The experimentally measured energies of the photoelectrons are given by:

$$E_k = h\nu - E_b - E_w \qquad\qquad (6)$$

where E_w is the work function of the spectrometer.

The XPS technique is highly surface specific due to the short range of the photoelectrons that are excited from the solid. The binding energy of the peaks is characteristic of each element. The peak areas can be used (with appropriate sensitivity factors) to determine the composition of the materials surface. The shape of each peak and the binding energy can be slightly altered by the chemical state of the emitting atom. Hence XPS can provide chemical bonding information as well. XPS and the related Auger electron spectroscopy (AES) can provide elemental analysis for essentially the entire periodic table. Because the electrons whose energies are analyzed arise from a depth of no greater than about 5 nm, the techniques are surface-sensitive.

X-ray Photoelectron spectra were acquired on a VG Microtech Multilab ESCA 3000 spectrometer using a non-monochromatized MgKα x-ray source (hν = 1253.6 eV) on '*in situ*' scraped fresh catalyst pellets and powder samples of spent catalysts at room temperature.

Selected spectra were recorded with AlKα x-ray (hν = 1486.6 eV) also to eliminate the overlap between different Auger and core levels. Base pressure in the analysis chamber was maintained at 3-6 x 10^{-10} Torr range. The energy resolution of the spectrometer was determined from the full width at half maximum of metallic gold and the value obtained is better that 0.8 eV for MgK$_\alpha$ radiation and 1.1 eV for AlK$_\alpha$ radiation respectively, at a pass energy of 20 eV. The error in the BE values [13,14] reported is ±0.1 eV.

2.3.2.9. Infrared adsorption studies

The most common application of IR in catalysis is to identify adsorbed species and to study the way in which these species are chemisorbed on the surface of the catalyst [15-17]. More specifically, IR spectroscopy has been used to study the adsorption of typical probe molecules like ammonia, pyridine and other bases, hydrocarbons, carbon dioxide which can monitor either the acidic or basic sites on oxide catalysts [18]. Investigation of adsorbed species in relation to their behavior in catalytic reactions is the main field of application of IR spectroscopy. IR studies if performed under conditions where some intermediates are actually detectable can give valuable information on the catalysis mechanisms.

2.3.3. Results and discussion

Chemical compositions (determined by XRF), structural and textural properties of $Cu_{1-x}Co_xFe_2O_4$ spinel system catalysts prepared in the present study are summarized in Table 2.1. XRF results display the bulk metal ion concentrations in line with starting composition.

Figure 2.2a shows the XRD patterns of calcined catalysts. It can be seen that, the fresh Cu-rich catalyst (x = 0.0) exhibit diffraction pattern attributed to cubic spinel phase [19] and a considerable amount of CuO and Fe_2O_3 phases. This indicates the spinel formation is not complete at 500^0C for x = 0.0 in agreement with literature reports [19-22]. Substitution of Cu by Co increases the overall crystallinity of spinel phase and all the peaks are indexed as reported in ASTM card (card no. 1-1121 and 3-0864, JCPDS card No: 3-864, 22-1086). However, trace amount of α-Fe_2O_3 impurity phase was also detected in Co-containing catalysts. The lattice constant, *a,* obtained for $CuFe_2O_4$ and $CoFe_2O_4$ are

8.3898 Å and 8.3997 Å respectively, close to the literature value [19,23,24]. The slight deviation of the value of lattice constant from the literature value may be due to the partial deformation of the anion sublattice due to the presence of extra phases.

Table 2.1: Chemical Analysis, XRD parameter and textural properties of $Cu_{1-x}Co_xFe_2O_4$

Catalyst Composition (x)	Metal Concentration (Wt. %)[a]			Crystallite Size (nm)[b]	a (Å)	Surface Area (m^2/g)	Micorpore Surface Area (m^2/g)	Total Pore Volume (cc/g)(10^{-3})	Average Pore Diameter (Å)
	Co	Cu	Fe						
0.0	--	27.1	46.2	15.25	8.3898	28.8	3.0	51.0	33.24
0.25	6.1	20.2	46.7	13.85	8.4051	34.0	7.8	66.7	33.47
0.50	12.4	13.5	47.1	13.17	8.4012	43.8	10.2	108.6	32.73
0.75	18.6	6.9	47.3	14.77	8.3982	36.6	4.3	63.6	33.34
1.0	25.1	--	47.6	14.13	8.3997	36.8	6.9	59.4	33.37

[a]Chemical analysis results obtained from XRF spectroscopy
[b]Obtained from Scherrer Equation (ref. 2)

The broad peaks seen in XRD indicate the fine particle size of the ferrite formed due to co-precipitation in contrast to the sharp peaks reported for materials prepared by ceramic method. It is also evidenced from the crystallite size of 13-16 nm for all samples (Table 2.1) estimated from most intense peak (311) using Scherrer equation [2]. The results are given in Table 2.1. However the crystallite size calculated by this method is not possible to separate the contribution from individual oxide phase over the FWHM of the diffraction maxima, it must be noted that with "crystallite size" we refer to the average size of coherent domains of diffraction which involve these two contributions.

It is very difficult to establish uniquely the distribution of cations among O_h and T_d sites in the Cu-Co-ferrite series from the intensity consideration of various hkl planes of spinel phase, since there are three kinds of cations distributed between the A and B sites, and all of the three cations have nearly equal scattering powers. The compound $CoFe_2O_4$ is reported to be an inverse spinel [24] or a partly inverse spinel [25,26]. Similarly the inverse nature of the $CuFe_2O_4$ is also well established in the literature [27]. However, most frequently spinel strurctures are only partially normal or inverse, with significant disorder in cation distribution.
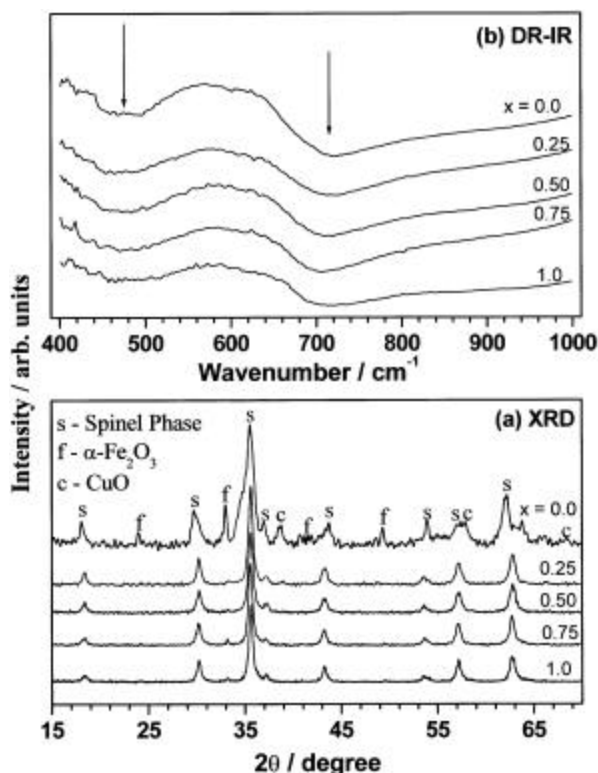
Figure 2.2: (a) X-ray diffractograms and (b) diffuse reflectance IR (DR-IR) of $Cu_{1-x}Co_xFe_2O_4$ samples recorded at room temperature after calcination at 500^0C. Arrows in DR-IR indicate ν_{M-O} of T_d (710 cm^{-1}) and O_h (460 cm^{-1}) coordinated cations.

IR studies were carried out to understand the band positions attributed to the lattice sites. Figure 2.2b shows the metal ions distributed in two different environments in spinel at 710 cm^{-1} (ν_1) and 460 cm^{-1} (ν_2) (solid arrows), attributed to T_d and O_h coordinated metal-oxygen bands respectively, and the phase formation can be very well assigned from the appearance of two broad DR-IR bands [28-31]. The broad absorption bands for $Cu_{1-x}Co_xFe_2O_4$ indicate the inverse nature of spinel for all the compositions. An examination of IR spectra of calcined samples reveal that the position of the absorption band changes slightly from one composition to another, the range of values being 710± 10 cm^{-1} and 460±15 cm^{-1}. However, the change observed in the absorption band positions in the present case is not very regular and might be due to the differences in the microstructure of the different compositions. Because of the differences in $Fe^{3+}-O^{2-}$ distances for the O_h and

T_d sites, the difference in the two band positions is expected. According to Waldron [30], T_d coordination bonds have the effect of substantially increasing $\nu_{cation-O}$, since these cations introduces a supplementary restoring force in a preferential direction along the M-O bond.

The results obtained from surface area analysis of $Cu_{1-x}Co_xFe_2O_4$ are summarized in Table 2.1. N_2 isotherms of all these compositions are of mixed type. N_2 adsorption desorption isotherms for a representative composition x = 0.50 is shown in Figure 2.3.
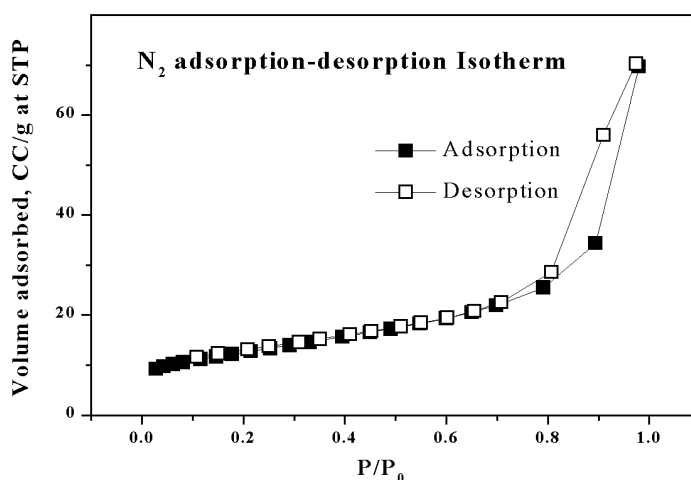
Figure 2.3: N_2 adsorption-desorption isotherm curve obtained from surface area measurement for the composition x = 0.50.

There is a gradual rise in volume depicted by all the curves with increasing relative pressure (P/P_0). At around $P/P_0 = 0.8$, a rapid rise in volume is observed. Thus these isotherms represent the combination of type IV and type II nature. The isotherms of type IV indicate the presence of mesoporosity present in the samples. The peak-to-peak diameter of the mesopores is around 33 Å for all the compositions indicating uniformity of the pores in the mesopore range. The external surface area obtained from the de Boer t plots exceeds the 75% values of the BET surface area of the individual compositions further confirming the presence of mesoporosity in the samples. Fraction of the micropore

pore volume per total pore volume is less than 6% for all the compositions calcined at 500^0C.

Scanning electron micrograms of calcined samples showed particles of size in the range 1-6 μm, which confirm the crystalline nature of the material. Figure 2.4 shows the SEM photographs of a representative sample for x =0.50. Sample dried at 80^0C shows fine particles of size in the range ≈10-50 nm (Figure 2.4a) against larger particles appeared for calcined samples (Figure 2.4b). Thus the crystalline nature of the material, as revealed from the XRD data, is supported by SEM images.

(a) Dried   **(b) Calcined**
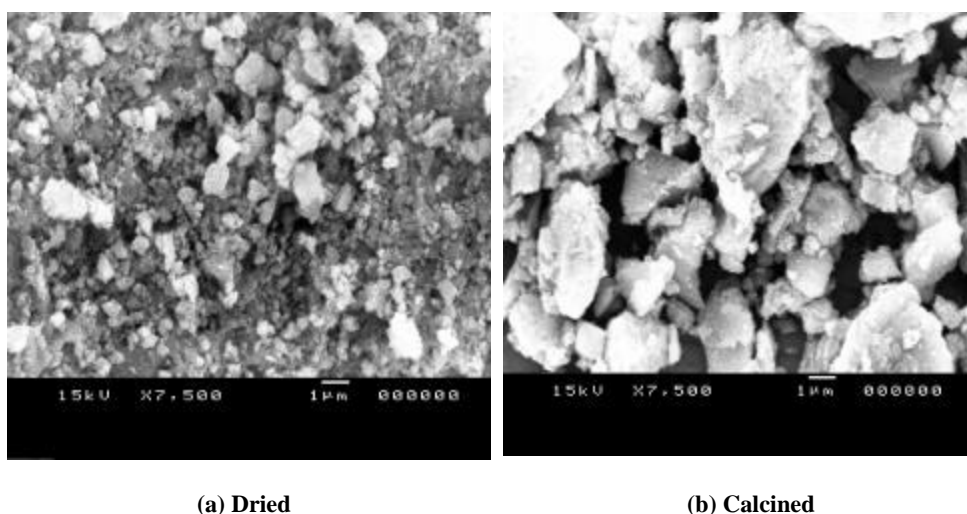
Figure 2.4: Scanning electron micrographs (SEM) of dried (a) and calcined (b) samples of the composition $Cu_{0.50}Co_{0.50}Fe_2O_4$.

TG and DTA curves for the dried samples of $Cu_{1-x}Co_xFe_2O_4$ series are presented in Figure 2.5. As shown in the figures, in the TG curve, the percent weight loss against the temperature is plotted (Figure 2.5a). For all samples there is a distinct weight loss from room temperature to 200^0C, which is due to dehydration of water. All catalysts displayed good thermal stability above 200^0C as indicated by the fairly horizontal portion of the TGA curves. However DTA curves show two peaks at 105^0C and ~ 520^0C. As expected, the peak at 105^0C is due to water loss and is an endothermic process (Figure 2.5b).

All the compositions containing Cu show an exotherm around ~520^0C. However, there is no weight gain/lost is observed in the TG curve at ~520^0C . From bibiliographic

data [32] the migration of Cu^{2+} ions from O_h to T_d sites is responsible for the exothermic peak around 520^0C. Ohnishi and Tarnishi [32] and Bergstein and Cervinka [33] considered the influence of intersite cationic migration on the transformations. As shown by Neel [34] and Ohnishi and Tarnishi [32], cupric ions can be displaced easily from one type of site to another by thermal treatments. The temperatures of order-disorder transformations depend on the content of O_h cupric ions and on the nonstoichiometry [32,35]. When placed in O_h sites, the Cu^{2+} ions need greater energy to migrate to the T_d sites and such a migration occurs above $400\text{-}450^0C$ for comparable heating rates [36]. Absence of such an exothermic peak in $CoFe_2O_4$ is a clear cut indication that Cu^{2+} ion is responsible for the exothermic peak observed at 520^0C.
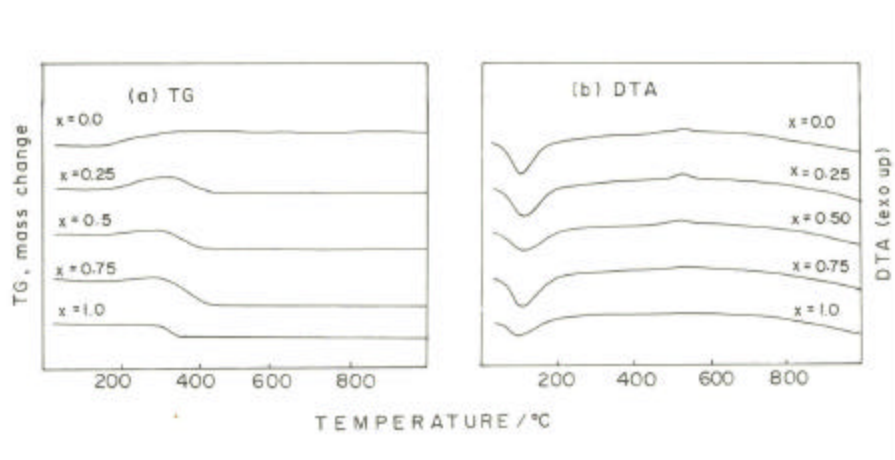
Figure 2.5: TG and DTA curves for the dried samples of $Cu_{1-x}Co_xFe_2O_4$

2.4. ACID-BASIC PROPERTIES

2.4.1. Introduction

The exposed cations and anions on oxide surfaces have been described as acid-base site pairs [37,38]. The oxygen anions can act as Bronsted or Lewis base sites; the metal cations are Lewis acid sites. Hydroxyl groups bound at certain oxide surfaces may exhibit considerable Bronsted acidity, but by and large we can neglect Bronsted acidity of oxide surfaces in surface science studies. Strong Bronsted acidity usually arises in mixed oxides rather than pure oxides, due to charge imbalances and/or coordination changes caused by incorporation of a second cation type [39,40].

A variety of physico chemical methods have been employed and widely applied to evaluate the strength and the amount of acid/basic sites on catalysts. A large variety of probe molecules have been utilized to both qualitatively ascertain the acidity and basicity and provide the measure and nature of these acidic and basic sites [41-48]. For example, pyridine was chosen as the base probe molecule to measure the acidity. When chemisorbed on a surface possessing acid properties, pyridine can interact with acidic protons, electron acceptor sites and H from neutral or weakly acidic hydroxyls [45,46]. CO_2 has been used to probe basic surface properties because it is amphoteric (but known by its acidic nature) and therefore it is expected to adsorb both acidic and more strongly on basic sites [47,48]. On the other hand, adsorption of certain organic molecules likes 7,7,8,8-Tetracyanoquinodimethane (TCNQ), 2,3,5,6-tetrachloro-1-4-benzoquinone (chloranil) and p-dinitrobenzene (PDNB) on the oxide surface will provide insight on the strength and distribution of electron donor sites on the oxide surfaces [49,50]. By probing the interaction of these molecules with the surface, information can be obtained on the oxidation state of the metal ion, the coordination symmetry, the degree of coordination unsaturation of the surface hydroxy groups and the presence and the nature of surface Lewis and Bronsted acid sites.

2.4.2. Experimental

FTIR adsorption of CO_2 and pyridine were operated in drift mode. Calcined powder sample was taken in a sample holder and placed in a specially designed cell. The samples were then heated *in situ* from room temperature to 400^0C at a heating rate of 5^0C/min and in a flowing stream (40 ml/min) of 99.99% N_2. The sample was kept at 400^0C for 3 hours and then the hydroxyl region of the spectra was measured. The sample was then cooled to 100^0C and pyridine vapour was introduced for 10 minutes in the N_2 flow. The low concentration of gas-phase pyridine was necessary in order to decrease the background pyridine signals in the IR spectra. The temperature was then slowly increased under the N_2 flow and IR spectra were recorded at different temperatures up to 400^0C. A resolution of 2 cm^{-1} is attained after averaging over 500 scans for all the IR spectra

reported here. For CO_2 adsorption, 99.99 % CO_2 (Linde Air) was introduced for 1 hour in N_2 at a flow rate of 40 ml/hr at room temperature after the *in situ* activation.

Adsorption studies with EA molecules were carried out over various compositions of $Cu_{1-x}Co_xFe_2O_4$ as described in the literature [49-51]. Adsorption studies were carried out over 0.5g calcined sample placed in a cylindrical glass vessel fitted with a mercury sealed stirrer. The catalysts were activated at 500^0C for two hours prior to each experiment. Before sealing, the sample was out gassed at 10 torr for one hour. 10 ml of a solution of an electron acceptor in acetonitrile was then admitted to the catalyst. Stirring was continued for 4 hours in a mechanically driven stirrer at 28^0C in a thermostated bath, and the oxide was collected by centrifuging the solution. The amount of electron acceptor adsorbed was determined from the difference in the concentration of electron acceptor in solution before and after adsorption, which was measured by means of a Shimadzu UV-VIS spectrophotometer (λ_{max} of electron acceptors in solvent: 393.5 nm for TCNQ, 288 nm for chloranil and 262 nm for PDNB). The amount adsorbed was calculated from the difference in the absorbance before and after adsorption.

2.4.3. Results

2.4.3.1. Hydroxyl groups on $Cu_{1-x}Co_xFe_2O_4$

FTIR spectra of surface hydroxyl groups of $Cu_{1-x}Co_xFe_2O_4$ are presented in Figure 2.6. The most intense band is found spread in the 3735-3710 cm^{-1} range and intensity of OH bands, in general, increases with increasing Co content. The above band comprised of terminal OH over T_d coordinated Fe^{3+}, Co^{2+} and Cu^{2+} ions and coordinatively unsaturated Fe^{3+} (O_h) ion [52-58]. In addition to the above the spectra show other broad bands centered approximately at 3695, 3680, 3660 and 3635 cm^{-1} is attributed to terminal OH over O_h coordinated Fe^{3+}, Co^{2+} and Cu^{2+} ions. Many of these bands are well documented in the literature for various oxides such as γ-Fe_2O_3, α-Fe_2O_3 [52-54], $MgFe_2O_4$ [52], $ZnFe_2O_4$ [52], $CoAl_2O_4$ [55,56], CoO [57], CuO [58] etc. A relevant list of the most intense ν_{OH} bands associated to different cations having different coordination number, oxidation state and cationic environment on various oxides are presented in Table 2.2.
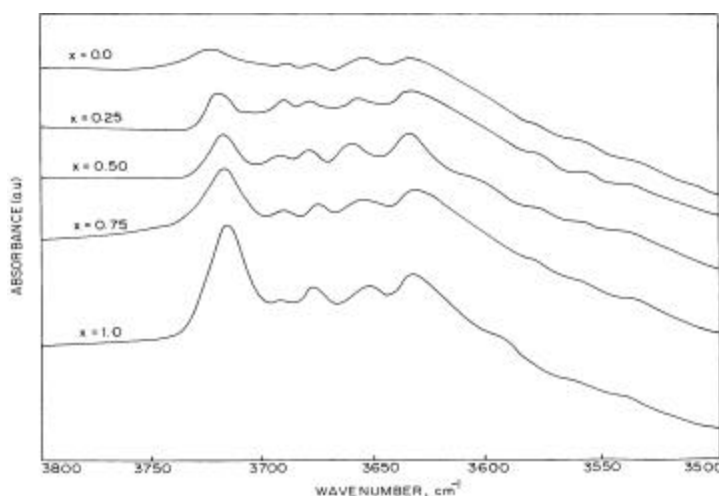
Figure 2.6: FTIR spectra of OH groups on $Cu_{1-x}Co_xFe_2O_4$ after *in situ* activation at 673 K.

Table 2.2: Assignments of the bands of surface hydroxyls on various oxide surfaces

Material	Position of n_{OH} (cm^{-1})	Assignments	References
γ-Fe_2O_3	3725	Terminal OH bonded to tetrahedral Fe^{3+}	52
	3675	Terminal OH bonded to octahedral Fe^{3+}	
	3640	Bridging OH	
α-Fe_2O_3	3720, 3680, 3635	Vibrations of three types of isolated OH group each liganded to a single Fe^{3+}	52-54
$MgFe_2O_4$	3690	Terminal OH over octahedral Fe^{3+}	52
$CoAl_2O_4$	3725	Terminal OH bonded to $_{IV}Co^{2+}$	55-56
	3580	Triply bridging OH or due to H bonded or more perturbed OH groups	
$ZnFe_2O_4$	3680	Terminal OH on tetrahedral Zn^{2+}	52
	3650	Terminal OH on octahedral Fe^{3+}	
	3610	Bridging OH's	
CuO	3690	Terminal OH	58
CoO	3680, 3658, 3639	Terminal OH	57

2.4.3.2. Pyridine adsorption

The IR spectrum of pyridine adsorbed on $Cu_{1-x}Co_xFe_2O_4$ at 373 K was recorded and shown in Figure 2.7. Four important pyridine ring modes occur approximately at 1606, 1573, 1485 and 1446 cm^{-1} termed ν_{8a}, ν_{8b}, ν_{19a} and ν_{19b} respectively [59,60] and listed in Table 2.3.
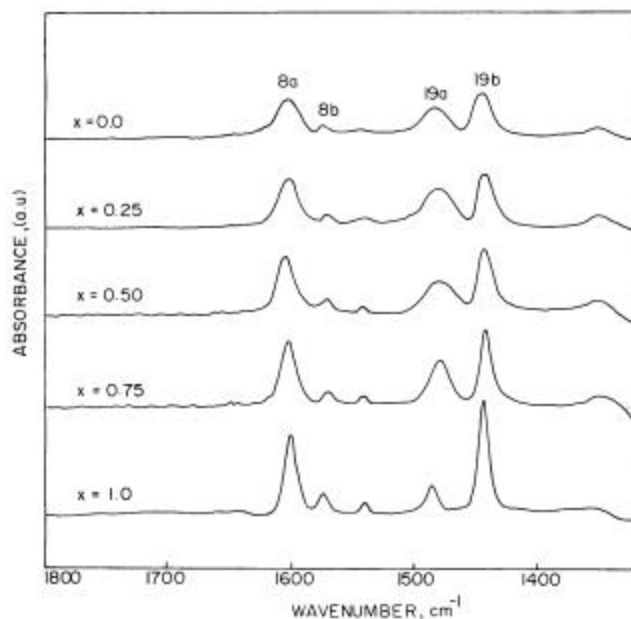
Figure 2.7: FTIR spectra of pyridine adsorbed on $Cu_{1-x}Co_xFe_2O_4$ surfaces at 373 K, after *in situ* activation at 673 K.

Table 2.3: Position of the various IR bands (in cm^{-1}) of pyridine and pyridinium ion adsorbed at 373 K over various compositions of $Cu_{1-x}Co_xFe_2O_4$

Composition	n_{8a}	n_{8b}	$n_{pyridinium-ion}$	n_{19a}	n_{19b}
$CuFe_2O_4$	1606	1573	1541	1485	1446
$Cu_{0.75}Co_{0.25}Fe_2O_4$	1608	1575	1541	1485	1446
$Cu_{0.5}Co_{0.5}Fe_2O_4$	1608	1573	1548	1485	1446
$Cu_{0.25}Co_{0.75}Fe_2O_4$	1608	1573	1543	1483	1446
$CoFe_2O_4$	1604	1575	1541	1487	1446

Note that the pyridine molecule can be retained on the surface of oxides in following three different modes [43] namely, (1) interaction of the N lone pair electron and the H atom of OH group, (2) transfer of a proton from surface OH group to the pyridine forming pyridinium ion (Bronsted acidity), and (3) pyridine coordination to an electron deficient metal atom (Lewis acidity). Predominant IR bands, ν_{8a} and ν_{19b}, confirm the major contribution of acidity is due to Lewis acid sites on all compositions. Among the above four vibration modes, ν_{8a} is very sensitive with respect to the oxidation state, coordination symmetry and cationic environment [45]. A broad ν_{8a} band at 1606 cm^{-1} at x = 0 decreases in width at higher 'x' values and indicates a decrease in the disorder of cation distribution in these spinels. ν_{8b} at 1575 cm^{-1} is found to be very labile and its stability on the surface is temperature dependent [52,55]. When the temperature increases above 373 K, ν_{8b} band completely disappears and confirms its labile nature. Hence, it is concluded that these species are bound to the terminal OH groups via H-bonding. This coordinative interaction is very weak and the molecule bound in this way gets desorbed at high temperature. A weak band centered at ~1540 cm^{-1} is attributed to pyridinium ion [45,61].

2.4.3.3. Temperature dependence of pyridine adsorption

FTIR spectra of pyridine adsorbed $Cu_{1-x}Co_xFe_2O_4$ samples were recorded between 373 K and 673 K. Above results for three selected compositions, x = 0, 0.50 and 1 are shown in Figure 2.8. Important changes in the spectral features are highlighted: (1) The bands corresponding to ν_{8a}, ν_{19a} and ν_{19b} modes display broad and intense peak for all the compositions up to 573 K. Presence of certain pyridine bands is observed even at 673 K on $CoFe_2O_4$ in contrast to no bands on Cu containing samples; (2) The bands correspond to ν_{8a} shifts to higher ν as the temperature increases for all compositions; (3) ν_{19a} and ν_{19b} bands are shifted to lower ν as the temperature increases for all the compositions. An apparent single band centered at 1446 cm^{-1} at temperature 373 K is split into two components at intermediate compositions (0<x<1) at higher temperatures; (4) On all compositions a band centered at ~1352 cm^{-1} increases in intensity as the temperature

increases up to 573 K, and (5) A weak band observed at ~1541 cm^{-1} due to pyridinium ion increases in intensity and width as the temperature increases to 473 K.
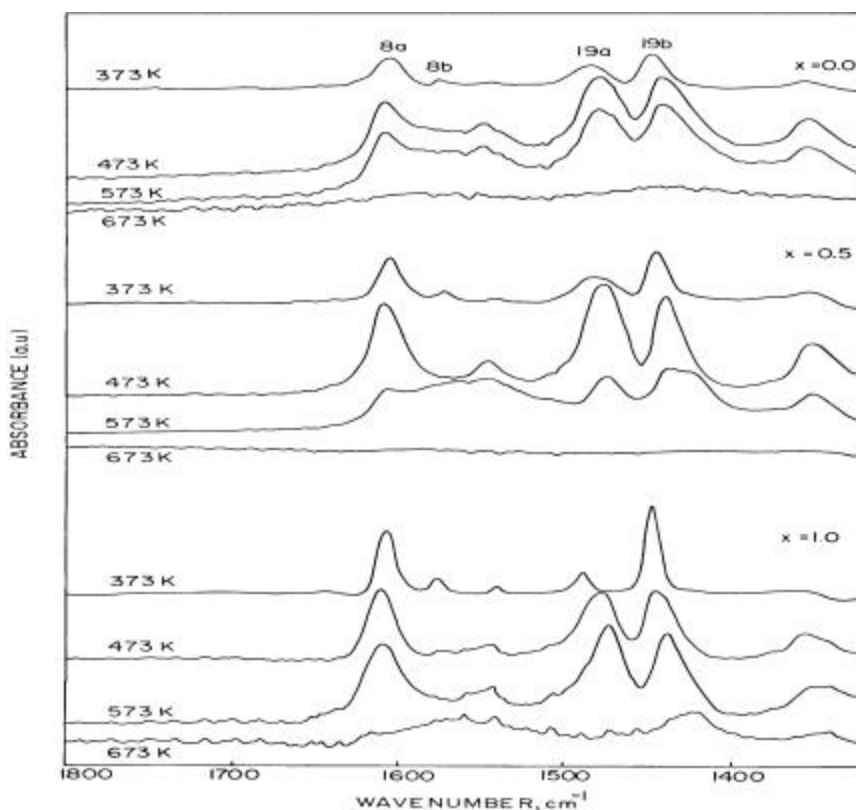
Figure 2.8: Temperature dependent FTIR spectra of pyridine adsorbed $Cu_{1-x}Co_xFe_2O_4$ surfaces on three selected compositions x = 0, 0.50 and 1 between 373 K and 673 K.

Figure 2.9 shows the difference IR spectra of pyridine adsorbed at 373 K and corresponding activated composition of $Cu_{1-x}Co_xFe_2O_4$. Difference spectrum shows negative bands corresponding to a lower intensity of the OH groups due to a perturbation by pyridine adsorption.
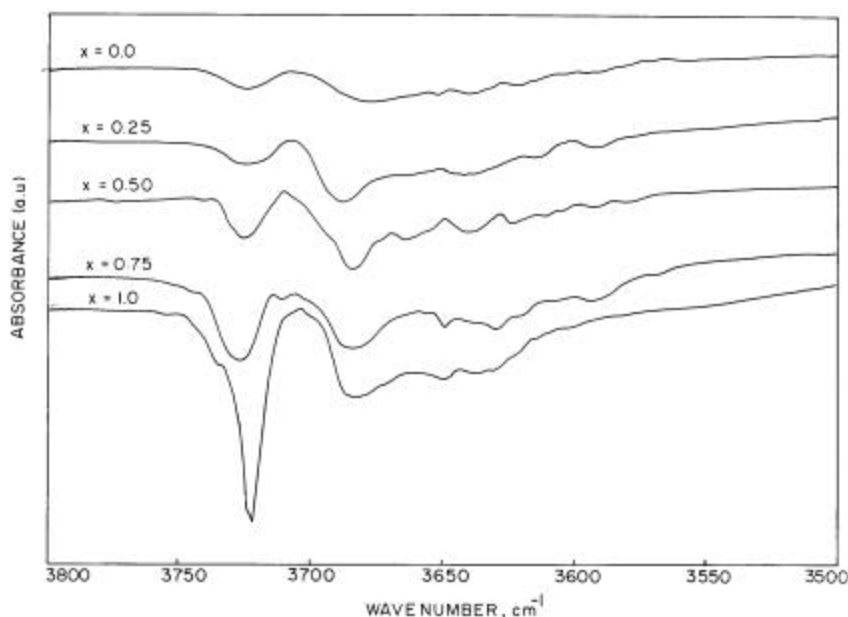
Figure 2.9: Difference IR spectra of the hydroxyl regions of $Cu_{1-x}Co_xFe_2O_4$ between pyridine adsorbed and calcined surfaces at 373 K.

2.4.3.4. Basicity

2.4.3.4.1. CO$_2$ adsorption

IR spectrum of CO_2 adsorbed on $Cu_{1-x}Co_xFe_2O_4$ at 298 K is shown in Figure 2.10. Asymmetric stretching of adsorbed CO_2 and carbonate vibrations are observed at 2400-2300 cm^{-1} and 1800–1200 cm^{-1} respectively [48,62-67]. The IR spectrum of adsorbed CO_2 demonstrates three different types of adsorptions as follows: (1) two sharp bands are observed at 2359 and 2341 cm^{-1} (corresponding CO_2 gas phase bands [68] are at 2358 cm^{-1} and 2338 cm^{-1}) resulting from the coordination of CO_2 on the surface Lewis acid sites. CO_2 retain its linear shape due to this mode of adsorption [62, 69]; (2) the intensity of various bands observed between 1700 cm^{-1} and 1260 cm^{-1} (symmetric OCO stretching of bidentate and unidentate carbonates at 1430-1260 cm^{-1}, asymmetric OCO stretching of unidentate carbonate and symmetric OCO stretching of bicarbonate at 1580-1435 cm^{-1} and asymmetric OCO stretching of bicarbonate and asymmetric OCO stretching of bidentate carbonates at 1680-1600 cm^{-1}) [64-67,69,70] generally decreases with increasing x, indicates a decrease in basicity from x = 0 to 1; and (3) the width and intensity of the

carbonate vibrations suggests the bidentate mode seems to be the dominant adsorption state on $Cu_{1-x}Co_xFe_2O_4$ and indicates the presence of coordinatively unsaturated ions. No other bands in the 2270–1700 cm^{-1} range suggests the absence of bridged CO_2 species on the oxide surface.
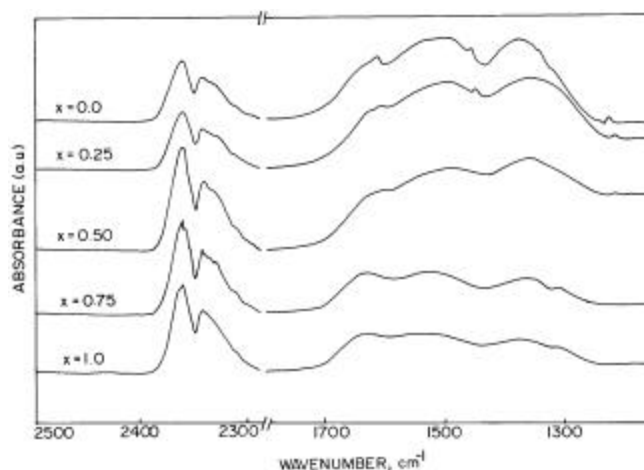
Figure 2.10: FTIR spectra of CO_2 adsorbed on $Cu_{1-x}Co_xFe_2O_4$ at room temperature (298K).

2.4.3.4.2. *Adsorption studies of TCNQ and chloranil*

Adsorption studies of three EAs, namely, TCNQ, chloranil and PDNB with electron affinity values 2.84, 2.40 and 1.77 eV, respectively, were performed on $Cu_{1-x}Co_xFe_2O_4$ [71,72]. Langmuir type of adsorption isotherms obtained on catalysts activated at 500^0C is shown in Figure 2.11 for (a) TCNQ and (b) chloranil and (c) the difference between TCNQ and chloranil for each composition. Since TCNQ is a strong EA it forms anion radicals upon adsorption from strong to weak donor sites. However, chloranil can accept electrons from both strong and moderately strong donor sites. Negligible adsorption of PDNB (results not shown) in all systems indicates the absence of very strong donor sites. This demonstrates that the adsorption sites on Cu-Co ferrites act as electron donors to the adsorbed molecule with electron affinity values >1.77 eV. EA adsorption studies indicate that the basicity of the $Cu_{1-x}Co_xFe_2O_4$ system decreases with increasing x. The difference between the limiting amounts of TCNQ and chloranil adsorbed (Figure 2.11c)

indicates that Cu-rich compositions possess large number of strong and moderately strong donor sites. Nonetheless with increasing x, the strength of the donor sites decreases.
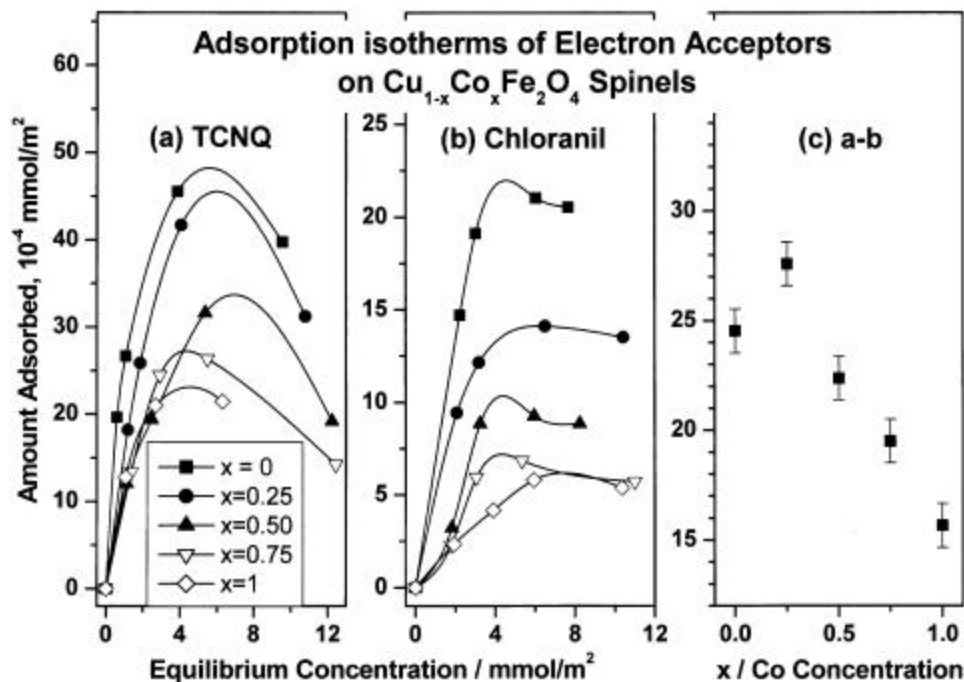
Figure 2.11: Adsorption isotherms of (a) TCNQ and (b) chloranil in acetonitrile on $Cu_{1-x}Co_xFe_2O_4$ system calcined at 500^0C. The difference between the limiting amounts of TCNQ and chloranil adsorbed at each composition is shown in (c).

2.4.4. Discussion

2.4.4.1. Composition dependence of hydroxy species on $Cu_{1-x}Co_xFe_2O_4$

Various OH bands seen in Figure 2.6 are due to terminal and bridging OH bonded over metal ions in T_d and O_h coordination and the strength of various OH bands is in the following order (Table 2.2): T_d coordinated terminal OH > O_h coordinated terminal OH > bridging OH. Although OH bonded over various ions are present on the surface, the contribution from each ion towards any specific band is different in terms of intensity and strength. It is clear that unlike CuO [58], oxides based on iron show a variety of OH bands and indicates a considerable role in the formation and stable existence of OH on the surface. Nevertheless, as the Co content increases the intensity of various OH bands increases indicating a direct influence in number and strength of the surface OH groups.

However, it is very difficult to isolate the contribution of each metal ion as the overlap is too large towards any OH bands by all the metals ions.

2.4.4.2. Acidity of $Cu_{1-x}Co_xFe_2O_4$

From Table 2.3 and Figure 2.7, it is clear that both Lewis and Bronsted acid sites are available on the $Cu_{1-x}Co_xFe_2O_4$ surfaces, but dominated by Lewis acid sites (ν_{8a}). ν_{8a} depends on the strength of the Lewis site, which in turn depends on the type of metal, coordination number, oxidation state, redox behavior and the presence of other metal ions surrounding to it [45]. The peak maxima of ν_{8a} bands lie at 1606 ± 2 cm^{-1} for all compositions suggest that pyridine preferably coordinate on all transition metal ions in O_h symmetry (Table 2.3). This is further supported from the temperature dependent IR studies of pyridine adsorbed surfaces on $CuFe_2O_4$ containing deliberate excess 0.5 mol CuO or 0.5 mol Fe_2O_3, where Cu^{2+} and Fe^{3+} have O_h symmetry, and the results are shown in Figure 2.12.
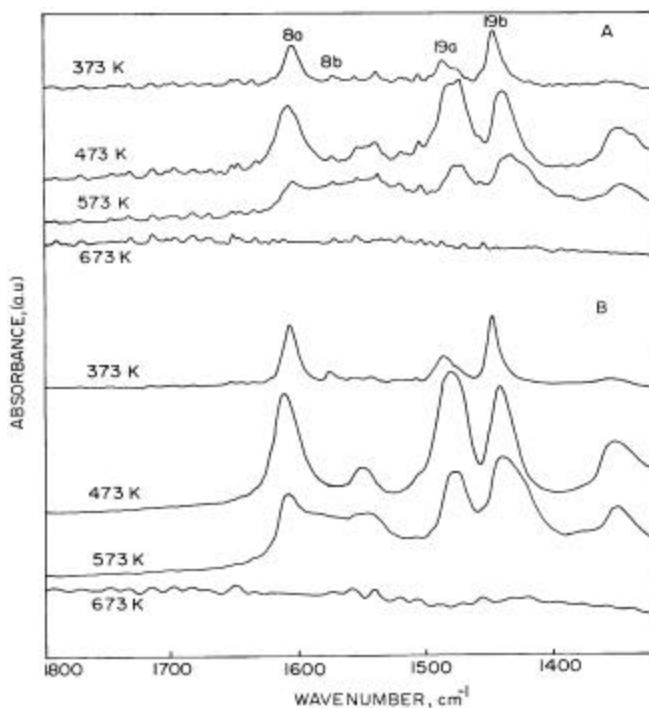
Figure 2.12: Temperature dependent FTIR spectra of pyridine adsorbed on $CuFe_2O_4$ containing excess 0.5 mol CuO (A) or 0.5 mol Fe_2O_3 (B) between 373 K and 673 K. Note an increase in intensity and width of several features at high temperatures.

This experiment was also performed with other Cu containing compositions. Though the T_d coordinated Fe^{3+} ions are diluted by O_h ions in these systems, all the compositions exhibit ν_{8a} band remains at 1606 cm^{-1}, exactly similar to $CuFe_2O_4$. Similar results were obtained with excess 0.5 mol CoO or 0.5 mol Fe_2O_3 with $CoFe_2O_4$ (Figure 2.13). This again indicates the predominant contribution of O_h ions to the ν_{8a} band upon pyridine adsorption than T_d ions. The above conclusion is supported by Jacobs et al [73] using low energy ion scattering, and revealed that mainly O_h cations are exposed on the surface of spinels. The above discussions leads to a conclusion that the contribution toward pyridine adsorption is larger due to O_h cations than from T_d ions.
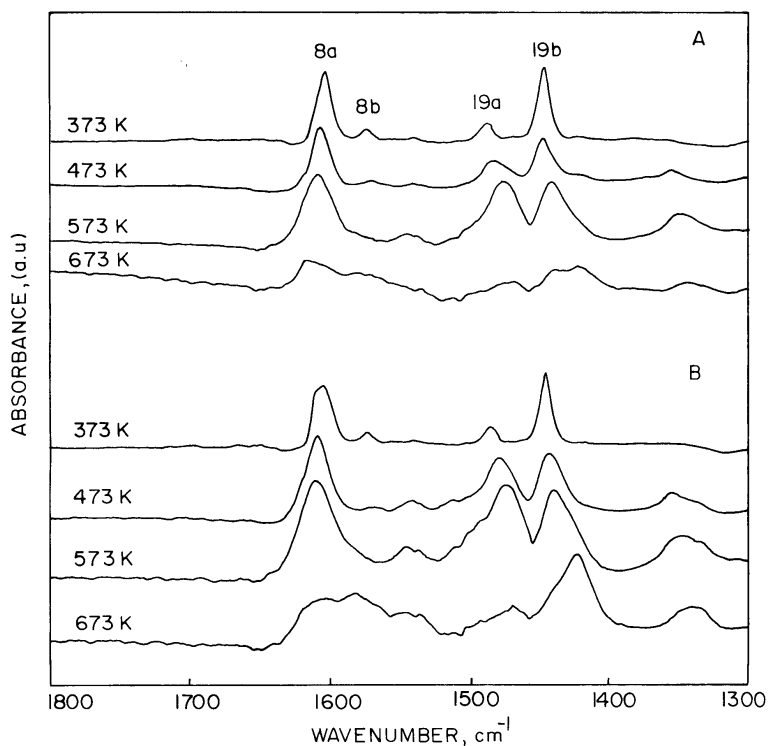
Figure 2.13: Temperature dependent FTIR spectra of pyridine adsorbed on $CoFe_2O_4$ containing excess 0.5 mol CoO (A) or 0.5 mol Fe_2O_3 (B) between 373 K and 673 K. Note the stability of adsorbed pyridine even at 673 K.

Considering the polarizing power [45] and statistical distribution of cations, it can be assumed that, among these surface O_h sites, Fe^{3+} prevails over Co^{2+} and Cu^{2+} and consequently contribute more towards the pyridine adsorption and imparting Lewis acidity.

This is further supported by increasing Fe/(Cu+Co) surface atomic ratio from 0 to 1, calculated from XPS analysis (See chapter 4, Table 4.7). Nevertheless, Cu^{2+} and Co^{2+} indirectly influence the nature of surface active sites is explained as follows. Upon pyridine adsorption there is electron flow from pyridine to spinel surface results in the reduction of highly vulnerable cations, like Cu^{2+}, and the extent of reduction increases at high temperature. Consequently, the charge density around Fe^{3+} is also modified and leads to a decreased interaction between pyridine and oxide surface and hence a less stable adsorbed complex. Contrarily, Co^{2+} is robust and no reduction is observed on pyridine adsorption, even at high temperature. Hence Co^{2+} acts as a structure stabilizer and stabilizes Fe^{3+} state in higher proportion, probably exceeding the stoichiometric 1:2 ratio corresponding to the A and B sites in spinels. Thus Co^{2+} and Cu^{2+} ions affect the surface state of Fe^{3+} upon pyridine adsorption, in an exactly opposite manner. An increase in Co content decreases the reducibility of Fe^{3+} ions and consequently strengthens the Lewis acidity of ferrites. Similar results are obtained from adsorption studies of n-butylamine followed by thermogravimetry by Ramankutty and Sugunan [74].

Parallel to the above reported spectral changes, pyridine adsorption causes decreases in intensity of various surface OH groups, seen as negative absorbance bands in the difference IR spectrum (Figure 2.9). Since the pyridinium ion is simultaneously detected on all these samples, it is likely that the reduction of the OH band intensity is due to the transfer of some protons of these OH groups to the adsorbed pyridine. Hydrogen bonded and bridged OH groups are expected to be less reactive than isolated terminal OH groups [53]. The large negative band observed at ~3720 cm^{-1} (Figure 2.9) indicates that, isolated OH groups bonded to Fe^{3+} and Co^{2+} ions are likely to be involved in pyridinium ion and α-pyridone formation. An increase in intensity of bands correspond to pyridinium ion and α-pyridone with increase in temperature up to 473 K (Figures 2.8 and 2.9) indicates that high temperature is essential to overcome the activation energy barrier for the formation of these species. Further, α-pyridone and bipyridyl formation is evident from the observation of a moderately intense band at 1352 cm^{-1} and unusual broadening of other bands with high intensity together with other minor features at high temperatures (Figure 2.8). Such bipyridyl species are observed on semiconducting oxides such as Fe_2O_3 and

SnO_2 and is formed via pyridine dimerization by heating [75,76]. The band observed at 1352 cm^{-1} corresponds to α-pyridone [77] and occurs through a nucleophilic attack of surface OH group at ~3720 cm^{-1} on to the 2-position of the aromatic ring [77,78].

2.4.4.3. Basicity of $Cu_{1-x}Co_xFe_2O_4$

The formation of carbonate like structures upon CO_2 adsorption reveals the surface basicity. Bicarbonates formation causes perturbation of OH groups in the 3800-3500 cm^{-1} range and formation of certain new OH bands (not shown). Additionally, a weak band observed at 1220 cm^{-1} is attributed to the C-O-H bending vibration of bicarbonate [67]. Broad IR bands in the 1800-1200 cm^{-1} range indicate bidentate species are predominant on the oxide surface due to CO_2 adsorption. On α-Al_2O_3 [79] and MgO [66, 80], where the entire cationic coordination is due only to O_h, bidentates are, by far, the most prevailing structure. The large formation of bidentate carbonates indicates the $Cu_{1-x}Co_xFe_2O_4$ surface possess mainly O_h coordinated ions and reiterates our earlier conclusion.

Adsorption studies with EA revealed that Cu-rich compositions possess maximum number of strong basic sites and the same decreases with increasing x considerably. We propose that the basic strength of a surface oxide ion is stronger with more coordinative unsaturations and weaker with greater polarising power of the cations to which it is bonded. The polarising power increases when there is a rise in charge and size declines and vice versa. Strong or moderately strong basic sites would arise from structures where surface oxide ions bridge over two or more bivalent ions, while weak basic sites are expected on oxide ions bridge over Fe^{3+} ions. Also the O_h coordinated cation is bigger than that of T_d and hence the polarizing power of the latter is higher than that of the former. Due to the above points, it is highly plausible that coordinatively unsaturated O_h cations, preferably divalent cations, offer strong basic sites and hence adsorbents like TCNQ, chloranil and CO_2 preferably adsorb on these sites. It is reasonable to conclude that adsorption of EA occurs mainly at the O_h sites. From these also it is clear that the O_h cation plays a significant role in determining the acid base properties of the system. The extent of spinel inversion decreases with increasing x on $Cu_{1-x}Co_xFe_2O_4$ indicates less divalent cations go to O_h sites and hence basicity decreases with increasing x.

Ferrospinels are generally n-type semiconductors, which lose lattice oxygen on heating, causing anion vacancies. The released electrons are accommodated by reduction of Fe^{3+} to Fe^{2+} ions and, in the case of Cu containing samples, by conversion of Cu^{2+} to Cu^+ (due to the high reducibility of Cu^{2+} ion). The presence of free electrons in defect sites causes an increased basicity and this is maximum for $CuFe_2O_4$. This can be due to the higher susceptibility of $CuFe_2O_4$ to the creation of defect sites with calcination, imposed by the high thermal instability [81] and the special coordination described as (4+2) coordination of Cu (II) oxide [82].

2.4.4.4. Correlation between theoretical and experimental results

In the following an attempt has been made to correlate experimental results with theoretical (empirical) quantities. According to Lewis definition, acidity and basicity are electron accepting and electron donating properties that could contribute to the formation of a covalent bond. Larger the electronegativity, the stronger the electron accepting power can be considered as a first approximation [83]. According to Sanderson [84] the electronegativity of the metal ion would be expected to change linearly with its charge. Later Zhang [85] has proposed a numerical scale for the acid strengths (Z) of cations and he defined it as

$$Z = P - 7.7 \chi_Z + 8 \quad \ldots\ldots\ldots\ldots..(7)$$

where P and χ_Z are the polarizing power and electronegativity of the ion respectively. The advantage of such a scale is the predictive power for thermochemical and physical properties that obviously depend on the nature of the chemical bond established between the acid cation and the basic anion. In the case of inorganic compounds, this bond is called iono-covalent, meaning that this bond involves simultaneously electrostatic force (ionic part) and covalent forces resulting from the combination of atomic orbitals. To express this duality, for a given cation, Zhang took into account (a) the polarizing power and (b) the electronegativity for the covalent part. He calculated the polarizing power, electronegativity and acid strength of various cations [85] and it is noted that the acid strength of cations relevant to our compositions are in the order $Fe^{3+}>Fe^{2+}\approx Co^{2+}>Cu^{2+} > Cu^+$.

When an organic molecule like electron donating pyridine adsorbs on the surface, cations get reduced due to charge transfer. Thus the easily reducible metal ions like Cu^{2+} undergo fast reduction to Cu^+ and hence the stability of metal ion-pyridine complex decreases. From the acid strength of various cations it is clear that reduced Cu^+ has very poor acidity. In other words, for a given ligand, corresponding stability constants of metal ions are in the order $Fe^{3+} > Co^{2+} > Cu^{2+}$ and hence the acidity of these ions also follow the same order, as shown earlier.

Recently Lebouteiller and Courtine [86] have developed a new theoretical approach to calculate the bulk optical basicity value for mixed oxide systems. The attractive feature of this method is that it includes both valence and coordination number of the ion present in the compound. The optical basicity (Λ) of various cations in different oxidation state and coordination environment is calculated and is available in their paper [86].

Λ value of all the compositions can be calculated for both normal and completely inverse case using equations 8 and 9.

$$\Lambda_{normal\ IV}A^{2+}{}_{VI}B^{3+}{}_2O_4 \quad = \quad 2/8 * \Lambda(_{IV}A^{2+}) + 6/8 * \Lambda(_{VI}B^{3+}) \tag{8}$$

$$\Lambda_{inverse\ IV}B^{3+}{}_{VI}A^{2+}{}_{VI}B^{3+}O_4 = 3/8 * \Lambda(_{IV}B^{3+}) + 2/8 * \Lambda(_{VI}A^{2+}) + 3/8 * \Lambda(_{VI}A^{3+}) \tag{9}$$

The results are tabulated and presented in Table 2.4.

From the table it is clear that as the Cu content increases basicity increases and thus $CuFe_2O_4$ is most basic and $CoFe_2O_4$ is the least. The results correlate well with the experimental results (as shown in Figure 4.29, Chapter 4). This suggests that the basic strength is dominated by global properties with respect to the chemical nature of the various compositions. Moreover, from the table it is clear that for a given composition, completely inverse structure has maximum basicity than the corresponding normal structure. $CoFe_2O_4$ is the least inverse and hence it should be the least basic and experimental results confirm the same.

Table 2.4: Calculated values of Optical Basicity (Λ) for various compositions of $Cu_{1-x}Co_xFe_2O_4$

Compositions	Structure	Coordination	Λ
$CuFe_2O_4$	Normal	$_{IV}Cu^{2+}$ and $_{VI}Fe^{3+}$	0.805
	Inverse	$_{IV}Fe^{3+}$, $_{VI}Cu^{2+}$ and $_{VI}Fe^{3+}$	0.811
$Cu_{0.75}Co_{0.25}Fe_2O_4$	Normal	$_{IV}Cu^{2+}$, $_{IV}Co^{2+}$ and $_{VI}Fe^{3+}$	0.796
	Inverse	$_{IV}Fe^{3+}$, $_{VI}Cu^{2+}$, $_{VI}Co^{2+}$ and $_{VI}Fe^{3+}$	0.804
$Cu_{0.50}Co_{0.50}Fe_2O_4$	Normal	$_{IV}Cu^{2+}$, $_{IV}Co^{2+}$ and $_{VI}Fe^{3+}$	0.788
	Inverse	$_{IV}Fe^{3+}$, $_{VI}Cu^{2+}$, $_{VI}Co^{2+}$ and $_{VI}Fe^{3+}$	0.796
$Cu_{0.25}Co_{0.75}Fe_2O_4$	Normal	$_{IV}Cu^{2+}$, $_{IV}Co^{2+}$ and $_{VI}Fe^{3+}$	0.779
	Inverse	$_{IV}Fe^{3+}$, $_{VI}Cu^{2+}$, $_{VI}Co^{2+}$ and $_{VI}Fe^{3+}$	0.789
$CoFe_2O_4$	Normal	$_{IV}Co^{2+}$ and $_{VI}Fe^{3+}$	0.770
	Inverse	$_{IV}Fe^{3+}$, $_{VI}Co^{2+}$ and $_{VI}Fe^{3+}$	0.781

2.4.5. Conclusions

A series of ferrospinels having a general composition of $Cu_{1-x}Co_xFe_2O_4$ (x = 0, 0.25, 0.50, 0.75 and 1) were prepared by co-precipitation method and characterized by FTIR for acid-base properties. The FTIR spectra of ferrospinels reveal Fe^{3+} and Co^{2+} ions are primarily responsible for various OH groups between 3740 and 3620 cm^{-1}. Further an increase in x increases the number and strength of OH groups. The FTIR spectrum of pyridine adsorbed $Cu_{1-x}Co_xFe_2O_4$ surfaces at 373 K demonstrates that the predominant modes of adsorption are ν_{8a} and ν_{19b}, and bolstering the dominant Lewis acid character. Pyridine adsorption on $Cu_{1-x}Co_xFe_2O_4$ and deliberately added excess metal oxide to the spinel phase reveals that O_h coordinated ions occupy predominantly on the surface and acts as centers of pyridine adsorption; further the contribution of various ions to the ν_{8a} band is in the following order $Fe^{3+} > Co^{2+} > Cu^{2+}$ in terms of its intensity and position. From the temperature dependent studies of pyridine adsorbed surfaces of $Cu_{1-x}Co_xFe_2O_4$ and deliberately added excess oxide to the spinel system, it is clear that both Co^{2+} and Cu^{2+} ions influence towards the stability of adsorbed pyridine complex in an opposite way that

Co^{2+} impart the stability to the surface. In general, the total intrinsic acidity of $Cu_{1-x}Co_xFe_2O_4$ increases with cobalt content. The formation of pyridinium ion indicates the presence of Bronsted acidity too, however it is weak.

CO_2 adsorption on $Cu_{1-x}Co_xFe_2O_4$ indicates the predominant bidentate complex on the surface, which requires coordinatively unsaturated O_h ions on the surface. Adsorption studies of electron acceptors indicate that basicity of the system decreases with increasing x. $CoFe_2O_4$ and $CuFe_2O_4$ shows inverse trends in their acidic and basic behaviour and for $0.25 \geq x \leq 0.75$ there is some compromise between the acidic and basic behavior.

The acidity of the catalysts correlated with the acid strength (Z) of the involved cations proposed by Zhang, where the polarizing power and electronegativity of the cations are considered. The acid strength of the cations are in the order of $Fe^{3+} > Co^{2+} > Cu^{2+}$. On the other hand, basicity correlated with the optical basicity ($\wedge$) of corresponding oxides proposed by Lebouteiller and Courtine, where both valence and coordination number of the cation present in the compound are considered.

2.5. REFERENCES

1   Ref. 43-47 and 49 of chapter 1

2   N. F. M. Henry, J. Lipson and W. A. Wooster, *"The interpretation of x-ray diffraction photographs"* Macmillan and Co Ltd., London, 1951.

3   P. Kubelka and F. Munk, *Z. Tech. Phys*., **12** (1931) 593.

4   P. Kortum, W. Braun and C. Harzog, *Angew. Chem. Int. Ed. Engl.*, **2** (1963) 333.

5   B. C. Lippens and J. H. de Boer, *J. Catal.*, **4** (1965) 319.

6   E. P. Barret, L. G. Joyner and P. H. Halenda, *J. Amer. Chem. Soc*., **73** (1951) 373.

7   R. Mossbauer, *Z. Phys*., **151** (1958) 124.

8   O. C. Kistner and A. W. Sunyar, *Phys. Rev. Lett*., **4** (1960) 412.

9   K. Lazar, G. Lejeune, R. K. Ahedi, S. S. Shevade and A. N. Kotasthane, *J. Phys. Chem. B.*, **102** (1998) 4865.

10   T. A. Carlson, *X-ray Photoelectron Spectroscopy*, Dowden, Hutchinson & Ross: Stroudsburg, PA, 1978.

11   *Practical Surface Analysis, Vol. 1: Auger and X-ray Photoelectron Spectroscopy*, 2nd ed., D. Briggs, M. P. Seah, Eds., Wiley, New York, 1990.

12   S. Hüfner, *Photoelectron Spectroscopy*, Springer-Verlag: Berlin, 1995.

13   M. K. Dongare, V. Ramaswamy, C. S. Gopinath, A. V. Ramaswamy, S. Scheurell, M. Brueckner and E. Kemnitz, *J. Catal.*, **199** (2001) 209.

14   V. L. J. Joly, P. A. Joy, S. K. Date and C. S. Gopinath, *J. Phys. Condens. Matt.*, **13** (2001) 649.

15   M. D. Baker, *Catal. Rev. Sci. & Eng*., **29** (1987) 269.

16   J. A. Lercher, C. Grundling and G. Eder-Mirth, *Catal. Today*, **27** (1996) 353.

17   J. C. Lavalley, *Catal. Today*, **27** (1996) 377.

18   M. C. Kung and H. H. Kung, *Catal. Rev. Sci. & Eng*., **27** (1985) 425.

19   Ref. 28 of chapter 1

20   J. Mexmain, *Ann. Chim (Paris)*, **4** (1969) 429.

21   J. Mexmain, *Ann. Chim(Paris)*, **6** (1971) 297.

22   T. Yamaguchi, *Proc. Fac. Eng. Keiogijuku Univ.*, **19** (1967) 776.

23   J. Smit and H. P. J. Wijn, *Advan. Electron. Electronphys.*, **6** (1954) 83.

24   G. H. Jonker, *J. Phys. Chem. Solids*, **9** (1959)165.

25   G. H. Sawatzky, F. Van der Woude and A. H. Morrish, *J. Appl. Phys.* **39** (1968) 1204.

26   G. H. Sawatzky, F. Van der Woude and A. H. Morrish, *Phys. Rev.* **187** (1969) 747.

27   E. J. W. Verwey and E. L. Heilmann, *J. Chem. Phys.*, **15** (1947) 174.

28   P. Tarte, *Spectrochim. Acta*, **19** (1965) 49.

29   J. Preudhomma and P. Tarte, *Spectrochim. Acta A*, **27** (1971) 961.

30   R. D. Waldron, *Phys. Rev.*, **99** (1955)1727.

31   W. B. White and B. A. De Angelis, *Spectrochim Acta A*, **23** (1967) 985.

32   H. Ohnishi and T. Teranishi., *J. Phys. Soc. Jpn.*, **16** (1961) 35.

33   A. Bergstein and L. Cervinka, *Czech J. Phys. Ser. B*, **11** (1961) 584.

34   L. Neel, *C. R. Acad. Sci. Paris*, (1950) 190.

35   H. M. O'Bryan, H. J. Levinstein and R. C. Sherwood, *J. Appl. Phys.*, **37** (1966) 1437.

36   C. Villette, Ph. Tailhades and A. Rousset, *J. Solid State Chem.*, **117** (1995) 64.

37   R. J. Kokes, *Intra-Sci. Chem. Rep.*, **6** (1972) 77.

38   R. L. Burwell, G. L. Haller, K. C. Taylor and J. F. Read, *Adv. Catal.*, **29** (1969) 1.

39   K. Tanabe, *Solid Acids and Bases*, Academic, New York, 1970.

40   H. H. Kung, *J. Solid state chem.*, **52** (1984) 191.

41   M.C. Kung and H.H. Kung, *Catal. Rev. – Sci. Eng.*, **27** (1985) 425.

42   P. Berteau and B. Delmon, *Catal. Today*, **5** (1989) 121.

43   G. Busca, *Catal. Today*, **27** (1996) 323.

44   J.A. Lercher, C. Grundling and G. Edermirth, *Catal. Today*, **27** (1996) 353.

45   G. Busca, *Catal. Today*, **41** (1998) 191.

46   J.C. Lavalley, *Catal. Today*, **27** (1996) 377.

47   G. Ramis, G. Busca and V. Lorenzelli, *Mat. Chem. Phys.*, **29** (1991) 425.

48   R. Philipp and K. Fujimoto, *J. Phys. Chem.*, **96** (1992) 9035.

49   S. Sugunan and G.D. Devika Rani, *Indian J. Chem.*, **32(A)** (1993) 993.

50   S. Sugunan and G.D. Devika Rani, *J. Material Science*, **28** (1993) 4811.

51   Ref. 44-46 of chapter 1

52   G. Busca, V. Lorenzelli, G. Ramis and R. J. Willey, *Langmuir*, **9** (1993) 1492.

53   C. H. Rochester and S. A. Topham, *J. Chem. Soc. Faraday Trans. I.*, **75** (1979) 1073.

54   C. H. Rochester and S. A. Topham, *J. Chem. Soc. Faraday Trans. I.*, **75** (1979) 1259.

55   G. Busca, V. Lorenzelli, V. S. Escribano and R. Guidetti, *J. Catal.*, **131** (1991) 167.

56   G. Busca, V. Lorenzelli and V. Bolis, *Mater. Chem. Phys.*, **31** (1992) 221.

57   G.Busca, R.Guidetti and V. Lorenzelli, *J. Chem. Soc. Faraday Trans.*, **86** (1990) 989.

58   G. Busca, *J. Mol Catal.*, **43** (1987) 225.

59   C. H. Kline and J. Turkevich, *J. Chem. Phys.*, **12** (1944) 300.

60   C. Morterra, A. Chiorino, G. Ghiotti and E. Garrone, *J. Chem. Soc. Faraday Trans. I.*, **75** (1979) 271.

61   S.Ghorpade, V.S.Darshane and S.G.Dixit, *Appl. Catal., A General*, **166** (1998) 135.

62   A. Ueno and C.O. Bennett, *J. Catal.*, **54** (1978) 31.

63   G. Busca and V. Lorenzelli, *Mater. Chem.*, **7** (1982) 89.

64   K. Nakamoto, "*Infrared and Raman Spectra of Inorganic and Coordination Compounds*", Third Edn., Wiley, New York, p. 243 (1978).

65   F. Solymosi and H. Knozinger, *J. Catal.*, **122** (1990) 166.

66   C. Morterra, G. Ghiotti, F. Boccuzzi and S. Coluccia, *J. Catal.*, **51** (1978) 299.

67   J. I. DiCosimo, V. K. Diez, M. Xu, E. Iglesia and C. R. Apesteguia, *J. Catal.*, **178** (1998) 499.

68   G. Keresztury, M. Incze, F. Soti and L. Imre, *Spectrochim. Acta A*, **36** (1980) 1007.

69   R. P. Eischens and W. A. Pliskin, *Adv. Catal.*, **9** (1952) 662.

70   D. M. Griffiths and C.H. Rochester, *J. Chem. Soc. Faraday Trans. I*, **73** (1977) 1988.

71   K. Esumi, H. Shimade and K. Meguro, *Bull. Chem. Soc. Japan*, **50** (1977) 2795.

72   K.Esumi, K.Miyata, F.Waki and K.Meguro, *Bull. Chem. Soc. Japan*, **59** (1986) 3363.

73   J. P. Jacobs, A. Maltha, J. R. H. Reintjes, T. Drimal, V. Ponec and H. H. Brogersma, *J. Catal.*, **147** (1994) 294.

74   C. G. Ramankutty and S. Sugunan, *Appl. Catal. A: General*, **218** (2001) 39.

75   G. Busca and V. Lorenzelli, *Mater. Chem.*, **6** (1981) 175.

76   P. G. Harrison and E. W. Thornton, *J. Chem. Soc. Faraday Trans. I*, **71** (1975) 1013.

77   H. Knozinger, H. Krietenbrink, H. D. Muller and W. Schulz, *Proc. Sixth Internat. Congress on Catalysis* (The Chemical Society, London, 1977), **Vol. 1**, p.183.

78   E.Borello, G.D.Gatta, B.Fubini, C.Morterra and G.Venturello, *J. Catal.*, **35** (1974) 1.

79   C. Morterra, S. Coluccia, G. Ghiotti and A. Zecchina, *Z. Physik. Chem. Frankfurt (N.F)*, **104** (1977) 275.

80   J. V. Evans and T. D. Whately, *Trans. Faraday Soc.*, **63** (1967) 2769.

81   J.L.G. Fierro and J.F. Garcia de la Banda, *Catal. Rev. – Sci. Eng*., **28** (1986) 265.

82   A.F. Wells, Structural Inorganic Chemistry, 4th Edition, ELBS, London, p. 890 (1979).

83   J. Kijenski and A. Baiker, *Catal. Today*, **5** (1989) 1.

84   R.T. Sanderson, Inorganic Chemistry, Reinhold: New York, p. 136 (1967).

85   Y. Zhang, *Inorg. Chem.*, **21** (1982) 3889.

86   A. Lebouteiller and P. Courtine, *J. Solid state Chemistry*, **137** (1998) 94.

CHAPTER 3
CATALYTIC ACTIVITY STUDIES
AND MECHANISM OF
PHENOL METHYLATION

SECTION I

3.1. INTRODUCTION

Phenol can be alkylated with methanol in the liquid or gas phase. Liquid phase phenol methylation is generally carried out in the presence of Lewis acid catalyst and it gives ortho and para substitution with low selectivity [l,2]. Further, it gives numerous side products and their separation is difficult. Moreover, it is technologically unfavourable due to long reaction times, high pressure, high consumption of catalyst and troublesome regeneration [1-3].

Among various methylation agents, methanol is the most promising and economically demanded than DMC and conventional methylating agents such as dimethyl sulphate and methyl chloride [1,3]. Conventional processes are atom inefficient and generate large amount of waste. For example, if one were to alkylate cresol stoichiometrically with dimethyl sulphate and neutralize the H_2SO_4 with sodium carbonate, the atom efficiency (AE) would be just 0.58. On the other hand, the direct methylation with methanol will have an AE of 0.87, the only byproduct being water. Besides, methanol is far cheaper and easier to handle than methyl sulphate. Though DMC is more environmental friendly than methanol, with the former less selectivity is achieved towards ortho methylation.

Vapour phase methylation of phenol with methanol using solid acid catalysts is the most recommended process for C-alkylation. Gas phase methylation of phenol by CH_3OH was reported by Ipatieff as early as 1925 [4]. Later, solid catalysts of the mixed oxides type containing basic sites, or acidic and basic sites, were found to catalyze efficiently the methylation of phenols with methyl alcohol with high selectivity for ortho methylation. Usually in the gas phase, methanol and phenol vapours react in a flow reactor under atmospheric pressure in the temperature range of $300\text{-}420^0C$. The catalyst used forms a stationary bed. Often water is added to the feed in an amount of 5-15 % by weight of the total amount of phenol and methanol.

3.2. RESULTS AND DISCUSSION OF PHENOL METHYLATION

3.2.1. Effect of MeOH:PhOH molar ratio

Phenol methylation was carried out at 350^0C on x = 0.50 using MeOH:PhOH molar ratios between 3 and 7 (Figure 3.1 – bottom panel) to obtain the optimum reactants composition for detailed studies; time dependence of phenol conversion for all catalyst compositions are also shown in Figure 3.1 (top panel).
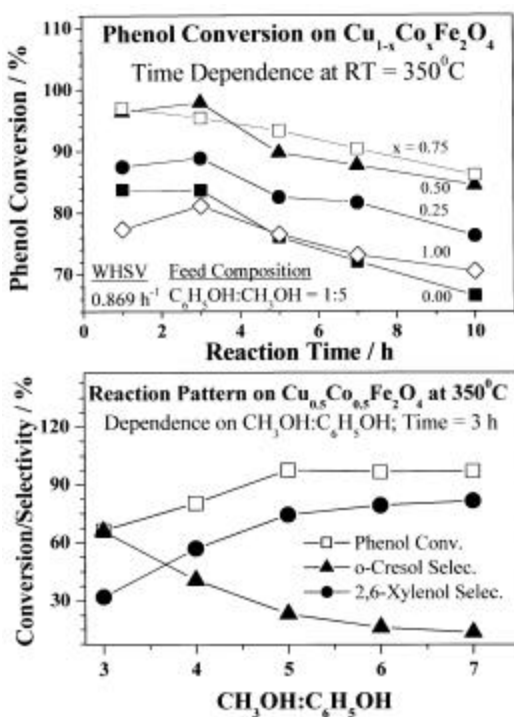
Figure 3.1: Time dependence of phenol conversion on $Cu_{1-x}Co_xFe_2O_4$ catalysts at 350^0C is shown in top panel. Bottom panel shows the methanol:phenol composition dependence of phenol conversion and ortho products selectivity on $Cu_{0.5}Co_{0.5}Fe_2O_4$, t = 3 h at 350^0C.

Phenol conversion gradually increases with the above ratio and a maximum of 98 mol% conversion is achieved at ≥5. Selectivity of major products, o-cresol and 2,6-xylenol, show a linear dependence but in an opposite direction with increasing MeOH. Although, conversion level is constant ≥5, a marginal increase in selectivity of 2,6-xylenol was observed at high molar ratios. These facts revealed that 2,6-xylenol is produced at the expense of o-cresol. Besides, a decrease in total ortho selectivity was observed at high MeOH:PhOH ratios (≥6) due to an increase in the formation of other methylated products

altogether to the level of 5.5 mol%. Excess methanol also causes more deactivation due to coking and it is confirmed from the large weight loss due to carbon burning in air in thermogravimetric analysis (data not shown). Above results demonstrate the MeOH:PhOH ratio of 5 is preferred from the conversion, desired selectivity and less deactivation point of view. Similar trend was observed at x = 0 and 1, suggests the MeOh:PhOH ratio to be 5:1, irrespective of catalysts composition.

It is clear that excess methanol is necessary, even though reaction stoichiometry suggests a MeOH:PhOH ratio of 2 for 2,6-xylenol. Since the reaction is performed in vapor phase set up, some amount of methanol will be lost due to unavoidable side reactions such as methanol reforming and simple gasification. Acidic nature of the catalyst might help to avoid the above side reactions to some extent. In view of the above we have studied the influence of water in the feed over an extended reaction period of 50 h on x = 0, 0.5 and 1 (Figure 3.2).
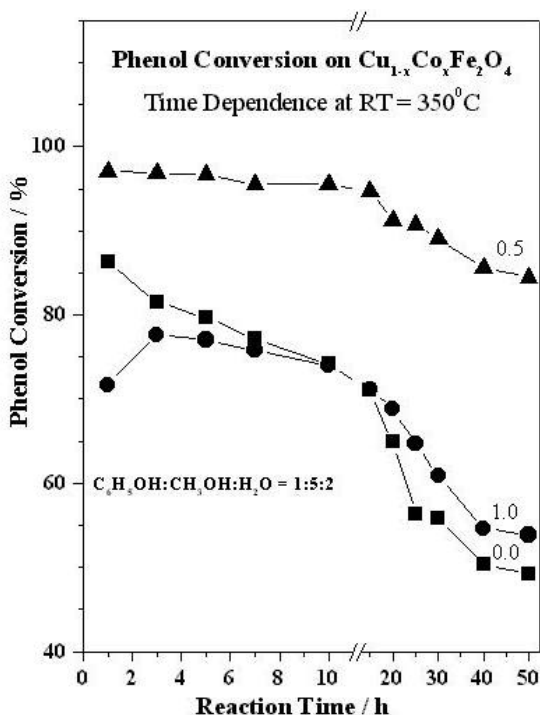
Figure 3.2: Effect of water on phenol methylation over three selected compositions x = 0.0, 0.50 and 1.0. Phenol methylation is carried out with phenol:methanol:water composition of 1:5:2 at 350^0C and at WHSV of 0.869 h^{-1}.

PhOH:MeOH:H_2O ratio of 1:5:2 was used in this study. Generally, a prolonged stability is observed with considerably low deactivation compared to the feed without H_2O. Needless to say the advantage of H_2O in the feed is that the steam will suppress coke formation by water gas shift reaction and will maintain catalytic activity for longer period. Further, methylation carried out in H_2 atmosphere showed fast deactivation of the catalyst with low PhOH conversion demonstrate large reduction of catalyst suppresses the methylation and hints the metallic species are not the methylation centers. Besides test reactions were carried out with MeOH alone on ferrospinels shows typical reformate products and after about 5h methanol started condensing additionally. Thermogravimetric analysis of the above catalysts clearly exhibit the amount of coke is comparable to that of treated with 1:5 ratio of PhOH:MeOH. This hints the coke formation is mostly due to MeOH decomposition and other routes like phenol-resin polymerization is less likely under our experimental conditions.

Figure 3.1 (top panel) shows decrease in phenol conversion, in general, with reaction time at any catalyst composition. Comparable high phenol conversion is observed at x = 0.5 and 0.75 and all other compositions show relatively lower conversion levels. Phenol methylation gave predominant (≥97.5 mol%) ortho methylated products viz. o-cresol and 2,6-xylenol over $Cu_{1-x}Co_xFe_2O_4$ (Figures 3.3 and 3.4). Minor products such as anisole, 2,4-xylenol, p-cresol and 2,4,6-trimethyl phenol (TMP) etc. were also produced altogether in 0.5-2.5 mol% range (Tables 3.1 and 3.2) irrespective of the composition and temperature. However, ≥375^{0}C a slight increase in side products up to 5 mol% was observed. Detailed results are presented in the following.

3.2.2. Effect of catalyst composition

Figure 3.3 shows the selectivity of (a) o-cresol and (b) 2,6-xylenol and (c) phenol conversion as a function of catalyst composition at different temperatures. The product distribution obtained from phenol methylation reaction over $Cu_{1-x}Co_xFe_2O_4$ under the optimized conditions (Temperature = 350^{0}C, PhOH:MeOH mole ratio = 1:5, WHSV = 0.869 h^{-1} and TOS = 3) is presented in Table 3.1.
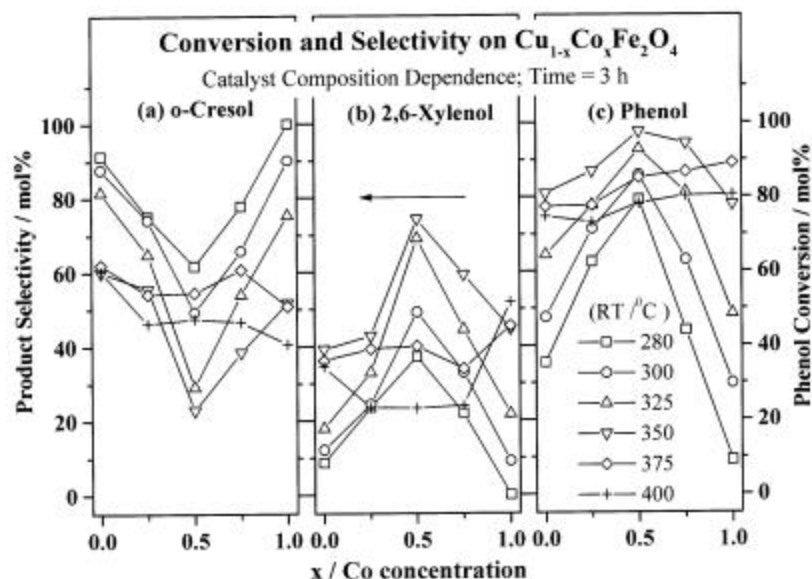
Figure 3.3: Composition dependence of selectivity of o-cresol (a) and 2,6-xylenol (b) and phenol conversion (c) is shown between 280 and 400^{0}C on Cu$_{1-x}$Co$_x$Fe$_2$O$_4$. It is to be noted that 2,6-xylenol selectivity increase at the expense of o-cresol and indicates the sequential methylation.

Table 3.1: Influence of catalyst composition on product distribution over Cu$_{1-x}$Co$_x$Fe$_2$O$_4$ (x = 0, 0.25, 0.50, 0.75 and 1). Phenol methylation is carried out with phenol:methanol = 1:5 at 350^{0}C and at WHSV = 0.869 h^{-1}.

Product distribution	Catalyst composition, x				
	0	**0.25**	**0.50**	**0.75**	**1**
Aromatics	0.07	0.55	0.21	0.15	0.04
Anisole	0.14	0.21	0.15	0.68	0.56
Unreacted phenol	19.07	13.15	2.59	5.64	22.09
o-Cresol	48.66	48.31	22.34	36.29	40.28
2,6-xylenol	31.74	37.14	72.31	55.93	34.77
p-Cresol	0.03	0.16	0.20	0.14	0.21
2,4-Xylenol	0.24	0.41	1.08	0.65	1.57
2,4,6-TMP	0.04	0.08	0.96	0.26	0.37
Other alkyl phenols	0	0	0.15	0.25	0.11

The influence of Cu-Co combination is an important factor to phenol conversion and 2,6-xylenol selectivity is evident from the following results listed below: (1) phenol conversion increases from end compositions ($x = 0$ and 1) to intermediate compositions ($0 < x < 1$) up to 350^0C and comparable conversion is observed $\geq 375^0C$ at all x values, though overall conversion decreases, (2) large selectivity of o-cresol found at $x = 0$ and 1 gradually changes towards 2,6-xylenol at $0 < x < 1$, (3) 2,6-xylenol is produced at the expense of o-cresol, and (4) a general decrease in phenol conversion and a change in product selectivity pattern is observed $\geq 375^0C$. $x = 0.5$ composition displays large phenol conversion and selective towards 2,6-xylenol at 350^0C, although other compositions too exhibit high conversion, ≥ 90 mol%, but not selective. This indicates an equal amount of Cu and Co is necessary in the bulk for the effective ortho dimethylation. A deviation from the above trend is observed at 400^0C with high 2,6-xylenol selectivity at end compositions and an increase in altogether secondary products selectivity to >20 mol% at $0 < x < 1$.

3.2.3. Reaction temperature dependence

The effect of reaction temperature on phenol methylation is shown in Figure 3.4 for $x = 0$, 0.5 and 1.
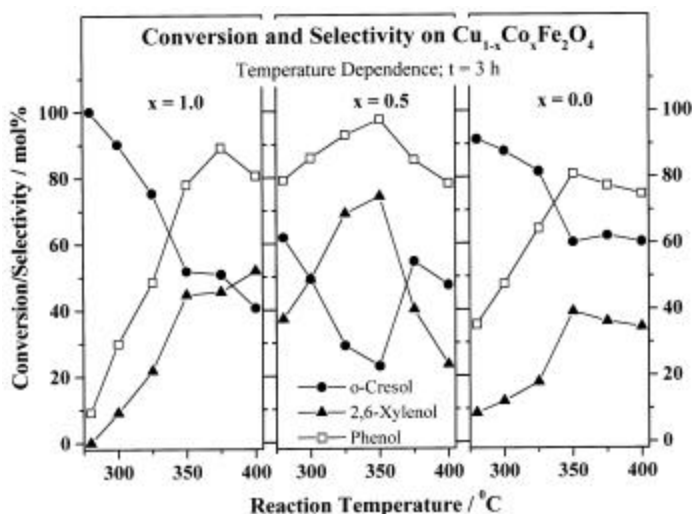
Figure 3.4: Temperature dependence of phenol conversion and products selectivity for $x = 1.0$ (a), 0.5 (b) and 0.0 (c). Linear increase in phenol conversion and 2,6-xylenol selectivity with increasing temperature indicates the first order dependence of phenol conversion.

Table 3.2 summarizes the effect of reaction temperature towards product distribution over x = 0.50 at a temperature range between 280 and 400^0C. These results have been presented above, but are displayed in a new way here to highlight the correlation between conversion and selectivity. Figure 3.4 and Table 3.2 demonstrates: (1) Phenol conversion increases linearly with temperature up to 350^0C and a concurrent increase (decrease) in 2,6-xylenol (o-cresol) selectivity is observed at any given x. (2) Positive and negative first order dependence on phenol conversion for 2,6-xylenol and o-cresol selectivity, respectively, for all composition up to 350^0C, (3) Decrease in o-cresol production is compensated by an increase in 2,6-xylenol selectivity explains the methylation is sequential and methylation rate also increases with temperature up to 350^0C, and (4) Importance of 1:1 ratio of Cu:Co combination in x = 0.5 at 280^0C by displaying comparable catalytic activity as that of end compositions at $T \geq 350^0C$.

Table 3.2: Effect of temperature on product distribution over $Cu_{0.50}Co_{0.50}Fe_2O_4$. Phenol methylation is carried out with phenol:methano1 = 1:5 at 350^0C and at WHSV = 0.869 h^{-1}.

Product Distribution	Temperature					
(Mol %)	280	300	325	350	375	400
Aromatics	0	0	0.13	0.21	1.34	18.79
Anisole	0.08	0.15	0.16	0.15	0.40	0.09
Unreacted phenol	20.83	14.10	7.26	2.59	14.82	21.80
o-Cresol	48.92	42.41	27.04	22.34	46.49	37.16
2,6-xylenol	29.47	42.28	64.00	72.31	34.10	18.29
p-Cresol	0.20	0.32	0.14	0.20	0.27	0.25
2,4-Xylenol	0.22	0.20	0.81	1.08	1.16	1.09
2,4,6-TMP	0.23	0.38	0.28	0.96	1.00	1.05
Other alkyl phenols	0.05	0.17	0.16	0.15	0.37	0.98
Biphenyls	0	0	0	0	0.05	0.53

3.2.4. Discussion

An important aspect of the methylation reaction to the discussion presented here is related to the dependence of the product selectivity on phenol conversion. High phenol conversion (98 mol%) and 2,6-xylenol selectivity (75 mol%) is achieved at x = 0.5 composition between 325 and 350^{0}C. However on moving either side of the above conditions, in terms of reaction temperature as well as catalyst compositions, increases the selectivity of o-cresol with decreasing phenol conversion (Figures 3.3 and 3.4). A linear relation is shown between increasing phenol conversion and 2,6-xylenol selectivity at temperatures upto 350^{0}C in Figure 3.4. Hence high phenol conversion becomes a prerequisite for dimethylation to produce 2,6-xylenol. However this is not the case with o-cresol, as its selectivity declines with increasing phenol conversion. These two points actually suggests the stepwise methylation of PhOH to 2,6-xylenol through o-cresol at high phenol conversion. Near total ortho products formation below 350^{0}C at all x values indicates, in general, the desorption of ortho products are high. At high MeOH:PhOH ratios ($\geq$6) high methylation capacity with low phenol on the catalyst surface leads to more secondary products.

Low selectivity of 2,6-xylenol observed at x = 0 and 1 is attributed to high gasification of MeOH than its decomposition. This is clearly supported by the low carbon content on the spent catalysts at x = 0 and 1 compositions (Chapter 4, Table 4.7 and Figure 4.6). Better selectivity of 2,6-xylenol and high C content observed clearly suggests the methanol decomposition is increasing at 0<x<1 (Figures 3.3 and 3.4). This is further clear from the very high 2,6-xylenol selectivity ($\geq$80 mol%) observed at x = 0.5 with high MeOH:PhOH ratio of 6 and 7 (Figure 3.1). Mixed metal oxides of CuO-Fe_2O_3 and CoO-Fe_2O_3 shows about 68% methanol gasification [5] at 350^{0}C supports our findings and the necessity of high methanol in this reaction on ferrospinels. Although x = 0 and 1 shows decreasing phenol conversion at T>375^{0}C, an increase in 2,6-xylenol selectivity indicates an increase in methanol decomposition and dimethylation capacity.

Introduction of Co in $CuFe_2O_4$ system (at x = 0.25) shows an increase in phenol conversion to 62 mol% from 35 mol% at x = 0.0 at 280^{0}C (Figure 3.3). Contrarily, introduction of Cu in $CoFe_2O_4$ (x = 0.75) displays an increase in phenol conversion five

times and 2,6-xylenol selectivity to 22% from no xylenol at 280^0C. Further, high phenol conversion achieved at 350^0C at x = 0.75 is 94 mol%, whereas the same is 87% in x = 0.25 case. This underscores the role of Cu is relatively higher than Co in phenol methylation.

3.2.5. Thermodynamic aspects of phenol methylation

The following pathways are possible with respect to the reaction mechanism of phenol methylation on mixed oxide catalysts based on mixed oxides of transition metals.

(1) The formation of 2-methyl phenol is due mostly to the direct methylation of phenol.

(2) Formation of anisole is negligible and anisole in turn, if at all formed, is scarcely methylated to form o-methyl anisole.

(3) Dimethyl phenol isomers are formed by a consecutive methylation of 2-methyl phenol, where upon it tends to form 2,6-dimethyl phenol dominantly rather than 2,4-dimethyl phenol.

(4) Dimethyl phenol isomers can also be formed by the simultaneous addition of two methyl groups at a time, i.e., by parallel reaction. Here also it tends to form 2,6-dimethyl phenol predominantly rather than any other dimethyl phenol isomer,

(5) And 2,4,6-trimethyl phenol is formed by further methylation of dimethyl   isomers.

For studying the thermodynamic aspects of the reaction between phenol and methanol leading to the formation of 2-methyl phenol and 2,6-dimethyl phenol as main products, the following reaction scheme are considered, based on the above pathways.

1. Main reaction (Reaction I): Single methylation of phenol to 2-methyl phenol (o-cresol).
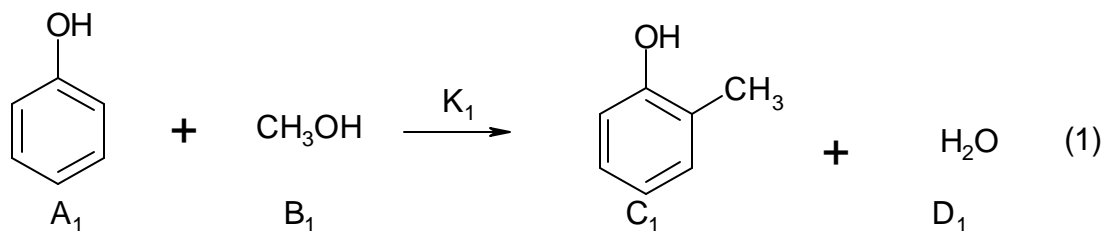
2. Consecutive reaction (Reaction II): Consecutive Methylation of 2-methyl phenol to 2,6-dimethyl phenol (2-6-xylenol).

$$A_2 + CH_3OH \xrightarrow{K_2} C_2 + H_2O \quad (2)$$
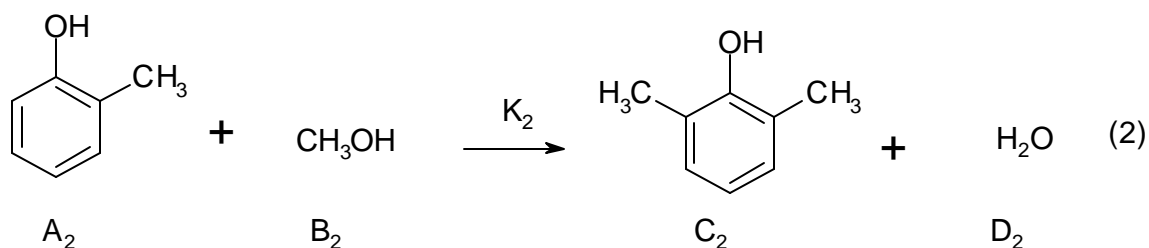
3. Parallel reaction (Reaction III): Simultaneous addition of two methyl groups at a time.

$$A_3 + 2CH_3OH \xrightarrow{K_3} C_3 + 2H_2O \quad (3)$$
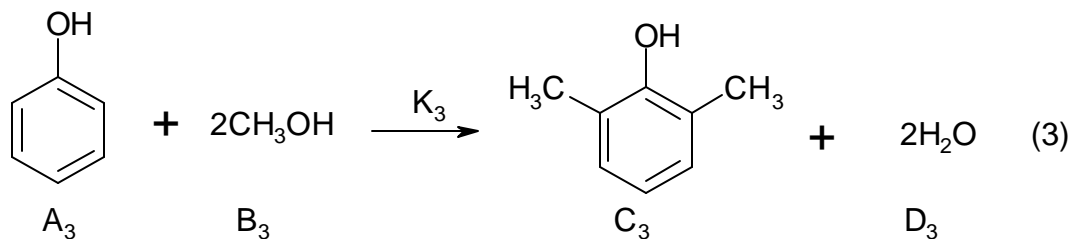
The comparative results of experimental and theoretical equilibrium rate constants K_1, K_2 and K_3 for reactions I, II and III are presented as Figure 3.5.
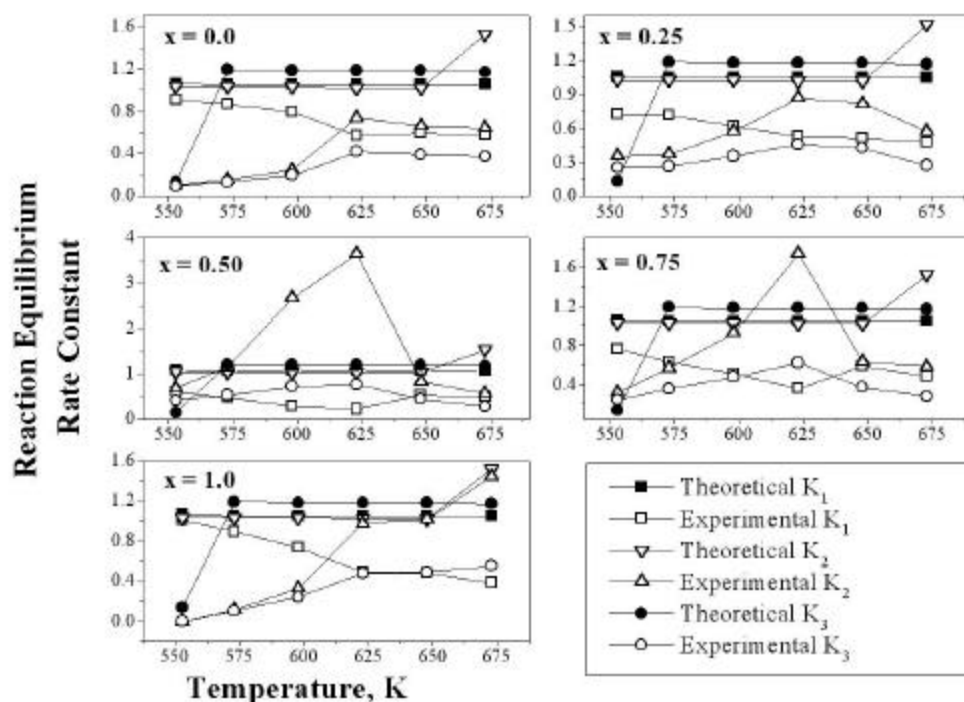
Figure 3.5: Theoretical and experimental comparison of reaction equilibrium rate constant for various compositions of $Cu_{1-x}Co_xFe_2O_4$.

There are three possible types of reaction occurring on catalyst surface. In order to minimize the complexity, the activity coefficient constant, γ assumed to be 1. This assumption does not affect the theoretical equilibrium constant, as the equilibrium constant values mostly depends on the mole fraction of the individual compound. The thermodynamic equilibrium constant or the thermodynamic equilibrium rate constants for the above three types of reaction in the vapour phase is considered and for a non-ideal system, it can be described as follows,

The thermodynamic rate constant [6-9] for reaction I can be written as

$$K_1 = [(a_{c1} \cdot a_{d1}) / (a_{a1} \cdot a_{b1})] = [(x_{c1} \cdot x_{d1}) / (x_{a1} \cdot x_{b1})] * [(?_{c1} \cdot ?_{d1}) / (?_{a1} \cdot ?_{b1})] = K_{X1} K_{?1} \quad (4)$$

$$?_{c1} = ?_{d1} = ?_{a1} = ?_{b1}$$

where $K_? = $ constant based on activity coefficients

The thermodynamic rate constant K_2 can be written as,

$$K_2 = [(a_{c2} \cdot a_{d2}) / (a_{a2} \cdot a_{b2})] = [(x_{c2} \cdot x_{d2}) / (x_{a2} \cdot x_{b2})] * [(\gamma_{c2} \cdot \gamma_{d2}) / (\gamma a_2 \cdot \gamma_{b2})] = K_{X2} K_{\gamma 2} \quad (5)$$

$$?_{c2} = ?_{d2} = ?_{a2} = ?_{b2}$$

And thermodynamic rate constant K_3 can be written as,

$$K_3 = [(a_{c3} \cdot a^2_{d3}) / (a_{a3} \cdot a^2_{b3})] = [(x_{c3} \cdot x^2_{d3}) / (x_{a3} \cdot a^2_{b3})] * [(\gamma_{c3} \cdot \gamma^2_{d3}) / (\gamma_{a3} \cdot \gamma^2_{b3})] = K_{X3} K_{\gamma 3} \quad (6)$$

$$\gamma_{c3} = \gamma_{d3} = \gamma_{a3} = \gamma_{b3}$$

The prediction of the equilibrium reaction rate constants K_1, K_2 and K_3 at each temperature was done by integration of Van't Hoff equation [6-9],

$$d(\ln K_{1,2,3})/dT = -?H/RT^2 \quad (7)$$

where R is the gas constant and ?H is the reaction enthalpy at temperature T. A general expression for the heat of reaction [6-9], in the vapour phase, is given by

$$? H = ?H^0_{(298K)} + {}_{298}\int^T ?C_p^0 (298K) \, dT \quad (8)$$

with

$$? H^0 = ? v_i ? H^0_{f,i} \quad (9)$$

and

$$? C^0_p = ? v_i C^0_{p,i} \quad (10)$$

where v_i, $C^0_{p,i}$ and $? H^0_{f,i}$ are the stoichiometric coefficient, molar heat capacity and the standard heat of formation at 298 K of component i in the vapour phase respectively.

By definition,

$$?G^0 \; = \; ? \; v_i \, G^0_i \; = \; - \, RT \ln K_{eq} \qquad\qquad (11)$$

or

$$K_{eq} = \; \exp(-?G/RT) \qquad\qquad (12)$$

where, G^0_i is the standard free Gibbs energy of formation of component i. The standard formation of enthalpy, molar heat capacity and free Gibbs energy for reactions I, II and III were calculated by equations 9,10 and 11 and is presented in Table 3.3.

Table 3.3: Standard formation properties for phenol methylation at 298 K for reactions I, II and III in vapour phase.

Component	$? H_f^0$ (Kcal/mole)	$? G^0_f$ (Kcal/mole)	$? C^0_{pf}$ (cal/mole^{0}K)
Reaction I	-17.43	-16.8	3.94
Reaction II	-64.32	-34.99	14.56
Reaction III	-52.11	-51.79	18.5

The reaction equilibrium rate constant can be evaluated at any temperature by substituting values from Table 3.3 in eqs (8) and (12), giving following expressions:

Reaction I

$$?H_1 = \; -17.43 + \,_{298}?^T \; (3.94\,) \; dT \qquad\qquad (13)$$

$$\text{and } K_{298} \; = \; 1.11 \; ^0K^{-1} \qquad\qquad (14)$$

Reaction II

$$?H_2 \; = \; -64.32 \; + \,_{298}?^T \; (\, 14.56\,) dT \qquad\qquad (15)$$

$$\text{and } \; K_{298} = 1.24 \; ^0K^{-1} \qquad\qquad (16)$$

Reaction III

$$? \; H_3 = \; -52.11 + \,_{298}?^T \; (18.5) \; dT \qquad\qquad (17)$$

$$\text{and } \; K_{298} = 1.37 \; ^0k^{-1} \qquad\qquad (18)$$

After substitution of equation 13-18 in equation (7).

Reaction I

$$\ln (K_1/1.11) \; = \; - \; ?H_1/R \; (1/T \; - \; 1/298) \qquad (19)$$

Reaction II

$\ln (K_2/1.24) = - ?H_2/R (1/T - 1/298)$ (20)

and

Reaction III

$\ln (K_3/1.37) = - ?H_3/R (1/T - 1/298)$ (21)

The comparison between experimental values and those predicted by eqns. 19, 20 and 21 is shown in Figure 3.5, for different compositions of catalysts. At 623 K, experimentally 2,6 dimethyl phenol formation increases by both consecutive and parallel path. As per the theoretical prediction both the path should increase marginally or almost constant with respect to temperature in the range of 570-650 K. In Figure 3.5, the experimental values of thermodynamic equilibrium constant K_1, K_2 and K_3 for reaction I, II and III for the composition $x = 0$ are not in agreement with the theoretical values.

The formation of 2,6-dimethyl phenol increases up to 623 K and it approaches more towards the theoretical values of K_1, K_2 and K_3. As the Co concentration increases from 25% to 50%, the 2,6-dimethyl phenol formation observed to be increased by the consecutive path. This increment in 2,6-dimethyl phenol is almost 3.5 folds higher than the theoretical one. A further increase in the Co content decreases the 2,6-dimethyl phenol formation observed experimentally, but it is higher than the theoretical value. This may be due to the favoring of parallel reaction along with consecutive reaction, decrease in the methanol concentration over the catalyst surface. This decrease in methanol concentration reduce the 2,6 dimethyl phenol formation by consecutive path. So, the further increase in % of Co from 0.50 to 0.75 does not show any improvement in activity. Similar observation is found for the composition $x = 1$. Thus from the thermodynamic study it can be concluded that at 623 K, the consecutive reaction equilibrium rate constant K_1 together with K_2 is more favoured than K_3, signifying high feasibility of consecutive pathway for formation of 2,6-dimethyl phenol from phenol through 2-methyl phenol over its direct dimethylation.

The curves of reaction equilibrium rate constants K_1, K_2 and K_3 for catalyst $Cu_{0.50}Co_{0.50}Fe_2O_4$ are more comparable with theoretical one, in the working temperature range of 553 – 673 K for a reaction period of 3 hrs. The values of K_1, K_2 and K_3 for other

studied catalyst are not closely comparable. This study thus allows us to compare the different spinels for reaction equilibrium rate constant, both by theoretically and experimentally.

3.3. PHENOL METHYLATION USING DIMETHYL CARBONATE (DMC)

Dimethyl carbonate (DMC) has two carbon centers at which a nucleophile may attack the carbonyl and the methyl group. When a nucleophile attacks carbonyl carbon of DMC, the cleavage of acyl-oxygen bond results in a methoxy carbonyl product. When the attack is on the methyl carbon of DMC, the methylation product is produced by the CH_3-O bond cleavage [10]. An important advantage of DMC is that it is non-toxic in nature. Alkylation of phenol with methanol is well established. However only a few reports are available on phenol methylation using dimethyl carbonate as methylating agent [11-17] and leads to the very selective O-methylation of phenol to anisole [12,15-17] in contrast to methanol.

The methylation of phenol over $Cu_{1-x}Co_xFe_2O_4$ is studied using a feed mixture of phenol and DMC (2:5) at 350^0C to understand the catalytic performance of this system. Figure 3.6a and Table 3.4 shows the influence of composition towards phenol conversion and selectivity of various products at 350^0C.
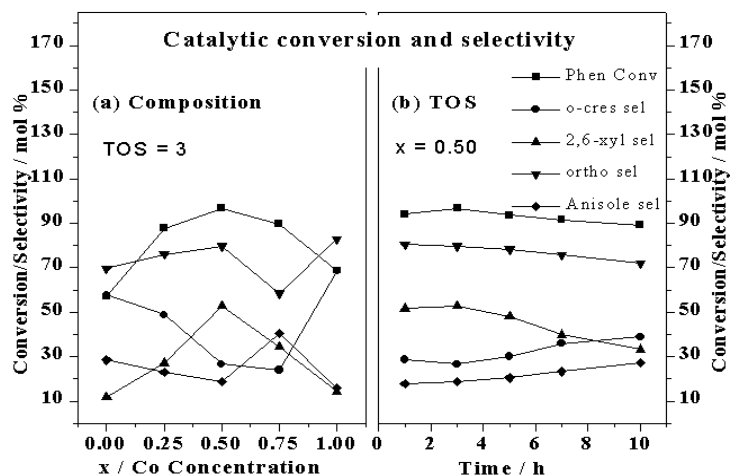
Figure 3.6: (a) composition dependence of phenol methylation over $Cu_{1-x}Co_xFe_2O_4$ (b) Time dependence of phenol methylation on $Cu_{0.50}Co_{0.50}Fe_2O_4$; Phenol methylation is carried out with phenol:dimethyl carbonate (DMC) composition of 2:5 at 350^0C and at WHSV of 0.869 h^{-1}.

The data thus obtained correspond to third hour time on stream (TOS = 3 h). From Table 3.4 and figure 3.6a it is clear that compositions containing both Cu and Co are highly active towards phenol conversion and among which x = 0.50 shows maximum activity. All the compositions are susceptible to form both O-alkylated (anisole) and C-alkylated (ortho alkylated products such as o-cresol and 2,6-xylenol). None of the compositions show high selectivity towards a particular product. However, among all the compositions, x = 0.50 shows maximum selectivity towards 2,6-xylenol, the most demanded product. Figure 3.6b shows the catalytic performance of x = 0.50 as a function of time. An important observation can be made from the data is the continues increase of anisole selectivity as time progresses. Similar trends are observed for other compositions also.

Table 3.4: Influence of catalyst composition on phenol conversion and product distribution over $Cu_{1-x}Co_xFe_2O_4$. Phenol methylation is carried out with phenol:dimethyl carbonate (DMC) composition of 2:5 at 350^0C and at WHSV of 0.869 h^{-1}.

Product distribution	Catalyst composition, x				
	0	**0.25**	**0.50**	**0.75**	**1**
Anisole	16.25	20.19	18.31	36.37	11.01
Unreacted Phenol	43.04	12.12	3.14	10.2	31.23
o-Cresol	32.90	42.94	25.86	21.52	47.02
2,6-xylenol	6.79	23.92	51.29	30.94	9.89
p-Cresol	0.10	0.16	0.03	0.15	0.19
2,4-Xylenol	0.68	0.23	0.94	0.42	0.31
2,4,6-TMP	0.53	0.44	0.44	0.40	0.35
Phenol conversion	56.96	87.88	96.86	89.8	68.77
o-Cresol selectivity	57.76	48.86	26.7	23.96	68.37
2,6-Xylenol selectivity	11.92	27.22	52.95	34.45	14.38
Total ortho selectivity	69.68	76.08	79.65	58.42	82.75
Anisole selectivity	28.53	22.97	18.90	40.50	16.01

3.4. CATALYTIC ETHYLATION OF PHENOL

3.4.1. Introduction

2-ethyl phenol resulting from the ethylation of phenol is a valuable chemical and it is used as a starting material for photochemicals [1]. It is also an intermediate for the synthesis of benzofuran, which in turn together with indene is the raw material used for the production of indene-coumarone resins [18]. Numerous studies have been devoted to the alkylation of phenol with ethanol or ethylene for the synthesis of mono and diethyl phenols [1,19-25]. 2-ethyl phenol and 2,6-diethyl phenol are produced industrially by ortho ethylation of phenol with ethylene in high-pressure autoclaves at 320-340^{0}C and 20mPa in the presence of 1-2 % aluminum phenolate. Various types of catalysts have been reported to prepare 2-ethyl phenol, including Th/Al oxides, Fe-Si-Mg oxides, phosphoric acid-SiO$_2$, Fe$_2$O$_3$, Cr$_2$O$_3$, magnetite, hydrotalcites, zeolites and Al$_2$O$_3$ oxides [1,19-25]. However these catalysts possess one or more of the drawbacks such as, low conversion, severe operative conditions, poor selectivity due to number of side products and lack of reproducibility.

3.4.2. Results

Reaction of phenol with ethanol provides ortho ethylated 2-ethyl phenol (EtPhOH) as major product over Cu$_{1-x}$Co$_x$Fe$_2$O$_4$. Side products such as para ethylated phenols, ethyl phenyl ether (phenitole), ethyl methyl phenols, cresols etc are also formed in very small quantities. Formation of 2,6-diethyl phenol occurs to an extent of 10-15 % selectivity at high temperatures.

3.4.2.1. Effect of Ethanol:Phenol mole ratio on Cu$_{1-x}$Co$_x$Fe$_2$O$_4$

In order to choose an optimum feed mix, phenol ethylation on x = 0.50 was carried out at 350^{0}C using molar ratios of EtOH:PhOH between 3 and 7 (Figure 3.7a). PhOH conversion varies in a volcano shape with increasing EtOH:PhOH ratio with a maximum conversion observed at a value of 5. PhOH conversion decreases above and below 5. Above trend hints the amount of EtOH is too less at a ratio of 3 for a better PhOH conversion. Nevertheless, low conversion at high EtOH:PhOH ratio might be due to excess

ethanol in the feed mix causes the decomposition of EtOH as one of the major reaction leaving little room for PhOH ethylation over the catalyst surface. Thus, it is apparent that ethanol is consumed in other simultaneous reactions, such as ethanol reforming, to form gaseous products such as H_2, CO, CO_2 and hydrocarbons. Formation of above gaseous products was confirmed by GC and GC-MS analysis. Hence EtOH:PhOH mole ratio of 5:1 was applied for all reaction results reported in this paper, unless otherwise stated. The ratio of 5:1 is optimal from the point of view of the conversion exceeds considerably the value desired by the stoichiometry to form both EtPhOH and 2,6-diethyl phenol. EtPhOH selectivity remains at a constant high value of 81±2% irrespective of feed ratio at time on stream = 3 h.
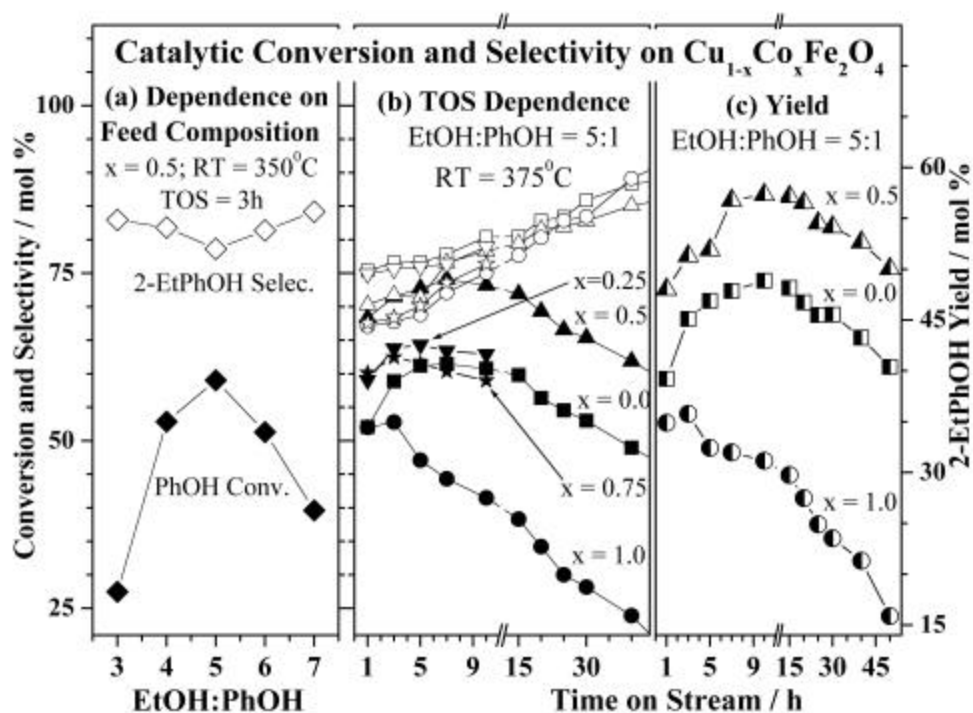
Figure 3.7: (a) Ethanol:phenol composition dependence of phenol conversion and 2-ethyl phenol selectivity on $Cu_{0.5}Co_{0.5}Fe_2O_4$, TOS = 3 h at 350^{0}C. (b) Time dependence of phenol conversion and 2-ethyl phenol selectivity at 375^{0}C; conversion and selectivity is denoted by solid and open symbols, respectively and x values are indicated. Note increasing product selectivity with increasing TOS and decreasing phenol conversion on Co-rich compositions. (c) TOS dependence of product yield at x = 0, 0.5 and 1, shows high and stable yield with Cu-containing compositions.

3.4.2.2. Effect of time on stream

The stability of the catalysts were studied from the time on stream (TOS) dependence at 375^0C for 50 (10) hours on compositions namely, x = 0, 0.5 and 1 (x =0.25 and 0.75) and shown in Figure 3.7b. From the results it is clear that an increase in PhOH conversion is observed initially up to 5 hours for x≤0.75; almost constant selectivity of EtPhOH is observed during the above time period with considerable amount of secondary products. Initial TOS up to 5 h is considered to be a transient state (TS). As the time progresses, PhOH conversion and EtPhOH selectivity reaches apparently to a steady state (SS) with a fluctuation of less than few percent up to 30 to 40 hours and thereafter deactivation starts very slowly. However large decrease in activity pattern with time is observed on $CoFe_2O_4$ from the beginning. x = 0.0 and 0.5 shows an excellent stability over the entire period of time studied with low deactivation above 30 h; however catalytic activity above 30 h is better or comparable to the TS activity. Moreover, progressive improvement of EtPhOH selectivity is observed on all compositions as time increases. This is due to the progressive suppression of secondary reactions with increasing TOS towards the formation of aromatics, alkyl phenols etc observed considerably at low TOS.

A better picture about the TS and SS can be seen in Figure 3.7c with EtPhOH yield against TOS for catalyst composition of x = 0, 0.5 and 1. Almost an invariable EtPhOH yield of 46±1% and 56±1% is seen in the SS for x = 0.0 and 0.5, respectively. No such SS, but a continuous decline in yield is seen at x = 1.0 and indicates the poor activity and stability of $CoFe_2O_4$ towards ethylation. Nonetheless, an equal bulk combination of Cu and Co at x = 0.5 displays a high and stable catalytic activity hints the combination is better than end compositions. Further, a product yield at 50 h is comparable or greater than that obtained at 1h is observed for x = 0.0 and 0.5, demonstrates their superior stability. TS and SS observed in the above indicate a considerable modification of the surface from the initial catalyst state to highly reactive state during SS.

3.4.2.3. Effect of catalyst composition

Figure 3.8 displays the influence of catalyst composition on PhOH conversion and EtPhOH selectivity at different temperatures and at TOS = 3h.
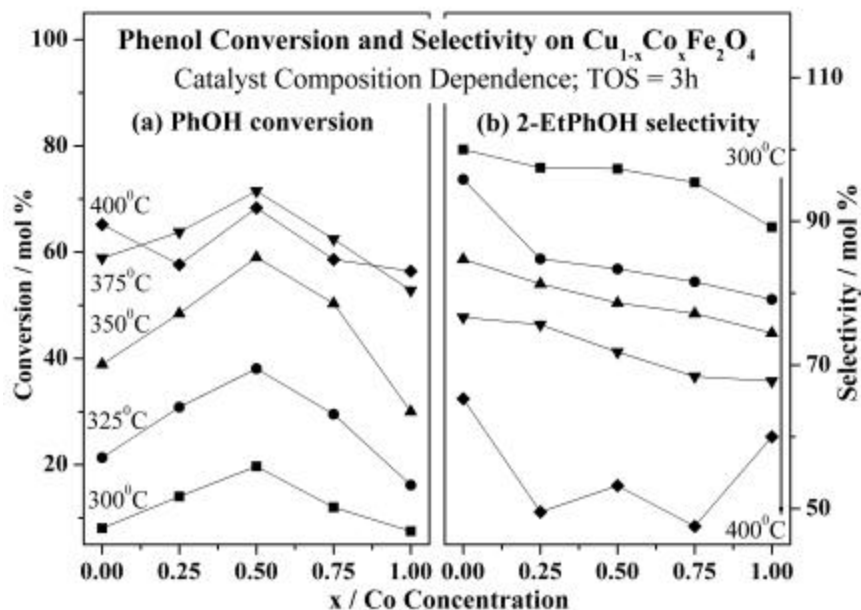
Figure 3.8: Composition dependence of phenol conversion (a) and 2-ethyl phenol selectivity (b) is shown at temperatures between 300^0C and 400^0C on $Cu_{1-x}Co_xFe_2O_4$. Relatively large phenol conversion with x = 0.5 and high selectivity with x = 0.0 is observed at all temperatures.

The product distribution obtained from phenol ethylation reaction over $Cu_{1-x}Co_xFe_2O_4$ under the optimized conditions (Temperature = 375^0C, PhOH:EtOH mole ratio = 1:5, WHSV = 0.869 h^{-1} and TOS = 3) is presented in Table 3.5. The influence of Cu+Co composition is an important factor towards PhOH conversion is evident from the comparatively large PhOH conversion at intermediate compositions (0<x<1) compared to end compositions (x = 0 and 1). x = 0.5 composition shows maximum PhOH conversion at all temperatures studied. However, $CuFe_2O_4$ shows the maximum selectivity for EtPhOH at all temperatures and the selectivity decreases with increase in x up to 375^0C. However, at 400^0C selectivity of EtPhOH falls off at intermediate compositions compared to end compositions. Also from the product analysis, it is found that 0<x<1 produce considerable amount of aromatic hydrocarbons such as benzene and toluene in contrast to end compositions at 400^0C.

Table 3.5: Influence of catalyst composition on phenol conversion and product distribution over $Cu_{1-x}Co_xFe_2O_4$. Phenol ethylation is carried out with phenol:ethanol mole ratio of 1:5 at 375^0C and at WHSV of $0.869\ h^{-1}$.

Product distribution	Catalyst composition, x				
	0	**0.25**	**0.50**	**0.75**	**1**
Aromatics	1.15	2.92	2.03	4.02	2.31
Phenylalkyl ethers	0.67	1.64	1.95	2.67	2.61
Unreacted Phenol	41.13	36.22	28.50	37.55	47.20
o-Cresol	0.62	0.63	1.62	3.50	3.35
2,6-Xylenol	0.02	0.04	0.17	0.24	0
2-Ethylphenol	45.10	48.23	51.32	42.71	35.78
Ethylmethyl phenols	0.84	2.59	2.08	2.60	1.84
2,6-Diethyl phenol	8.91	6.29	9.73	4.86	6.25
Other alkyl phenols	1.55	1.43	2.60	1.87	0.66
Phenol conversion (%)	58.87	63.78	71.50	62.45	52.80
2-Ethylphenol selectivity (%)	76.62	75.62	71.78	68.39	67.77
Total ortho ethyl selectivity	91.75	85.48	85.39	76.17	79.61

3.4.2.4. Effect of reaction temperature

The reaction temperature dependence of PhOH conversion and EtPhOH selectivity were investigated on all five compositions and displayed in Figure 3.9. These results have been presented above, but are displayed in a new way here to highlight the correlation between conversion and selectivity. (a) All the compositions show an increase in PhOH conversion linearly up to 375^0C and then decreases with further increase in temperature for $0<x<1$, but increases marginally for $x = 0$ and 1. However, $x = 0.5$ still shows large PhOH conversion at 400^0C. (b) As the temperature increases the selectivity of EtPhOH decreases linearly for all compositions, with highest selectivity at $x = 0.0$. (c) Positive and negative first order dependence of PhOH conversion and EtPhOH selectivity, respectively, for all compositions up to 375^0C. (d) At low TOS, high temperature tends to an increase in above

mentioned side products, due to which the EtPhOH selectivity decreases. First and second point indicates the importance of Cu+Co combination in PhOH conversion and Cu-species in ethylation.
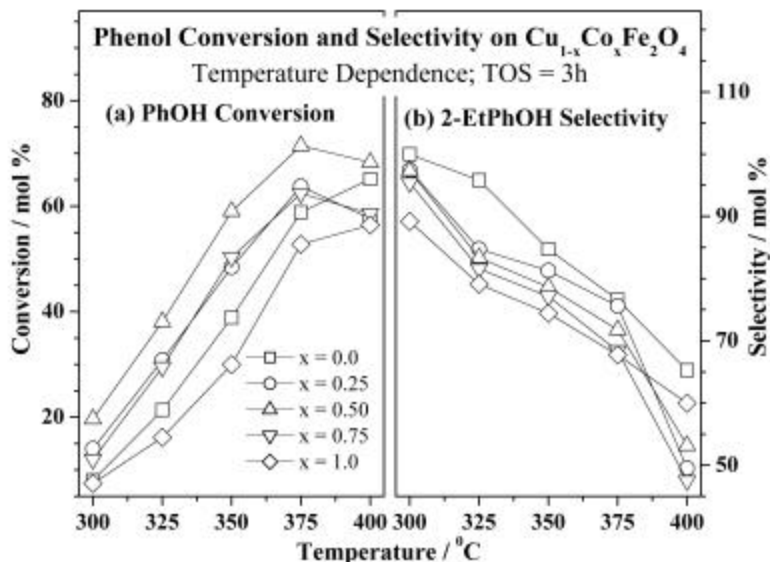
Figure 3.9: Temperature dependence of (a) phenol conversion and (b) 2-ethyl phenol selectivity is shown for all compositions. Linear increase in phenol conversion and a decrease in 2-ethyl phenol selectivity with increasing temperature indicate the first order dependence of reaction.

3.4.3. Discussion

From the catalytic activity data (Figures 3.7-3.9), it is clear that compositions containing both Cu and Co are found to have better catalytic performance than the end compositions and x = 0.50 shows high catalytic performance. Nonetheless, $CoFe_2O_4$ shows poor activity. Second important aspect is the selectivity of EtPhOH decreases with decreasing bulk Cu-content and increasing temperature. This is due to the formation of various C-alkylated products and aromatics. Third is the PhOH conversion shows a volcano type performance with x at all temperatures (Figure 3.8) and a maximum conversion always at x = 0.50. Above points hints the ethylation activity is mainly due to Cu+Co combination and among them Cu is highly active towards ethylation.

Ethylation leads to O-alkylation also to a marginal extent. However with the present series of catalysts, selectivity of O-alkylated product was found to be <5% irrespective of temperature and composition. Again C-alkylation can take place either by a direct route or by the rearrangement of the ethyl phenyl ether (also called isomerization). To decide between these two routes, phenitole vapour was passed over the catalyst on x = 0.50 at 375^0C. No isomerized products were observed and hence the present catalyst can be considered to catalyze the C-alkylation of PhOH directly without the rearrangement of alkyl phenyl ether as reported by Pillai et al [26]. However, this observation is in contrast to the behavior of alumina [19], on which alkyl phenyl ethers undergo isomerization to alkyl phenols.

Two important aspects of the ethylation reactions to the discussion presented here are (a) an increase in the selectivity of EtPhOH with increasing TOS, and (b) constant EtPhOH yield during SS for x<1. An increase in EtPhOH selectivity is observed as time progresses (Figure 3.7b) with simultaneous decrease of other side reactions. Above observations are attributed to the redistribution of active cations from the fresh catalyst surface to the surfaces at SS, is strongly supported from a good change in surface composition (Chapter 4, Table 4.10). XPS analysis demonstrates the above changes are necessary from the reaction point of view is discussed later.

TOS studies of x = 0 and 1 in Figure 3.7b clearly illustrates the importance of Cu in ethylation. Same initial activity is observed for both x = 0 and 1. A continuously decreasing activity with x =1 with TOS is in stark contrast with high and stable activity at x = 0. However a high EtPhOH selectivity with x = 1 indicates that phenol conversion is a limiting factor. A careful look at the surface atomic ratio of x = 1 in Table 4.10 (Chapter 4) indicates the initial Fe-rich surface converted to Fe:Co ratio of 1:1 after reaction at 375^0C for 10 h. This indicates the large surface segregation of Co leads to lower activity. Replacement of 50% Co (x = 0.5) by Cu leads to an enhanced and stable ehtylation activity ascertain that it is the combination of Cu+Co that works better than any single metal-ion enriched surfaces.

The kinetic parameters were evaluated from the PhOH conversion data in the temperature range between 300^0C and 375^0C in an Arrhenius fashion to highlight the

nature of ethylation reaction. Experimental results showed that PhOH ethylation over $Cu_{1-x}Co_xFe_2O_4$ follows first-order kinetics with respect to PhOH conversion and hence the rate is assumed to be:

$$\text{Rate} = \ln (\theta/1-\theta) = \ln A_0 - (E_a/RT) \tag{22}$$

where $\ln A_0$ is the apparent Arrhenius frequency factor, which includes contact time and initial PhOH concentration, θ is the PhOH conversion and E_a is the apparent activation energy. The representative Arrhenius plots for PhOH conversion employing Eq. (22) for the catalysts composition of $x = 0$, 0.5 and 1 and the values of E_a and $\ln A_0$ are plotted in Figure 3.10 a and b, respectively.
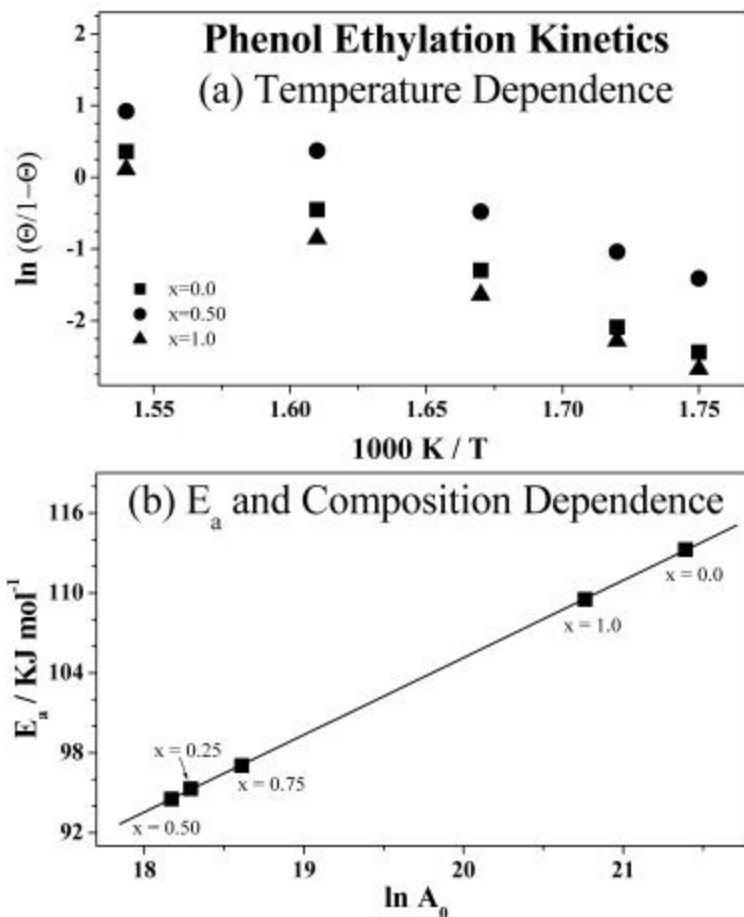

Figure 10: (a) Arrhenius plots shows a linear increase in phenol conversion with increasing temperature and (b) activation energy against frequency factor. Note the low activation energy associated with intermediate compositions compared to end compositions of catalyst.

From the kinetic parameters it is clear that compositions containing both Cu and Co exhibit relatively low E_a towards PhOH conversion than end compositions. There are hardly any reports available regarding the kinetic parameters for phenol ethylation. However, the E_a values for the PhOH methylation have been reported in the range of 20-130 KJ/mol over MnO [27], anions loaded $AlPO_4$-Al_2O_3 [28], HZSM-5 [29] and Mg-Al hydrotalcites [30]. The E_a evaluated in the present study varies almost in the same and close range (94-113 KJ/mol) supports the validity of the model assumed for the evaluation of kinetic parameters.

It has been shown by several authors that a good correlation exists between E_a and ln A_0 for different reactions taking place over one catalyst [31-33]. Such a correlation is termed as 'compensation effect' or 'isokinetic effect' and can be written as:

$$E_a = a + b \cdot \ln A \tag{23}$$

where a and b are constants called correlation parameters [33]. A plot of E_a versus ln A_o for the $Cu_{1-x}Co_xFe_2O_4$ (x = 0 to 1) series shows a straight line (Figure 3.10b) with a very high linear regression coefficient of 0.9999 indicating the existence of a good compensation effect and hints the mechanism of PhOH ethylation remains the same over the entire $Cu_{1-x}Co_xFe_2O_4$ series. Value of a and b evaluated from this plot are 10.83 and 5.80 KJ/mol respectively. ln A_o for the various compositions can be related to the entropy of activation of the reactant species [34], and it is found that the intermediate compositions offers less entropy of activation than x = 0 and 1.

3.5. ISOPROPYLATION OF PHENOL

3.5.1. Introduction

An extensive study of the alkylation of phenol, both with propanol and isopropanol in the presence of alumina has been published [35,36]. Industrially, 2-isopropyl phenol is produced from phenol and propene using γ-Al_2O_3 as the catalyst at a temperature 250-300^{0}C and 10Mpa pressure [1]. Alkylation of phenol with propene resulted isopropyl alcohol due to the formation of more stable 2^0 carbocation intermediate [1,37]. Kannan etal [35] observed that, in the alkylation of phenol with 1-propanol over γ-Al_2O_3, O-alkylation takes place without any isomerisation of the propyl moiety while a

mixture of n-propyl and isopropyl phenols were noticed in the C-alkylation. On the other hand, no such isomerisation was observed by Karuppannasamy etal over thoria [26]. In the alkylation of phenol with propanol, many alkylated products were observed over Al_2O_3 [35,36] and Al-containing hydrotalcites [23, 38]. Other catalysts used for propylation involve Cr_2O_3, condensed phosphoric acid-kieseghur, zeolites and $MgO-CeO_2$ [19, 39].

3.5.2. Results and discussion

Reaction of phenol with isopropanol (iPrOH) provides ortho alkylated product, viz., 2-isopropyl phenol as major product over the $Cu_{1-x}Co_xFe_2O_4$ catalyst system. Trace amount of lower alkylated products such as o-cresol and 2,6-xylenol and 2,6-diisopropyl phenol are also formed.

In order to choose an optimum feed mix, phenol isopropylation on x = 0.50 was carried out at 350^0C using molar ratios of iPrOH:PhOH between 2 and 6 (Figure 3.11a).
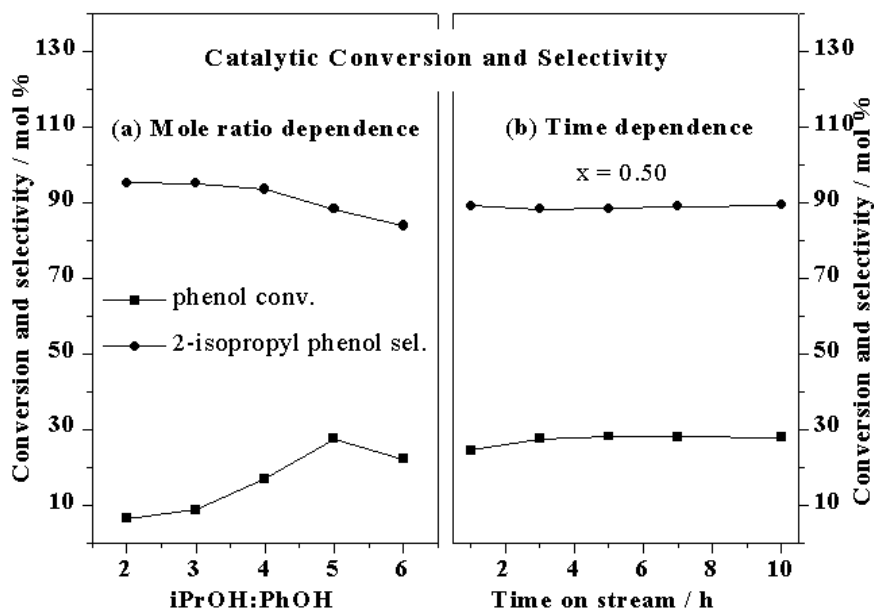

Figure 3.11: (a) Isopropanol:phenol composition dependence of phenol conversion and 2-isopropyl phenol selectivity on $Cu_{0.5}Co_{0.5}Fe_2O_4$, TOS = 3 h at 350^0C. (b) Time dependence of phenol conversion and 2-isopropyl phenol selectivity on $Cu_{0.5}Co_{0.5}Fe_2O_4$ at 350^0C with isopropanol:phenol mole ratio of 1:5.

PhOH conversion varies in a volcano shape with increasing iPrOH:PhOH ratio with a maximum conversion observed at a value of 5. PhOH conversion decreases above and below 5. Above trend hints the amount of iPrOH is too less at a ratio of 3 for a better PhOH conversion. Nevertheless, low conversion at high iPrOH:PhOH ratio might be due to excess isopropanol in the feed mix causes the decomposition of iPrOH as one of the major reaction leaving little room for PhOH isopropylation over the catalyst surface. Thus, it is apparent that isopropanol is consumed by its own decomposition to form gaseous products such as H_2, CO, CO_2, acetone and hydrocarbons. Formation of above gaseous products was confirmed by GC and GC-MS analysis. Hence iPrOH:PhOH mole ratio of 5:1 was applied for all reaction results, unless otherwise stated. The ratio of 5:1 is optimal from the point of view of the conversion exceeds considerably the value desired by the stoichiometry to form 2-isopropyl phenol (iPrPhOH). The stability of the catalysts were studied from the TOS dependence at 350^0C for 10 hours on x = 0.5 (Figure 3.11b). From the results it is clear that both phenol conversion and 2-isopropyl phenol remains almost constant during the above time period. Thus the catalyst is quite stable towards phenol isopropylation reaction.

The reaction temperature dependence of PhOH conversion and 2-isopropyl phenol selectivity were investigated on x = 0.50 and displayed in Figure 3.12b. The products were collected after TOS = 3 h by using fresh catalyst in each run. A linear dependence on phenol conversion with temperature is observed up to 350^0C. However, further increase of temperature causes a decrease in phenol conversion. High temperature causes the decomposition of isopropanol a faster process that reduces the availability of isopropanol for alkylation. As the temperature increases the selectivity of 2-isopropyl phenol decreases. Higher temperatures tends to an increase in the formation of lower alkyl phenols such as o-cresol and 2,6-xylenol due to which selectivity of 2-isopropyl phenol decreases.

Figure 3.12a and Table 3.6 displays the influence of catalyst composition on PhOH conversion and 2-isopropyl phenol selectivity at 350^0C and at TOS = 3 h.
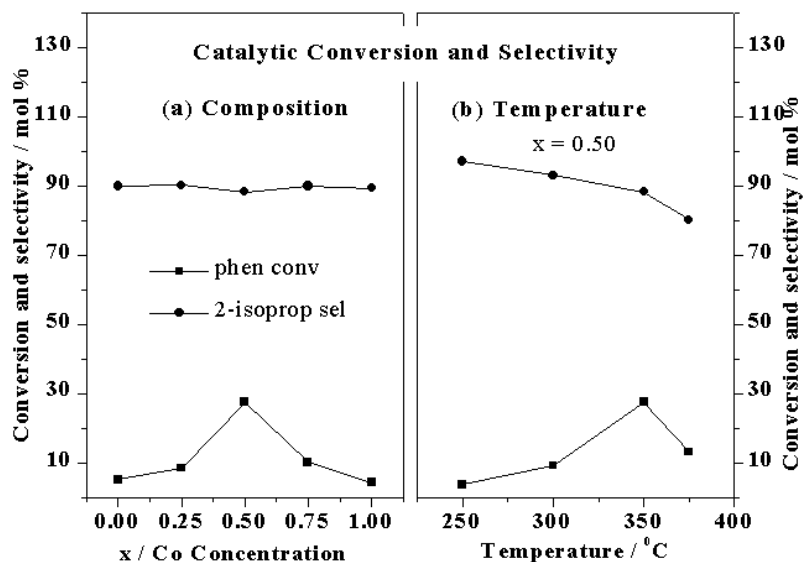
Figure 3.12: (a) composition dependence of phenol conversion and 2-isopropyl phenol selectivity over $Cu_{1-x}Co_xFe_2O_4$ at 350^0C with isopropanol:phenol mole ratio of 1:5 and WHSV of 0.869 h^{-1} (b) Temperature dependence of phenol conversion and 2-isopropyl phenol selectivity on $Cu_{0.5}Co_{0.5}Fe_2O_4$ at 350^0C with isopropanol:phenol mole ratio of 1:5.

Table 3.6: Influence of catalyst composition on phenol conversion and product distribution over $Cu_{1-x}Co_xFe_2O_4$ (x = 0, 0.25, 0.50, 0.75 and 1). Phenol isopropylation is carried out with phenol:isopropanol mole ratio of 1:5 at 350^0C and at WHSV of 0.869 h^{-1}.

Product distribution	Catalyst composition, x				
	0	**0.25**	**0.50**	**0.75**	**1**
Unreacted phenol	94.82	91.49	72.53	89.87	95.7
o-Cresol	0.17	0.20	0.82	0.34	0.17
2,6-xylenol	0.21	0.44	1.21	0.53	0.15
2-isopropyl phenol	4.66	7.68	24.24	9.02	3.84
2,6-diisopropyl phenol	0.11	0.13	1.03	0.13	0.10
Others	0.03	0.06	0.17	0.11	0.04
Phenol conversion	5.18	8.51	27.47	10.13	4.30
2-isopropyl phenol selectivity	89.96	90.24	88.24	89.93	89.30

Though all are less active towards phenol isopropylation, compositions containing both Cu and Co show comparatively high activity. Among Cu-Co mixed compositions, $x = 0.50$ shows considerably large phenol conversion. Irrespective of the compositions, all are highly selective towards ortho alkylation and show ~90% selectivity in 2-isopropyl phenol formation.

3.6. TERTIARY BUTYLATION OF PHENOL

3.6.1. Introduction

Tertiary butylation of phenol has been studied extensively owing to industrial interest in the production as antioxidants, in the synthesis of various agrochemicals, fragrance compounds, ultraviolet absorbers, thermoresistant polymers and heat stabilizers of polymeric materials [1]. Both tertiary butyl alcohol and isobutene used extensively for this purpose. Various catalysts reported for this reaction involve, Cr_2O_3, ion exchange resins, zeolites, zirconia and sulphated zirconia [19,23,40-47]. It is reported that the molecular sieve based catalysts like SAPO–11, HY, Hβ, AlMCM-41 and FeMCM-41 were proved to be potential catalysts for the tertiary butylation of phenol among the various solid acid catalysts [43-47]. However, unlike other phenol alkylation the reaction of tertiary butylation of phenol gives numerous products depending on the nature of the catalysts as well as on the reaction conditios.

3.6.2. Results and discussion

Tertiary butylation of phenol was carried out with isobutene (gas) at 200^0C. The main products of t-butylation of phenol on $Cu_{1-x}Co_xFe_2O_4$ are 2-tertiary butyl phenol (2-TBP), 4-tertiary butyl phenol (4-TBP) and 2,4-di tertiary butyl phenol (2,4-DTBP). 2,6-di tertiary butyl phenol is also formed, but in trace amount. Figure 3.13a shows the results of alkylation of phenol with isobutene over $x = 0.5$ at 200^0C with various isobutene:phenol ratio (1 to 7). It can be seen that an increase of phenol conversion is observed as the isobutene/phenol mole ratio increases to 5 and thereafter decreases. However, comparatively high yield for 2-TBP was noticed at 1:3 feed ratio. Hence, this feed ratio was maintained throughout the study. Figure 3.13b shows the change in phenol conversion

and selectivity of various products with TOS over x = 0.5 at 200^{0}C. The conversion of phenol was 31.89 at TOS = 1 h. It is then sharply decreased to 4% at 10 h. Moreover, the selectivity of 2-TBP remains more or less same over the entire period of time studied. The effect of WHSV on the catalytic performance is studied in the range 0.5 – 2 h^{-1} using x=0.50 catalyst at 200^{0}C (Figure 3.13c). It can be seen from the data that both high and low value of WHSV is not helpful for high catalytic performance. Maximum phenol conversion with a reasonable good selectivity of 2-TBP is achieved at WHSV=1.
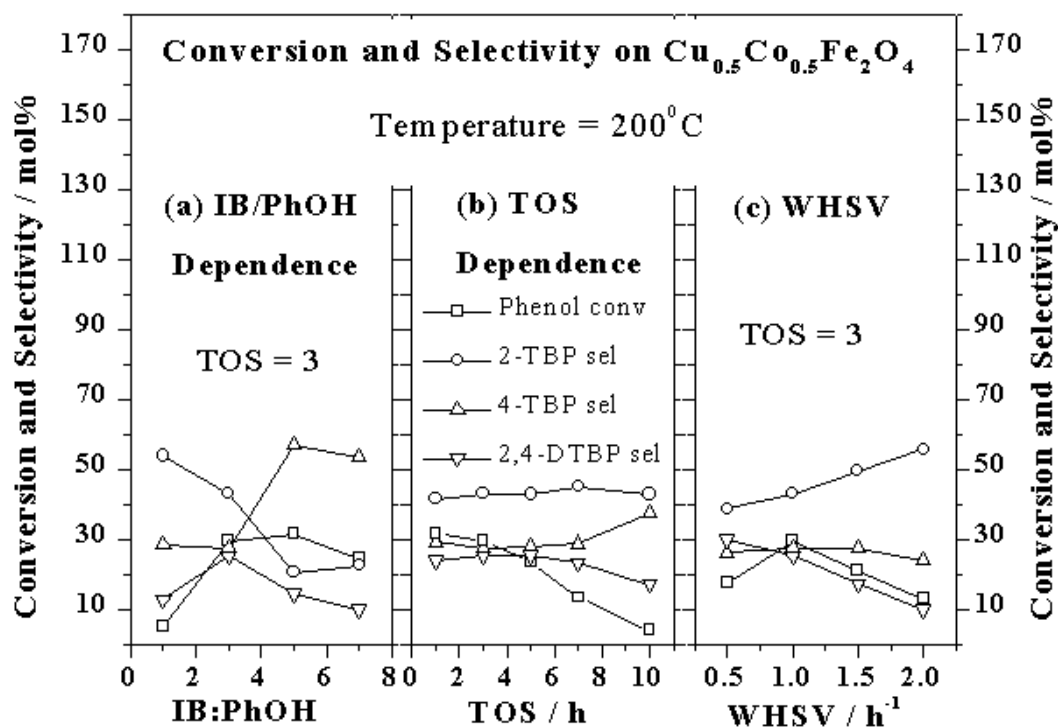
Figure 3.13: (a) Isobutene:phenol composition dependence of phenol conversion and selectivity of various butylated phenols on $Cu_{0.5}Co_{0.5}Fe_2O_4$, TOS = 3 h at 200^{0}C (b) Time dependence of phenol conversion and butylated phenols selectivities on $Cu_{0.5}Co_{0.5}Fe_2O_4$ at 200^{0}C with isobutene:phenol mole ratio of 1:3 (c) The effect of WHSV on the catalytic performance for phenol butylation at 200^{0}C with isobutene:phenol mole ratio of 1:3.

Figure 3.14a shows the effect of reaction temperature on the conversion of phenol and selectivity of various products over x = 0.50 at a space velocity of 1 and TOS = 3 h. Maximum phenol conversion is observed at 200^0C. Phenol conversion increases from 3.19 % to 29.62 % as the temperature was changed from 175^0C to 200^0C. However, rise of temperature causes gradual decrease in phenol conversion. Further, selectivity of 2-TBP decreases as the temperature increases.
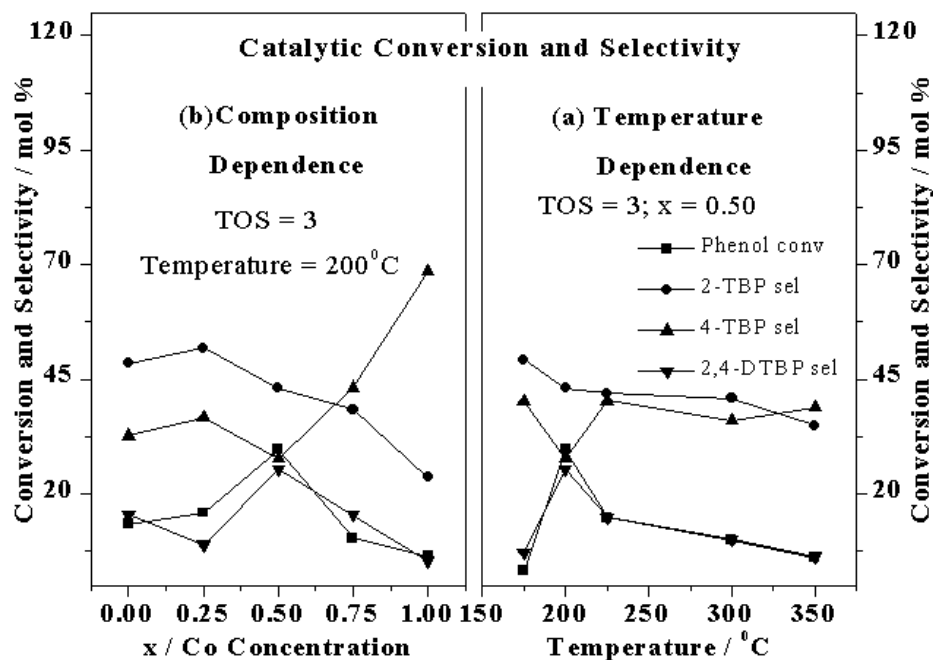
Figure 3.14: (a) Temperature dependence of phenol conversion and various butylated phenol selectivities over $Cu_{1-x}Co_xFe_2O_4$ at 200^0C with isobutene:phenol mole ratio of 1:3 and WHSV of 1 h^{-1}. (b) composition dependence of phenol conversion and various butylated phenol selectivities over $Cu_{1-x}Co_xFe_2O_4$ at 200^0C with isobutene:phenol mole ratio of 1:3 and WHSV of 1 h^{-1} .

The results of the butylation of phenol with isobutene over $Cu_{1-x}Co_xFe_2O_4$ is presented in Table 3.7 with all side products.

Table 3.7: Influence of catalyst composition on phenol conversion and product distribution over $Cu_{1-x}Co_xFe_2O_4$ (x = 0, 0.25, 0.50, 0.75 and 1). Phenol butylation is carried out with phenol:isobutene mole ratio of 1:3 at 200^0C and at WHSV of 1 h^{-1}.

| Product distribution	Catalyst composition, x				
	0	**0.25**	**0.50**	**0.75**	**1**
Unreacted phenol	86.60	84.08	70.38	89.66	93.63
o-Cresol	0.17	0.21	0.38	0.13	0.08
2,6-xylenol	0.04	0.03	0.07	0.03	0
2-tirtiary butyl phenol	6.49	8.25	12.76	3.97	1.50
4-tirtiary butyl phenol	4.38	5.83	8.19	4.46	4.37
2,6-ditirtiary butyl phenol	0.17	0.13	0.48	0.12	0
2,4-ditirtiary butyl phenol	2.08	1.41	7.49	1.59	0.34
Others	0.08	0.06	0.25	0.04	0.08
Phenol conversion	13.40	15.92	29.62	10.34	6.37
2-TBP selectivity	48.43	51.82	43.08	38.39	23.55
4-TBP selectivity	32.69	36.62	27.65	43.13	68.60
2,4-DTBP selectivity	15.52	8.86	25.29	15.38	5.34
Total ortho selectivity	49.70	52.64	44.70	39.45	23.55

The important observations are:

(1) Cu rich samples show high phenol conversion than Co rich samples. Phenol conversion increases from x=0 to x=0.5 and then decreases with further increase of x.

(2) 2-TBP selectivity decreases as the Co content increases whereas reverse is true for 4 TBP selectivity.

(3) Among various compositions x = 0.50 shows maximum activity towards 2,4-DTBP formation.

SECTION II

3.7. INTRODUCTION

IR technique is ideally suitable for investigating the nature of adsorbed surface intermediates on the oxide surface during catalytic reactions. The spectra of adsorbed species can provide information about the chemistry occurring on the surface. In the following we have attempted to study the adsorption behavior of phenol, methanol, mixture of phenol and methanol, formic acid and various methylated phenols separately to get an insight on the mechanism of phenol methylation on the surface of $Cu_{1-x}Co_xFe_2O_4$. FTIR of above adsorbed molecules was recorded in drift mode and the experimental procedure is as described in chapter 2 (Section 2.4.2).

3.8. RESULTS

3.8.1. Adsorption of methanol

The IR spectra of methanol adsorbed at different temperatures on three selected compositions x = 0, 0.50 and 1 were recorded in the region 1000-1800 cm^{-1} and 2700-3100 cm^{-1} are shown in Figure 3.15 and Figure 3.16, respectively.
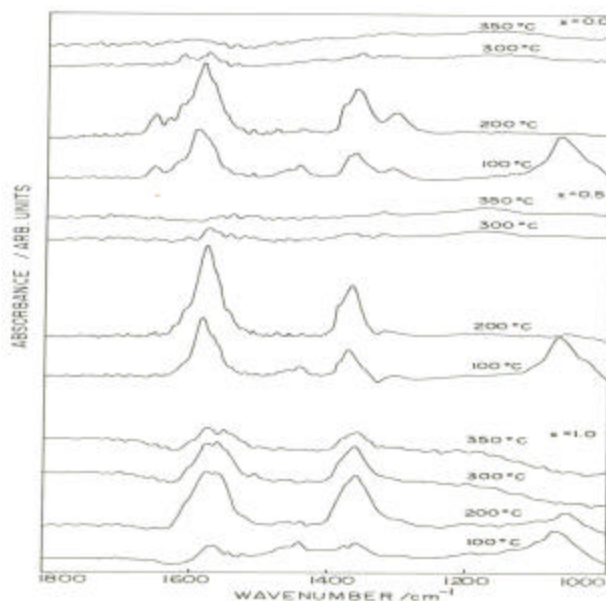
Figure 3.15: FTIR spectra of methanol adsorbed on $Cu_{1-x}Co_xFe_2O_4$ for three selected compositions x = 0.0, 0.50 and 1.0 in the range 1000-1800 cm^{-1} at different temperatures.
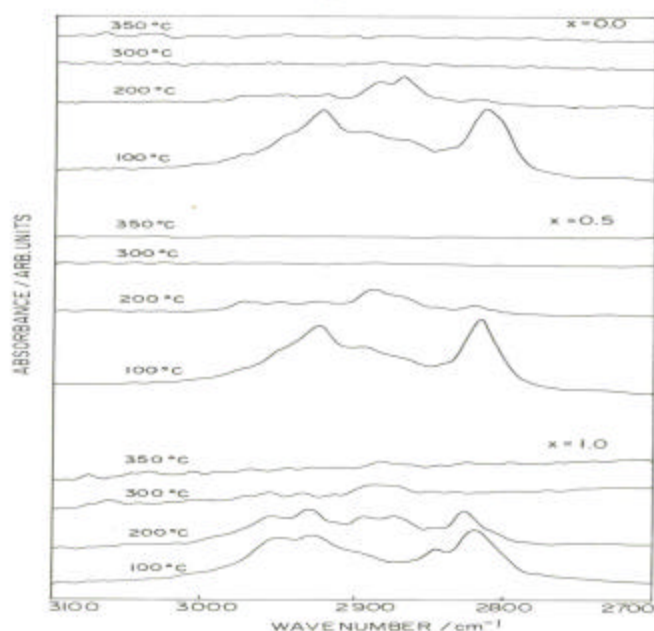
Figure 3.16: FTIR spectra of methanol adsorbed on $Cu_{1-x}Co_xFe_2O_4$ for three selected compositions $x = 0.0$, 0.50 and 1.0 in the range 2700-3100 cm^{-1} at different temperatures.

The spectra obtained from the chemisorption of methanol on $Cu_{1-x}Co_xFe_2O_4$ at $\leq 100^0C$ are composed of the superimposed spectra of surface methoxy and formate groups. Methanol adsorption causes strong absorption bands spread in the range 1020-1100 cm^{-1}, 1340-1390 cm^{-1}, 1550-1600 cm^{-1}, 2810-2850 cm^{-1} and 2915-2960 cm^{-1}. Bands approximately at 2950, 2924, 2816, 1460, 1440 and 1070 cm^{-1} characterize the surface methoxy groups [48-60]. The various bands and their assignments correspond to methoxy vibrations due to methanol adsorption on $x = 0$, 0.50 and 1 are summarized in Table 3.8 along with the literature data. The bands due to methoxy vibration observed at ~2950 cm^{-1} (ν_s CH$_3$) and at 2816 ($2\delta s$ (CH$_3$)) are in fermi resonance with each other [49]. The presence of adsorbed methoxy species during methanol oxidation is also indicated by C-O stretching mode at 1070 cm^{-1} [49-52]. Other low frequency –OCH$_3$ modes include symmetric and asymmetric methyl bends at ~ 1440 cm^{-1} and ~ 1460 cm^{-1}, appear as low intense shoulders.

Table 3.8: Bands corresponding to methoxy species obtained from the FTIR adsorption of methanol on $Cu_{1-x}Co_xFe_2O_4$ and variety of supports (from literature).

Assignment	Methanol gas (ref. 58, 72)	Al_2O_3 (ref. 51)	V-Ti-O (ref. 60)	TiO_2 (ref. 49)	Fe_2O_3 (ref. 48)	Present study		
						x = 0.0	x = 0.50	x = 1.0
ν_{as} (CH₃)	2962	2970	2965	2965		2950	2948	2949
ν_s (CH₃)		2955	2935	2930	2920	2924	2924	2926
$2\delta_s$ (CH₃)	2844	2844	2830	2830	2815	2816	2816	2818
δ_{as} (CH₃)	1455	1472	1452	1462	1460	1460	1456	1460
δ_s (CH₃)		1458	1438	1436	1440	1443	1441	1440
r (CH₃)	1150	1200	1150	1151				
ν (CO)	1034	1095	<1080	1125		1069	1067	1072
δ (COH)	1340		1370	1370				

Vibrations due to formate species are observed at 2975, 2890, 2867, 1580, 1375 and 1365 cm^{-1} [48-60]. All these bands are well assigned and in good correspondence with the literature values, summarized in Table 3.9.

Table 3.9: Bands corresponding to formate species obtained from the FTIR adsorption of methanol on $Cu_{1-x}Co_xFe_2O_4$ and different supports (from literature).

Assignment	$ZnAl_2O_4$ (ref. 69)	ZnO (ref. 69)	V-Ti-O (ref. 60)	TiO_2 (ref. 49)	Fe_2O_3 (ref. 48)	Present study		
						x = 0.0	x = 0.50	x = 1.0
ν_{as} (COO⁻) + δ (CH)	2970	2960	2972	2970, 2950		2976	2976	2975
ν (CH)	2900	2882	2883	2885, 2870	2880	2887, 2868	2889, 2867	2891, 2873
ν_s (COO⁻) + δ (CH)	2770	2740						
δ_{as} (COO⁻)	1590	1580	1565, 1540	1575, 1560	1555	1583	1585	1575, 1562
δ (CH)	1395	1382	1378	1390, 1380	1376	1375	1378	1377
ν_s (COO⁻)	1375	1365	1370, 1358	1372, 1360	1348	1364	1367	1357

The band observed at 2975 cm^{-1} is due to the fermi resonance vibration of both asymmetric COO$^-$ stretching and CH deformation [49]. Separate adsorption of formic acid on x = 0.5 enables the differentiation of formate and methoxy species formed on the surface of these oxides. Adsorption of HCOOH on x = 0.5 display bands at 2974, 2877, 1576, 1373 and 1365 cm^{-1} (Figure 3.17).
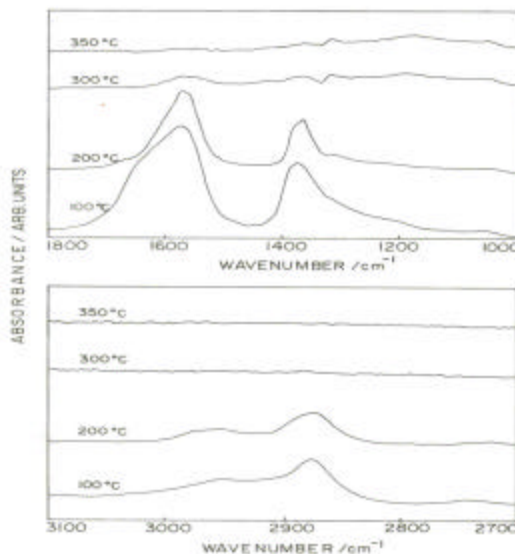
Figure 3.17: FTIR spectra of formic acid adsorbed on Cu$_{0.50}$Co$_{0.50}$Fe$_2$O$_4$ at different temperatures.

These species can readily be identified as formate ions, assigning the maximum of 2877, 1576, 1376 and 1365 cm^{-1} respectively to C-H stretching, COO$^-$ asymmetric stretching, C-H deformation and COO$^-$ symmetric stretching vibrations [48-50]. Surface formates were already detected after adsorption of formic acid on Fe$_2$O$_3$ [48,53], using IR reflectance spectroscopy, as well as on a number of other oxides by different research groups [49,54-57]. Thus the spectroscopic features of formate species produced by adsorption of formic acid are quite similar to those detected after oxidation of methanol.

In addition to the above, comparatively strong bands are observed at 1645 and 1309 cm^{-1} on x = 0, that may be assigned to adsorbed formaldehyde [48,50]. These bands persist even at high temperature and whose intensity increases from 100^{0}C to 200^{0}C and thereafter decreases at > 200^{0}C. However as the 'x' increases, the intensity of these bands decreases considerably. A weak band observed at 1622 cm^{-1} (on Cu containing samples)

can be assigned to a species coordinatively bonded through the carbonyl oxygen to Lewis acid sites [48].

Heat treatments under N_2 atmosphere and above 100^0C cause considerable decrease in intensity of the bands associated with methoxy species; however, the species responsible for formate grows in intensity (Figures 3.15 and 3.16). Thus, the absorbances appear as high intense peaks at 2950 cm^{-1}, 2923 cm^{-1} and 1067 cm^{-1} have become low intense peaks as the temperature increases to 200^0C. On the other hand, the bands appear as low intense peaks at 100^0C at 2976, 2887, 2868, 1645, 1583, 1375 and 1364 cm^{-1} have become high intense peaks with minor changes in their positions as the temperature increases. These bands correspond to those, which appear after adsorption of formic acid on the same surface and can be assigned to surface formate ions obtained by oxidation of methoxy groups. Similar observations have already been detected on various metal oxides such as Fe_2O_3 [48], TiO_2 [49,52], SnO_2 [57], ZrO_2 [59], V_2O_5 [59,60], Cr_2O_3 [61] etc. However the shifts observed on $Cu_{1-x}Co_xFe_2O_4$ in comparison with the single component oxides are significant enough to conclude that species formed on $Cu_{1-x}Co_xFe_2O_4$ are indeed characteristic of a mixed phase and not due to the adsorption on one component, CuO, CoO or Fe_2O_3. Further increase in temperature causes splitting as well as reduction in intensity of several bands indicate the adsorbed methanol species are unstable on the surface.

The adsorption behavior of methanol over $Cu_{1-x}Co_xFe_2O_4$ shows slight differences between Cu containing samples and pure $CoFe_2O_4$. The important difference between x = 1 and Cu containing compositions towards methanol adsorption are:

(1) The amount of methanol adsorbed at 100^0C (in terms of intensity) on x =1 is relatively low in comparison with Cu containing samples indicates comparatively high temperature is needed for the activation of methanol on x = 1.

(2) The concentration of methoxy species is high and it persists even at 300^0C on x = 1 where as on Cu containing samples, methoxy species are quite unstable and it is evident from the very low concentration of these species even at 200^0C. Parallel to this the concentration of formate species increased to considerable extent at this temperature. This clearly shows methanol is highly susceptible to oxidation on Cu containing samples. For

example on $CoFe_2O_4$, irreversible adsorption of CH_3OH at 100^0C led to two sharp bands at 2949 cm^{-1} and 2926 cm^{-1} characteristic of methoxy species, whereas on Cu containing samples band due to 2949 cm^{-1} appear only as a shoulder. Also the band due to C-O stretching of methoxy group persists even at 200^0C on x = 1, whereas it is completely disappeared on Cu containing samples from 100^0C to 200^0C.

(3) Both methoxy and formate species have stable existence on x = 1 even at 350^0C; whereas both these species are hardly found on Cu containing samples even at 300^0C, indicates methanol is completely reacted on Cu containing surfaces to CO_2, CO and H_2.

All these bands are in good correspondence with the bands arised due to methanol adsorption, thus confirming formate species are the intermediate before converting to CO_2, CO and H_2.

3.8.2. Adsorption of phenol

FTIR spectra of phenol adsorbed on $Cu_{1-x}Co_xFe_2O_4$ samples were recorded between 100^0C and 350^0C. The results for three selected compositions, x = 0, 0.50 and 1 are shown in Figures 3.18 and 3.19.
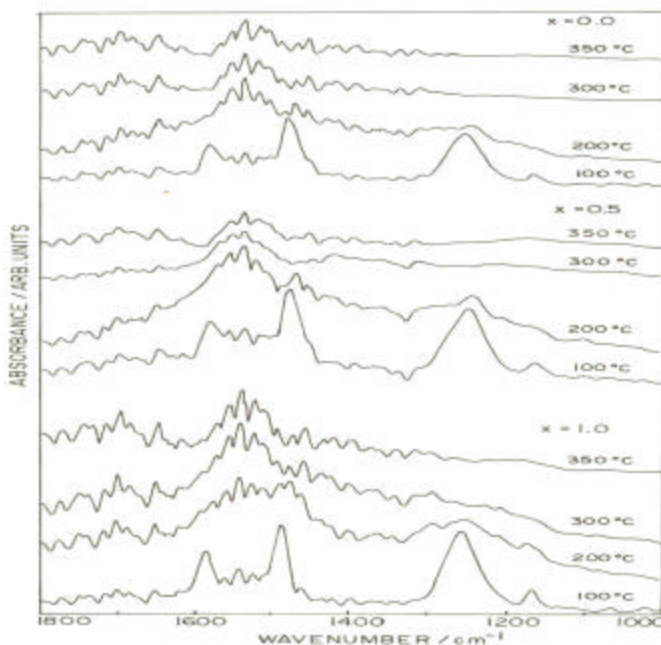
Figure 3.18: FTIR spectra of phenol in the region of aromatic ring vibrations adsorbed on $Cu_{1-x}Co_xFe_2O_4$ for three selected compositions x = 0.0, 0.5 and 1.0 at different temperatures.
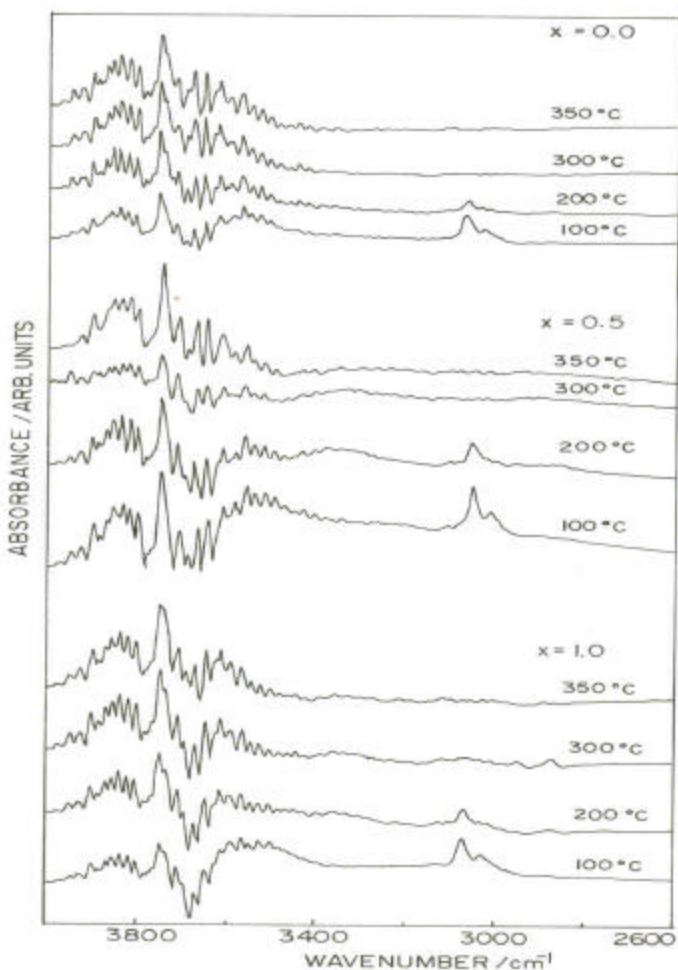
Figure 3.19: FTIR spectra of phenol in the region of C-H and O-H stretching vibrations adsorbed on $Cu_{1-x}Co_xFe_2O_4$ for three selected compositions x = 0.0, 0.5 and 1.0 at different temperatures.

IR adsorption of phenol resulted strong adsorption bands at 1587 cm^{-1}, 1485 cm^{-1} and 1256 cm^{-1}. In addition, there is a series of bands in the range 1000-1800 cm^{-1}, which are approximately spaced by 20 cm^{-1}. Among these minor components, peaks at 1775, 1745, 1700, 1650, 1540, 1460, 1396, 1370 and 1165 cm^{-1} are quite evidenced.

The band at 1587 and its shoulder at 1595 cm^{-1} can be assigned to the 8a and 8b deformation vibration of the aromatic ring [62-63]. These bands are slightly displaced to lower wavenumbers as compared with phenol in CCl$_4$ solution where they occur at 1596 and 1604 cm^{-1} [63]. The single broad intense band occurred at 1485 cm^{-1} is resolved into two components at higher temperatures having peak value at 1475 and 1485 cm^{-1} are

ascribed to normal modes 19a and 19b of the ring. The intensive broad absorption band at 1255 cm^{-1} is due to C-O stretching vibration. The low intense broad bands having components at 1360 and 1375 cm^{-1} and the broad band at 1396 cm^{-1} are mainly attributed to the in-plane C-O-H bending vibration of phenol. The presence of series of bands in the region 1650-1800 cm^{-1} is an indication of its perpendicular orientation of phenol over these oxides as reported in the literature [64]. The spectrum in the C-H stretching region depicted in Figure 3.19 shows absorption maxima at 3068, 3028 and 2943 cm^{-1} is typical of the C-H stretching vibration of the aromatic ring of phenol.

Figures 3.18 and 3.19 shows the effect of thermal treatment in N$_2$ flow on the IR spectrum of phenol adsorbed on x=0, 0.5 and 1. Heating to 200^{0}C and high temperatures leads to depletion of band intensity of main peaks at 1587, 1485, 1255 cm^{-1}. All these three bands looking single and quite broad at 100^{0}C are resolved into several components as the temperature increases to 200^{0}C and higher. The band at 1587 cm^{-1} is shifted to 1575 cm^{-1} and the shoulder associated with this band is well resolved at 200^{0}C and appear at 1590 cm^{-1}. The band observed at 1485 cm^{-1} at 100^{0}C is an apparent single component, started splitting at 200^{0}C into two components at 1475 cm^{-1} and 1485cm^{-1}. As the sample is further heated to 300^{0}C, the band at 1485 cm^{-1} disappears and the components corresponding to 1475 cm^{-1} and 1485 cm^{-1} grow as separate peaks.

The broad band at 1255 cm^{-1} corresponding to ν_{C-O} vibration is clearly split in to lower and higher frequency components whose bands occur at 1207, 1251, 1260 and 1294 cm^{-1}. This clearly indicates, phenol on Cu$_{1-x}$Co$_x$Fe$_2$O$_4$ results different phenolic species. The appearance of C-O stretching bands at 1270 and 1294 cm^{-1} after heating to 200^{0}C is indicative of deprotonated phenol, in which the C-O bond is further strengthened. A high frequency shift of the ν_{C-O} vibration to 1270 cm^{-1} has been reported for phenolate in basic aqueous solution [65,66]. However increase in temperature causes rise in intensity among peaks at 1541, 1521, 1651, 1701 and 1370 cm^{-1}. The H$^+$ ion thus deprotonated from phenol is adsorbed on nearby oxygen atom and appear as surface hydroxy groups as evidenced from Figure 3.19.

3.8.3. Adsorption of Anisole

In the Figure 3.20, spectra of anisole on x = 0.5 is given at different temperatures, as difference spectra from anisole adsorbed and pure compound. In the region of ring vibrations prominent peaks are observed at 1600 and 1496 cm^{-1}. Corresponding peaks for liquid anisole are at 1601 and 1498 cm^{-1}, which shows that adsorbed anisole is less strongly bonded on the surface of x = 0.5. The major peak observed at 1247 cm^{-1} is ν_{C-O} vibration. In addition to this, several minor features are observed at 1570, 1550, 1530, 1460, 1309, 1180, 1076 and 1041 cm^{-1}. No bands are detected in the range 1650-1800 cm^{-1} neglects the perpendicular orientation of benzene ring. Bands at 3062 cm^{-1} and 3010 cm^{-1} are due to C-H stretching of the aromatic ring of the phenol molecule. Additionally, vibrations due to CH$_3$ group of anisole are observed at 2952, 2922 and 2837 cm^{-1}.
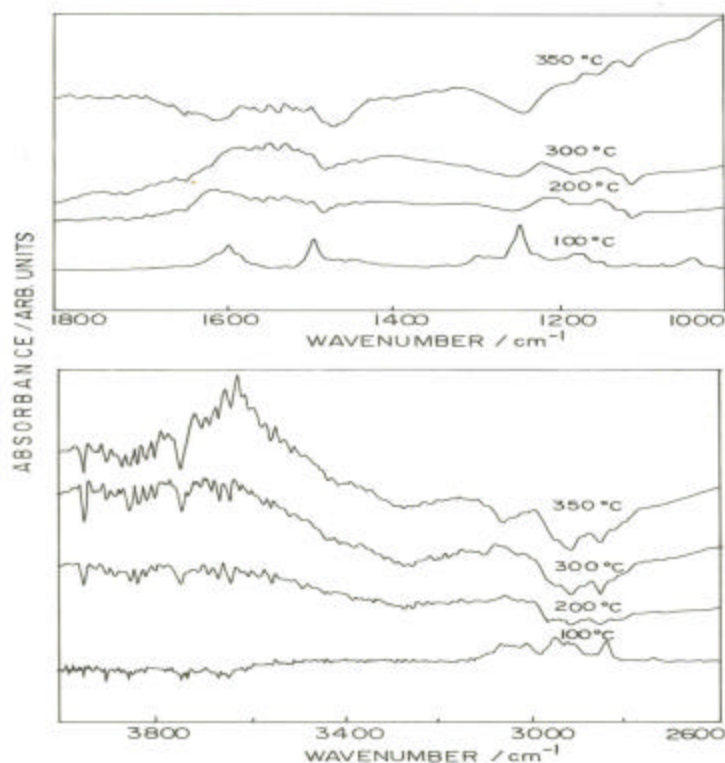
Figure 3.20: FTIR spectra of anisole adsorbed on x = 0.50 at different temperatures. Top panel represents the spectra in the region of aromatic vibrations. Bottom panel represents aromatic C-H and O-H stretching and CH$_3$ vibrations.

Figure 3.20 also shows the effect of temperature for the adsorption of anisole on x = 0.5. On varying the temperature of adsorption from 100^0C to 200^0C, some minor variation of these peaks are observed, which imply that interaction of anisole to surface of oxide is not only through π electrons of the aromatic ring but through oxygen lone pair electrons also. High temperature causes shift of bands as well as negative bands confirm its weak interaction with the surface and desorb fast from the surface as the temperature increases.

3.8.4. Adsorption of o-cresol

In the region of aromatic ring stretching vibrations, o-cresol adsorbed on $Cu_{1-x}Co_xFe_2O_4$ at 100, 200, 300 and 350^0C are presented in Figure 3.21.
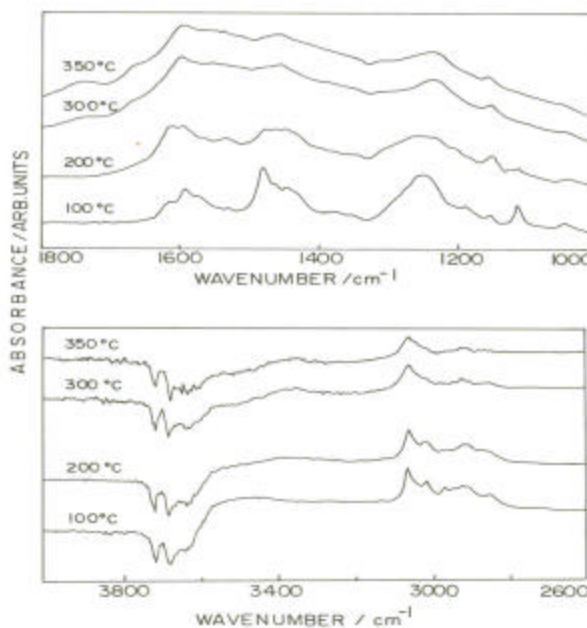
Figure 3.21: FTIR spectra of o-cresol adsorbed on $Cu_{1-x}Co_xFe_2O_4$ at different temperatures. Top panel represents the spectra in the region of aromatic vibrations. Bottom panel represents aromatic C-H and O-H stretching and CH_3 vibrations.

Spectra are almost similar to those of adsorbed phenol with some minor changes. The spectra show major bands at around 1615, 1593, 1483 and 1450 cm^{-1} due to aromatic ring

vibrations.   However the intensity of above peaks due to aromatic vibrations are quite low in comparison with phenol indicate its comparatively lower interaction with catalyst surface. The broad band observed at 1248 cm^{-1} is due to the stretching vibration of C-O bond.   The low intense band observed at 1379 cm^{-1} is due to the symmetrical bending mode vibration of CH_3 group.   Unlike phenol, adsorption of o-cresol on x = 0.50 didn't produce any bands in the range 1650-1800 cm^{-1}.   However, at 300^{0}C a new band develops at 1744 cm^{-1}.   All these observations lead to a conclusion that the benzene ring of o-cresol is slightly tilted towards the surface.   The bands observed at 2965, 2925, 2860 and 2730 is attributed to the various vibrations of –CH_3 group of o-cresol.

Increase in temperature causes simultaneous depletion of all bands clearly indicate the orientation of o-cresol on the surfaces of these oxides is more or less same irrespective of the temperature.   Also it indicates combined interaction of π electrons of aromatic ring and lone pair of electrons of OH side chain.   However the intensity of C-O bond is slightly higher than the intensity of various aromatic ring vibrations.   This indicates the interaction of o-cresol on the surface is mainly through OH side chain.   Though the intensity decreases as the temperature increases, majority of the bands persist even at 350^{0}C suggest o-cresol also is reasonably well bound to the surface.

3.8.5. Adsorption of 2,6 – xylenol

The IR spectrum of 2,6-xylenol adsorbed on x = 0.50 at different temperatures is shown in Figure 3.22.   Adsorption of 2,6-xylenol on x = 0.5 produces major peaks in the aromatic region at around 1615, 1573, 1483 and 1450 cm^{-1}.   The band produced at 1483 and 1450 cm^{-1} can be attributed to the aromatic ring stretching vibrations ν_{13a}, ν_{13b} respectively.   The band at 1371 cm^{-1} is prominent in this case compared to o-cresol. This is due to the symmetric bending vibration mode of CH_3 group.   Unlike phenol and o-cresol the intensity of band due to ν_{C-O} stretching is decreased considerably and observed at 1242 cm^{-1}.   Again, the intensity of 1615, 1573 and 1371 cm^{-1} bands increased very much.   These results can be understood, considering that 2,6-xylenol interacts on the surface mainly through aromatic ring and its orientation is almost parallel to the surface.   Its interaction through C-O is comparatively less on the surface.   Irrespective of temperature, no bands

are observed in the range 1650-1800 cm^{-1} suggests the benzene ring of xylenol is highly parallel to the catalyst surface than o-cresol. This might be due to the steric hindrance of two methyl groups forces the benzene ring to orient parallel to the oxide surface. The bands due to –CH$_3$ groups appear at 2960, 2954, 2870 and 2733 cm^{-1}. Moreover the intensity of 2870 cm^{-1} is higher than that of due to the CH$_3$ group of o-cresol.
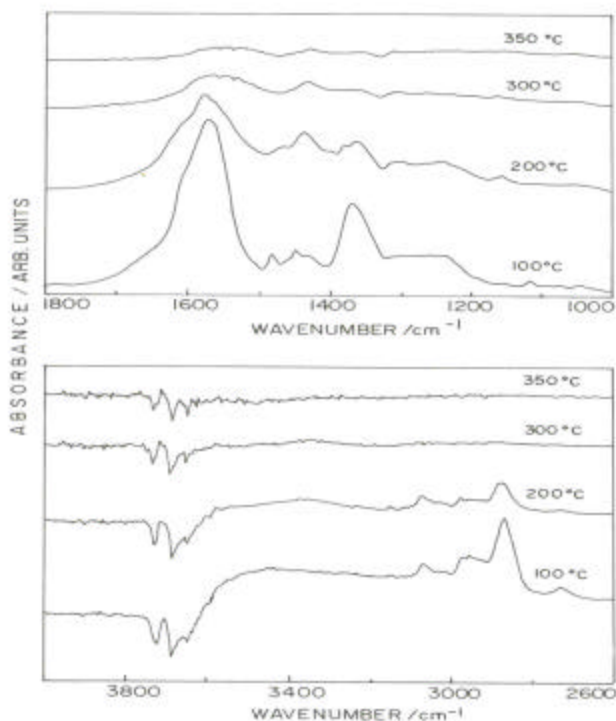
Figure 3.22: FTIR spectra of 2,6-xylenol adsorbed on x = 0.50 at different temperatures. Top panel represents the spectra in the region of aromatic vibrations. Bottom panel represents aromatic C-H and O-H stretching and CH$_3$ vibrations.

Increase in temperature causes reduction of band intensity of all peaks indicates its interaction with surface decreases rapidly as the temperature increases. Thus, 2,6-xylenol desorbs quite fast from the surface as temperature increases. Increase in temperature does not cause any change in peak position of C-O stretching vibration confirming its negligible interaction with the surface. However it causes change of peak position for vibrations due to both aromatic stretching and CH$_3$ stretching. This again confirms the interaction of 2,6-

xylenol on the surface is mainly through aromatic π electrons and hence its orientation is more or less parallel with respect to the surface. Unlike phenol and o-cresol, the intensity of various bands arised due to 2,6-xylenol adsorption decreases considerably above 300^0C. This indicates 2,6-xylenol desorbs fast as the temperature increases. The IR observations of o-cresol and 2,6-xylenol clearly hints longer residence time of the former leads to second methylation and leads to the latter and its subsequent fast desorption at reaction temperatures.

3.8.6. Coadsorption of phenol and methanol

Figure 3.23 demonstrates IR spectrum of phenol coadsorbed with methanol. It was obtained after adsorption of phenol and methanol (using phenol:methanol mole ratio 1:5) at 100^0C and subsequent heating to 350^0C.

Figure 3.23: FTIR spectra of phenol and methanol coadsorbed on $Cu_{1-x}Co_xFe_2O_4$ at different temperatures (phenol:methanol = 1:5 mole ratio is used for coadsorption).

Apparently, the decomposition as well as oxidation of methanol is retarded in the presence of phenol. Remarkably, the intensity of C-O stretching bands of methoxy moiety at 1067 cm^{-1} is significantly decreased when methanol was heated in the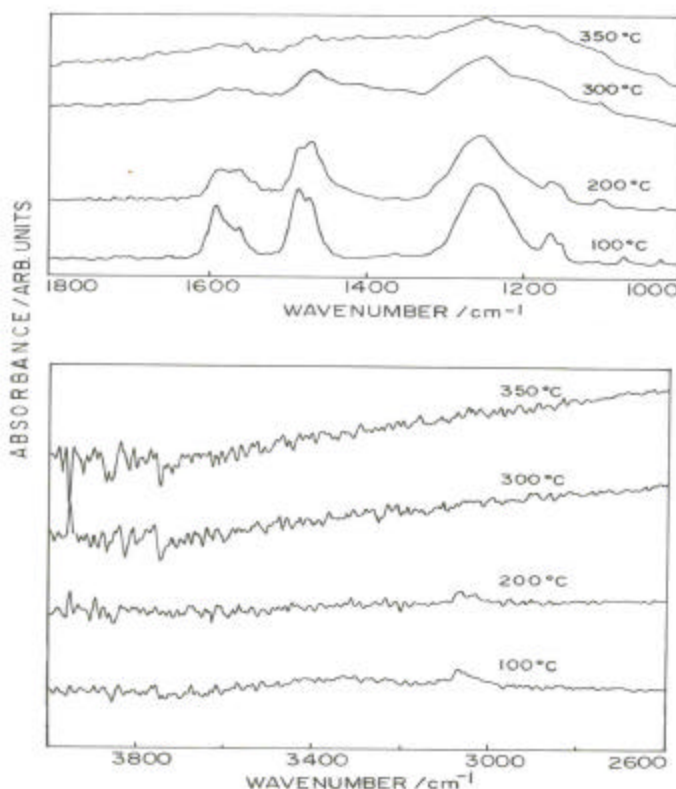 presence of phenol. The aromatic ring vibration of phenol at 1585 cm^{-1} is shifted to 1591 cm^{-1} and exhibits a shoulder at 1570 cm^{-1}. The narrow band at 1481 cm^{-1} observed on phenol adsorption is shifted to 1487 cm^{-1} and overlapped with an additional band at 1472 cm^{-1}. Above four bands are characteristic bands of o-cresol and 2,6-xylenol. It is important to note that the bands due to formate species observed at 1580, 1375 and 1365 cm^{-1} when methanol was sole reagent is either lost or decreased in intensity when methanol is coadsorbed with phenol. Another important change to be noted is that the methyl vibrations observed at 2950, 2924 and 2816 cm^{-1} is lost when methanol is in coadsorbed state.

Number of bands disappeared in the phenolic region when phenol is coadsorbed with methanol in contrast to adsorption of phenol alone. Additionally a number of bands observed in the C-H region of aromatic at 3114, 3099, 3070, 3051, 3033 and 3026 cm^{-1}. This hints coadsorption leads to some sort of interaction between phenol and methanol. The bands exhibited on phenol adsorption in the range 1650-1800 cm^{-1} is disappeared when phenol is coadsorbed with methanol. This behavior is similar to the behavior exhibited by o-cresol and 2,6-xylenol.

As the temperature increases from 100^{0}C, the band at 1591 cm^{-1} is shifted to 1585 cm^{-1}. The band at 1560 cm^{-1} appear as a shoulder along with the band at 1591 cm^{-1} grows in intensity as the temperature increases to 200^{0}C and is slightly split from the main band. The two separated bands observed at 1487 cm^{-1} and 1471 cm^{-1} at 100^{0}C decrease in intensity and merge together (whose center is at 1465 cm^{-1}) as the temperature increases to 300^{0}C. The broad band at 1253 cm^{-1} at 100^{0}C further broadens when the temperature increases. Above 300^{0}C, the intensity of various bands decreases considerably indicates the products formed during the reaction desorbs fast. This behavior is similar to that exhibited by either o-cresol or 2,6-xylenol.

3.9. DISCUSSION

3.9.1. Reactivity of methanol

A comparison of the IR spectrum of pure $Cu_{1-x}Co_xFe_2O_4$ with that of the same oxide adsorbed with either CH_3OH or $HCOOH$ indicates methoxylation as well as oxidation of methanol occur on these oxides. Methoxy species are observed at 100^0C along with the oxidation products of methanol. Two most likely mechanisms are proposed for methoxy formation on the surface of oxides:

(i) esterification

$$MOH \quad + \quad CH_3OH \quad \longrightarrow \quad MOCH_3 \quad + \quad H_2O$$
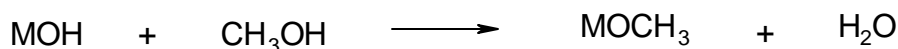
(ii) dissociative chemisorption
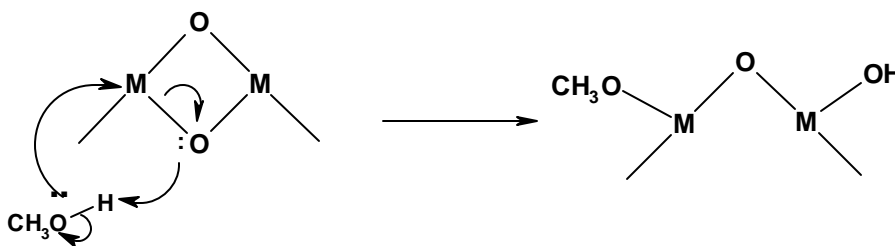
In the present system, only trace amount of Bronsted acid sites are observed during pyridine adsorption and no molecular water is produced during the methanol chemisorption process. This suggests the most likely mechanism is dissociative chemisorption. A similar type of mechanism has been proposed for the formation of methoxy groups on MgO [67] and SnO [57]. This again is confirmed from the formation of series of surface hydroxy groups with change in band position on the surface of these oxides during methanol adsorption. However these bands are quite broad indicating the H bond interaction of surface methoxy group with neighboring OH group.

Above 100^0C methoxylated oxide surfaces are progressively converted to formate species indicate, irrespective of the composition, all these oxides are highly reactive towards methanol. Moreover such formate species were not thermally very stable and even at 300^0C it transform into CO_2, CO, as Kotanigawa reported on $ZnFe_2O_4$ [68]. Formate

concentration in the case of Cu containing samples is higher than that on $CoFe_2O_4$ indicating the presence of Cu has a promoting role in their formation. The promoting action of Cu on methanol decomposition has been reported in the literature [69]. However it is very difficult to detect bands due to methanol adsorption on Cu ions of such a complex catalyst system. The only conclusion that can be drawn is a decrease in the thermal stability of methoxy and formate species adsorbed on Cu containing ferrites due to the presence of Cu^{2+} ion. Though all the compositions show general trend towards methanol adsorption, the methoxy and formate species formed on x = 1 is quite stable even at 350^0C suggest methanol seems to be activated only at high temperature.

3.9.2. Reactivity of phenol and phenolic products

IR adsorption of phenol on $Cu_{1-x}Co_xFe_2O_4$ shows signals of both undissociated phenol and phenolate like species. Phenolate species are formed due to the dissociative adsorption of phenol on an acid-base pair site. Phenolate ion is adsorbed on metal cation (Lewis acid site) where as the dissociated H adsorbs as a H^+ on a nearby O atom. Thus a series of O-H bands are formed in the region 3500-3800 cm^{-1} (shown in Figure 3.19).

Examination of bands in the region 1600-1800 cm^{-1} for phenol and methylated phenol reveals a number of low intensity out of plane combination bands [64] at 1650, 1700, 1745 and 1775 cm^{-1} for phenol; however these bands are either hardly detected, or the intensity is small on methylated phenols. Also these bands are practically disappeared for the phenol in the coadsorbed state with methanol. Karagounes and coworkers [70,71] have interpreted a decrease in the intensity of out of plane C-H vibrations of chemisorbed aromatic molecules to indicate that these molecules are adsorbed with the plane of the aromatic ring parallel to the adsorbent surface. Applying a similar interpretation to the above observations leads to the conclusion that the chemisorbed phenol molecule is adsorbed through O atom to the Lewis acid site whose aromatic ring is almost perpendicular to the plane of the oxide. On the other hand, situation is quite different in the case of co-adsorption of phenol and methanol. Methanol is adsorbed onto the protons released by phenol, which in turn interact to the ortho position of the phenolic oxygen. This interaction govern the orientation of aromatic ring of phenol and from the absence of

bands in the IR spectrum in the range 1650-1800 cm^{-1}, it is possible to suggests that, aromatic ring of phenol tilts slightly toward the surface while interacting with methanol. This is again confirmed from the adsorption state of methylated products of phenol such as o-cresol, anisole and 2,6-xylenol. In all these cases, the chemisorbed phenol molecule also has its benzene ring more or less coplanar with the surface such that interaction with the surface results in a lack of bands in the region 1650-1800 cm^{-1}. Though the phenolic ring is more or less coplanar, it is tilted upward such that the para position is more removed from the surface than the ortho.

The C-O stretching band for chemisorbed methyl phenols found in a relatively wide region between 1220-1320 cm^{-1} in comparison with phenolic C-O stretching band. Same inference can be made from phenol in the presence of methanol where it is found that the nature and appearance of C-O band is similar to that observed in the case of o-cresol. Moreover, as the methyl group increases the intensity of C-O stretching band decreases, which indicates the interaction through phenolic oxygen to the surface decreases from phenol to o-cresol to 2,6-xylenol. Thus it is highly plausible that the aromatic ring of these phenolic compounds have become more parallel, but tilted upward as the number of methyl groups increases. Also as the temperature increases the intensity of various bands decreases tremendously as goes from phenol to o-cresol to 2,6-xylenol. Above details leads to a conclusion that the methylated phenols have got weak interaction with the surface and are highly susceptible to desorb from the surface as the temperature increases. This is an essential requisite for achieving efficient methylation. However for x=1, it requires relatively high temperature than the Cu containing samples. Kinetic data also leads to the same conclusion and it is found that unlike Cu compounds, CoFe$_2$O$_4$ shows maximum conversion and selectivity at 375^{0}C where as for other compounds it is at 350^{0}C.

3.9.3. Mechanism of phenol methylation

IR studies clearly showed that surface bound alkoxides or strongly polarized O-H bands were formed when methanol is adsorbed to Cu$_{1-x}$Co$_x$Fe$_2$O$_4$. Similarly phenol is dissociatively adsorbed on nearby acid base pair site as phenoxide ion and proton. The dissociated proton has a governing role on the fate of methanol molecule, which facilitates

the formation of carbocation quite easily by protonating methanol. Thus the chemisorption of phenol on the oxides undoubtedly facilitates the protonation of methanol. It has been reported that methylation of phenol is initiated by the protonation of methanol with the aid of a Lewis acid base pair [68]. Probably the protonation of methanol occurs on the oxides by accepting protons released from the adsorbed phenol and the protonated methanol attacks at the ortho position of phenol to form the ortho methylated products.

There are two potential sites for methanol adsorption: OH groups and Lewis acid base center. Since the hydroxy group of present catalyst system are incapable of protonating even such strong bases like pyridine, it is improbable that they could not interact with methanol, being a weaker base. Hence, Lewis acid-base sites are the most probable sites for methanol chemisorption on $Cu_{1-x}Co_xFe_2O_4$. This is true when methanol is a sole reagent. However the situation is quite different when methanol co-adsorbs with phenol. Both reactants may adsorb competitively on the same active center. Since phenol is capable of releasing its proton faster, it comparatively adsorb on nearby acid-base pair site. Since the protons released from phenol is quite mobile is capable of protonating methyl molecule leading to $CH_3^{\delta+}$ cation (Figure 3.24). Thus the methanol molecule is directed to adsorb on H^+ released from phenol rather than on already existing surface hydroxy group for causing methylation. Thus the active center for the ortho methylation is an acid-base pair site.
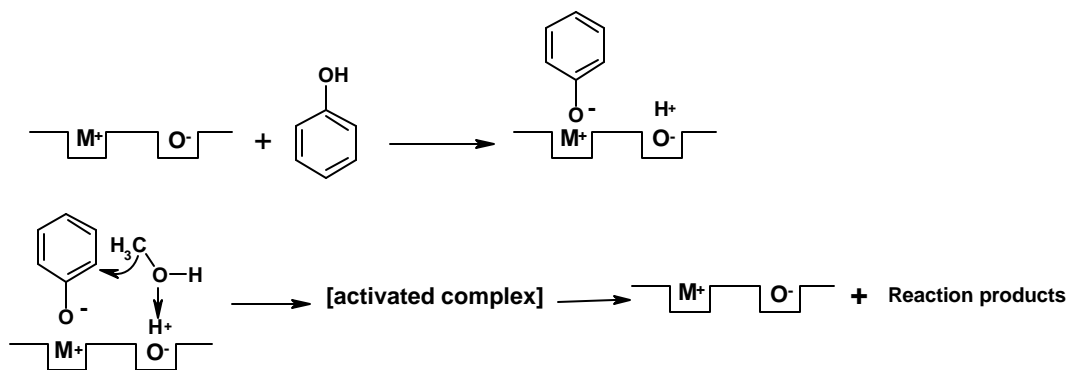
Figure 3.24: Mechanism of phenol methylation.

C-alkylation can take place either by a direct route or by the isomerization of O-alkylation product. To decide between these two routes, anisole were passed over the catalyst under optimum condition. No isomerized products were obtained. Thus these compounds do not have any activity for the transformation of anisole into o-cresol in the catalytic conversion of anisole at 350^0C. Therefore, they have no acidic sites that catalyze the methyl migration of anisole. It may be recalled that this is in contrast to the behavior of alumina, on which alkyl phenyl ethers undergo isomerization to C-alkyl phenols [19].

3.10. REFERENCES

1   H. Fiege, A. G. Bayer and Leverkusen, Federal Republic of Germany, in "*Ullmann's Encyclopedia of Industrial Chemistry*". *A19*, 324.

2   M. Inoue and S. Enomoto, *Chem. Pharm. Bull*., **24** (1976) 2199.

3   S. Patinuin and B. S. Friedman, in: *Alkylation of Aromatics with Alkenes and Alkanes in Friedel Crafts and Related Reactions*, Interscience, New York, G. A. Olah (ed.), **Vol. 3** (1964).

4   V. N. Ipatieff, N. Orloff and G. Razuvaeff, *Bull. Soc. Chim. Fr*., **37** (1925) 1576.

5   Ref. 107 and 133 of chapter 1

6   Perry's Chemical Engineers Handbook, 1984, 6th ed., New York, McGraw Hill.

7   J. M. Smith and H. C. Van Ness, 1987, *Introduction to chemical engineering thermodynamics*, 4th ed., New York, Mc Graw Hill.

8   R. C. Reid, J. M. Prausnitz and B. E. Poling, 1987, *The properties of gases and liquids*, 4th ed., New York, Mc Graw Hill.

9   D. R. Stull, E. F. Westrum and G. C. Sinke, G.C., 1969, *The chemical thermodynamics of organic compounds*, John Wiley & Sons, Inc. New York.

10   Y. Ono, *Catalysis Today*, **35** (1997) 15.

11   A. Bomben, M. Selva, P. Tundo and L. Valli, *Ind. Eng. Chem. Res*., **38** (1999) 2075.

12   T. M. Jyothi, T. Raja, M. B. Talwar, K. Sreekumar, S. Sugunan and B. S. Rao, *Synth. Commun*., **30** (2000) 3929 .

13   Y. Ono, *Appl. Catal. A*, **155** (1997) 133.

14   T. Beutel, *J. Chem. Soc., Faraday Trans*., **94** (1998) 985.

15   Z. Fu and Y. Ono, *Catal. Lett*., **21** (1993) 43.

16   F. M. Bautista, J. M. Campelo, A. Garcia, D. Luna, J. M. Marinas and A. A. Romero, *React. Kinet. Catal. Lett*., **63** (1998) 261.

17   F. M. Bautista, J. M. Campelo, A. Garcia, D. Luna, J. M. Marinas, A. A. Romero and M. R. Urbano, *React. Kinet. Catal. Lett*., **62** (1997) 47.

18   H. Saltonstall and Settle., *J. Am. Chem. Soc*. **71** (1949) 943.

19   M. Inoue and S. Emoto, *Chem. Pharm. Bull*. **20** (1972) 232.

20   R. Stroh, R. Seydel and W. Hahn, in "*Neuere Methoden der praparatively organischen chemie*", W. Foerst (ed.), Verlag Chemie, Weinheim **Vol. II** (1960) 231-246.

21   Z. P. Aleksandrova, *J. Gen. Chem. (U. S. S. R)*. **12** (1942) 522.

22   A. G. Bayer, EP 102 493, 1983.

23   S. Velu and C. S. Swamy, *Res. Chem. Intermed.*, **26** (2000) 295.

24   J. Das and A. B. Halgeri, *Appl. Catal. A.*, **194** (2000) 359.

25   P. B. Venuto, L. A. Hamilton, P. S. Candis and J. J. Wise, *J. Catal.*, **5** (1966) 81.

26   S. Karuppannasamy, K. Narayanan and C. N. Pillai, *J. Catal.*, **66** (1980) 281.

27   K. Li, I. Wang and K. Chang, *Ind. Eng. Chem. Res.*, **32** (1993)1007.

28   F. M. Bautista, J. M. Campelo, A. Garcia, D. Luna, J. M. Marinas, A. Romero, J. A. Navio and M. Macias, *Appl. Catal.*, **99** (1993)161.

29   E. Santacesaria, M. Diserio, P. Ciambelli, D. Gelosa and S. Carra, *Appl. Catal.* **64** (1990) 101.

30   S. Velu and C. S. Swamy, *Appl. Catal. A.*, **145** (1996) 225.

31   P. L. Yue and O. Olaofe, *Chem. Eng. Res. Des.*, **62** (1984) 167.

32   F. M. Bautista, J. M. Campelo, A. Garcia, D. Luna and J. M. Marinas, *J. Catal.*, **107** (1987) 181.

33   A. Corma, F. Llopis, J. B. Monton and S. Weller, *J. Catal.*, **142** (1993) 97.

34   A. B. Hart and R. A. Ross, *J. Catal.*, **2** (1963) 121 and 251.

35   S. V. Kannan and C. N. Pillai, *Indian J. Chem.*, **8** (1970) 1144.

36   L. H. Klemm and D. R. Taylor, *J. Org. Chem.*, **45** (1980) 4320, 4326.

37   B. Choudhri and M. M. Sharma, *Ind. Eng. Chem. Res.*, **30** (1991) 227.

38   S. Velu and C. S. Swamy, *Catal. Lett.*, **40** (1996) 265.

39   S. Sato, R. Takahashi, T. Sodesawa, K. Matsumoto and Y. Kamimura, *J. Catal.*, **184** (1999) 180.

40   A. Sakthivel, N. Saritha and P. selvam, *Catal. Lett.*, **72** (2001) 225.

41   K. G. Chandra and M. M. Sharma, *Catal. Lett.*, **19** (1993) 309.

42   R. A. Rajadhyakasha and D. D. Chaudhari, *Ind. Eng. Chem. Res.*, **26** (1987) 1276.

43   S. K. Badamali, A. Sakthivel and P. Selvam, *Catal. Lett.*, **65** (2000) 153.

44   K. Zhang, H. Zhang, G. Xu, S. Xiang, D. Xu, S. Liu and H. Li, *Appl. Catal. A.*, **207** (2001) 183.

45   S. K. Badamali, A. Sakthivel and P. Selvam, *Catal. Today.*, **63** (2000) 291.

46   S. Subramanian, A. Mitra, C. V. V. Satyanarayana and D. K. Chakrabarty, *Appl. Catal. A.*, **159** (1997) 229.

47   K. Zhang, C. Huang, S. Xiang, S. Liu, D. Xu and H. Li, *Appl. Catal. A.*, **166** (1998) 89.

48   G. Busca and V. Lorenzelli, *J. Catal.*, **66** (1980) 155.

49   G. Busca, A. S. Elmi and P. Forzatti, *J. Phys. Chem.*, **91** (1987) 5263.

50   K. Nakamoto, "*Infrared Spectra of Inorganic and Coordination Compounds*", p. 199. Wiley, New York, 1963.

51   G. Busca, P. F. Rossi, V. Lorenzelli, M. Benaissa, J. Travert and J. C. Lavalley, *J. Phys. Chem.*, **89** (1985) 5433.

52   G. Busca, P. Forzatti, J. C. Lavalley and E. Tronconi, In "*Catalysis by Acids and Bases*", B. Imelik etal., Eds.; Elsevier: Amsterdam, p.14 (1985).

53   N. Takezawa, *J. Chem. Soc. Chem. Commun.*, 1451 (1971).

54   Y. Noto, K. Fukuda, T. Onishi and K. Tamaru, *Trans. Faraday Soc.*, **63** (1967) 2300.

55   A. Ueno, T. Onishi and K. Tamaru, *Trans. Faraday Soc.*, **66** (1970) 756.

56   G. Munuera, *J. Catal.*, **18** (1970) 19.

57   E. W. Thornton and P. G. Harrison, *J. Chem. Soc. Faraday Trans. I*, **71** (1975) 2468.

58   M. A. Natal-Santiago and J. A. Dumesic, *J. Catal.*, **175** (1998) 252.

59   L. J. Burcham and I. E. Wachs, *Catal. Today*, **49** (1999) 467.

60   L. J. Burcham, G. Deo, X. Gao and I. E. Wachs, *Top. Catal.*, **11/12(1-4)** (2000) 85.

61   A. A. Davydov, W. M. Shchekochikhin, P. M. Zajcev, Y. M. Shchekochikhin and P. Keier, *Kinet. Katal.*, **12** (1971) 694.

62   E. B. Wilson, *Phys. Rev.*, **45** (1934) 706.

63   J. H. S. Green, *J. Chem. Soc.*, 2236 (1961).

64   D. R. Taylor and K. H. Ludlum, *J. Phys. Chem.*, **76** (1972) 2882.

65   M. I. Tejedor-Tejedor, E. C. Yost and M. A. Anderson, *Langmuir*, **6** (1990) 979.

66   L. Palmisano, M. Schiavello, A. Sclafani, G. Martra, E. Borello and S. Coluccia, *Appl. Catal B: Environmental*, **3** (1994) 117.

67   R. O. Kagel and R. G. Greenler, *J. Chem. Phys.*, **49** (1968) 1638.

68   T. Kotanigawa, *Bull. Chem. Soc. Jpn.*, **47** (1974) 950.

69   C. Chauvin, J. Saussey, J. C. Lavalley, H. Idriss, J-P. Hindermann, A. Kiennemann, P. Chaumette and P. Courty, *J. Catal.*, **121** (1990) 56.

70   G. Karagounis and O. Peter, *Z. Elektrochem.*, **61** (1957) 827.

71   G. Karagounis and O. Peter, *Z. Elektrochem.*, **61** (1957) 1094.

CHAPTER 4

CHARACTERIZATION OF

SPENT CATALYSTS AND

Co-Cu SYNERGISM

SECTION I

4.1. INTRODUCTION

Properties of the fresh and spent catalysts are compared to understand the changes that happened in bulk and on the surface due to the reaction. Various physicochemical characterization techniques are used for this purpose with special emphasize on XRD, Mössbauer, TPR and TPD, TG-DTA and XPS. Most of the characterization results clearly demonstrate that the changes that occurred to the catalysts surfaces are similar and irrespective of any alkylation. Due to this methylation spent catalysts are given in detail. For higher alkylation catalysts, important and new results are highlighted. Irrespective of the alkylating agent, composition x = 0.50 shows maximum activity in terms of phenol conversion and corresponding ortho alkyl selectivity. Hence the analysis of the spent catalyst after various phenol alkylations with x = 0.50 composition is given a special consideration.

4.2. METHYLATION OF PHENOL

Specifically, the spent (methylation) catalysts were obtained after 10 h of reaction at optimized conditions for 2,6-xylenol formation (methanol to phenol ratio of 5, reaction temperature 350^0C). In correlation with the catalytic performance, (shown in vapour-phase methylation – chapter 3), attention is focussed to electronic and structural changes, in particular the following four aspects: (i) any changes in the oxidation state of metal ions and the surface atomic ratio of metal ions remain the same during reaction (ii) any phase separation Cu_2O + Fe_3O_4 that might occur in the mixed Cu-Co ferrites, (iii) there is any variation in the Fe^{3+} to $Fe^{2+/3+}$ ratio and redistribution between (A) and [B] sites, and (iv) formation of carbonaceous deposits.

4.2.1. Bulk characterization (XRD and Surface area)

Diffractograms of the fresh and the spent catalysts are shown in Figure 4.1. The spent catalysts are crystalline and all the peaks are indexed. It can be seen that at x = 0.0 few lines are observed in contrast to the same fresh catalyst and 'd' values are the same in both

cases. Some peaks disappear corresponding to CuO and α-Fe$_2$O$_3$, however new peaks appears matching to Cu and Cu$_2$O (JCPDS card No: 5-667) and their intensity decreases at higher x. Furthermore, weak reflections of zerovalent iron phase (carbidic and/or metallic - hard to distinguish) are also detected in x = 0.25, 0.5 and 0.75 samples. This indicates that the 10 h reaction treatment results in the reduction of catalysts to some extent. The lattice constant, 'a', on all the spent samples are consistently larger than those found on the fresh samples and supports the reduction of the catalysts. No significant changes in the XRD pattern of fresh and spent CoFe$_2$O$_4$ are observed.
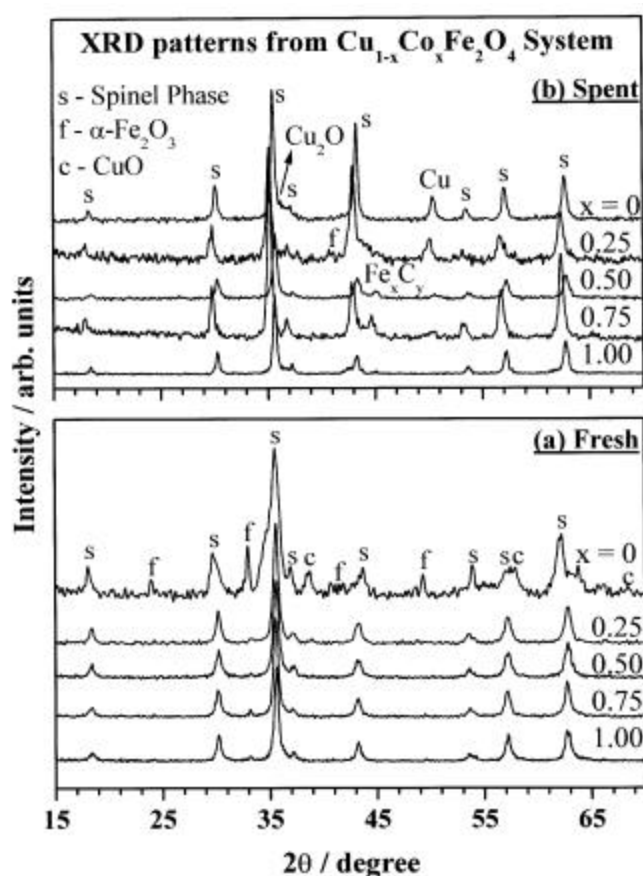

Figure 4.1: X-ray diffractograms of fresh (a) and spent (b) Cu$_{1-x}$Co$_x$Fe$_2$O$_4$ catalysts. XRD from spent catalysts are after phenol methylation reaction at 350^{0}C for 10 h with 1:5 composition of phenol:methanol.

Surface area decreases on spent catalysts due to carbon deposition compared to fresh catalysts; however at x = 0.5 and 0.75 an increase in surface area indicates segregation of active species on the surface. The results obtained from XRD and surface area analysis of the spent samples are summarized in Table 4.1.

Table 4.1: XRD parameters, surface area and pore volume of fresh and spent $Cu_{1-x}Co_xFe_2O_4$ catalysts.

Catalyst Composition (x)	Crystallite Size ($\mathring{A}$)[b] Spent[a] (Fresh)	a ($\mathring{A}$) Spent (Fresh)	S_{BET} (m^2/g) Spent (Fresh)	Pore Volume (cc/g) (10^{-2}) Spent (Fresh)
0.0	18.68 (15.25)	8.4069 (8.3898)	23.0 (28.8)	3.4 (5.1)
0.25	14.49 (13.85)	8.4120 (8.4051)	32.8 (34.0)	5.7 (6.7)
0.50	15.78 (13.17)	8.4082 (8.4012)	53.2 (43.8)	7.1 (10.9)
0.75	19.72 (14.77)	8.4029 (8.3982)	43.4 (36.6)	6.0 (6.4)
1.0	19.48 (14.13)	8.4020 (8.3997)	27.6 (36.8)	4.7 (5.9)

[a]Spent catalysts are after phenol methylation at 350^0C with 1:5 composition of $CH_3OH:C_6H_5OH$ for 10h.

[b]Obtained from Debye-Scherrer analysis.

4.2. 2. Infrared spectroscopy

IR of the spent catalysts is shown in Figure 4.2 recorded by drift mode. This study reveals that the absorption band around 460 cm^{-1} is split and hints that the catalytic reaction caused severe changes on O_h sites. Thus the presence of reduced ions such as Fe^{2+}, Cu^+ etc is on O_h site is evidenced by its band splitting. On the other hand reaction did not cause any splitting of T_d band on $CoFe_2O_4$ even though its band intensity is decreased which indicates reaction hardly affects the overall status of the T_d sites. However this does not mean that migration of ions between T_d and O_h sites did not occur during the course of the reaction. For example reduction of Fe^{3+} ion might occur on both

T_d and O_h sites, however, the reduced Fe^{2+} ion preferably occur on O_h sites by considering factors such as crystal field stabilization energy, Madelaung constant etc [1].
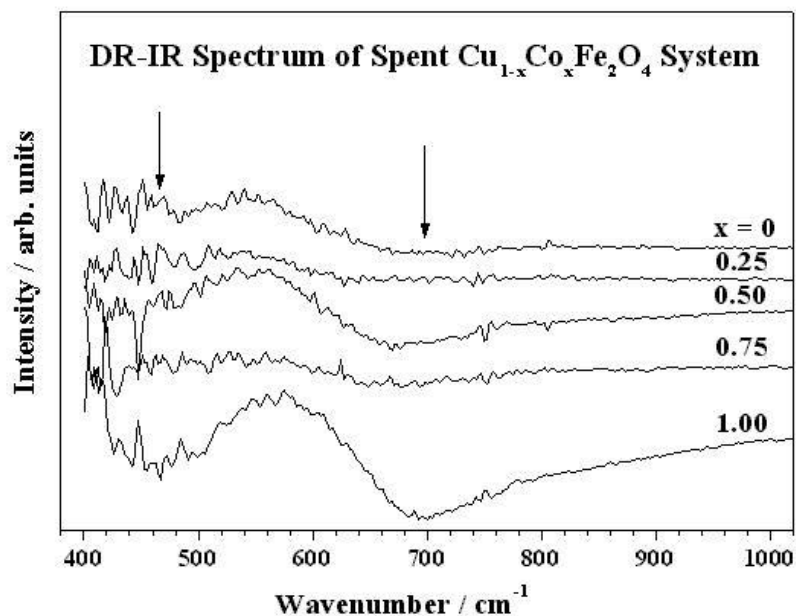
Figure 4.2: Drift IR spectrum of spent $Cu_{1-x}Co_xFe_2O_4$ catalysts. DR-IR from spent catalysts are after phenol methylation reaction at 350^0C for 10 h with 1:5 composition of phenol:methanol.

4.2.3. Mössbauer spectroscopy

Mössbauer spectra were recorded both on the fresh and spent samples (Figure 4.3). Data extracted from the fits are compiled in Table 4.2. For interpreting the data the detailed reviews on iron spinels and oxides can be used [2,3]. To distinguish the T_d (A) sites of iron from the O_h [B] positions in ferrispinels, it can be mentioned that the internal magnetic hyperfine field (MHF) experienced in the (A) sites is always smaller than that exerted in the [B] sites. The opposite is valid for most of the ferri/ferro-spinels: the contribution of Fe^{2+} to the internal magnetic field is usually significantly smaller that that of ferric ions (see e.g. magnetite). Furthermore, the isomer shift (IS) values for ions located in (A) sites are significantly smaller than those characteristic of [B] sites (indicating that

Fe^{3+} ions are in (A) sites whereas in [B] sites Fe^{2+} and Fe^{3+} ions formally alternate, referred as $Fe^{2+/3+}$ in the text throughout).
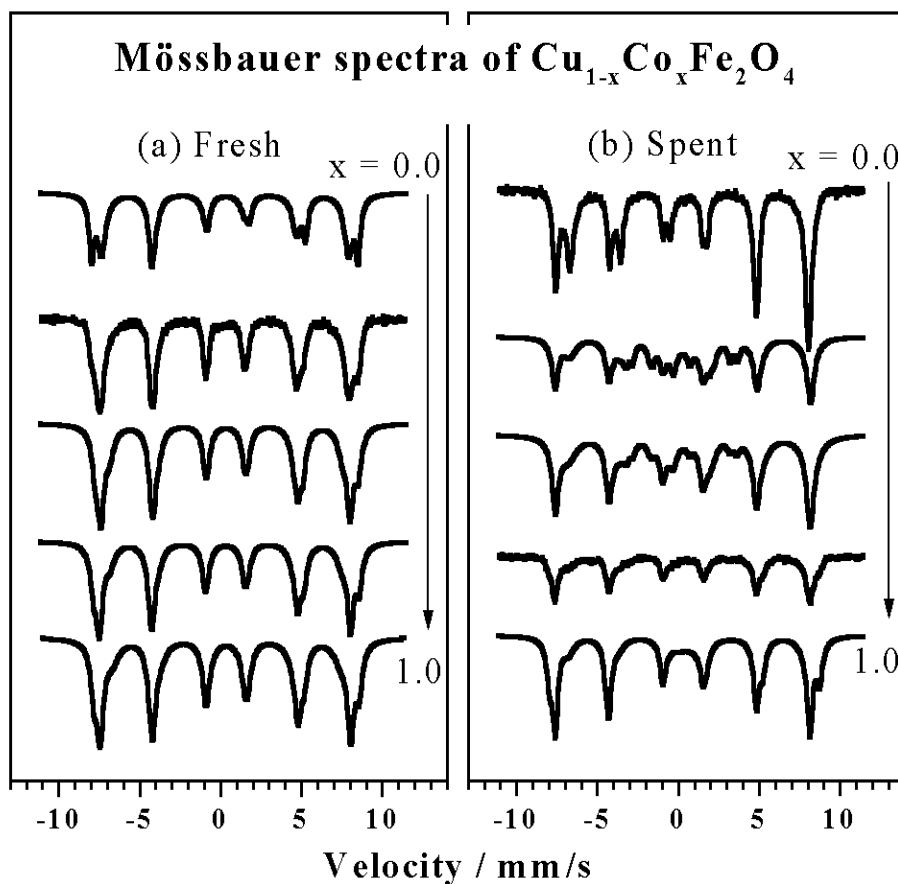
Figure 4.3: Mössbauer spectra recorded on fresh (left) and spent (right) $Cu_{1-x}Co_xFe_2O_4$ catalysts.

The assignments presented in Table 4.2 correspond to the previous notes. In fresh catalysts ferric iron is present in both the (A) and [B] sites. The reduction of iron in the octahedral sites is clearly manifested in each sample upon the exposure to the reaction mixture for 10 h, as reflected in the Fe^{3+}[B] $\rightarrow$ $Fe^{2+/3+}$[B] conversion by the increase of the respective IS and the decrease of MHF values. On the other hand, the reaction hardly influences the state of iron located in the tetrahedral (A) sites, the IS and MHF parameters of Fe^{3+}(A) are preserved within the experimental accuracy.

Table 4.2: Mössbauer spectral data extracted from the 300 K spectra of fresh and spent $Cu_{1-x}Co_xFe_2O_4$ ferrites.

Sample		Fresh			Spent			
x	Comp.	IS	MHF	RI	IS	QS	MHF	RI
0.0	$Fe^{3+}(A)$	0.26	47.5	66	0.26	-	48.7	44
	$Fe^{3+}[B])$	0.36	51.2	34				
	$Fe^{2+/3+}[B]$				0.62	-	45.5	56
0.25	$Fe^{3+}(A)$	0.26	47.5	72	0.27	-	49.1	40
	$Fe^{3+}[B]$	0.36	50.5	28				
	$Fe^{2+/3+}[B]$				0.67	-	46.1	29
	Fe^0 Carb.(I)				0.20	-	21.3	10
	Fe^0 Carb.(II)				0.16	-	18.7	9
	$Fe_{paramag}$				0.61	1.94	-	10
0.50	$Fe^{3+}(A)$	0.29	47.8	45	0.26	-	48.9	48
	$Fe^{3+}[B]$	0.38	50.3	32				
	$Fe^{2+/3+}[B]$				0.70	-	46.8	30
	$Fe^{3+}(mix)$	0.32	44.8	22				
	Fe^0 Carb.(I)				0.19	-	21.0	8
	Fe^0 Carb.(II)				0.16	-	18.7	4
	$Fe_{paramag}$				0.64	2.15	-	10
0.75	$Fe^{3+}(A)$	0.26	48.2	49	0.28	-	49.2	76
	$Fe^{3+}[B]$	0.37	50.9	27				
	$Fe^{2+/3+}[B]$				0.62	-	45.5	24
	$Fe^{3+}(mix)$	0.32	44.9	23				
1.0	$Fe^{3+}(A)$	0.27	48.6	53	0.26	-	48.9	45
	$Fe^{3+}[B]$	0.37	51.3	24	0.38	-	51.7	27
	$Fe^{2+/3+}[B]$				0.52	-	45.6	18
	$Fe^{3+}(mix)$	0.34	44.3	22				
	$Fe_{paramag}$				0.65	1.12	-	10

(IS: isomer shift, mm/s, relative to α-iron; QS: quadrupole splitting, mm/s; MHF: magnetic hyperfine field, Tesla; RI: relative spectral area, %)

A third component, $Fe^{3+}(mix)$, is also present in the spectra of those fresh samples in which the Co content is equal or prevails the amount of Cu ($x \geq 0.5$). It is a minor component with partial contributions to the full spectra (with relative intensity, RI values of 22 - 23 %). This component is probably originated from iron sites with Co ions in their

close vicinity resulting in the damping of the magnetic exchange, i.e. lowering the experienced MHF.

In the spectra of spent samples two new features appear. In the mixed samples of the larger Cu content (x= 0.25 and 0.5) another composed magnetic structure appears with low MHF values (21 and 19 T) in a minor intensity. This feature can probably be assigned to combination of iron sites in χ- iron carbide (Fe_5C_2) [4]. Another minor component can be isolated in the spectra of certain spent samples, namely the one exhibiting non-zero quadrupole splitting (QS). For this component the long range magnetic interactions are absent, due to significant reduction of magnetic domain size (i.e. this component is probably superparamagnetic: the number of coupled spins is limited beyond a threshold value).

4.2.4. Temperature programmed reduction and desorption (TPR, TPD)

TPR profiles of fresh catalysts were obtained up to 750^0C (Figure 4.4, left side). The amounts of hydrogen consumed for reduction in this temperature range are presented in Table 4.3.
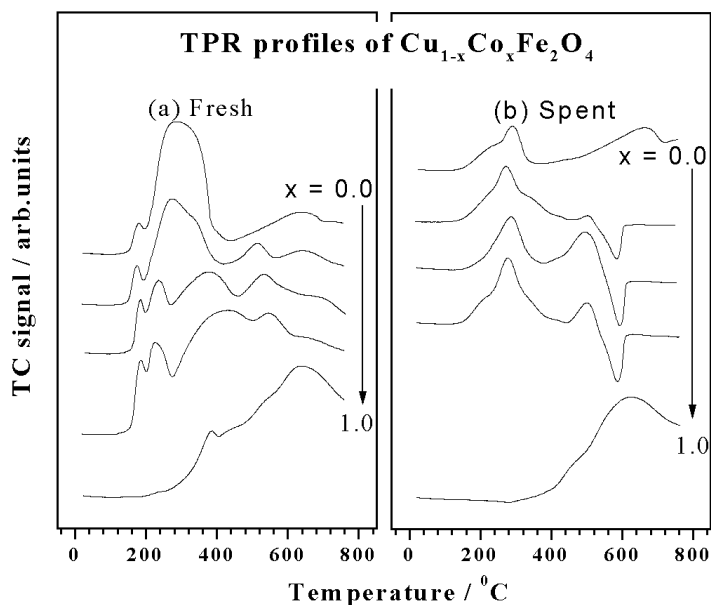

Figure 4.4: TPR profiles of fresh (left) and spent (right) $Cu_{1-x}Co_xFe_2O_4$ catalysts.

Table 4.3: H_2 consumption in the TPR experiments for the $Cu_{1-x}Co_xFe_2O_4$ samples

Catalyst composition (x)	H_2 consumed (mekv/mmol)[a]
0.0	3.32
0.25	3.72
0.50	4.00
0.75	3.20
1.0	2.26

[a] Hydrogen consumed by the fresh catalysts in the $30 - 750^0C$ range.

For interpretation of the profiles, $Cu^{2+} \rightarrow Cu^+$ (1 mekv H_2 / mmol cat), $Fe_2O_3 \rightarrow Fe_3O_4$ (0.67 mekv H_2 / mmol cat), $Cu^+ \rightarrow Cu^0$, (1 mekv H_2 / mmol cat) and the remainder $Fe^{3+} \rightarrow Fe^{2+}$ (1.33 mekv H_2 / mmol cat) should be considered in the order of the increasing temperature of reduction. It is worth mentioning that only the $Cu_{0.5}Co_{0.5}Fe_2O_4$ sample is reduced to the extent of the sum of the mentioned processes (4.0 mekv H_2 / mmol cat), the degree of reduction is less on the other samples. The four mentioned processes in the x = 0.5 sample can probably be attributed to peaks centered around 180, 240, 390 and 530 ^0C. The first peak characterizes the $Cu^{2+} \rightarrow Cu^+$ reduction proceeding only in a certain part of Cu. The fifth, smeared peak around 670 ^0C probably corresponds to a starting $Fe^{2+} \rightarrow Fe^0$ reduction in the vicinity of Cu^0-rich regions. As the copper content increases, the temperature ranges of the $Fe_2O_3 \rightarrow Fe_3O_4$ and the $Cu^+ \rightarrow Cu^0$ reduction approach each other, as the comparison of x = 0.75, 0.5 and 0.25 samples show. In the x = 0, $CuFe_2O_4$ sample the formation of magnetite and metallic copper proceeds practically in one step, completed below 400 ^0C. The other end of the composition range, sample $CoFe_2O_4$, exhibits diametrically different profile with significantly less tendency to reduction than found in any sample containing copper.

TPR profiles were recorded also on the spent samples (Figure 4.4, right side). The Cu-Co mixed samples exhibit a particular feature: instead of hydrogen consumption an apparent evolution is shown above 480 ^0C. Furthermore, the amounts of the consumed

hydrogen corresponding to the first peak in the lower temperature region (130 – 420 ^{0}C) are small on these samples: 0.46, 0.47, and 0.28 mekv H_2 / mmol cat in the order of the increasing cobalt content (x = 0.25, 0.5, and 0.75, respectively).

TPD measurements were performed in pure helium to obtain more information on the origin of the apparent high-temperature evolution peaks. Simultaneously with the TC signal mass numbers corresponding to H_2, H_2O, CO, O_2, and CO_2 were also monitored by a QMS detector. TC signals are shown in Figure 4.5.

Temperature programmed desorption on spent $Cu_{1-x}Co_xFe_2O_4$
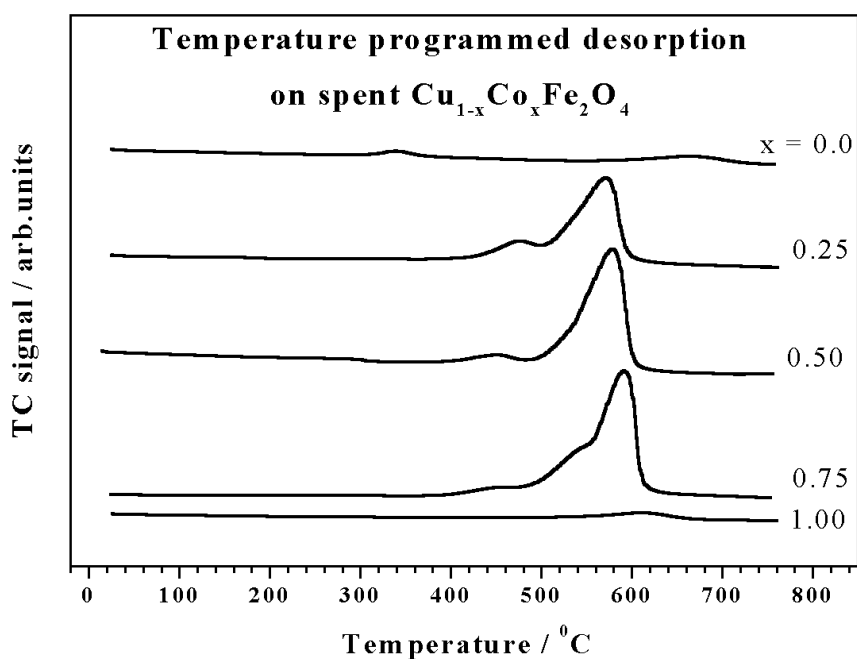
Figure 4.5: Temperature programmed desorption on spent $Cu_{1-x}Co_xFe_2O_4$ catalysts: thermal conductivity signals.

The intense TC peaks of Cu-Co mixed samples are primarily composed from H_2 and CO. In average, the ratios of these dominant components are close to 1:1. More precisely, hydrogen dominates the first evolution peak (420 – 500 ^{0}C). In the second, more intense desorption stage (500 – 620 ^{0}C) the ratio of the amounts of the evolved H_2 : CO depend systematically on the composition: c.a. 1.25, 1.1 and 1.0 values can be found in the

order of x = 0.25. 0.5 and 0.75, respectively. Thus, the higher the Cu content the larger is the amount of hydrogen in the carbonaceous deposit. The third most intense component is CO_2, amounting to c.a. 20 % of the total intensity. Contributions originated from H_2O and O_2 are practically negligible (only a few per cent of the total amount). Furhermore, it is worth mentioning that there is a shift in the temperatures of the maximal desorption shown in the thermal conductivity signal: 570, 587 and 591^0C values are characteristic for x = 0.25. 0.5 and 0.75 samples, respectively.

4.2.5. Thermogravimetry and differential thermal analysis (TG and DTA)

The weight change and the detected heat evolution upon heating of the spent samples are shown in Figure 4.6 and Table 4.4.
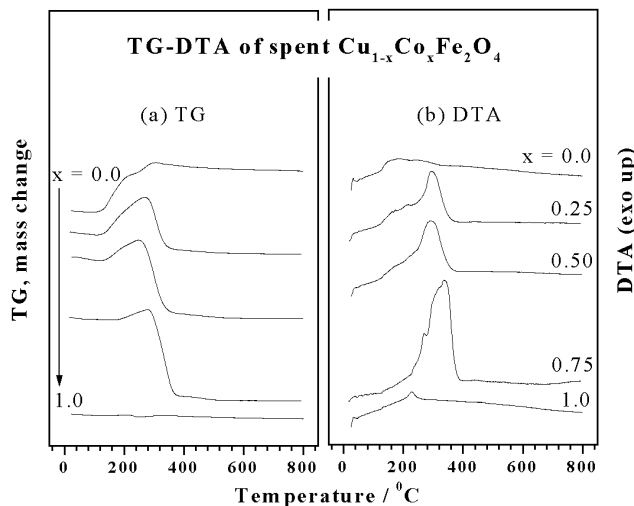
Figure 4.6: Thermogravimetry (left) and differential thermal analysis (right) of spent $Cu_{1-x}Co_xFe_2O_4$ catalysts.

Three stages can be distinguished in the TG curves (Figure 4.6a): (i) a weight increase in the 130 – 190 ^0C region, (ii) a further weight gain commencing at c.a. 230 ^0C, and (iii) an expressed weight drop, starting at c.a. 260 ^0C. The first, lowest temperature weight increase can probably be assigned to an oxygen uptake by the $Cu^+ \rightarrow Cu^{2+}$ process. This feature is correlated with the copper content: it is very high in the $CuFe_2O_4$, and is not

128

detected in the Co-rich samples. The second weight increase is present practically in each samples, thus, it can probably be attributed to an $Fe^{2+/3+} \rightarrow Fe^{3+}$ oxidation. The third feature, the loss of weight, is due to the removal of the carbonaceous deposit accumulated on the surface in the course of the preceeding catalytic reaction. Three observations are worth to note when comparing the removal of carbonaceous deposit by oxidation. First, the weight loss can only be detected on the three-component mixed Cu-Co catalysts. The second observation is that the amount of removed (i.e. the previously accumulated) deposit is correlated with the Co content (x): greater x corresponds to larger amount of carbon, the highest quantity of carbonaceous deposit is removed from the x= 0.75 sample, amounting to 12 % of the starting mass. The third phenomenon is that the temperature of the highest rate of removal of carbon is also different on the mixed Cu-Co samples, the lowest temperature is found on the x= 0.5 sample (310 ^{0}C), whereas the highest temperature is shown by the x= 0.75 sample (335 ^{0}C).

Table 4.4: Thermogravimetric and differential thermal analysis data for spent samples of composition $Cu_{1-x}Co_xFe_2O_4$

Composition (x)	Step	TGA		DTA		Process
		Temp range (^{0}C)	Wt.Loss/gain (%)	DTA Peak temp (^{0}C)	Enthalpy	
0.0	I	127-380	6.14 (gain)	213	exothermic	Oxidation
0.25	I	132-320	5.84 (gain)	232	exothermic	Oxidation
	II	320-462	7.50 (loss)	347	exothermic	Burning of coke
0.50	I	145-282	2.40 (gain)	253	exothermic	Oxidation
	II	284-449	8.40 (loss)	301	exothermic	Burning of coke
0.75	I	153-282	1.31 (gain)	268	exothermic	Oxidation
	II	283-459	12.46 (loss)	299	exothermic	Burning of coke
1.0	I	214-387	5.12 (loss)	317	exothermic	Burning of coke

It may also be noted that unlike other compositions, spent $CuFe_2O_4$ continues to gain weight up to 380^0C and as the Co content increases the maximum temperature shown for complete oxidation process decreases. The TG curves indicate that the temperature

range of oxidation is narrowed down as the Co content increases. Thus the gain in weight for spent samples due to air oxidation is observed in the temperature range 175-380, 130-320, 145-280 and 155-280^{0}C for x = 0, 0.25, 0.50 and 0.75 respectively. The narrowed temperature range of oxidation of Co rich spent samples clearly show that the extent of reduction is the lowest and hence they are structurally more integrated even after the reaction.

The DTA profiles exhibit similarity and difference as well depending on the composition (Figure 4.6b). Namely, the x = 0.25 and 0.5 samples are similar; the exothermic processes commence around 130 ^{0}C, then a more expressed heat evolution is detected with maxima at 290 ^{0}C. In the x = 0.75 sample the profile is different, the heat evolution is concentrated in steps at the higher temperature region with a maximum at 340 ^{0}C.

4.2.6. XPS analysis

4.2.6.1. Oxygen 1s core level

Atmospheric degradation of solids can be identified from C 1s and O 1s spectra before and after '*in situ*' cleaning [5,6]. Figure 4.7 displays the O 1s core level spectra recorded before and after '*in situ*' scraping for $Cu_{0.5}Co_{0.5}Fe_2O_4$. A shoulder is visible on unscraped surface at a binding energy (BE) around 532 eV; however the same disappear mostly after scraping in the vacuum chamber and significant increase in O 1s intensity is also observed. The main peak becomes more symmetrical and does not shift after scraping and observed at 530.2 eV as in unscraped surface. Carbonate species disappear completely after scraping in C 1s spectra (data not shown). Shoulder at 532 eV on unscraped surface is attributed to impurities such as OH$^-$ and CO_3^{2-} species and the main peak is to oxide ions in the spinel phase. Measurements after repeated "*in situ*" scraping did not change the small intensity of the high BE indicates that it is inherent from the catalyst surface. Obviously the energy difference between oxygen species that are associated with Fe, Cu and Co might be small and hence they overlap to a great extent and difficult to resolve. No considerable difference is observed on the BE of O 1s peak at different compositions. Similar contamination is observed on other fresh

catalysts. XPS results on fresh catalysts in the following sections are after thorough scraping. However spent catalysts are analyzed in powder form as used in reaction.
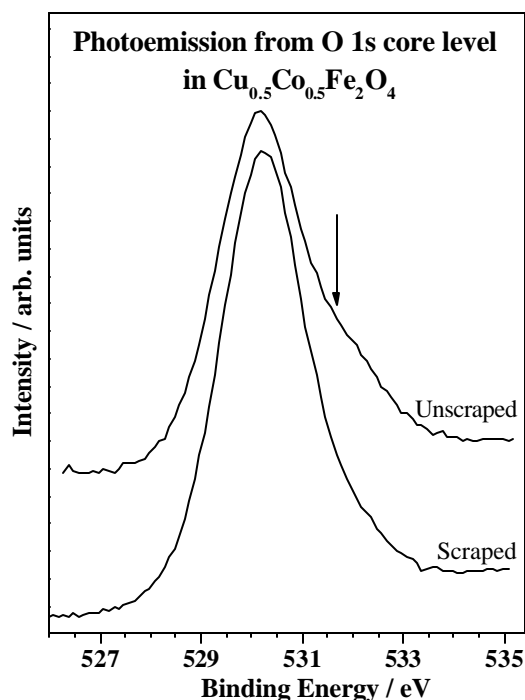

Photoemission from O 1s core level in $Cu_{0.5}Co_{0.5}Fe_2O_4$

Intensity / arb. units

Unscraped

Scraped

527   529   531   533   535

Binding Energy / eV

Figure 4.7: O 1s core level photoemission spectra from fresh $Cu_{0.5}Co_{0.5}Fe_2O_4$ catalyst obtained on as received and *'in situ'* scraped surfaces. Note a large decrease in the shoulder intensity around 532 eV, indicated by arrow demonstrate the atmospheric degradation.

4.2.6.2. Cu 2p core level

Electronic structure of ferrospinels is investigated by XPS. Figure 4.8 presents the Cu 2p core level photoemission spectra from fresh or calcined (a) and spent (b) $Cu_{1-x}Co_xFe_2O_4$ catalysts. Spent catalysts analyzed by XPS are after methylation reaction at 350^0C for 10h with 1:5 composition of PhOH:MeOH, unless otherwise stated. Relevant XPS results of the present system and standard compounds [7-10] are given in Table 4.5. It can be noticed that all fresh catalysts (Figure 4.8a) exhibits the Cu $2p_{3/2}$ main peak at 934.2±0.2 eV with a FWHM of 3.0 eV. Cu 2p BE does not change with Co content and indicates the electron density on Cu remains the same. Good satellite intensity (I_s) is observed at all x values around 942 eV

indicating the existence of Cu^{2+} species. The intensity ratio between the satellite and main line (I_s/I_m) is between 0.5 and 0.6 in all cases (inset in Figure 4.8a), which is very close to that of pure CuO [7].
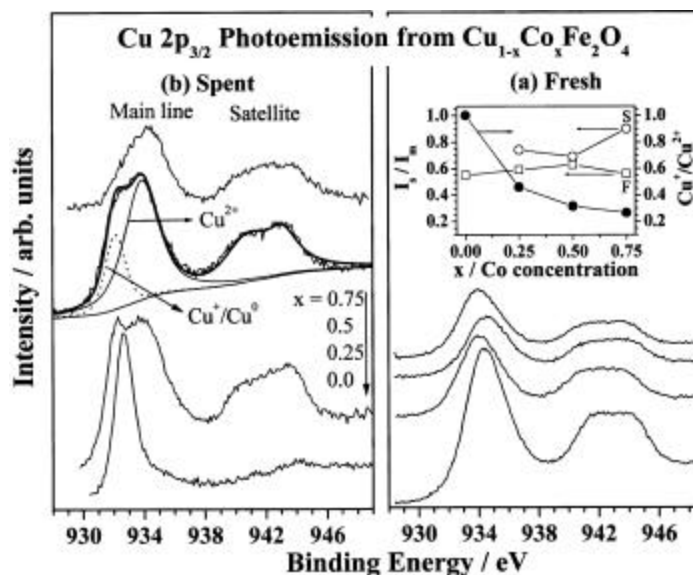

Figure 4.8: Cu 2p photoemission spectra of fresh (a) and spent (b) $Cu_{1-x}Co_xFe_2O_4$ catalysts. Deconvolution clearly shows both Cu^+ (Cu^0) and Cu^{2+} on spent catalysts. Inset in the right panel shows the satellite to main line intensity ratio (I_s/I_m) for fresh (F) and spent (S) catalysts (open symbols) and the ratio of reduced Cu to that of total Cu on spent catalyst (closed symbols). Note the decrease in the reducibility of Cu with increasing x.

Cu $2p_{3/2}$ XPS results from spent catalysts are interesting and new features can be seen compared to fresh catalysts. At x = 0.0, a peak at 932.6 eV with a FWHM of 1.4 eV is observed without any satellite. However at x ≥ 0.25, there is a large broadening observed with a satellite feature at high BE. Deconvolution reveals the contribution of different species. For simplicity, it is shown only for x = 0.5 in Figure 4.8b and the results are given in Table 4.5. Important points to be noted are: Cu species got reduced during reaction and the extent of reduction decreases with increasing Co content, and Cu^{2+} BE decreases by 0.4 eV at x = 0.5, with a concurrent decrease in I_s/I_m compared to other x values (inset in Figure 4.8). Above points clearly demonstrate that there is a strong influence from Co on Cu and its reducibility. Inset in Figure 4.8a shows the I_s/I_m of fresh (F) and spent (S) catalysts and the reducibility of

Cu. Reducibility of Cu, calculated as the amount of reduced Cu to Cu^{2+} content, decreases with increasing x. High polarizability induced by the formation of Co-containing Cu-spinel would change the nature of Cu-O bond [11,12].

Table 4.5: XPS and XAES parameters of $Cu_{1-x}Co_xFe_2O_4$ catalysts and relevant reference compounds

Compounds and x	BE of Cu $2p_{3/2}$ (FWHM) (eV)	KE of Cu $L_3M_{45}M_{45}$ (eV)	α' (eV)	Reference
Cu	932.6	918.4	1851.0	8, 9
Cu_2O	932.5	916.5	1849.0	8, 9
CuO	933.8	917.6	1851.4	7
$Cu_{0.92}Fe_{2.08}O_4$	933.7, 935.7	NA	NA	10
0.00^F	934.3 (3.0)	917.2	1851.5	Present work
0.25^F	934.0 (2.9)	917.6	1851.6	Present work
0.50^F	934.4 (3.0)	917.8	1852.2	Present work
0.75^F	934.0 (3.0)	917.5	1851.5	Present work
0.00^S	932.6 (1.4)	916.4	1849.0	Present work
0.25^S	932.6, 934.3 (3.9)	917.0	1849.6,1851.3	Present work
0.50^S	932.1, 933.9 (3.7)	917.3	1849.4,1851.2	Present work
0.75^S	932.5, 934.3 (3.0)	916.9	1849.4, 1851.2	Present work

F and S indicate the fresh and spent catalysts.

4.2.6.3. Cu $L_3M_{45}M_{45}$

Generally modified Auger parameter (α') [7], have been calculated to distinguish the different oxidation (and final) states of Cu in the same or closely related compound, is defined as:

$$\alpha' = h\nu + (KE\ Cu_{LMM} - KE\ Cu\ 2p_{3/2}) \hspace{2cm} (1)$$

where, KE Cu_{LMM} and KE Cu $2p_{3/2}$ are kinetic energies of Auger electron and Cu $2p_{3/2}$ level, respectively. The Cu $L_3M_{45}M_{45}$ Auger spectra of fresh (a) and spent (b) catalysts are shown in Figure 4.9.
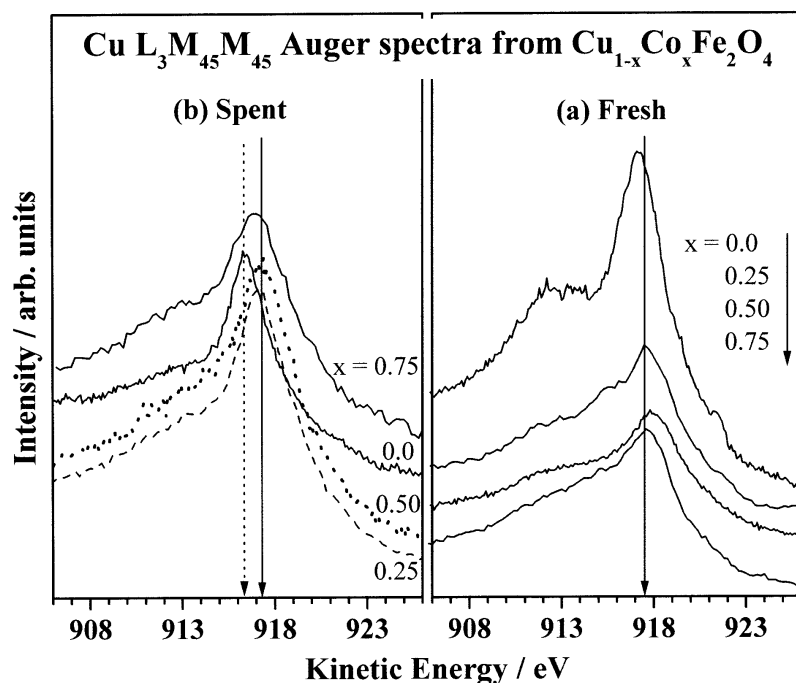
Figure 4.9: X-ray initiated Auger electron spectra (XAES) from Cu $L_3M_{45}M_{45}$ fresh (a) and spent (b) $Cu_{1-x}Co_xFe_2O_4$ catalysts. Note the changes in shift and broadening of Auger transitions from spent catalysts. Spent catalysts spectra are normalized for better presentation.

It can be seen that, the $CuFe_2O_4$ exhibits the Cu $L_3M_{45}M_{45}$ line at a KE of 917.2 eV. Co concentration increases the above value up to 917.8 eV. Note that for pure CuO this line appears at 917.6 eV [7]. However, depending on the chemical environment and geometry, the position of this line has been found to shift significantly. α' determined (Table 4.5) is in the 1851.5 and 1852.2 eV range, which is very close to that of CuO, has been obtained for fresh catalysts.

Contrary to the fresh, spent catalysts shows interesting observations in Cu $L_3M_{45}M_{45}$ spectra (Figure 4.9b) as in Cu 2p core level. At x = 0.0, above transition is observed with a relatively sharp peak at 916.4 eV, which is typical for Cu_2O. However, at 0.25≤x≤0.75 exhibit a broad peak structure, at high KE 917.5 eV. It is to be noted that the fresh catalysts too exhibit a single peak around 917.5±0.3 eV in this region. This clearly indicates the increasing contribution of Cu^{2+} at higher x. However, the broadening indicates the contribution of Cu^+ species at low KE. At x = 0.5, an extra broadening seen on the high KE side at 918.6 eV

indicates Cu^0 contribution; $\alpha' = 1851.2$ eV also indicates the contribution of both Cu^0 and Cu^{2+} on $x = 0.5$ (see Table 4.5). Owing to a large overlap of the Auger transitions with a significant background in the spectra, a reliable estimation of individual Cu species is difficult. Above XPS and XAES of Cu suggests the distortion of Cu^{2+} environment at intermediate compositions from fresh to spent catalysts.

4.2.6.4. Co 2p core level and Co-$L_3M_{45}M_{45}$ auger transitions

Co 2p photoemission spectra for fresh (a) and spent (b) catalysts are shown in Figure 4.10. It displays a main line and a satellite for Co 2p spin orbit doublets. XPS results are given with the reference compounds in Table 4.6 [13-15].
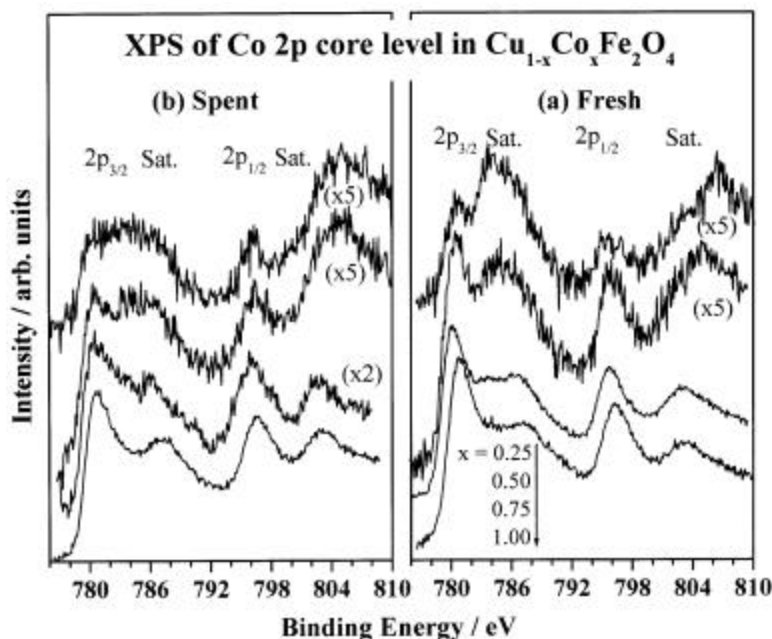
Figure 4.10: Co 2p core level photoelectron spectra of fresh (a) and spent (b) $Cu_{1-x}Co_xFe_2O_4$ catalysts. Note the increase in energy gap between spin-orbit doublets of 2p levels and decreasing satellite intensity with increasing x on fresh and spent catalysts.

Figure 4.10 and Table 4.6 shows: (1) I_s observed at a BE around 785 eV decreases with increasing x, (2) Energy gap between Co 2p spin orbit doublets increases from 15 eV (15.5 eV) at $x = 0.25$ ($x \geq 0.5$) on fresh to 15.5 eV (16.0 eV) on spent catalysts, (3) Energy gap

between main line and satellite also increases with increasing x on both fresh and spent catalysts, and (4) At x = 0.75 and 1, two satellites are discernible on fresh catalyst from the large broadening; but only one satellite is seen on spent catalyst (Table 4.6). A comparison of BE of catalysts to that of reference compounds in Table 4.6, clearly indicates the catalysts surfaces are in general composed of both Co^{2+} and Co^{3+}. High I_s for x $\leq$ 0.5 suggests the contribution of Co^{2+} and high spin Co^{3+}, since low spin Co^{3+} shows poor I_s [13-15].

Table 4.6: XPS parameters from Co 2p core level in $Cu_{1-x}Co_xFe_2O_4$ catalysts and relevant reference compounds.

Material	BE of Co $2p_{3/2}$ (Satellite)[#] (eV)	Satellite Intensity	$2p_{3/2}$-$2p_{1/2}$ Gap (eV)	Reference
Co metal	778.0	—	15.1	13
CoO	780.1±0.3	Strong	15.5	13-15
$Co(OH)_2$	780.9±0.2	Strong	16.0	13-15
Co_2O_3	779.6	Weak	---	14
Co_3O_4	780.5	Weak	15.0	15
$ZnCo_2O_4$	780.3	Weak	15.0	15
$CoAl_2O_4$	781.9±0.5	Strong	16	14, 15
x = 0.25[F]	780.7 (4.0)	Strong	15.1	Present work
x = 0.5[F]	780.5 (4.7)	Strong	15.5	Present work
x = 0.75[F]	780.2 (3.4 and 6.1)	Intermediate	15.6	Present Work
x = 1.0[F]	780.9 (4.6 and 6.1)	Intermediate	15.5	Present work
x = 0.25[S]	780.4 (4.1)	Strong	15.5	Present work
x = 0.5[S]	780.5 (4.4)	Strong	15.9	Present work
x = 0.75[S]	780.6 (4.5)	Intermediate	16.1	Present work
x = 1.0[S]	780.7 (6.6)	Intermediate	16.0	Present work

[#] indicates the energy gap between Co $2p_{3/2}$ main line and satellite.

Co-$L_3M_{45}M_{45}$ Auger spectra of x = 0.5, 0.75 and 1 compositions are shown in Figure 4.11, exhibit broad features between 760 and 780 eV. Two features seen at 767 and 772 eV are identical for fresh and spent catalysts at x = 1.0. However, at x = 0.5 and 0.75 a shift in energy is seen for lower KE component on spent catalyst compared to fresh; further, a change in intensity ratio of the two features is observed. Significant changes on spent catalyst at x = 0.5 and 0.75 implies the final state of the low KE feature is different compared to that of other final state and indicates site specific and/or near neighbor interaction.
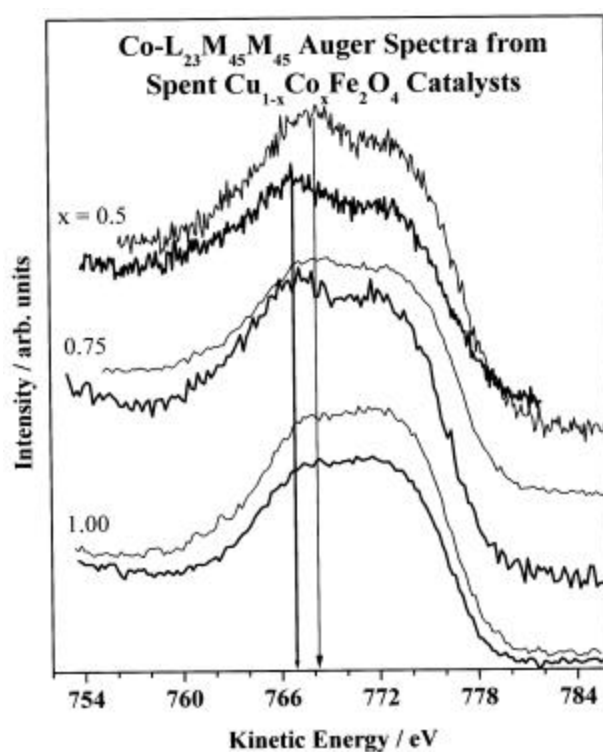
Figure 4.11: XAES from Co $L_3M_{45}M_{45}$ of fresh (thin lines) and spent (bold lines) $Cu_{1-x}Co_xFe_2O_4$ catalysts for x = 0.5, 0.75 and 1. Note the changes observed in energy and intensity at x = 0.5 and 0.75 from fresh to spent catalysts by thin and thick arrows, respectively.

4.2.6.5. Fe 2p core level and Fe-$L_3M_{45}M_{45}$

Photoemission spectra from Fe 2p core levels normalized to x = 0.0 are displayed in Figure 4.12 for fresh (a) and spent (b) $Cu_{1-x}Co_xFe_2O_4$ catalysts. It displays a main line and a satellite for both spin orbit doublets; satellite associated with $2p_{1/2}$ level is not shown, as there

is some interference from O-KVV Auger transitions. Although for the first glance Fe 2p spectra look alike on fresh and spent catalysts, there are two important differences between them. (a) Clear satellite, due to predominant Fe^{3+}, is observed on fresh catalysts; on the other hand, I_s is weak on spent catalysts, and (b) spent catalysts indicates a shoulder around 709.5 eV, characteristic of Fe^{2+} species [16,17], is shown after deconvolution in the inset in Figure 4.12 for x = 0.5. This feature is observed at 0<x<1 with $Fe^{2+}:Fe^{3+}$ ratio of 1:2. Further it is accompanied with a clear shift in Fe $2p_{1/2}$ main peak to lower BE to 724.3 eV, compared to 725 eV for x = 0 and 1 (Figure 4.12b). It is to be emphasized here that Fe^{2+}-O bond length should be significantly different from that of Fe^{3+}-O and it influences Fe-O hybridization [17] and Cu or Co ions that are in the octahedral sites.
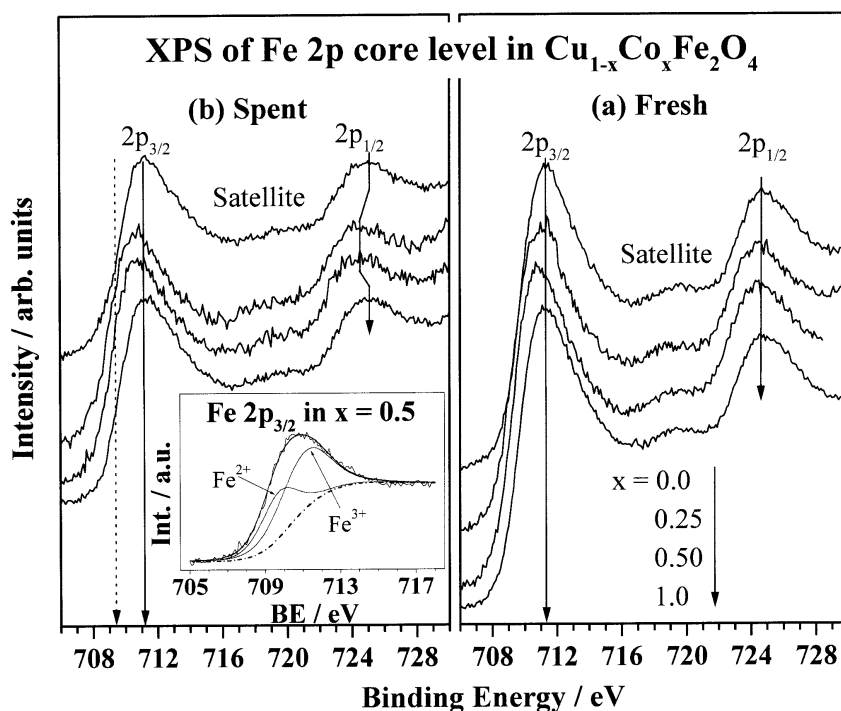
Figure 4.12: Fe 2p core level XPS of fresh (a) and spent (b) $Cu_{1-x}Co_xFe_2O_4$ catalysts. A shoulder is seen below 710 eV on spent catalysts (dotted line) for 0<x<1 with low satellite intensity. Deconvolution of Fe $2p_{3/2}$ peak demonstrate Fe^{2+} and Fe^{3+} on spent catalyst at x = 0.5, in the inset on left panel. Broadening and shift in BE is clear with Fe $2p_{1/2}$ level and indicated by arrow.

Figure 4.13 displays the Fe-$L_3M_{45}M_{45}$ spectra for x = 0, 0.5 and 0.75 catalysts. Spent catalyst spectrum is normalized to fresh for better presentation. Fresh catalysts are similar and no difference is observed. Significant changes are clear on the spent catalyst at x = 0.5 and 0.75. A shoulder seen at KE 697 eV (dotted arrow in Figure 4.13) corresponds to Fe^{2+}; however the intensity of this feature is less at x = 0.75. Although there is some line broadening on spent catalyst at x = 0.0, it is not considerable as in x = 0.5. Fe 2p and Fe LMM results indicates the partial reduction of Fe^{3+} and the extent of reduction might be small at x = 0 and 1and high at 0<x<1.
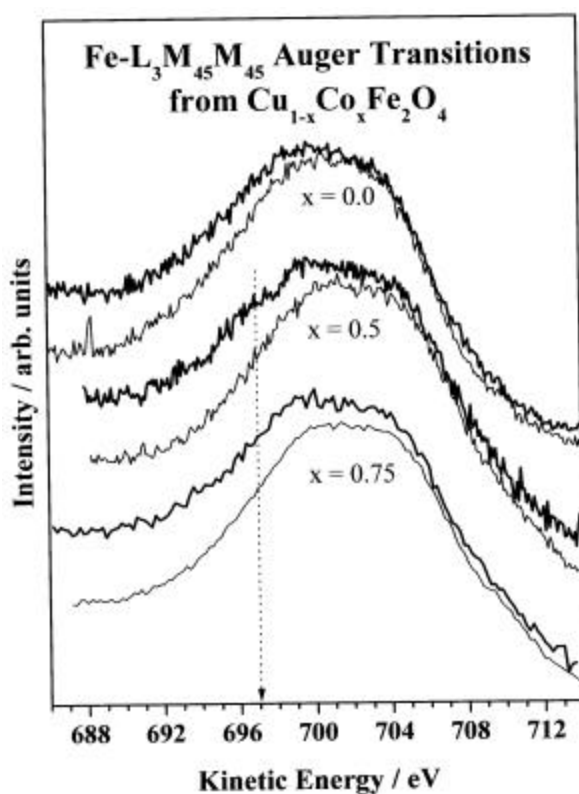
Figure 4.13: XAES from Fe $L_3M_{45}M_{45}$ of fresh (thin lines) and spent (bold lines) $Cu_{1-x}Co_xFe_2O_4$ catalysts for x = 0.0, 0.5 and 0.75 compositions. A shoulder observed at 697 eV on spent catalysts at x = 0.5 and 0.75 is indicated by dotted line.

4.2.6.6. Valence band photoemission

XPS spectra of the valence band (VB) region obtained from fresh (a) and spent (b) $Cu_{1-x}Co_xFe_2O_4$ catalysts are shown in Figure 4.14. The main VB observed below 9 eV have

contributions from 3d bands of Cu, Co and Fe. At $h\nu$ = 1253.6 eV employed in these experiments, the photoionization cross section (σ) value (Cu 3d = 0.021, Co 3d = 0.0067, Fe 2p = 0.0045 and O 2p = 0.0005 Mb) [18] is the dominating factor in formulating the spectral intensity. The above data suggest Cu 3d should have large contributions to the VB and contribution from O 2p is negligible. The VB assignments are straightforward from the intensity and the BE of the bands. High intensity VB is observed with a satellite around 12 eV from Cu $3d^8$ final state [19] on fresh $CuFe_2O_4$ and the intensity of above features decreases at higher x with an additional peak growing around 2 eV. Further an overlapping band with significant intensity is discernible between 4 and 8 eV and it is clear on $CoFe_2O_4$. These observations demonstrate the position of Cu and Co 3d bands around 2, 4 eV (solid and dotted lines) and Fe 3d bands between 4-8 eV, respectively. A dip in intensity between 3 and 4 eV denotes the absence of Cu 3d contributions at x = 1. Intensity variation observed from x = 0 to 1 is mostly due to the high σ of Cu 3d bands.
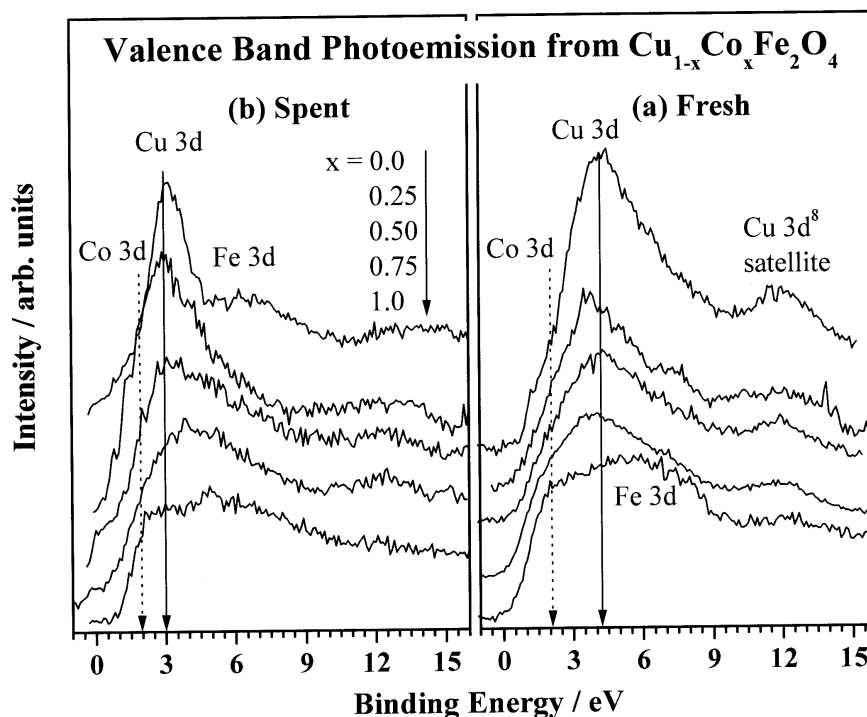

Figure 4.14: Valence band XPS of fresh (a) and spent (b) $Cu_{1-x}Co_xFe_2O_4$ catalysts. A significant decrease in energy gap between the 3d levels of Cu and Co and a decrease in overall band width is observed on spent catalysts. Fe 3d level BE decreases on spent catalysts at $0.25 \leq x \leq 0.75$.

Dramatic changes observed on spent catalysts from core levels are reflected strongly in the VB spectra too are listed below: (1) Cu 3d bands shifted towards that of Co by ≥ 1 eV (arrows in Figure 4.14b) accompanied an enormous narrowing of the Cu 3d bands. (2) Satellite disappears on x = 0.0; however a broad band (satellite) appears between 10 and 15 eV for x = 0.25 to 0.75. (3) There is a clear shift in the onset of photoemission to 1 eV for x = 1 compared to emission from 0 eV on x $\leq$ 0.5. (4) Shift in Fe 3d bands to lower BE at 0<x<1 is discernible. (5) Co 3d band remains at the same BE on fresh and spent catalysts. The above points demonstrate a large interaction among 3d bands of metal ions on spent catalysts compared to fresh catalysts. Finite photoemission at 0 eV also reflects the metallic conductivity, probably due to Cu^0, on x $\leq$ 0.5.

4.2.6.7. Bulk and surface composition

Bulk and surface composition values for all the catalysts are given in Table 2.1 (chapter 2) and Table 4.7, respectively.

Table 4.7: Surface atomic ratio of fresh and spent $Cu_{1-x}Co_xFe_2O_4$ catalysts

x	Fresh			Spent			Spent		
	Cu/Fe	Co/Fe	(Cu+Co)/Fe	Cu/Fe	Co/Fe	(Cu+Co)/Fe	Fe/C	Cu/C	Co/C
0.00	1.17	--	1.17	0.30	--	0.30	0.503	0.152	--
0.25	1.04	0.20	1.24	1.57	0.17	1.74	0.110	0.171	0.019
0.50	0.79	0.32	1.11	1.24	0.40	1.64	0.140	0.173	0.056
0.75	0.50	0.50	1.00	0.60	0.31	0.91	0.091	0.055	0.028
1.00	--	0.75	0.75	--	1.25	1.25	0.282	--	0.354

This exercise is mainly to know about the distribution of metals ions and their heterogeneity on the surface, as it directly influences the catalytic activity. On fresh catalysts, there is a linear relation between the input amount (x) and bulk and surface concentrations measured by XRF and XPS, respectively. High Cu/Fe ratio is found on spent catalysts at 0.25$\leq$x$\leq$0.75. Good amount of C deposition is evident from Table 4.7, however it is relatively less on x = 0 and 1.

It is to be emphasized here (a) the predominant Fe enriched surface at x = 0 changes to Cu+Co enriched surface at x = 0.25 and 0.5 (Table 4.7), on spent catalysts, (b) high coke content and low Co-concentration is observed at x = 0.25 and 0.75, irrespective of its bulk concentration, and (c) (Cu+Co)/Fe varies in a small range of 1±0.25 on fresh catalysts, but the variation is high on spent catalysts. Last point indicates an apparent support like interaction of Fe part of the catalyst and indicates the larger part of Cu and Co in the methylation reaction.

Figure 4.15 displays Cu/(Co+Fe) (Co/Fe for x = 1) ratio calculated from XPS results in left panel and phenol conversion with products selectivity for all compositions in right panel.
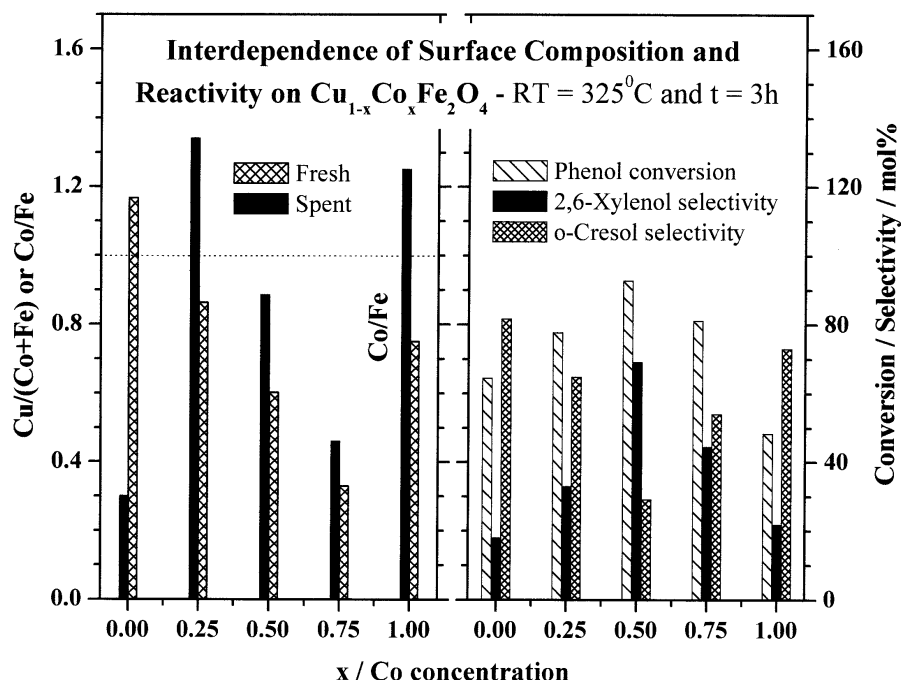
Figure 4.15: Comparison of phenol conversion and ortho products selectivity performance of $Cu_{1-x}Co_xFe_2O_4$ catalysts at 325^{0}C, TOS = 3 h (right panel) and Cu/(Co+Fe) (or Co/Fe) ratio of Cu containing (Cu less) catalysts (left panel). Note the large production of desired 2,6-xylenol and Cu/(Co+Fe) = 0.9 at x = 0.5 composition on spent catalyst.

A correlation between them hints that no single ion but a combination of metal ions, specifically the heterogeneity of the surface, decides the course of the reaction towards high 2,6-xylenol selectivity. When the surface is dominated by a single metal ion (x≤0.25 and x=1),

desired reactivity is not achieved. Further, it is speculated here that it might be the pair of hetero-atoms, say Cu-Co or Cu-Fe, is preferred for two different reactants to be adsorbed in nearby sites for the above desired selectivity and avoid any diffusion. Same trend shown by both Cu/(Co+Fe) and (Cu+Co)/Fe for all x values supports the above points.

4.3. PHENOL ETHYLATION

Properties of the fresh and the spent catalysts that results due to ethylation reaction are compared to understand the changes happened both in bulk and on the surface. Specifically, the spent catalysts were obtained after 10 h reaction (ethanol to phenol ratio of 5, reaction temperature 375^0C). Since the properties of fresh catalysts are already discussed, emphasize is given to discuss much on spent catalysts. However for comparison purposes graphical data for fresh catalysts is also reproduced here along with spent catalysts.

4.3.1. Characterization of $Cu_{1-x}Co_xFe_2O_4$

Figure 4.16 shows XRD patterns of selected compositions of fresh and all spent catalysts. Spent catalysts analyzed by XRD and XPS are after ethylation at 375^0C for 10h with 1:5 composition of PhOH:EtOH, unless otherwise stated.

XRD of spent catalysts shown in Figure 4.16 also displays all characteristics reflections and ascertain the integrity of the spinel structure. In the case of $CuFe_2O_4$ the diffractogram is more uniform, however, presence of metallic Cu, Fe and Fe_xC_y phases are also observed. The intensity of metallic Cu and Fe peaks varies linearly with x, but in an opposite trend indicating the ease in reducibility of Cu>>Fe, for Cu-rich compositions. Decreasing Cu-content (and not an increase in Co-content) increases the reducibility of Fe and very small amount of Fe^0 is seen at x = 1. The above observations demonstrate the reduction conditions simulated during reaction is likely due to ethanol reforming. No change in XRD pattern is observed between fresh and spent $CoFe_2O_4$ hints an irreducible and more robust structure. A small increase in '*a*' and an enhancement of crystallite size is observed on spent catalysts.
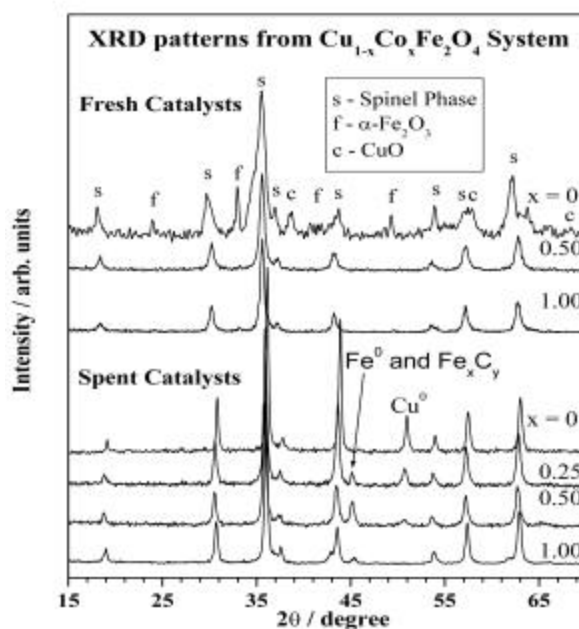
Figure 4.16: X-ray diffractograms of selected compositions of fresh and spent (ethylation) $Cu_{1-x}Co_xFe_2O_4$ catalysts. XRD from spent catalysts are after phenol ethylation reaction at 375^0C for 10 h with 1:5 composition of phenol:ethanol. Note an opposite trend in the intensity of metallic Cu and Fe on spent catalysts.

4.3.2. XPS Analysis

4.3.2.1. Cu 2p core level and CuL$_3$M$_{45}$M$_{45}$

Figure 4.17 displays the photoemission spectra of Cu $2p_{3/2}$ core level from fresh (a) and spent (b) $Cu_{1-x}Co_xFe_2O_4$ catalysts. Several interesting and new features can be seen from the Cu $2p_{3/2}$ XPS results of spent catalysts (Figure 4.17b) compared to fresh catalysts. The main features in this spectral region are due to Cu^{2+} species exhibited at a BE of 934.2 along with the satellites around 942 eV and Cu^+ (and/or Cu^0) at 932.6±0.1 eV. Deconvolution reveals the contribution of the above two Cu-species and Cu-reducibility in terms of Cu^+/Cu^{2+} is shown in Figure 4.17c along with I_s/I_m. For simplicity, deconvolution is shown only for x = 0.75 in Figure 4.17b and the results are given in Table 4.8.

Main results from Figure 4.17a-c are highlighted in the following: (1) Cu^{2+} species got partially reduced to Cu^+ at all x values during reaction; however Cu reducibility

remains close to 0.44 between x = 0 and 0.5, whereas this ratio is 0.3 at x = 0.75. (2) I_s/I_m ratio of x = 0.75 composition increased considerably from fresh to spent, while other compositions does not show a considerable change. Above two points clearly indicates that only at relatively large Co-concentration (x = 0.75), it influences the electronic state of Cu-species significantly.
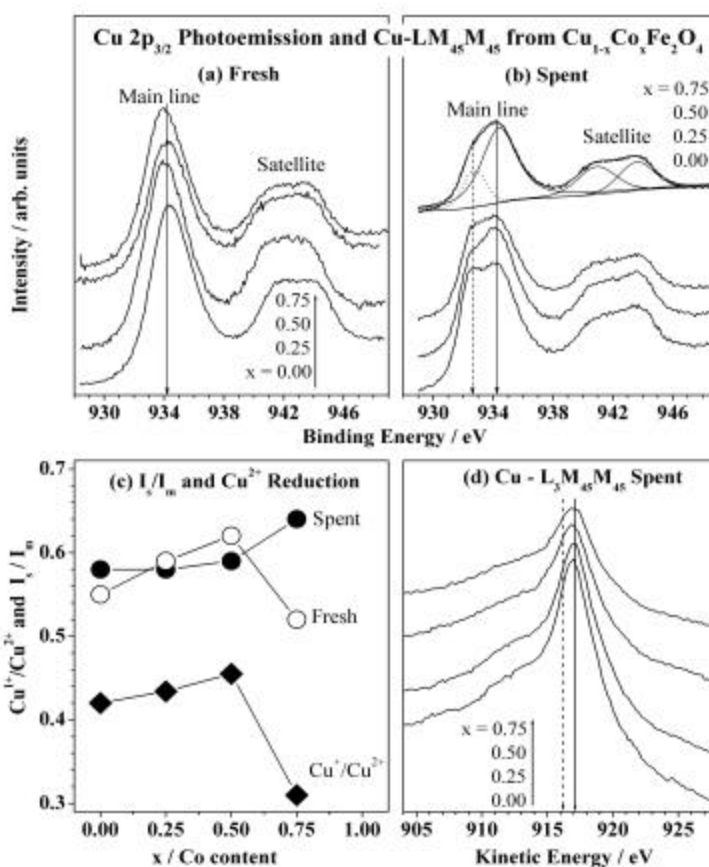
Figure 4.17: Cu 2p photoemission spectra of (a) fresh and (b) spent (ethylation) $Cu_{1-x}Co_xFe_2O_4$ catalysts. Deconvolution clearly shows both Cu^+ and Cu^{2+} on spent catalysts. Panel c shows the satellite to main line intensity ratio (I_s/I_m) for fresh (F) and spent (S) catalysts and the ratio of reduced Cu to that of Cu^{2+} on spent catalyst. Note a slight increase in the reducibility of Cu from x = 0 to 0.5 and a sudden decrease at x = 0.75. (d) Cu $L_3M_{45}M_{45}$ Auger electron spectra from spent catalysts.

Table 4.8: XPS and XAES parameters of $Cu_{1-x}Co_xFe_2O_4$ catalysts

Catalyst composition (x)	BE of Cu $2p_{3/2}$ (FWHM) (eV)	KE of Cu $L_3M_{45}M_{45}$ (eV)	a' (eV)
0.00^S	932.4, 934.1 (4.0)	916.3, 917.0	1848.7, 1851.1
0.25^S	932.6, 934.3 (3.8)	916.2, 917.0	1848.8,1851.3
0.50^S	932.6, 934.3 (3.9)	916.3, 916.8	1848.9,1851.1
0.75^S	932.6, 934.4 (3.6)	916.1, 916.9	1848.7, 1851.3

F and S indicate the fresh and spent catalysts.

Lower valent Cu species can be distinguished by examining the Cu $L_3M_{45}M_{45}$ Auger peaks. The Cu $L_3M_{45}M_{45}$ Auger spectra of spent catalysts are shown in Figure 4.17d and the modified Auger parameter (α') [7] values calculated are given in Table 4.8. All the compositions exhibit a peak around 917.0 eV (solid arrow) with a broadening at lower kinetic energy (KE) of 916.2 eV (dotted arrow). It should be noted here that the KE of Cu $L_3M_{45}M_{45}$ peak for CuO, Cu_2O and Cu occur at 917.6, 916.5 and 918.4 eV (Table 4.5) respectively [7-9], and depending on the chemical environment and geometry, the KE of this line has been found to shift significantly. The present value suggests the contribution of both Cu^+ and Cu^{2+} and no Cu^0 on spent samples. In conclusion, there is no significant distortion of Cu^{2+} from fresh to spent catalysts for x≤0.50 and the distortion is considerable at x = 0.75. High polarizability induced by the formation of Co-containing spinel would change the nature of Cu-O bonds, especially at high Co-content [12].

4.3.2.2. Co 2p core level and Co-$L_3M_{45}M_{45}$ auger transitions

Figure 4.18 shows Co $2p_{3/2}$ XPS of (a) fresh and (b) spent catalysts and (c) Co-$L_3M_{45}M_{45}$ Auger spectra of x = 0.5 and 1. Main XPS derived values of Co 2p levels are given in Table 4.9. The important features observed from Co 2p spectra (Figure 4.18, Table 4.6 and Table 4.9) are: (1) I_s decreases with increasing x. (2) The energy gap between $2p_{3/2}$ peak and its satellite increases with increase in Co-content, especially on

spent catalysts (arrow in Figure 4.18b). (3) Energy gap between Co 2p spin orbit doublets (data not shown) increases from fresh to spent catalysts. (4) Two satellite peaks are discernible at x = 0.75 and 1; however only the high BE satellite appears at x = 1 on spent catalyst. A comparison of catalysts and various Co-compounds reported in the literature [20], clearly indicates that the catalysts are in general composed of both Co^{2+} and Co^{3+}. High I_s for x≤0.5 suggests the contribution of Co^{2+} and high spin Co^{3+}, as low spin Co^{3+} shows poor I_s [13-15].

Co-$L_3M_{45}M_{45}$ Auger spectra of x = 0.5 and 1 compositions are shown in Figure 4.18c exhibit broad features between 760 and 780 eV. Two features seen at 768 and 772 eV are virtually the same for both fresh and spent catalysts for x =1. However at x = 0.50 (and 0.75) a shift in energy is seen for lower KE component on spent catalyst compared to fresh. These changes indicate a definite Cu-Co interaction from near neighbor sites and probably a site-specific interaction.
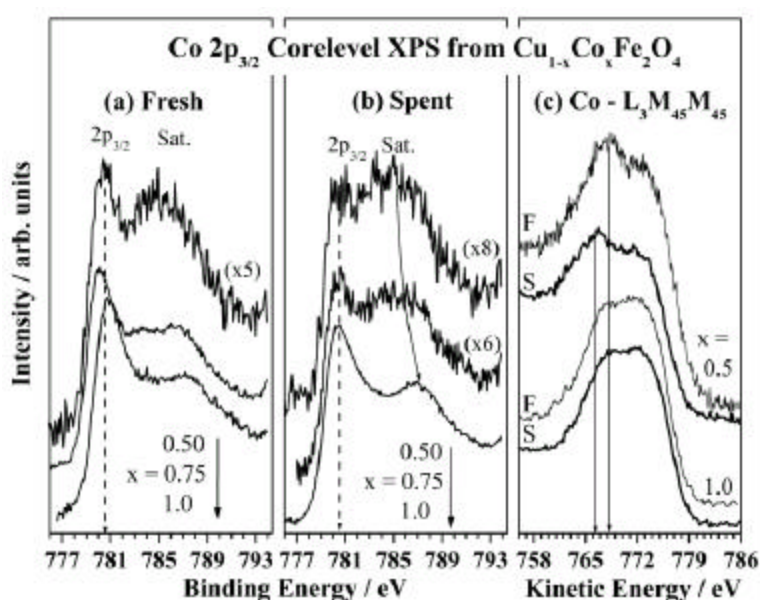
Figure 4.18: Co 2p core level photoelectron spectra of (a) fresh and (b) spent (ethylation) $Cu_{1-x}Co_xFe_2O_4$ catalysts. Note a decreasing satellite intensity with increasing x on fresh and spent catalysts. (c) XAES from Co $L_3M_{45}M_{45}$ of fresh and spent $Cu_{1-x}Co_xFe_2O_4$ catalysts for x = 0.5 and 1. Note the changes observed in energy and intensity at x = 0.5 from fresh to spent catalysts by two arrows, respectively.

Table 4.9: XPS parameters from Co 2p core level in $Cu_{1-x}Co_xFe_2O_4$ catalysts

Composition (x)	BE of Co $2p_{3/2}$ mainline (mainline-satellite energy gap) (eV)	$2p_{3/2}$-$2p_{1/2}$ mainline energy gap (eV)
0.5^S	780.7 (3.5 and 5.5)	15.8
0.75^S	780.6(3.9 and 5.6)	16
1.0^S	780.5 (6.5)	15.9

F and S indicate the fresh and spent catalysts.

4.3.2.3. Fe 2p core level and Fe-$L_3M_{45}M_{45}$

Figure 4.19 shows the Fe $2p_{3/2}$ peak and the satellite associated for both (a) fresh and (b) spent $Cu_{1-x}Co_xFe_2O_4$ catalysts. Fresh catalysts exhibit predominant Fe^{3+} at a BE of 711 ± 0.2 eV and spent catalysts shows mixed valent Fe.

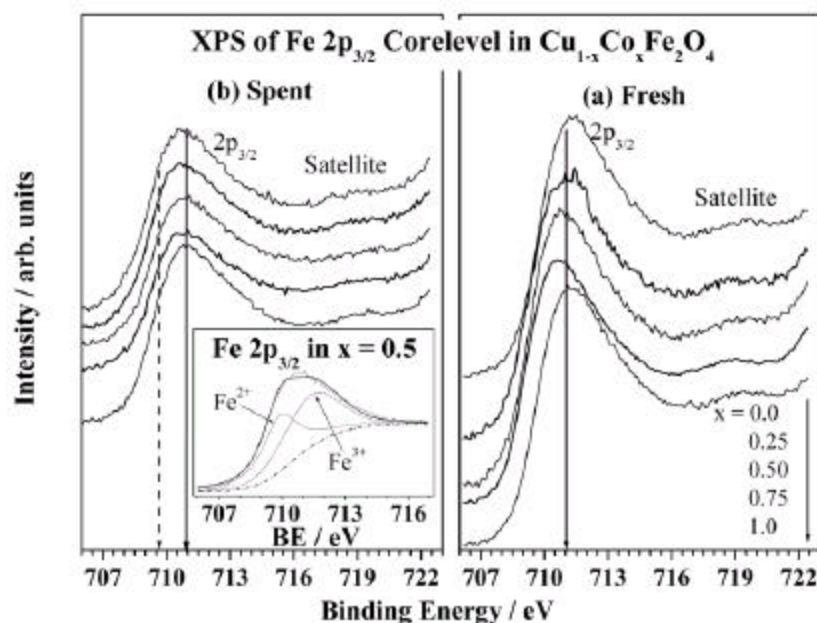**Figure 4.19:** Fe 2p core level XPS of (a) fresh and (b) spent (ethylation) $Cu_{1-x}Co_xFe_2O_4$ catalysts. A shoulder is seen below 710 eV on spent catalysts (dotted line) indicates the partial reduction of iron. Deconvolution of Fe $2p_{3/2}$ peak demonstrate Fe^{2+} and Fe^{3+} on spent catalyst at x = 0.5, in the inset on left panel.

Three important differences between the fresh and spent catalysts are: (a) a clear satellite, due to predominant Fe^{3+} in O_h coordination, is observed on fresh catalysts; (b) partial reduction of iron is evident on all spent catalysts from the shoulder around 709.6 eV and weak I_s, characteristic of Fe^{2+} in T_d coordination [16,17] (broken line in Figure 4.19b) and, (c) ratio of Fe^{2+}:Fe^{3+} on spent catalysts, (shown by deconvolution for x = 0.5 in the inset in Figure 4.19b), for all compositions is close to 1:1 indicates the partial reduction of Fe. Fe LMM Auger spectral results (not shown) also indicate the partial reduction of Fe^{3+} occurs on spent catalysts.

4.3.2.4. Valence band studies

Figure 4.20 shows the VB photoemission spectra of $Cu_{1-x}Co_xFe_2O_4$ for both fresh and spent catalysts.
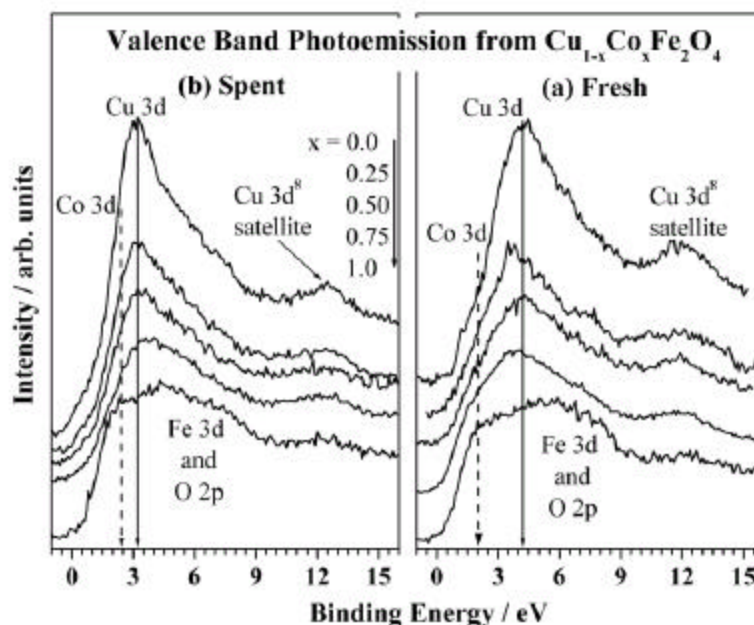
Figure 4.20: Valence band XPS of (a) fresh and (b) spent (ethylation) $Cu_{1-x}Co_xFe_2O_4$ catalysts. A significant decrease in energy gap between the 3d levels of Cu and Co and a decrease in overall band width is observed on spent catalysts.

Changes observed on spent catalysts from core levels are reflected strongly in the VB too. The main VB observed below 10 eV have contributions from metal 3d and O 2p bands and

the assignments of various bands are from the photo ionization cross section values (σ) at $h\nu = 1253.6$ eV [18] and as explained in methylation case [20]. Briefly, σ of various bands decreases Cu 3d>Co 3d>Fe 3d>>O 2p and indicates large and negligible contribution from Cu 3d and O 2p, respectively to VB.

The important observations made from VB region are listed below. (1) Cu and Co 3d bands are separated by more than 2 eV on fresh catalysts; however on spent catalysts the 3d bands overlap strongly in such a way that the energy gap is less than 1 eV (arrows in Figure 4.20b). (2) Satellite responsible for Cu^{2+} still appears on all Cu-containing spent catalysts with diminished intensity between 10 and 15 eV. (3) Considerable amount of density of states is observed close to 0 eV BE on spent catalysts compared to no intensity on fresh catalysts. (4) A clear shift in Fe 3d bands to lower BE is discernible on all spent catalysts compared to fresh catalysts. (5) Co 3d bands remains at the same BE on fresh and spent catalysts. (6) A general narrowing of metal ions 3d bands on spent catalysts is observed. Above points illustrate a large increase in overlap of 3d bands of metal ions on spent catalysts compared to fresh catalysts.

4.3.2.5. Surface composition

Surface composition values for both fresh and spent catalysts from XPS are given in Table 4.10. This data is helpful to understand the distribution of metal ions and their heterogeneity on the surface, as it directly influences the catalytic activity.

Table 4.10: Surface atomic ratio of fresh and spent $Cu_{1-x}Co_xFe_2O_4$ catalysts after ethylation.

x	Fresh			Spent			Spent		
	Cu/Fe	Co/Fe	Cu/Co+Fe	Cu/Fe	Co/Fe	Cu/Co+Fe	Fe/C	Cu/C	Co/C
0.00	1.17	--	1.17	1.26	--	1.26	0.35	0.44	--
0.25	1.04	0.20	0.86	1.45	0.18	1.23	0.36	0.53	0.065
0.50	0.79	0.32	0.60	1.45	0.30	1.12	0.21	0.31	0.063
0.75	0.50	0.50	0.33	1.42	0.33	1.07	0.13	0.19	0.044
1.00	--	0.75	0.75[a]	--	1.05	1.05[a]	0.46	--	0.49

The important points worth mentioning are as follows: (1) Cu/Fe, Co/Fe and Cu/Co+Fe ratio changes linearly with x on fresh catalysts; however the surfaces are generally dominated by Cu^{2+} ions considering the bulk Cu-content, (2) high Cu/Fe and Cu/Co+Fe ratios were found on spent catalysts in comparison with fresh catalysts, in spite of increasing Co-content; however, Co-content on the spent catalysts surface do not vary proportionately with bulk concentration for x<1, (3) good amount of coke deposition is evident at all compositions, however it is high at x = 0.75, (4) nearly same Cu/Fe ratio (1.45) is found at 0>x<1 indicates the surface dominance by Cu on spent catalysts too, and (5) heterogeneity of the surface due to distribution of all metal ions is high at x = 0.50 and 0.75.

Figure 4.21 displays Cu/Fe and Co/Fe ratio calculated from XPS results for fresh and spent catalysts in left panel and PhOH conversion with EtPhOH yield at a reaction temperature of 375^0C and TOS = 10 h in right panel, for all compositions.
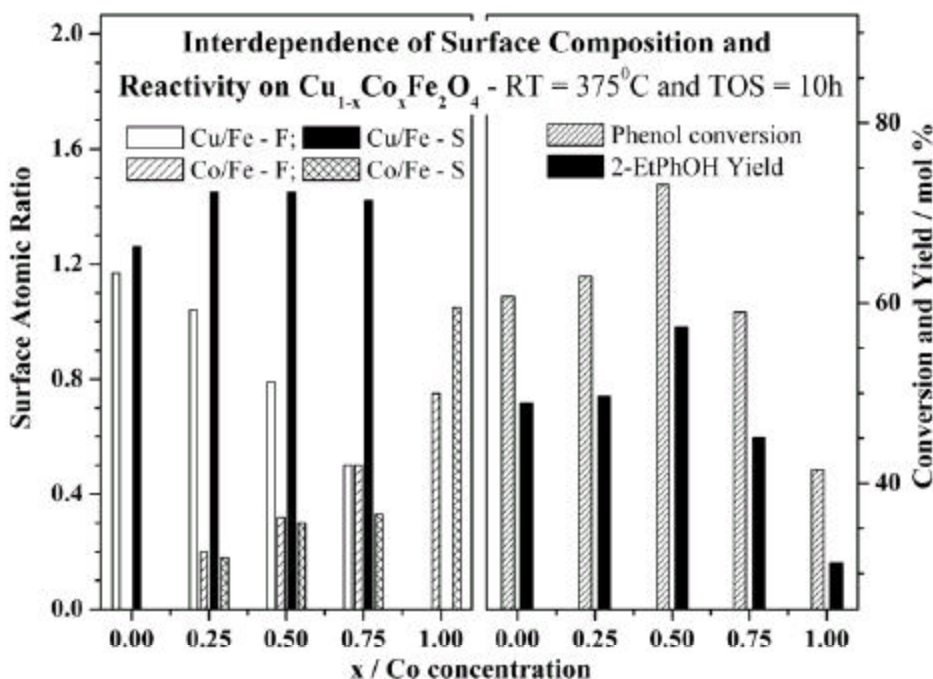

Figure 4.21: Comparison of phenol conversion and 2-EtPhOH yield on $Cu_{1-x}Co_xFe_2O_4$ catalysts at 375^0C, TOS = 10 h (Right panel) and atomic ratio of Cu/Fe and Co/Fe for all fresh (F) and spent (S) catalyst compositions. Note the influence of Co-content and product yield, which is high at x=0.5 (Left panel).

It is very clear that the combination of Cu+Co species decides the catalytic activity rather than a single metal ion and it is evident from the excellent correlation of atomic ratio with reactivity at $0 > x < 1$. Better activity at $x = 0.5$ hints the importance of 1:1 bulk ratio of Cu:Co. A heterogeneous distribution of reactive Cu species with a combination of Co and Fe is seen at all intermediate compositions. Low PhOH conversion at $x = 1$ hints the poor catalytic activity of $CoFe_2O_4$.

4.4. COMPARISON OF DIFFERENT PHENOL ALKYLATIONS

Figure 4.22 shows a comparative study of phenol alkylation using different alcohols and or alkene as alkylating agent.
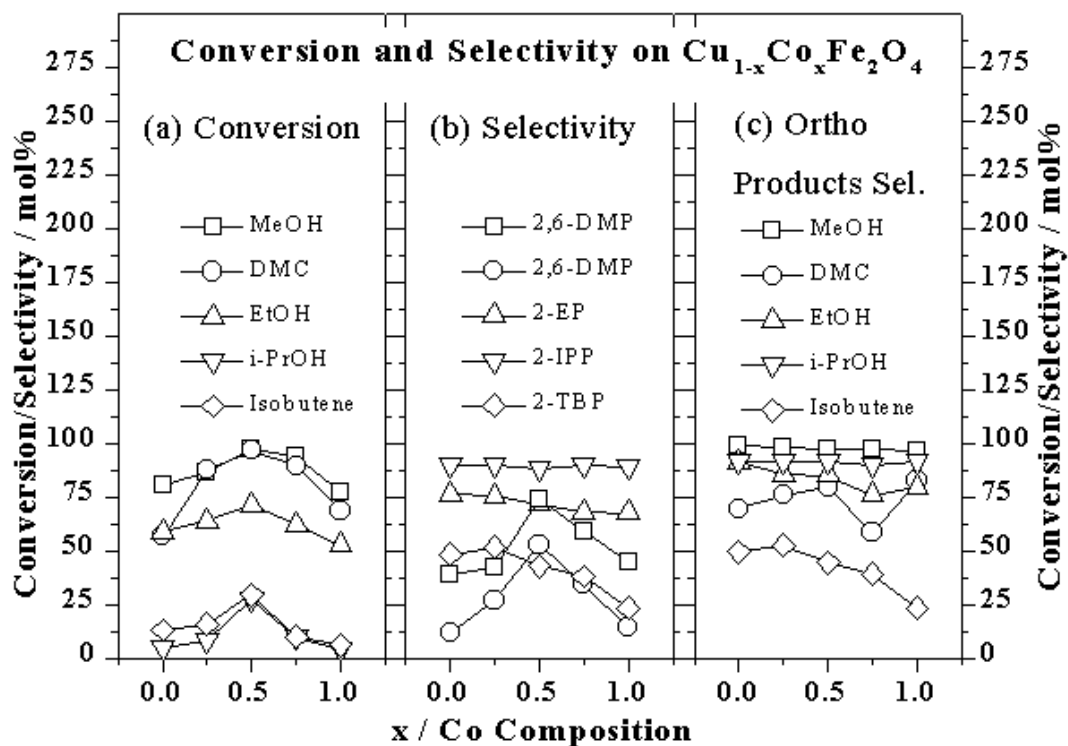

Figure 4.22: Composition dependence of (a) phenol conversion (b) major product selectivity and (c) total ortho alkyl phenol selectivity for different alkylating agents. Same symbol is used for a particular alkylating agent in all panels.

From the kinetic results, it is clear that x = 0.50 composition shows better activity irrespective of the alkylating agent. Hence XRD and XPS analysis were carried out on x = 0.50 composition after the alkylation reaction at optimum conditions. The spent catalysts are obtained after TOS = 10 h under the optimum conditions for each alkylation reaction. The optimum reaction temperature for phenol methylation (for both methanol and DMC) and isopropylation are 350^0C; for ethylation at 375^0C and for butylation at 200^0C. It is interesting to note the dependence of surface composition with activity when different alkylating agents used for phenol alkylation.

4.4.1. Characterization of $Cu_{0.50}Co_{0.50}Fe_2O_4$

Figure 4.23 shows XRD patterns of composition x = 0.50 of fresh and all spent catalysts.
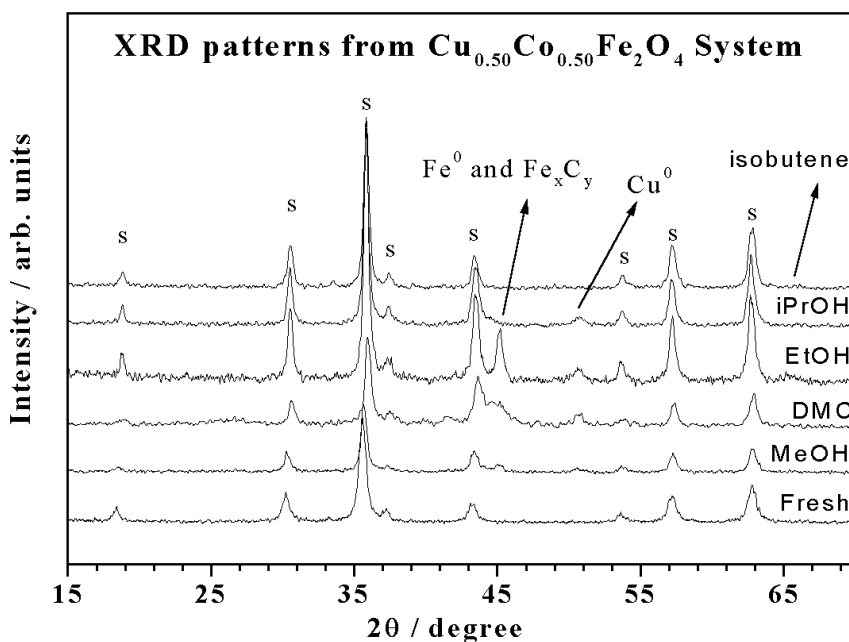
Figure 4.23: X-ray diffractograms of fresh and spent $Cu_{0.50}Co_{0.50}Fe_2O_4$ catalysts. XRD from spent catalysts are after phenol alkylation reaction using different alkylating agents under the respective optimum conditions for 10 h.

XRD of spent catalysts shown in Figure 4.23 also displays all characteristics reflections and ascertain the integrity of the spinel structure. Presence of metallic Cu, Fe and Fe_xC_y phases are observed on all the spent catalysts except for butylation. The intensity of metallic Cu and Fe peaks varies as the alkylating agent changes. This demonstrates the reduction conditions simulated during reaction varies with the alkylating agent. A small increase in '*a*' and an enhancement of crystallite size is observed on spent catalysts.

4.4.2. XPS Analysis

4.4.2.1. Cu 2p core level

Figure 4.24 presents the Cu 2p core level photoemission spectra of fresh as well as spent catalysts that results due to various phenol alkylation reaction on x = 0.50.

Figure 4.24: Cu 2p photoemission spectra of fresh and spent $Cu_{0.50}Co_{0.50}Fe_2O_4$ catalysts. Spent catalysts are obtained after phenol alkylation using different alcohols / alkene as alkylating agent at optimum conditions.

Several interesting and new features can be derived from the Cu $2p_{3/2}$ XPS spectra of spent samples compared to the fresh one. The main features in the Cu $2p_{3/2}$ spectral region of spent catalysts are Cu^{2+} and Cu^+ species at BEs of 934.2±0.1 eV and 932.5±0.1 eV respectively.

Following important points can be drawn out from Cu 2p photoemission spectra:

(1) Cu^{2+} species got fully reduced to Cu^+ in the case of DMC and isopropyl; however partially reduced to Cu^+ in all other cases.

(2) Presence of Cu^{2+} species is confirmed from the associated satellite feature around 942 eV on above partially reduced alkylation cases.

(3) The extent of reduction on Cu^{2+} species depends on the alkylating agent.

The above features are further confirmed from XAES results (not shown).

4.4.2.2. Co 2p core level

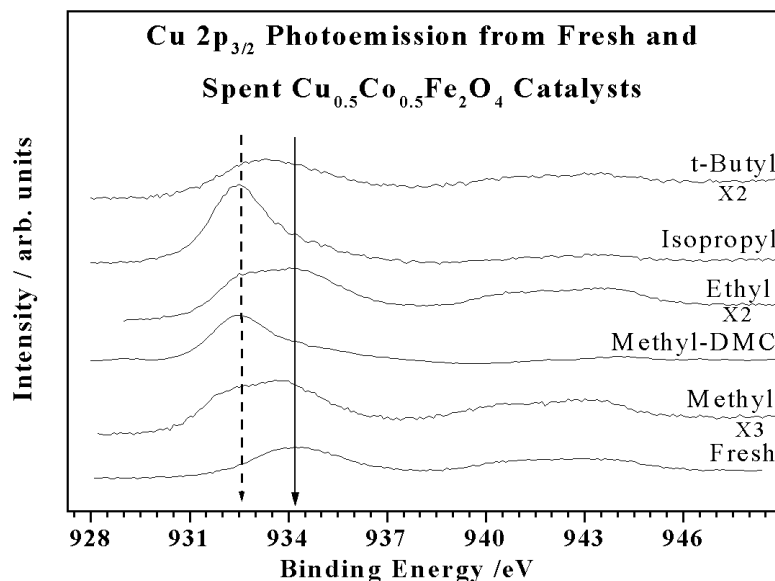Co 2p photoemission spectra of spent catalysts are shown in Figure 4.25 along with the fresh one.
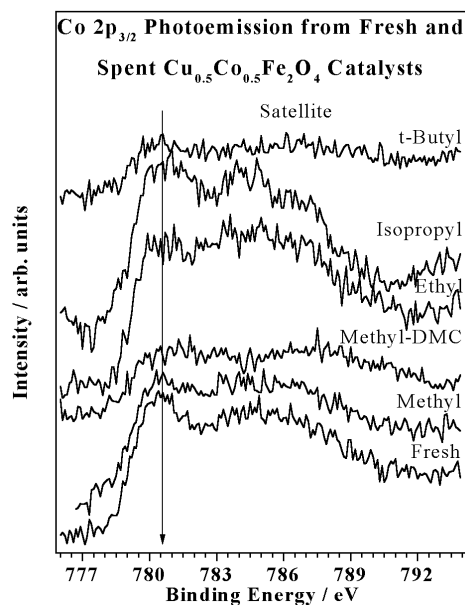
Figure 4.25: Co 2p photoemission spectra of fresh and spent $Cu_{0.50}Co_{0.50}Fe_2O_4$ catalysts. Spent catalysts are obtained from phenol alkylation using different alcohols / alkene as alkylating agent at optimum conditions.

The important feature observed from Co 2p photoemission spectra is the intensity of $2p_{3/2}$ peak and its associated shake up satellites is decreased very much for spent $x = 0.50$ composition obtained after methylation with DMC and t-butylation reaction in comparison with other alkylating agents.   Apart from the above, there is no significant difference among all the spectra.

4.4.2.3. Fe 2p core level

Figure 4.26 shows the Fe $2p_{3/2}$ peak and the satellite associated with $2p_{3/2}$ level for $x = 0.50$ composition after various alkylation reactions along with the fresh catalyst.
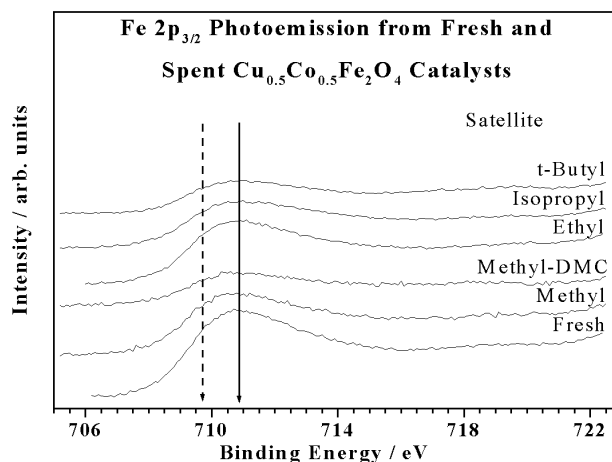
Figure 4.26: Fe $2p_{3/2}$ photoemission spectra of fresh and spent $Cu_{0.50}Co_{0.50}Fe_2O_4$ catalysts. Spent catalysts are obtained from phenol alkylation using different alcohols / alkene as alkylating agent at optimum conditions.

The important features derived from the spectra due to various alkylation reactions are:

(1) The intensity of $2p_{3/2}$ peak at 710.8 eV and the associated satellite diminishes from fresh to spent and it is pronounced more on spent resulted after methylation reaction (with both methanol and DMC as alkylating agents).

(2) Partial reduction of iron is evident on all spent catalysts from the shoulder around 709.7 eV and weak I, characteristic of Fe^{2+} in T_d coordination (broken line in Figure 4.26), as explained in methylation and ethylation cases, earlier.

4.4.2.4. Valence band photoemission

Figure 4.27 shows the VB photoemission spectra of fresh as well as spent catalysts for x = 0.50 composition after various alkylation reactions.

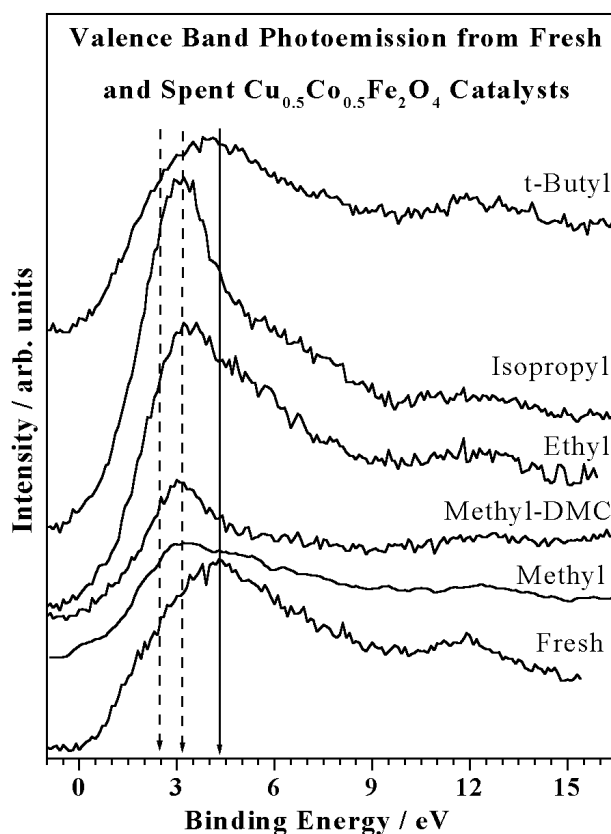**Figure 4.27:** Valence band XPS of fresh and spent $Cu_{0.50}Co_{0.50}Fe_2O_4$ catalysts. Spent catalysts are obtained from phenol alkylation using different alcohols / alkene as alkylating agent at optimum conditions. A significant decrease in energy gap between the 3d levels of Cu and Co and a decrease in overall band width is observed on all spent catalysts except for butylation.

The important observations derived from VB region are:

(1) The Cu and Co 3d band separation of 2 eV observed on fresh x = 0.50 composition is reduced to 1 eV on spent catalysts. However the catalysts after butylation reaction shows almost similar pattern as that of fresh one.

(2) Except butylation, considerable amount of density of states is observed close to 0 eV BE on other spent catalysts compared to no intensity on fresh catalysts.

(3) The Cu 3d bands centered at 4.3 eV on fresh x = 0.50 composition is found to be shifted towards Co 3d region accompanied with the narrowing of Cu 3d bands.

(4) Satellite responsible for Cu^{2+} still appears on all spent catalysts with diminished intensity between 10 and 15 eV.

(5) Shift in Fe 3d bands to lower BE is discernible for all the spent except butylation.

(6) Co 3d bands remains at the same BE on fresh and spent catalysts.

All the above points illustrate a large increase in overlap of 3d bands of metal ions on spent catalysts compared to the fresh x = 0.50 except after butylation.

4.4.2.5. Surface composition

Surface composition in terms of Cu/Fe and Co/Fe atomic ratio for all the spent catalysts for x = 0.50 are given in Figure 4.28 (left panel). Phenol conversion and the respective ortho alkyl phenol selectivity are given in Figure 4.28 (right panel).

The important observations from surface analysis are:

(1) Cu/Fe ratio is higher than Co/Fe ratio on all spent catalysts, eventhough bulk Cu:Co ratio is 1.

(2) Highest (Cu+Co)/Fe ratio is found on spent resulted from methylation with DMC and lowest (Cu+Co)/Fe ratio is on butylation spent.

(3) Generally as the size of alkyl group increases (Cu+Co)/Fe ratio decreases on spent.
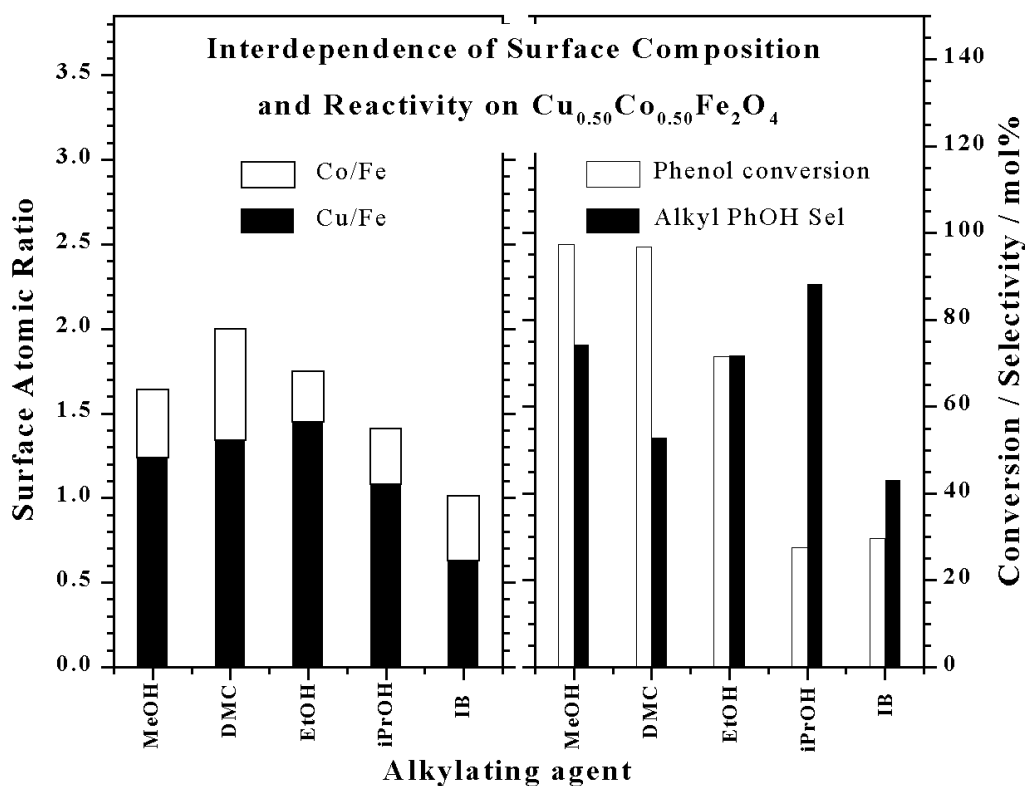
Figure 4.28: Comparison of phenol conversion and ortho products selectivity performance of $Cu_{0.50}Co_{0.50}Fe_2O_4$ catalyst for different alkylating agents at optimum condition, t = 3 h (right panel) and Cu/Fe and Co/Fe ratio (left panel).

From the comparison between surface atomic ratio and phenol alkylation activity, it is clear that spent catalysts having high Cu/Fe atomic ratio show high catalytic performance. Thus spent catalysts resulted after methylation (with both methanol and DMC) and ethylation possess relatively high Cu/Fe atomic ratio and in all these three cases high phenol conversion is observed. Whereas for the spent catalysts of both isopropylation and butylation cases low Cu/Fe atomic ratio is observed and the phenol conversion is less for both cases. Thus it can be concluded that high Cu-content on the surface is an essential requisite for better catalytic performance and large Fe-content on the surface, reduces the catalytic activity, as already explained in methylation cases (x = 0.00) cases.

SECTION II

4.5. INTRODUCTION

Observations derived from the analysis of the spent catalysts are discussed in detail in this section. The analysis of the spent catalysts obtained from various phenol alkylations revealed similar structural changes. Hence we restrict this discussion part in terms of catalytic activity to methylation, and structural changes are discussed in detail.

Regarding phenol methylation the results fullfill the expectations: the mixed Cu-Co ferrites exhibit the highest activities, the conversion of phenol exceeds significantly the activities shown by the $x = 0$ and $x = 1$ samples at $T \leq 350 \ ^0C$. The three dominant effects of the mixing of the Cu and Co ferrites, viz. possible changes in the bulk structure (occasional phase separation), changes in the oxidation state of the altervalent ions (included the redistribution of iron in (A) and [B] sites), and formation of different carbonaceous deposits are discussed in the forthcoming paragraphs. The most important finding is for efficient dimethylation Cu-Co interaction in the $Cu_{1-x}Co_xFe_2O_4$ spinel system is very much essential, which is demonstrated through the changes in oxidation state and overlap of 3d bands of transition metal ions, elucidated from XPS studies.

4.6. DISCUSSION

4.6.1. Chemical state and distribution of transition metal ions in $Cu_{1-x}Co_xFe_2O_4$ system

Spent catalysts show predominant spinel phase and small amount of metallic Cu, iron carbide and Cu_2O due to reductive atmosphere under methylation conditions. Nonetheless Cu^0 and Fe^0 are not observed in XPS results (Figures 4.8 and 4.12) at any composition hints the surface metal atoms are oxidized. However, coke deposition prevents the oxidation of metal species in the bulk and seen in XRD. This also indicates the inevitable structural collapse to some extent at $x = 0.0$; nevertheless, the structural integrity retained is high at $x \geq 0.25$ and confirmed from XRD. Surface area increases after reaction on $x = 0.5$ and 0.75 and the same decreases at other compositions. At $x = 0.0$ and 0.25 it is probably due to agglomeration of Fe and Cu particles, respectively, (Figure 4.15). Nonetheless, $x = 0.5$ shows uniform distribution

of all the ions and copper being the major species supports its high activity. All the above indicates there is a considerable redistribution of the cations under reaction conditions, especially at 0<x<1.
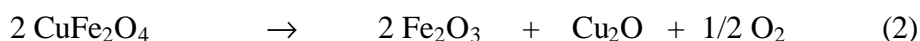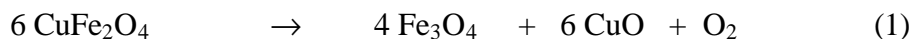
It is evident that above such modifications occurs in the case of ethylation spent catalysts too. Seemingly, there is an apparent correlation between surface area and phenol conversion. It is to be noted here that the surface area of $Cu_{1-x}Co_xFe_2O_4$ system prepared by high temperature glycine nitrate combustion method [21] exhibit <2 m^2/g for all compositions and show low methylation activity (results not shown) but follows the same trend as that of samples prepared by co-precipitation. This indicates the surface area is not a dominating factor in methylation reactions.

The reaction conditions imposed over the catalyst due to other phenol alkylation reaction were also reducing. However the extent of reduction depends on the alkylating agent as well as the reaction conditions. Decomposition of alcohols occurs along with alkylation results in formation of CO, H_2 and hydrocarbons, which are sufficient enough to reduce the fresh catalyst. Thus the reaction ended with the reduction of Cu^{2+}, Fe^{3+} and Co^{3+} ions to its lower oxidation states as in the case of methylation but to different extents. Spent catalysts show predominant spinel phase and small amount of Cu, $\propto$-Fe, Fe_xC_y and Cu_2O.

4.6.2. Changes in the bulk structure - extent of the expected phase separation

It is known that the $CuO + Fe_2O_3 = CuFe_2O_4$ process is slightly endothermal, thus decomposition of the Cu ferrite might proceed spontaneously. In fact, for the Cu ferrite, this presumption has clearly proven by XRD, TG-DTA and Mössbauer studies. The X-ray diffractograms recorded both on the fresh and spent $CuFe_2O_4$ samples display the presence of other Cu, CuO, Fe_2O_3, etc. phases as well. In addition, the comparison of the fresh and spent catalyst exhibits far the largest shift in the value of 'a' lattice parameter, indicating a noticeable change in the structure upon treatment. In correspondence, the Mössbauer spectra recorded on the $CuFe_2O_4$ samples exhibit characteristic shapes, e.g. the spectrum of the spent catalyst might be used as a textbook illustration for magnetite.

TG data also provide some insight about to what extent the reduction and the associated phase separation is occurred on various compositions due to reaction. If we assume only Fe^{3+} and Cu^{2+} ions are reduced and if it is happened only to the level of Cu^{+} and Fe^{2+}, then theoretically it is possible to calculate the degree of reduction [22]. This can be illustrated by considering the reduction of $CuFe_2O_4$. Following three important cases is considered for calculating the degree of reduction.

$$6\,CuFe_2O_4 \quad \rightarrow \quad 4\,Fe_3O_4 \;+\; 6\,CuO \;+\; O_2 \qquad (1)$$

$$2\,CuFe_2O_4 \quad \rightarrow \quad 2\,Fe_2O_3 \;+\; Cu_2O \;+\; 1/2\,O_2 \qquad (2)$$

$$6\,CuFe_2O_4 \quad \rightarrow \quad 4\,Fe_3O_4 \;+\; 3\,Cu_2O \;+\; 5/2\,O_2 \qquad (3)$$

Degree of reduction = {1 – (reduced species/oxidized species)} * 100

For example, the degree of reduction for the first case can be expressed as

Degree of reduction = { 1 – ($4Fe_3O_4$, $6CuO$/ $6CuFe_2O_4$)} * 100

The degree of reduction for other two cases as well for other compositions is calculated in this way and the results are given in Table 4.11 along with experimental weight gain.

Table 4.11: Experimental and calculated values of degree of reduction of spent samples of composition $Cu_{1-x}Co_xFe_2O_4$

Composition	Degree of reduction (%)			
(x)	Experimental value	Calculated value for different type of reaction		
		Fe^{3+}®Fe^{2+}	Cu^{2+}®Cu^{+}	Fe^{3+}®Fe^{2+} & Cu^{2+}®Cu^{+}
0.0	6.14	2.23	3.35	5.58
0.25	5.84	2.24	2.52	4.76
0.50	2.40	2.25	1.69	3.94
0.75	1.31	2.26	0.85	3.11
1.0	Not detected	2.27	-	2.27

From the Table 4.11 it is clear that composition x = 0 and 0.25 exceed the calculated value of all the above three cases (note that process 3 is the algebraic sum of processes 1 and 2). This indicates in these two cases reaction brought reduction of Fe^{3+} and Cu^{2+} to significant extent and reduction did not end to the level of Cu^+ and Fe^{2+}. It is further reduced partially to metallic state in Cu-rich catalysts. As the Co content increases, the degree of reduction also decreases in the same trend and the experimental weight gain for the remaining three cases is less than the calculated value indicate reduction might occur partially on both Cu^{2+} and Fe^{3+}. The results are in well agreement with the observation from XRD, Mossbauer, TPR and XPS studies.

For the mixed Cu-Co ferrite catalysts (0 < x < 1), phase separation is hardly detected. At the x= 0.25 sample a slight segregation of copper may still occur, however simultaneous incorporation of copper into the spinel phase is unambigous (The 'a' lattice parameter is different, the change is less expressed upon reaction. Mössbauer spectra display more homogeneous distribution for iron – i.e. [B] sites start to accommodate Cu and later Co ions as well).

4.6.3. Structural effects due to the reducing reaction conditions

The reaction conditions applied over the catalyst were definitely reducing, since the used optimal methanol to phenol ratio was 5, far exceeding the value of 2 (nominal by the reaction stoichiometry). The reducing effects can primarily be reflected in three aspects. First, reduction may proceed on the separate CuO phase as $Cu^{2+} \rightarrow Cu^+$ and in a second stage to metallic Cu. The second group can be composed from further indirect signs of the reduction occuring in the spinel phase. Concerning the third manifestation for structural changes, the redistribution of altervalent ions in the bulk spinel lattice can be considered. (It is possible to follow the change of the distribution of iron ions between (A) and [B] sites by applying Mössbauer spectroscopy.)

As for the first process, the reduction of copper is clearly proven by XRD with detecting the appearance of metallic copper. (In the previous subsection occasional phase separation was assumed for Cu ferrite, and in a smaller extent to the x= 0.25 sample. Thus, the phase separation may indirectly promote reduction as well.) It should also be noted that

copper may probably play a significant role in promoting the reduction – even without forming an extended separate metallic copper phase. For example, in TPR profiles the temperature of the Fe^{3+} to $Fe^{3+/2+}$ is significantly shifted to lower temperatures in the copper-rich x= 0, 0.25 and 0.5 samples. Another evidence for the Cu-enhanced reduction is the appearance of χ-iron carbide phase in detectable amounts in Mössbauer spectra of the Cu-rich mixed samples (c.a. 20 % spectral area in the x= 0.25, and c.a. 12 % contribution in the x= 0.5 sample). The third evidence is the appearance of zerovalent iron in the X-ray diffractogram of the x= 0.5 sample.

The second group of signs for reduction consists of some indirect observations. Among these, the effect of reduction is clearly proven by XRD. Namely, the 'a' lattice parameter is significantly larger for the spent catalysts. This increase can simply be attributed to reduction, since ions in lower valent state have larger ionic radii than those exhibited by the same altervalent ions in higher oxidation states. With regard to the extent of reduction, the samples vary in dependence of composition. It is seen e.g., when comparing the 'a' lattice constants of the fresh and spent catalysts; 1.7, 0.7, 0.7, 0.5, and 0.2 pm-s are found as x varies from 0 to 1 in the samples, respectively. Another evidence for reduction is that the amounts of consumed hydrogen were almost an order of magnitude smaller on the spent catalysts than the respective amounts taken up by the fresh, oxidized samples in the TPR studies in the low temperature region (130 – 420 ^{0}C). The extent of reduction is strongly correlated with the copper content as clearly revealed in TPR profiles (Figure 4.4). For the cobalt ferrite (x= 1) only a slight commencement of reduction can be detected below the reaction temperature, cobalt and iron ions are hardly reduced at 360 ^{0}C > T.

The third effect of the reduction is the change of distribution of ions between the (A) and [B] sites. It should also be added here, that not only the distribution and the oxidation state may be influenced by the redox processes; the full amount of lattice cations may change, as well. (For example: both magnetite, Fe_3O_4 and maghemite, γ-Fe_2O_3, have the same spinel structure, in the latter structure cation vacancies compensate the exclusive Fe^{3+} oxidation state). As for the [A] and [B] positions, the $CuFe_2O_4$ is in full accordance with the previous observations on the extended reduction and phase separation: upon

reaction the $Fe^{3+}(A)$ sites are partially depleted and the $Fe^{2+/3+}[B]$ positions are filled up, leaving only small space to Cu ions for staying inserted in the lattice (the ratio of the $Fe^{3+}(A)$ to $Fe^{2+/3+}[B]$ populations < 1; Table 4.2). In the catalytically most active mixed samples (0 < x < 1) distinct changes are seen: in the spent samples the ratio of the $Fe^{3+}(A)$ to $Fe^{2+/3+}[B]$ populations reverses to > 1, i.e. Co (and occasionally Cu) ions may occupy [B] sites in higher proportions. At the same time however, the reducibility is maintained for iron sites in the octahedral [B] positions: the full amounts of $Fe^{3+}[B]$ are converted to $Fe^{2+/3+}[B]$ upon exposing the fresh samples to the reaction mixture. In the cobalt ferrite the extent of reduction is the smallest among all the samples, for example, the Fe^{3+} state is mostly maintained in [B] sites, it prevails over the $Fe^{2+/3+}$ proportion in the spent catalyst.

Due to the lower coordination number of the tetrahedral cations, the attractive force for a single tetrahedral M-O bond will be strong [1]. Since each octahedral cation is surrounded by more number of anions, the octahedral M-O bond will be weaker and hence will be more polar. Jacobs et al [23] in a study, using LEIS (Low energy ion scattering, a technique which is sensitive to the outer most atomic layer), revealed that spinel surface sites are mainly octahedral and, hence, the octahedral cations are mainly exposed on the surface. Narasimhan and Swamy reported that weak octahedral M-O bonds act as strong alcohol adsorption centers [24]. The DR-IR studies of spent samples also show the pronounced splitting of octahedral bands. All these observations help to conclude that the octahedral sites are the main centers of organic molecule adsorption which causes the reduction of respective ions more on octahedral sites than on tetrahedral.

4.6.4. Carbonaceous deposits formed in the process of alkylation

Formation of carbonaceous deposits is clearly revealed on the catalytically most active, mixed Cu-Co ferrites. For example, TG measurements reveal a significant weight loss, amounting to 8 – 12 wt %, upon heating the samples in air. In this aspect, the different nature of the carbon deposit is worth to point out, namely, the deposits formed on the two copper-rich x= 0.25 and 0.5 samples exhibit similar behaviour, whereas the deposit formed on the cobalt rich x= 0.75 sample shows different properties. Three similarities for the x= 0.25 and 0.5 samples can be mentioned. First, their carbonaceous

deposits contain hydrogen in a significant proportion, the H_2 : CO ratio exceeds 1 as the mass spectroscopy of the TPD studies show. The second feature is the comparatively low temperature of the removal of the deposit: either in air (in TG) or in helium (in TPD) the deposits are removed at similar temperatures (around 580 K). The third feature is the formation of iron carbide in detectable amounts. This feature is due to the strong reducing potential exerted by these hydrogen-rich carbonaceous deposits: the carbon exists probably in a reactive form which is able to form iron carbide in detectable amounts in the two copper-rich mixed samples.

The cobalt–rich mixed ferrite is different in the aspects mentioned above. First, it does not contain hydrogen in high proportion. (The weight loss shown by TG is the largest, as well as the released amount of heat detected by the DTA). The second point is that the characteristic coke burning temperatures are the highest (c.a. 610 K for TG and TPD). Third, no iron carbide is formed (in detectable amount) in contrast to the highest amount of removed deposit (12 wt %).

On the basis of these three mentioned differences it is plausible to suggest that the structures of the carbonaceous deposits are different for the copper-rich and for the cobalt-rich samples. In the former x= 0.25 and 0.5 samples the layer is probably more porous, containing hydrogen and reactive carbon constituents, whereas probably more dense deposit is formed on the spent cobalt-rich ferrite sample. The structural difference in the carbonaceous deposit is probably correlated with the weaker extent of reduction in the x= 0.75 sample.

On the other hand, the properties of the carbonaceous deposit are also correlated with the acidity of catalysts. The acid-base properties of $Cu_{1-x}Co_xFe_2O_4$ reveal that acidity (basicity) increases (decreases) as 'x' increases. Moreover from pyridine adsorption it is found that acidity is mainly due to Lewis and presence of pyridinium ions at 1541 cm^{-1} (Bronsted sites) was hardly detected. Considering the previous finding, that the best catalytic performance is at the x = 0.5 composition, it can be assumed that a medium acidity is preferred for the reaction. This is also correlated with the composition of the carbonaceous deposits since on the preferred catalyst a high H : C ratio (> 1, i.e. "soft" deposit [25]) was detected.

4.6.5. Surface state – XPS

Number of changes observed from fresh to spent catalysts throws more light on the transformations that are occurring under experimental conditions. Main points from the XPS results can be summarized in a nutshell as below: Decrease in reducibility of copper with increasing x, increasing 3d bands overlap and redistribution of metal ions on spent catalysts. There is no static charging observed on any of the spent catalysts and a weak photoemission at 0.0 BE, except at x = 1, demonstrates the bulk conducting nature of the catalysts, in agreement with XRD results. Main observations from XPS in combination with the desired reaction pattern at x = 0.5 suggest the metal ions should be distributed optimally to have a large 3d band overlap. These factors demonstrate a hand-in-hand change and enhances the heterogeneity of the surface chemically and integrate the material electronically in such a way that multi-reactions are carried out in close proximity. This also indicates the synergism and effective utilization of reactants in this ferrospinel catalyst at 0<x<1. Large production of 2,6-xylenol with high phenol conversion and a ratio of 0.9 for Cu/Co+Fe at x = 0.5 insist on the optimum distribution of active species to have a highly heterogeneous surface.

Spent catalysts of composition x = 0.50 obtained from various phenol alkylations show high surface Cu/Fe atomic ratio though Cu:Co atomic ratio is 1:1 in the fresh. Very low Cu/Fe atomic ratio observed on butylation spent shows low and decreasing catalytic activity with reaction time. This clearly hints that Cu^{2+} is the species that enhances the alkylation activity largely and there is a sizeable redistribution of the cations on the catalyst surface during time on reaction conditions.

4.6.6. Cu-Co Synergism

XPS results in the present study clearly indicate that the Cu and Co 3d bands and their overlap play a central role in the catalytic performance in the methylation reaction. The Cu-rich composition (x = 0.0) exhibits the total reduction of Cu species and low surface Cu atomic % is possibly due to significantly large CH_3OH reforming and H_2 production. Contrarily, at x = 1.0, no significant chemical changes are observed with Co in XPS. However at intermediate compositions CH_3OH reforming is suppressed to a considerable level is also evident from the enhancement in the total amount of Cu species on the surface, Cu^{2+} content and methylation

activity compared to x = 0.0 (Figure 4.15). The decreasing amount of reduced Cu species with increasing x is attributed to the participation of Co in the hydrogenation activity under the present experimental conditions. Hydrogenation by Co consumes considerable amount of H_2 and converts C and CO into methane, methyl and MeOH species [26-30], which are utilized again through normal methylation route. This is in addition to Co activating MeOH for methylation. The above process might be preferred in the presence of Co rather than the reduction of Cu^{2+} to Cu, as in x = 0.0.

Low phenol conversion and 2,6-xylenol selectivity at x = 1, changes very significantly and favorably by the addition of Cu at x = 0.75 and 0.5 clearly demonstrates the prime importance of Cu in phenol adsorption and combined effect of Cu+Co for 2,6-xylenol selectivity in this system, as discussed in the previous paragraphs. It is the latter factor known as Cu-Co synergism that plays a major role in the phenol methylation reaction is clearly evident from the above discussions. In the fresh catalysts Co 3d band is the top most energy level. Observation of metallic copper on the spent catalysts clearly hints the broad Cu 4s band [31] also overlaps with 3d bands of Cu, Co as well as Fe at intermediate compositions under experimental conditions and makes these materials integrated chemically and electronically.

Recently we have shown the Cu-Co mixed oxide hydrotalcite catalyst performs oxidative steam reforming [32] with high rate of H_2 production and low levels of CO through hydrogen spillover mechanism as on Cu-ZrO_2 [33]; XPS results also demonstrate a close similarity between fresh and reduced catalysts. The above results support the Cu-Co synergism in the present ferrospinel environment also to perform methanol reforming to produce H_2 as well as hydrogenation of carbon species under methylation. The observed shift in the Fe 3d levels also suggests that Fe is not a silent spectator and involves in the electronic structure of the catalyst, at least at all intermediate compositions. A change in spin state of Co is also speculated from fresh to spent catalysts from the change in energy gap between Co 2p spin-orbit doublets and I_s [34] along with redistribution of Co in T_d and O_h sites (Figures 4.10 and 4.11). At x = 0.5 the above changes is accompanied with changes in Cu and Fe photoemission too and supports the spin-state also can influence the conversion and selectivity. IR studies on the above catalysts for acid-base properties support the above conclusions and a good correlation is observed with catalytic activity [35].

Desired reaction pattern observed in the case of other alkylations except butylation for the composition x = 0.50 is due to an optimum distribution of metal ions on surface and bulk and larger 3d band overlap. These factors enhances the heterogeneity of the surface chemically and integrate the material electronically in such a way that multi reactions are carried out in close proximity. This also indicates the synergetic and effective utilization of reactants in this ferrospinel catalyst. The relatively low Cu+Co/Fe ratio on the surface might be the reason for fast deactivation for butylation.

4.6.7. Comparison of different phenol alkylation reactions

Comparison of phenol alkylation with various alcohols brings out the similarities and differences between them. Figure 4.22 displays comparison of the activity data for various phenol alkylations under the respective optimum conditions with x = 0.50 composition. The optimum conditions required for better performance are different as the alkylating agent changes. With regard to the alkylating ability of the alcohols studied, the total conversion of the phenol follows the order: methanol $\approx$ DMC > ethanol > isopropanol $\approx$ isobutene. Hence the primary alcohols are the best alkylating reagents. This ability decreases with the size and branching of the hydrocarbon chain. One reason for this general trend can be explained by the easier dehydration of 2^0 and 3^0 alcohols to olefins. High temperatures do not favour alkylation, with the exception of methanol and DMC.

An important difference between methylation and higher alkylation is the reluctance of the later to form exclusive alkylated products at ortho position. Among methylation itself, a big difference was observed in the selectivity of methylated products between methanol and DMC when used as alkylating agents. The selectivity for 2,6-xylenol was higher with methanol than with DMC. Instead, the selectivity for the O-alkylated product was considerably higher in the methylation with DMC, whereas with methanol, negligible amount of O-alkylated product is formed.

Another important aspect derived from kinetic data is the difference in activity towards the formation of ortho dialkylated products as the alkylating agent changes. For example, although ortho dimethylation is highly favoured, in addition to ortho methylation, the same for dialkylation is found to be significantly low with other alcohols and it is

hardly formed with higher alkylating agents such as isopropanol and isobutene. Moreover higher alcohols result other side products like p-alkylated products that reduces the ortho selectivity. In the experiments with ethanol, isopropanol and isobutene, lower alkyl phenols are also formed, by cracking of a $C_{aliphatic}$ - $C_{aliphatic}$ bond in the chain of the initially formed alkyl phenols. This infers, the steric factor of alkylating agent is an important criterion for efficient ortho alkylation. Kinetic and thermodynamic studies on phenol methylation indicate that dimethylated product is formed through sequential methylation. Hence, single ortho methylated product is very much essential to reside sufficiently long time, but not too long, on catalyst surface for its further methylation to form orthodimethylated product. A very large residence time of ortho methylated phenol might lead to second methylation at all possible positions; however except 2,6-xylenol other products are not observed suggests the residence time is not too long. This indicate the steric hindrance of alkyl group is not favourable for proper orientation and hence the geometric fitting over the present catalyst system for subsequent ortho alkylation.

Number of changes observed in XPS from fresh to spent catalysts of composition x = 0.50 for different phenol alkylation throws more light on the changes that are occurring under experimental conditions. The following important observations can be derived from XPS data of spent catalysts:

(1) A clear reduction of Cu is seen on all spent; however the extent of reduction depends on the alkylating agent.

(2) A definite partial reduction of all metal ions after reaction and a consequent increase in the overlap of 3d bands is observed on all spent catalysts, except butylation catalysts.

Main observations from XPS in combination with the desired reaction pattern suggest overlap of '3d' orbitals of all the three ions in the valence level is very much essential for high activity towards phenol alkylation. This is evidenced from the VB photoemission spectra of the spent x = 0.50 composition, where it has been found that the VB spectra of the spent catalyst is narrowed down due to better overlap in comparison with the fresh. The time on stream studies indicate that the catalyst is stable towards all the alkylation except butylation. The relatively low Cu+Co/Fe ratio on the surface might be the reason for fast deactivation for butylation. Desired reaction pattern observed in the

case of methylation and ethylation is due to an optimum distribution of metal ions on surface and bulk and larger 3d band overlap. These factors enhances the heterogeneity of the surface chemically and integrate the material electronically in such a way that multi reactions are carried out in close proximity. This also indicates the synergetic and effective utilization of reactants in this ferrospinel catalyst.

4.6.8. Acid-base strength and methylation activity performance

A detailed study on the performance of $Cu_{1-x}Co_xFe_2O_4$ catalysts towards phenol methylation has already been discussed in section I of this chapter. Figure 4.29 displays a comparison between the catalytic performance in terms of phenol conversion and selectivity of 2,6-xylenol obtained at a reaction temperature of 325^0C with a phenol:methanol composition of 1:5, and relative acidity obtained from the area of ν_{8a} and ν_{19b} bands in FTIR spectra of pyridine adsorbed catalysts.

In this reaction methylation is sequential and 2,6-xylenol is produced at the expense of o-cresol and for simplicity o-cresol selectivity is not given in Figure 4.29. A steep increase in relative acidity with Co concentration (Figure 4.29) clearly supports an increase in acidity both in terms of strength and number. It is clear from Figure 4.29 that neither highly acidic nor weakly acidic (or basic) catalyst at x = 1.0 and 0.0, respectively, is active towards phenol conversion to produce 2,6-xylenol. However $0.25 \geq x \leq 0.75$ show better catalytic performance and x = 0.5 is superior and demonstrates an intermediate acidity character. This clearly indicates that an optimum acid-base property favours the overall reaction. It is also interesting to note that usually Friedel-Crafts alkylation reactions require highly acidic catalysts, which is not entirely true in the present case. The extent of secondary methanol reforming reaction decreases from x = 0 to 1, as seen from reduced Cu-species in XPS results might be a reason for the above contradiction. It is clear that substitution of Co^{2+} for Cu^{2+} creates an increase in acidity with a concomitant decrease in the amount of basic sites. XPS results on $Cu_{1-x}Co_xFe_2O_4$ demonstrate that x = 0.5 composition exhibits Cu-Co synergism and the same is correlated with the catalytic performance. Cu-Co synergism and low coke content at x = 0.5 among intermediate compositions suggests that intermediate acidity enhances methylation activity in a way that

coke is hydrogenated to methyl species. This is further supported by the fact that the activity of Fischer-Tropch catalyst are enhanced when Co-is introduced into the system [28].
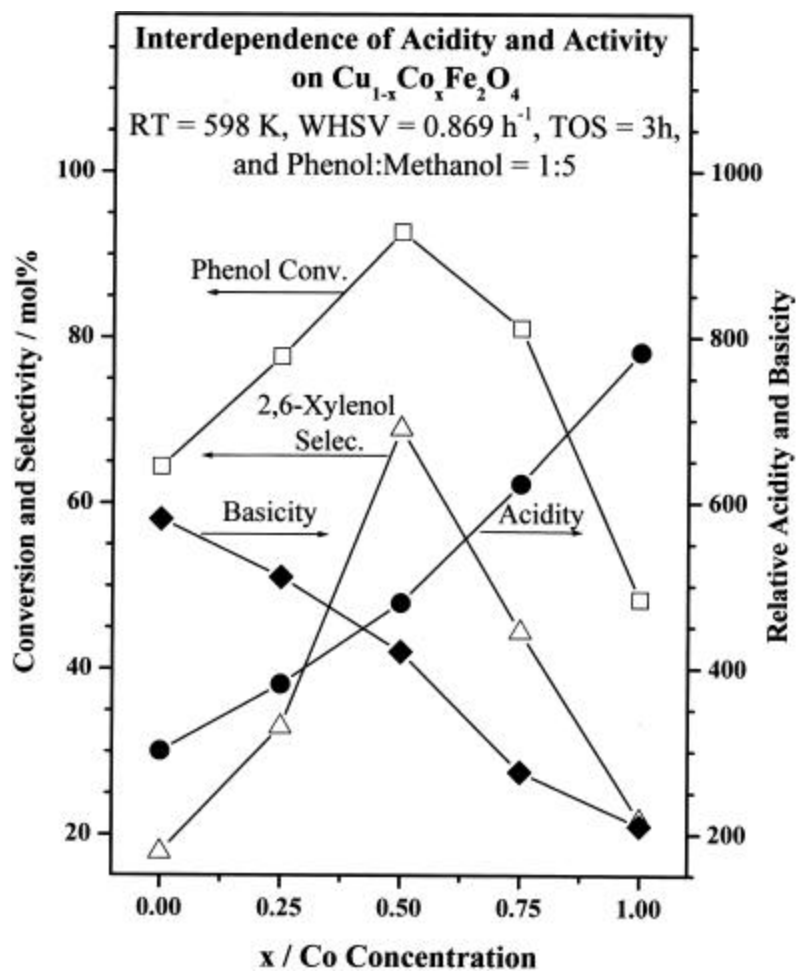
Figure 4.29: A comparison between the catalytic performance (phenol conversion and selectivity of 2,6-xylenol), the relative acidity obtained from the area of ν_{8a} and ν_{19b} bands from pyridine adsorbed on $Cu_{1-x}Co_xFe_2O_4$ catalysts at 373 K and the relative basicity obtained from the area of the bands between 1700 and 1250 cm^{-1} from CO_2 adsorbed on $Cu_{1-x}Co_xFe_2O_4$ catalysts at 298 K. Note the good correlation between the intermediate acid-base property and high catalytic activity.

4.7. REFERENCES

1   Ref. 18-20 of chapter 1

2   E. Murad and J. H. Johnston, in: *Applications of Mössbauer Spectroscopy to Inorganic Chemistry*, ed. G. J. Long, Plenum Press, New York, Vol. **2** (1985) p. 507.

3   E. Vandenberghe and E. de Grave, in: *Applications of Mössbauer Spectroscopy to Inorganic Chemistry,* eds: G. J. Long and F. Grandjean, Plenum Press, New York, Vol. **3** (1986) p. 59.

4   W. Niemantsverdriet, A. M. van der Kraan, W. L. van Dijk and H. S. van der Baan, *J. Phys. Chem.*, **84** (1980) 3363.

5   C. S. Gopinath, S. Subramanian, M. Paranthaman and A. M. Hermann, *Phys. Rev. B*, **48** (1993) 15999.

6   C. S. Gopinath, S. Subramanian, P. S. Prabhu, M. S. R. Rao and G. V. S. Rao, *Physica C*, **218** (1993) 117.

7   G. Moretti, G. Fierro, M. L. Jacono and P. Porta, *Surf. Interface Analysis*, **14** (1989) 325.

8   S. Poulston, P. M. Parlett, P. Stone and M. Bowker, *Surf. Interface Analysis*, **24** (1996) 811.

9   B. R. Strohmeier, B. E. Leyden, R. S. Field and D. M. Hercules, *J. Catal.*, **94** (1985) 514.

10   V. A. M. Brabers, *Mat. Res. Bull.*, **18** (1983) 861.

11   Y. Okamoto, K. Fukino, T. Imamaka and S. Teranishi, *J. Phys. Chem.*, **87** (1983) 3740.

12   G. Van der Laan, C. Westra, C. Haas and G. A. Sawatzky, *Phys. Rev. B,* **23** (1981) 4369.

13   M. S. Stranick, M. Houalla and D. M. Hercules, *J. Catal.*, **106** (1987) 362.

14   N. S. McIntyre and M. G. Cook, *Anal. Chem.*, **47** (1975) 2210.

15   Z. Zsoldos and L. Guczi, *J. Phys. Chem.*, **96** (1992) 9393.

16   P. Mills and J. L. Sullivan, *J. Phys. D*, **16** (1983) 723.

17   T. Fujii, F. M. F. de Groot, G. A. Sawatzky, F. C. Voogt, T. Hibma and K. Okada, *Phys. Rev. B*, **59** (1999) 3195.

18   J. J. Yeh and I. Lindau, *At. Data Nucl. Data Tables*; **32** (1985) 1.

19   L. H. Tjeng, C. T. Chen, J. Ghijsen, P. Rudolf and F. Sette, *Phys. Rev. Lett.*, **67** (1991) 501.

20   T. Mathew, N. R. Shiju, K. Sreekumar, B. S. Rao and C. S. Gopinath, *J. Catal.*, **210** (2002) 405.

21   L. A. Chick, L. R. Pederson, G. D. Maupin, J. L. Bates, L. E. Thomas and G. J. Exarhos, *Mater. Lett*., **10** (1990) 6.

22   T. Kotanigawa, M. Yamamoto, K. Shimokawa and Y. Yoshida, *Bull. Chem. Soc. Japan.*, **44** (1971) 1961.

23   J. P. Jacobs, A. Maltha, J. R. H. Reintjes, T. Drimal, V. Ponec and H. H. Brogersma, *J. Catal.*, **147** (1994) 294.

24   C. S. Narasimhan and C. S. Swamy, *Appl. Catal.*, **2** (1982) 315.

25   M. Guisnet, in: *Handbook of Heterogeneous Catalysis,* eds: G. Ertl, H. Knözinger and J. Weitkamp, VCH, Weinheim, Vol. **2** (1997) p. 626.

26   G. Fierro, M. L. Jacono, M. Inversi, R. Dragone and P. Porta, *Topics in Catal.*, **10** (2000) 39.

27   A. J. Marchi, J. I. Di Cosino and C. R. Apesteguia, *Catal. Today*, **15** (1992) 383.

28   G. Fornasari, A. D. Huysser, L. Mintcher, F. Trifiro and A. Vaccari, *J. Catal.*, **135** (1992) 386.

29   C. Cabet, A. C. Roger, A. Kiennemann, S. Läkamp and G. Pourrow, *J. Catal.*, **173** (1998) 64.

30   E. Iglesia, *Appl. Catal. A*, **161** (1997) 59; and references therein.

31   A. J. Dekker, "*Solid State Physics*", Prentice Hall, UK, 1981.

32   S. Velu, K. Suzuki and C. S. Gopinath, *J. Phys. Chem. B*, (In press, 2002).

33   K. D. Jung and A. T. Bell, *J. Catal.*, **193** (2000) 207.

34   V. L. J. Joly, P. A. Joy, S. K. Date and C. S. Gopinath, *J. Phys. Condens. Matt.*, **13** (2001) 649.

35   T. Mathew, N. R. Shiju, B. B. Tope, S. G. Hegde, B. S. Rao and C. S. Gopinath, *Phys. Chem. Chem. Phys.*, **4** (2002) 4260.

CHAPTER 5

SUMMARY

AND CONCLUSIONS

The various conclusions drawn based on the work are summarized in this chapter.

Chapter 1 presents a general introduction to catalysis and various types of catalysts. It mainly describes the published literature on the structure, preparation and catalytic aspects of spinels with special emphasize on ferrites. The acid-base properties, an important aspect of heterogeneous catalysis, and its origin on oxide surfaces are discussed briefly in this chapter. It presents the use of various alkyl phenols and the importance of phenol methylation. Various catalysts reported for phenol methylation are discussed. The necessity of developing a catalyst system for phenol methylation and why ferrites based on Cu and Co are employed for this are described. The necessity of using XPS being a surface science technique in catalysis is described.

Chapter 2 describes the procedure for the synthesis of various compositions of the $Cu_{1-x}Co_xFe_2O_4$ (x = 0, 0.25, 0.50, 0.75 and 1) were prepared by co-precipitation method and characterized by XRD, XRF, SEM, surface area (by N_2 sorption), IR and TG-DTA. Theory and experimental procedure for each technique are described briefly under the respective technique. Theory and experimental procedure employed for other techniques such as Mössbauer, XPS, TG-DTA, TPR and TPD are also discussed in this section. The experimental set up for gaseous phase reaction is mentioned in this secton.

X-ray diffraction of fresh catalysts revealed the formation of spinel phase along with a mixture of CuO and α-Fe_2O_3 phases at x = 0.0, while trace amount of α-Fe_2O_3 for x$\geq$0.25. IR spectra of calcined samples reveal that the metal ions distributed in two different environments in spinel at 710 cm^{-1} (ν_1) and 460 cm^{-1} (ν_2), attributed to tetrahedral (T_d) and octahedral (O_h) coordinated metal-oxygen bands respectively. Scanning electron micrograms of calcined samples showed particles of size in the range 1-6 μm, which confirm the crystalline nature of the material.

The acid-base properties of the system is evaluated by using different probe molecules and is discussed in detail. The IR spectra of ferrospinel reveals Fe^{3+} and Co^{2+} ions are mainly responsible for various hydroxy groups on the surface. The IR adsorption of pyridine is carried out to evaluate the acidiy of the system. Temperature dependent IR studies of pyridine adsorbed spinels and on deliberately added metal oxide to the spinel phase exemplifies the contribution of metal ions and its coordination state towards Lewis

acidity. IR studies of spinel surface adsorbed with CO_2 and adsorption studies of electron acceptors such as 7,7,8,8-tetracyanoquinodimethane, 2,3,5,6-tetrachloro-1-4-benzoquinone and p-dinitrobenzene are carried out to evaluate the nature of basic sites and the strength and distribution of electron donor sites present on the spinel surface. It is found that acidity (basicity) of the $Cu_{1-x}Co_xFe_2O_4$ spinel system increases (decreases) from x = 0 to 1.

Chapter 3 is divided into two parts. **Section I** presents the catalytic activity data of phenol alkylation in the vapour phase over $Cu_{1-x}Co_xFe_2O_4$. Among various alkylation reactions, methylation of phenol is studied extensively. Kinetic and catalysis aspects of phenol methylation is discussed in this section. The optimization of phenol methylation is carried out by varying reaction parameters such as temperature, methanol/phenol mole ratio, space velocity and influence of water in the feed mixture. Phenol methylation gives two major products namely o-cresol and 2,6-xylenol. Large phenol conversion and 2,6-xylenol production is observed at 350^0C and x = 0.5 shows good catalytic performance. Increase in selectivity of 2,6-xylenol at the expense of o-cresol demonstrates the phenol methylation is sequential.

Phenol alkylation is also carried out by employing various alkylating agents such as DMC, ethanol, isopropanol and isobutene. Alkylation of phenol with DMC results both C- and O- alkylated products. Reaction of phenol with ethanol provides ortho ethylated 2-ethyl phenol (EtPhOH) as major product over $Cu_{1-x}Co_xFe_2O_4$. Kinetic parameters calculated from Arrhenius analysis for phenol ethylation are in good agreement with experimental results that intermediate compositions exhibit relatively low activation energy (E_a) towards phenol conversion than end compositions. Compensation effect observed between frequency factor and E_a suggests the ethylation reaction mechanism remains the same at all x values. Reaction of phenol with isopropanol (iPrOH) provides ortho alkylated product, viz., 2-isopropyl phenol as major product over the $Cu_{1-x}Co_xFe_2O_4$ catalyst system. The main products of t-butylation of phenol with isobutene as alkylating agent are 2-tertiary butyl phenol (2-TBP), 4-tertiary butyl phenol (4-TBP) and 2,4-di tertiary butyl phenol (2,4-DTBP), of which 2-TBP predominates over the others.

It has been found that influence of Cu+Co composition is a decisive factor towards PhOH conversion and is evident from the comparatively large PhOH conversion at

intermediate compositions ($0<x<1$) compared to end compositions ($x = 0$ and 1) for any type of phenol alkylation. Irrespective of the alkylating agent, $x = 0.5$ composition shows maximum PhOH conversion at all temperatures studied.

Section II describes the mechanistic aspects of phenol methylation over the surfaces of $Cu_{1-x}Co_xFe_2O_4$. FTIR adsorption of reactants and products of phenol methylation were carried out over $Cu_{1-x}Co_xFe_2O_4$ to understand the mechanism of phenol methylation. The spectra obtained from the chemisorption of methanol onto $Cu_{1-x}Co_xFe_2O_4$ at $\leq 100^0C$ are composed of the superimposed spectra of surface methoxy and formate groups. Methoxy formation on the surface of these oxides is most likely due to dissociative chemisorption. IR adsorption of phenol on $Cu_{1-x}Co_xFe_2O_4$ shows signals of both undissociated phenol and phenolate like species. Phenolate species are formed due to the dissociative adsorption of phenol on an acid-base pair site. Phenolate ion is adsorbed on metal cation (Lewis acid site) whereas the dissociated H adsorbs as a H^+ on a nearby O atom. It is found that methylation of phenol is initiated by the protonation of methanol with the aid of a Lewis acid base pair. Probably the protonation of methanol occurs on the oxides by accepting protons released from the adsorbed phenol and the protonated methanol attacks at the ortho position of phenol to form the ortho methylated products. Thus the active center for the ortho methylation is an acid-base pair site.

Chapter 4 is divided into two parts. **Section I** describes the characterization of spent catalysts to understand the various aspects of physicochemical changes that occur both in bulk and on surfaces of all the compositions of the system $Cu_{1-x}Co_xFe_2O_4$ due to phenol methylation. XRD, TG-DTA, DRIFT IR, surface area, TPR and TPD, Mössbauer and XPS were carried out for this purpose and the results were discussed in detail in this section.

Though kinetic studies of phenol alkylation using various alcohols and or alkene is carried out over $Cu_{1-x}Co_xFe_2O_4$, special emphasize for characterizing the spent sample has taken mostly for phenol methylation and ethylation. XRD of the spent catalysts displayed better crystallinity hints the integrity of the structure. Various structural changes have been observed due to exposure of the fresh catalysts to the reaction mixture. Namely, phase separation to Cu_2O and magnetite in x= 0 and 0.25 samples, various extents of reduction

(decreasing monotonously with the copper content, and resulting in partial reduction and redistribution of iron in tetrahedral (A) and octahedral [B] sites) and formation of carbonaceous deposits are detected. The catalyst performance is correlated with the discussed three structural changes, viz. with the occasional phase segregation, with the partial reduction of metal ions, including the appearance of $Fe^{2+/3+}$ ions in various proportions in the [B] sites, and with the formation of carbonaceous deposits.

The occasional phase segregation is mostly revealed in Cu-rich (x= 0, and 0.25) samples. Stable magnetite formation is observed, and separate Cu_2O (and, after reduction, metallic copper) regions appear. The copper phase opens path for reduction in the neighboring regions in further stages of reaction. The reaction conditions, optimized for production of 2,6-xylenol, were extensively reducing. Thus, iron ions located in the octahedral [B] sites became reduced to the $Fe^{2+/3+}$ state. During reaction the ratios of Fe^{3+}(A) to $Fe^{2+/3+}$[B] were also changed, and incorporation of Cu and Co to the [B] sites had also taken place. Thus, strength and distribution of Lewis centers, necessary for reaction were also modified.

The carbonaceous layer formed is the trace of the progress of reaction: it is strongly correlated with the appearance and extent of the catalytic activity. It can be suggested that in the catalytically most active Cu-rich x= 0.25 and 0.5 samples the Lewis centers are prevailing, the carbonaceous deposit contains hydrogen, and the carbon is rather reactive in this layer. In the Co-rich x= 0.75 sample the deposit is less abundant in hydrogen, the carbon present is more dense, e.g. less reactive.

X-ray photoelectron spectroscopy and x-ray induced Auger electron spectroscopy revealed the presence of Cu^{2+}, Fe^{3+}, Co^{2+} and Co^{3+} species on fresh catalysts. Metal ions got reduced partially to lower oxidation states on spent catalysts. Reducibility of Cu^{2+} species decreases with increasing x. Valence band photoemission studies demonstrated a clear increase in the overlap between 3d bands of Cu, Co and Fe from fresh to spent catalysts.

Irrespective of the alkylating agent, composition x = 0.50 shows maximum activity in terms of phenol conversion and corresponding ortho alkyl selectivity. Hence the analysis of the spent for various phenol alkylations are restricted only to x = 0.50 composition. However only XRD and XPS has chosen to examine the changes in surface

and the oxidation states of various metal ions for different alkylations. XRD of spent catalysts resulted from various phenol alkylations displays all characteristics reflections and ascertain the integrity of the spinel structure. Presence of small amount of metallic Cu, Fe and Fe_xC_y phases are observed on all the spent except for butylation. The intensity of metallic Cu and Fe peaks varies as the alkylating agent changes. XPS analysis of the spent catalyst of composition x = 0.50 obtained from various phenol alkylations revealed that reduction of Fe^{3+}, Co^{3+} and Cu^{2+} ions have occurred and the extent of reduction depends on the alkylating agent.

Various features and conclusions arrived due to the characterization of spent catalysts were discussed in **Section II**. The importance of Cu-Co synergism that plays a major role in the efficient dimethylation of phenol to 2,6-xylenol is discussed in this section. The better catalytic results observed with x = 0.5 is attributed to an optimum distribution of Cu-species with heteroatom neighbors on the surface and the maximum overlap between the Cu and Co 3d bands makes the ferrospinel integrated chemically and electronically. Low phenol conversion and 2,6-xylenol selectivity at x = 1, changes very significantly and favorably by the addition of Cu at x = 0.75 and 0.5 clearly demonstrates the prime importance of Cu in phenol adsorption and combined effect of Cu+Co for 2,6-xylenol selectivity in this system. It is the latter factor known as Cu-Co synergism that plays a major role in the phenol methylation reaction. Cu-Co synergism in the present ferrospinel environment also to perform methanol reforming to produce H_2 as well as hydrogenation of carbon species under methylation. The observed shift in the Fe 3d levels also suggests that Fe is not a silent spectator and involves in the electronic structure of the catalyst, at least at all intermediate compositions.

Different phenol alkylations are compared in this section. With regard to the alkylating ability of the alcohols studied, the total conversion of the phenol follows the order: methanol $\approx$ DMC > ethanol > isopropanol $\approx$ isobutene. An important difference between methylation and higher alkylation is the reluctance of the latter to form exclusive alkylated products at ortho position. Spent catalysts of composition x = 0.50 obtained from various phenol alkylations show high surface Cu/Fe ratio and segregation of Cu on the surface. Very low Cu/Fe ratio observed on propylation and butylation spent catalysts

show low and decreasing catalytic activity with reaction time. This clearly hints that Cu^{2+} is the species that enhances the alkylation activity largely and there is a sizeable redistribution of the cations on the catalyst surface during reaction conditions.

Main observations from XPS in combination with the desired reaction pattern suggest overlap of '3d' orbitals of all the three metal ions in the valence level is very much essential for high activity towards phenol alkylation. This is evidenced from the VB photoemission spectra of the spent x = 0.50 composition, where it has been found that the VB spectra of the spent catalyst is narrowed down due to better overlap in comparison with the fresh. A correlation between acidity, basicity and catalytic performance reveals that an intermediate acid-base character enhances the phenol methylation activity.